Terahertz Imaging and Spectroscopy: Application to Defense and Security in front of the examination panel

Joyce Bou Sleiman

université de BORDEAUX

THESIS PRESENTED

TO OBTAIN THE GRADE OF

DOCTOR AT

UNIVERSITY OF BORDEAUX

Department of Physics and Engineering

Specialty

Laser, Materials and Nanoscience

Presented by

Joyce BOU SLEIMAN

Entitled

Terahertz Imaging and Spectroscopy: Application to Defense and Security

Presented the 2 of June 2016, in front of the examination panel:

Bruno Bousquet	Associated professor, Univ. of Bordeaux	Member
Laurent Chusseau	Research director, Univ. of Montpellier	Member
Dominique Coquillat	Research director, Univ. of Montpellier	Referee
Christelle Defaye-Geneste	Head of Customs and International Trade, La Poste	Invited
Yann Deval	Professor, Univ. of Bordeaux	Member
Bernd Fischer	Doctor, Research Institute of Saint-Louis	Member
Jean-Paul Guillet	Associated professor, Univ. of Bordeaux	Member
Jean-François Lampin	Research director, Univ. of Lille	Referee
Patrick Mounaix	Research director, Univ. of Bordeaux	Supervisor

Acknowledgements

§ Thank you! §

Table of Contents

LIST OF FIGURES

LIST OF TABLES

INTRODUCTION

Security has always been an important issue for governments and organizations. The need for more rigorous and systematic system, providing the highest level of security, leads to increase studies to develop more precise and efficient systems able to detect all kind of threats. Every institution is looking for the best level of security, specifically the postal chain institution around the world. Nowadays, transportation of goods is made all over the world through different types of transport such as planes, rails, trucks, etc., and this adduces the danger at different moment: during the transportation and inside the sorting centers. Thus, postal chain institutions are looking for new ways to increase their potential in securing and protecting the commodities and the people while parcels run through the warehouses. The unique challenge they are facing, is the need of ensuring high security level, while keeping the efficiency and flexibility of the supply chain. Part of the parcel inspection is manual and law conditions prohibit post members from opening the parcels. It needs the intervention of a custom member to do so. This decelerates the scanning flow because the suspicious package goes off the scanning chain and is stored waiting for the customs opening and inspection. So the probability of suspicion in the parcel should be very high before extracting it from the chain. Also, the human control has three other main disadvantages:

1- Slowing down the flow of parcels and delaying the shipment procedure, due to the need of sending the parcels for lab analysis.
2- Inducing a danger of facing risky chemicals while opening specific parcels.
3- Need more manpower and inspectors.

Our work will provide preliminary methods that can be developed and adapted for the postal chain to strengthen security while reducing human's efforts in manual inspection, by presenting the potential of terahertz techniques in parcel inspection.

This PhD is a part of the InPoSec (Integrated Postal Chain Security) project, dedicated to finding complementary applications to the existing ones, in order to provide a technology exhibiting the same level of performances compared to conventional daily used equipment's in the postal chain centers, which can be easily used by workers without any dangerous effect on their health. The entire project is divided in different axes.

One of our missions is to provide all imaging supplies and spectroscopic data for other members of the project. In this aim, analysis was performed at Chronopost center and CDG airport to retrieve statistical information about parcels and to carry out measurements on several parcels in X-ray systems used in the sorting center. We fabricated these parcels with false threats and suspicious objects, and analyze it with the terahertz imaging systems. Thus, the performance of several Terahertz imaging techniques can be compared to x-ray scanners. Some of these data are transferred to other project members for two basic studies:

1- Development of the Bayesian algorithm in collaboration with Datalone to be applied to the statistical postal data to study the risk assessment of a parcel, based on several information, such as expedition country, weight, size, etc.
2- Object shape recognition algorithm in collaboration with Spykenet technology. The aim is to automatically identify the presence of a weapon in a high velocity scanning flow. This algorithm is applied to x-ray data extracted from the post center at CDG as well as terahertz data obtained from our systems.

However, our main part of the work is the demonstration of the potential and capabilities of the terahertz technology for parcels and letters screening and inspection to detect sought threats in parcels and letters, as weapons, explosives, bombs, radioactive materials, etc. Therefore, terahertz technology is chosen for several reasons:

1- It is a non-contact technique that is able to inspect objects through packaging,
2- Non-destructive for objects in inspection,
3- Non-invasive radiation that has no dangerous effects on human health,
4- It provides a chemical signature that can identify powders and dangerous material.

This study describes and explains a new process of parcels inspection by positioning the terahertz technology as complementary to X-ray scanner and not a substituted method. As Figure 0.1 shows, the processes of scanning passes first by the X-ray system that gives the first feedback on the contents and compare it to the declaration of the owner. Here, most of the parcels are classified as safe and can be distributed, yet, for several parcels the doubt in their content leads to pass them on the second scanning stage. Here, terahertz imaging can inspect the parcels and provides similar information compared to the x-ray scanner. However, two additional aspects can be provided by terahertz. The first one is the identification of low, dense amorphous materials that are almost transparent for x-ray radiations. Secondly, having the possibility of terahertz spectral imaging will provide chemical recognition and thus identification of a powder on the image through packaging. After this step, if suspicious doubt remains on the parcels content, then it passes to the last stage which is the examination by the inspector. This process is able to provide more reliable information and accelerate the process.

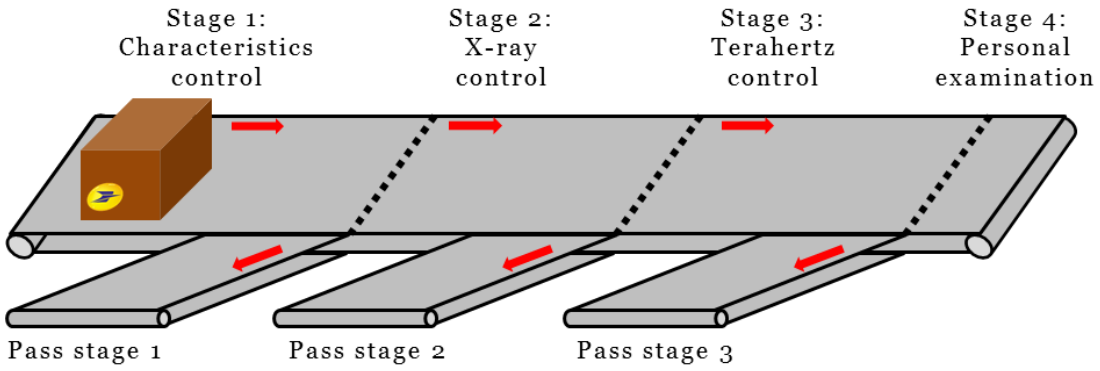

Figure 0.1: Intended concept with the presence of terahertz technology in the postal chain scanning process.

To demonstrate the ability of terahertz waves and the limits in achieving these objectives, the present study is constituted of three main analysis methods: spectroscopy, imaging and spectral imaging. The main interest is given to parcels inspection because letter inspection was considered for

the project as further objective, due the fast flow and the impossibility to control it. The report is divided in three chapters.

The first chapter presents a global idea on terahertz technology, the main sources and detectors developed and the basic application of terahertz in several domains. Moreover, it discusses the main threats that are sought in packages and having an impact on safety while transporting it, such as weapons and explosives. The main used techniques for detection of these threats are listed, and their physical concepts, advantages and disadvantages are developed and compared to terahertz potential. The last part of this chapter highlights the advanced research in terahertz imaging and spectroscopy for security applications.

The second chapter presents terahertz time-domain spectroscopy and spectral imaging for explosives detection. Terahertz spectroscopy analysis of several packaging materials used in postal chain, are represented and their dielectric response is extracted. A database of explosives was created and two specific explosives presenting complex spectra, as well as their mixture are analyzed. However, for industrial applications as the postal chain, the analysis of explosive needs a tool that construes the response of explosives in order to identify them. Thus, chemometric tools were used and applied to terahertz spectra and spectral imaging to construct qualitative and quantitative analyses. First, the chapter introduces the chemometric tools and the way to deal with a multivariate analysis for better understanding of the terahertz data. Three basic chemometric tools are used: (i) principal component analysis is applied to describe a set of unknown data and identify similarities between sample, (ii) partial least square-discriminant analysis model is used to create classes and then classify unknown samples inside or outside one of these classes, (iii) partial least square analysis algorithm is performed in order to create a model able to quantify several explosives concentration, with special spectra features, in pure state or in mixtures.

The third chapter discusses terahertz 2D and 3D imaging methods applied to parcel inspection to provide internal information about the packages without opening it. Three different imaging setups are presented and results of packages screening are shown. The first system is based on millimeter passive imaging, the second is a home-made millimeter continuous wave setup, and the third is a millimeter frequency modulated continuous wave commercial system. The performances of these systems on packages that contain false threats are compared. Furthermore, three dimensional imaging configurations are developed to provide data for tomography reconstruction. Thus, the last part presents the tomographic reconstruction method where a special algorithm is developed to take into account the Gaussian distribution of the terahertz beam while reconstructing a 3D volume. The results of this reconstruction as well as image processing tools are presented for packaging inception.

CHAPTER I

GENERAL INTRODUCTION TO TERAHERTZ WAVES AND APPLICATIONS TO THREATS ANALYSIS.

This chapter discusses the basic physics of terahertz radiations and presents some of the terahertz sources and detectors that can be advantageous for specific applications. In addition, a general idea of the applications domain of terahertz wave is provided. Then, a brief description of the techniques used in security application for detection of weapons, explosives, bombs, drug, etc. is presented and a comparison of the advantages and the disadvantages of each technique are discussed for postal chain security applications. Finally, some of the terahertz studies in security applications are presented, especially THz imaging and spectroscopy for postal security application.

I. TERAHERTZ TECHNOLOGY

I.1. INTRODUCTION

Electromagnetic (EM) spectrum contains several regions with different properties allowing specific developments and achievements in many application fields. Since the mid twentieth century, a particular region of the EM spectrum has been extensively studied, ranging between infrared and microwaves, and known as terahertz domain [1]. In this domain, the frequencies of the EM waves are ranging between 0.1 and 30 THz (1 THz = 10^{12} Hz), which correspond to the wavelengths between 3 mm and 10 μm. Figure I.1 shows the localization of the terahertz domain within the Electromagnetic spectrum. In this positioning, THz waves share the characteristics of both infrared and microwaves domains, namely:

- Non-ionizing: photons in the THz region have low energies, ranging between 0.41 meV and 124 meV. This low energy has no ionizing effect on biological tissues.
- Chemical signature/fingerprints: solid, liquid or gas, several materials have their own signature after interaction with the THz waves, which allow their identification. This property is widely exploited in THz spectroscopy applications as for example the case of powders identification.
- High transmission/penetration in non-dielectric materials: many amorphous materials are transparent for THz waves, such as plastic, textile, paper, etc. This permits non-contact inspection applications and imaging
- Absorption of polar liquids such as water: this particularity highlights the potential of THz waves in specific applications. Also, being absorbed by water, THz waves cannot penetrate more than several dozen of microns through the skin for example.

One main limitation of the terahertz waves is that they are not able to pass through metal. But the combination of all the other characteristics mentioned before, provides the THz radiations with a high potential in many applications. However, both THz generation and detection systems must be robust to make the THz-based solutions reliable. Although the unique position of the terahertz band within the EM spectrum between microwave and infrared provides another very interesting advantage: the possibility to find either electronic or optical devices for the generation/detection processes. Despite the advanced development of THz systems, the basic problem nowadays is the limitation of the power emitted from the THz sources. Consequently, many application fields have not switched to the THz radiations up to now and the EM range 0.3 - 10 THz is still considered as a

technological gap due to the fewer available high power cheap sources in this range. As shown in Figure I.2 [2] that represents the output power versus frequency for numerous terahertz sources, the generated power decreases dramatically with frequency and limits the choices of accessible frequency bands with acceptable power for applications. Yet, scientists continue their efforts to achieve better performances on THz devices. Currently, the challenges consist in the development of high output power compact sources and high sensitivity compact detectors, which should also be portable, tunable and low cost.

A good knowledge of the THz devices is very important in order to use them in the best conditions. Thus, a brief description of the existing sources and detectors is given in this chapter and limiting the discussion to the most interesting sources and detectors in the area, that can produce high power and can be used in security applications.

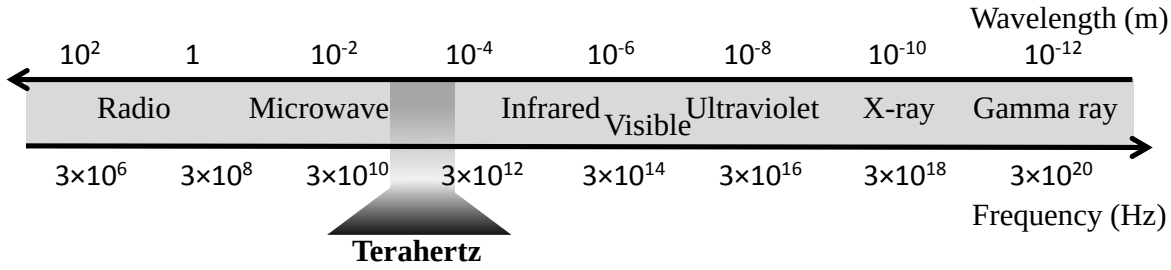

Figure I.1 : Terahertz positioning in the electromagnetic spectrum, the terahertz band is localized between microwaves and infrared.

I.2. TERAHERTZ SOURCES

Many terahertz source technologies were developed during the last years, providing broadband waves or narrow-linewidth continuous waves (CW), with an output power going from nW to several tens of watts. High power sources are the most needed for real time imaging security application due to the deeper penetration ability, but it is not the main criterion in the choice of the sources. There is also an importance for the frequency band emitted, the mode of emission, i.e. pulsed or continuous, the access of amplitude and phase information, the employment of simple detectors, the ability to be set into very compact systems, etc. Here we will discuss several terahertz sources, such as thermal sources, solid-state electronics, vacuum sources, and emitters driven by lasers.

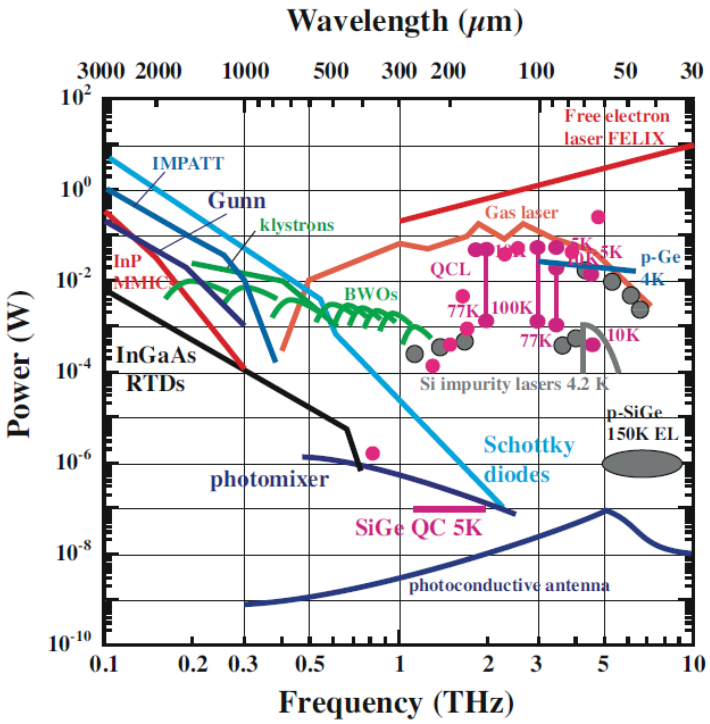

Figure I.2 : Logarithmic plot of the emitted power as a function of frequency of different THz source technologies.

I.2.1. Thermal sources

All objects surrounding us, with a temperature greater than 10 K, emit naturally terahertz electromagnetic waves in all directions as black-body radiation. However, the emitted radiations have a very low average power of several nW. This type of terahertz source has been used for many years, especially for astronomy and FTIR applications, and basically, it is well employed in passive setups. It will be discussed in detail in the next chapters in the passive imaging setup [3], [4].

I.2.2. Solid-state electronic sources

These sources are the most commercially used, among them, the diode-based sources such as Gunn diode, IMPATT diodes (IMPAct ionization Transit Time), TUNNETT (Tunneling Transit Time) diodes, and transistors-based sources such as the CMOS (complementary metal-oxide semiconductor) and the HEMT (High-electron-mobility transistor). A detailed description of the difference between each of these sources is given in [5]; also a comparison between the output powers of the solid-state electronic sources is shown in Figure I.3. For the diode-based sources, a maximum of 27 dBm at 150 GHz is achieved with a Si IMPATT, corresponding to 0.5 W; and for the transistor-based sources, a maximum of 7 dBm is obtained at 130 GHz with the SiGe HBT, and the power is in the order of 5 mW. Even with a power of several mW, Gunn diodes, which are based on negative

differential resistance (NDR), are widely used as commercial millimeter-wave and terahertz sources. More details about Gunn diodes are given in the next chapters, because it is used as a source in one of the imaging setups presented in this report. The disadvantage of the solid-state electronic sources is the limitation in the frequency range and the power associated, with a maximum of 0.5 THz achieved with the Gunn diodes.

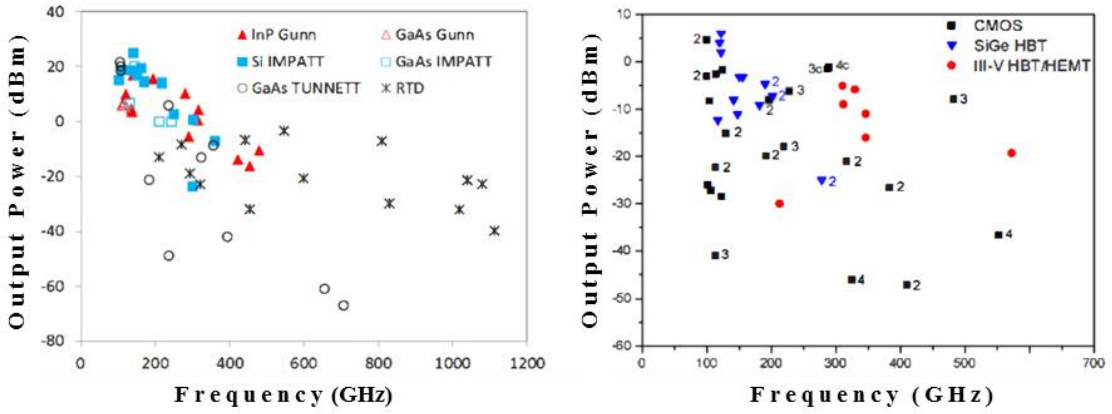

Figure I.3 : Output power vs. oscillation frequency of various diode-based and transistor-based sources.

I.2.3. Vacuum electronic sources

Vacuum electronic sources are: backward wave oscillator (BWO), extended-interaction klystron (EIK), gyrotrons, free-electron lasers (FEL) and synchrotrons. The principal of these sources is based on the conversion of the kinetic energy of electrons into electromagnetic field energy. The bandwidth accessible with these sources ranges between 0.1 and 10 THz emitted in continuous or pulsed mode. Unlike the solid-state electronic sources, the electrons are moving in vacuum instead of a semiconductor, and this particularity is one of the vacuum electronic devices that allow generating high power, that goes from mW to few GW in pulsed regime [6].

Until now, free electron laser sources are the most powerful source of THz coherent radiation. They are frequency tunable and operate in pulsed or continuous mode. Several studies have examined the application of FELs to perform basic scientific research and imaging applications [7]–[10]. However, their bulky sizes and high cost prevent their use outside laboratory applications. One of the most powerful THz-FEL is the Novosibirsk terahertz FEL (NovoFEL), it can produce radiation with an average power of up to 500 W and peak power of up to 0.5 MW in a spectral range of 1.2 - 2.7 THz [11].

Gyrotrons are one of the most widely used electron-beam sources. Their operation is based on the interaction of a high-energy electron beam with a strong magnetic field inside resonant cavities or waveguides, which results in an energy transfer between the electron beam and an electromagnetic wave. THz gyrotrons have the potential to provide narrow bandwidth, high power coherent radiation at frequencies well above 1 THz in pulsed and continuous wave operation. In 2006, Idehara *et al.*

presented the design of a gyrotron that can exceed 1 THz frequency [12]. The main potential of gyrotrons is the possibility to reach an output power of several hundred kilowatts at sub-THz band. Dammertz *et al.* developed a continuous wave gyrotron delivering power of 1 MW at 140 GHz in pulsed regime [13], [14].

As for BWO sources, they have the advantages of high output power and ease of operation. They are commercially available and used for spectroscopy and imaging applications with high spectral resolution [15], [16]. A comparison in the imaging results of two systems based on BWO and femtosecond time domain spectroscopy, at 0.59 THz is shown in [17].

I.2.4. Terahertz laser sources

Solid-state lasers are the principal components to achieve pulsed and continuous modes of terahertz wave generation. Terahertz laser sources are gas, semiconductors and quantum-cascade lasers (QCL). For gas laser sources, usually a CO_2 pump laser beams is injected into low-pressure flowing-gas cavities that lases to produce the terahertz beams with a power level of tens of milliwatts. In conventional semiconductor lasers, light is generated by the radiative recombination of conduction band electrons with valence band holes across the bandgap of the active material; in contrast, electrons in a quantum-cascade laser propagate through the connection of coupled quantum wells, where the conduction band is split by quantum confinement into a number of distinct sub bands. Started in 1994 by J. Faist as pulsed operation, quantum-cascade lasers are one of the most compact and powerful terahertz semiconductor laser sources and well applied to imaging applications [18]. In 2002, Williams *et al.* presented pulsed QCL at 3.44 THz with 2.5 mW peak power[19]. Also, a QCL emitting at 2 THz and operating in pulsed and continuous mode is detailed by Worrall *et al.* and delivering peak power of tens of mW [20]. In 2006, Lee *et al.* reported a 50 mW at 4.3 THz QCL used in real time reflection and transmission imaging and applied for mail screening by imaging the inside of an envelope [21]. Also broadband QCL designs are presented in [22], with a frequency band lying between 2.2 and 3.2 THz with 15 mW peak power in pulsed mode.

I.2.5. Sources driven by lasers

Among these sources, there are the continuous sources such as photomixers and mechanical resonance; as well as the pulsed sources such as the photoconductive switches, magnetic dipoles, terahertz parametric oscillator, optical rectification.

Photoconductive (PC) antennas are coherent terahertz sources. They are among the most used candidates for developing compact, portable, low-power-consuming, rugged, and low-cost spectroscopy and imaging systems for various broadband terahertz applications [23]. They are small size tunable devices, operating at room temperature. They can generate waves in continuous or pulsed mode, with short pulses having high peak powers even if the average powers are low. The most advantage of these sources is the access of the amplitude and phase allowing the determination of the complex dielectric properties of materials [24]. The generation of terahertz waves by PC antenna is the result of the illumination of the PC gap by a laser beam with photon energy larger than the bandgap energy of the PC material and is achieved by coherent detection technique. This illumination,

at femtosecond time scale, generates electrons and holes in the PC active layer. Due to the DC voltage applied to the PC electrodes, a transient photo-induced current is formed by these electrons and holes, which radiates a terahertz field. These sources are used in the time-domain spectroscopy system involved in the present study, and are discussed in more details in chapter II.

Optical rectification is another way of generating short terahertz pulses. It is a nonlinear process generated by ultra-short laser pulses in electro-optic crystals or gases as rectification media [25], [26]. In the optical rectification mode, the THz pulse duration is comparable to the optical pulse duration and the frequency spectrum is mainly limited by the bandwidth of the laser pulse. A 5 MW peak power at 0.5 THz is reported by Yeh *et al.* in 2007 [27].

I.3. TERAHERTZ DETECTORS

Many terahertz detectors have been developed and are commercially available. The choice of the detector depends on the source and the application. When choosing a detector, several performance parameters should be considered, namely Noise Equivalent Power (NEP), bandwidth, response time, and sensitivity. The NEP is defined as the incident optical power required to obtain signal-to-noise ratio equal to 1 in a bandwidth of 1 Hz. Two types of detectors can be set up: the first one corresponds to coherent detectors that provide both the amplitude and phase of the electromagnetic wave. This is the case of photoconductive antennas and electro-optical detection techniques; the second type corresponds to incoherent detectors that only provide intensity or energy information of the electromagnetic wave. Some of these detectors are the bolometers [28], the Schottky-diode based detectors, Field Effect Transistors [29] and Golay cell [30].

I.3.1. Photoconductive antenna

Photoconductive antennas can also be used as detectors. The electric field, carried by the THz pulse focused onto the antenna, generates an electric field between the electrodes. In a pump-probe like experimental setup, a probe laser pulse creates carriers exactly where the THz beam is focused between the two electrodes. It allows the detection of the terahertz pulse by sampling technique. The carriers in the semiconductor active layer have a short lifetime, typically hundreds of femtosecond, thus the terahertz electric field is consequently sampled on a short time interval. A delay line finally allows for sampling the entire electric THz field waveform. Then the THz pulse is reconstructed point by point.

The bandwidth related to the use of PC antenna is limited by the laser pulse duration for both the generation and detection. It typically reaches 10 THz for femtosecond laser pulses. PC antennas have better signal-to-noise ratio than electro-optical devices and don’t need any cooling cool to achieve a measurement with a reasonable signal-to-noise ratio. Indeed, the peak intensity of the THz pulse is well above the thermal background-noise level. Finally, the PC antennas are used in pulsed mode for several applications in imaging and spectroscopy [23], [31], [32].

I.3.2. Electro-optic sampling

Similar to the optical rectification for terahertz wave generation, a crystal material associated to the Pockels effect are used for terahertz wave detection. The electro-optic (EO) detection method is a nonlinear coupling between the terahertz electric field and the optical pulse of the laser beam in the sensor crystal material. The noise sensitivity and frequency response in the EO detection is determined by the choice of crystal and its thickness [33], [34].

I.4. BASIC APPLICATIONS

Sources and detectors are two of the components of imaging or spectroscopic terahertz system, and the choice of these two essential components defines the performance of the system. In imaging systems based on raster scanning, sources and detectors are mono-element. Consequently, the object has to be moved in order to reconstruct an image pixel by pixel. Such active imaging system presents high dynamic range but is time-consuming due to the point-by-point reconstruction and consequently, not applicable to moving targets. Another type of imaging system uses matrix of detectors to provide real time imaging. They are semiconductor or bolometer cameras that allows higher image rate, than the raster scanning, but characterized by a low sensitivity in the THz range. In addition, their surface areas are too small to provide high-resolution images of large dimension targets. For spectroscopy, systems based on the pulsed mode, provide a broadband spectrum at the opposite of continuous systems that give access to narrowband spectrum. Each of these systems is conventional for specific application.

First, terahertz is having a great interest in biology, medicine and biomedical applications due to lower energy levels (several mev) of the terahertz radiation that limits the damage to cells and tissues due to thermal effects. The radiation effects of two frequencies, 120 and 130 GHz, on biological samples is discussed in [35] and no dangerous impact is demonstrated. Terahertz imaging and spectroscopy have been already applied by different groups around the world for recognition of protein structural states [36], analysis of DNA components [37] and performing label-free DNA sequencing [38]. Also, it is well applied to disease diagnostics in vivo and ex vivo, in pulsed mode [39], [40], as well as in continuous mode [41]. Although its limitation in the frequency bandwidth, CW system can provide data with a frequency resolution not achievable with pulsed systems.

In pharmaceutical applications, terahertz imaging is used for the analysis of the coating quality of tablet [42] and terahertz spectroscopy is used for polymorphism analysis. It was demonstrated that two different polymorphs of drugs could be discriminated using their terahertz spectra [43], [44].

Other application domains of terahertz imaging and spectroscopy are art, archeology and anthropology. One of the reasons that give attention to terahertz waves in these domains is because a nondestructive contactless inspection of materials on sites. It has the potential to determine the spectroscopic features of a hidden sub-layer of a painting without destroying it [41] [42]. In 2010, the analysis of painting sub-layers was demonstrated using a time-domain spectral imager system. This work showed the possibility to reveal buried layers information such as a graphite handmade sketch covered by several layers of painting, also demonstrated the possibility to evaluate painting thickness

[47]. Besides, 2D imaging and THz tomography give new information in the study of ancient cultures by studying the internal structure of some of the objects of these cultures [48].

Wi-Fi and mobile communication rely on microwave frequencies. But the increasing demands for data transfer in communication will become more than microwaves can handle. For that, scientists are looking for terahertz application in communication due to his ability in delivering data up to one hundred times faster than today. Also, terahertz waves have much higher frequency and therefore more potential bandwidth and bit rate up to 46 Gbps for wireless communications [49]. Unfortunately, terahertz wave attenuation is high for long distances [50] and power levels are nowadays low, thus it is difficult to use these waves for long ranges communication. However, it is very promising for point-to-point bandwidth in wireless short-range communications [51].

Security and screening is one of the most attractive applications of terahertz due to the ability of these waves in producing imaging and spectroscopic analysis through several types of materials. One of the studies in the context of mail security and screening was using THz-TDS for barcode identification [52]. This domain of application is the main interest in our work and a detailed discussion of the state of art is presented further in this chapter.

II. PARCEL THREATS INSPECTION

Major events over the past couple of years, including 9/11/2001 in the United States and recently 11/13/2016 in Paris, have dramatized the vulnerability of the global security, and increase the need of more technological development to detect any type of threats. The problem of threat detection can be considered on several different axes, as follows:

1- Location: airports, public buildings, postal center, vulnerable high-value facilities;

2- Target: airplanes in luggage, in cargo, in parcels, in letter, on people;

3- Threat: weapons, drugs, explosives (solid and liquid), bombs, nuclear dirty weapons.

In our study, we focus on two specific threats: weapons and explosives in parcels that can be transported in airplanes, trains, and stored in the post sorting centers through postal chain transportation.

Weapons have no instant danger on the transporter or the post center and systems used for weapon detection are mostly X-ray systems. The notion of X-ray technology is discussed later in this chapter. However, explosives can have a high danger mainly because of the risk of detonation during transportation, by accident or by terrorist activity. For this purpose, a part of this work was on the study of explosives detection by THz techniques. Several methods are already used in the detection of weapons and explosives in airports, postal centers and public places. Although the high technological level achieved by the other techniques, the instant detection of explosives in parcels is a hard task. In this chapter, we will briefly present the main physical and chemical tools able to inspect objects.

II.1. EXPLOSIVES COMPOSITION

Bombs transportation is an important issue in the national security. The transported explosives can be tempted to use in a terrorist attack, also it can create a great danger during transportation. The screening of the shipping containers and parcels that enter a country is a necessity and screening technologies are always in development to provide more precision and robust detection. A bomb is composed of four functional parts: a control system, a detonator, a booster, and a main charge. An example of a bomb diagram is the pipe bomb image presented in Figure I.4 (a) [53], [54]. The pipe bombs are the most prevalent type of improved explosive devices.

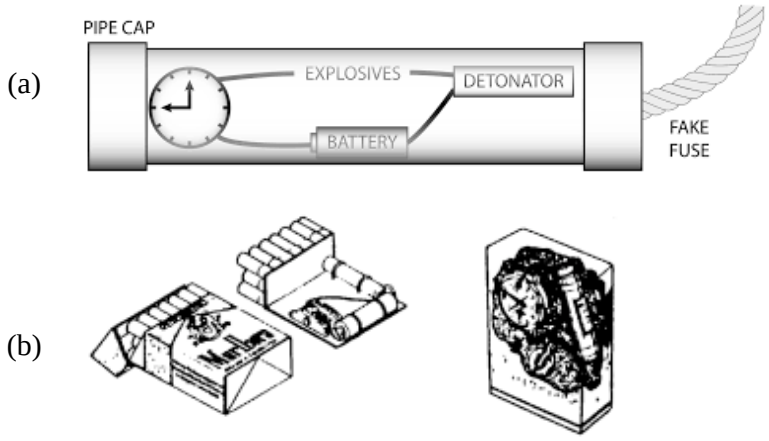

Figure I.4 : (a) Internally fused pipe bomb diagram, (b) example of a bomb configuration: bomb hidden in a cigarette box.

Nowadays, threats may take any physical form which makes difficult to detect them. Hundreds of configurations can be found, and as an example, the bombs represented in Figure I.4 (b), where the functional parts are hidden in a cigarette box. Here comes the importance of spectral imaging and shape recognition to identify the recoupments of the four functional parts as a threat. Thus, the possibility of bomb detection by the THz spectral imaging is discussed in this work, and we focus on the identification of the chemical composition of the imaged samples.

The control system in a bomb is an initiation timing device can be an ordinary item such as clockwork, batteries, electronic circuitry, cameras, mobile telephones, etc., and its presence is not necessarily an indicator of bomb presence.

The detonator is an initiator system that comes in three categories: electric, non-electric and electronic. The development of electronic detonators started in 1990. The electronic detonators are the most dangerous for transportation security. They consist of microchips to control the timing of the explosion start. They have the same fundamental structure but can be found in different designs [55].

The actual classification of explosives separated them into primary, secondary, and tertiary high explosives. Primary explosives are the most sensitive, being readily initiated by heat, friction,

impact, or spark. They are used only in very small quantities; they are typically extremely sensitive but not particularly powerful. In some detonator, they are used to initiate secondary explosive, thus the need to differentiate the chemical identity of two powders imaged next to each other's. Secondary explosives include all of the major military and industrial explosives. They are much less easily brought to detonation than primary explosives and are less hazardous to manufacture. Tertiary are so insensitive that they generally are not considered explosive [56], [57]. Table I.1 resumes some properties of common explosives such as the detonation velocity and pressure as well as the energy of the explosive, to give a preliminary idea on the effect of explosion using these powders.

Table I.1 : Some properties of common secondary explosives.

Explosive name	Symbol	Composition	Detonation velocity (km/s)	Detonation pressure (kbar)	Explosive energy (cal/g)
Cyclotrimethylenetrinitramine (hexogen or cyclonite)	RDX	$C_3H_6N_3(NO_2)_3$	8.0	347	1320
Pentaerythritol tetranitrate	PETN	$C(CH_2ONO_2)_4$	7.9	300	1510
Trinitrotoluene	TNT	$CH_3C_6H_2(NO_2)_3$	6.9	190	900
Cyclotetramethylenetetranitramine (octogen)	HMX	$C_4H_8N_4(NO_2)_4$	9.1	393	1350
Triaminotrinitrobenzene	TATB	$C_6H_6N_3(NO_2)_3$	7.9	315	829
Pentolite		50/50 TNT/PETN	7.7	245	1100
Composition B		49/50/1 TNT/PDX/wax	8.0	294	1100

Moreover, explosives are distributed in several categories:

Military explosives: They should have a high performance and they ability to be safely stored for a long period. The most common military explosives are HMX, PETN, RDX, and TNT.

Plastic explosives: The military explosives are plasticized to make a molded material, flexible binder. Plastic explosives are used for military demolitions as well as in terrorist bombs. For these explosives, the plasticizer is more volatile than the explosive component which makes it harder to be detected in the vapor detection based systems. The most known plastic explosives are C4 and Semtex.

Commercial explosives: They come in assorted shapes and consistencies including gels, and standard dynamites. Modern commercial explosives are generally mixtures of AN/fuel to form the ANFO, the most widely used explosives.

Peroxide explosives: Those explosive does not contain NO_2 groups. The most known are the TATP and hexamethylene triperoxide diamine (HMTD). They are popular with terrorists because they are easily prepared from readily obtainable ingredients.

Propellant: They are intended to deflagrate more than to detonate. They have been frequently used in pipe bombs and similar devices. They contained smokeless powders based on NC (collodion cotton).

Exotic explosives: They include chemical explosives, not suitable for use by military or industry, improvised explosives, detonable, energetic materials. They are generally used by terrorists.

Figure I.5 shows the molecular structure of two of the most used military explosives: RDX and PETN. These two explosives are chosen in our study due to the specificity of their absorbance spectra as well as their mixture. This specificity will be discussed in detail in the next chapters.

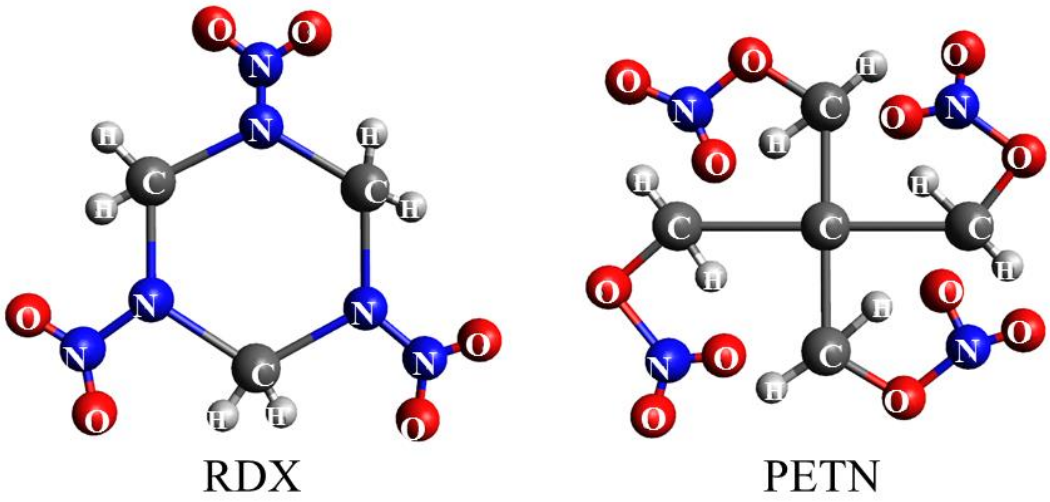

Figure I.5 : Molecular composition of the two military explosives: RDX and PETN.

II.2. EXPLOSIVES DETECTION TECHNIQUES

Detection of explosives is divided into bulk and trace technologies. Bulk detection looks for a mass with certain properties considered indicative of an explosive, such as density, amounts of oxygen and/or nitrogen, absorbance spectra in the case of THz technology, etc. Yet, the trace detection looks for a specific chemical from a library of target compounds. The probability of false alarm is significantly lower in trace detection than for bulk detection techniques. However, positive trace detection provides no spatial or quantitative information to aid in decision-making, and is limited to the explosives provided in the library. Some of the problem that faces trace detection is the difficulty to obtain the sample into the detector and the inefficiency collection of vapor or particulate by the detector. Known that the explosive number of molecules present in the atmosphere is very small, for example, several ppb (particle per billion) for TNT explosive and several ppt (particle per trillion) for RDX, that to say one molecule of explosives among billion of air molecules for TNT and

among 1000 billions of air molecules for RDX. This makes the detection of these molecules difficult and consists to have sensitive detectors.

Most used methods for explosives detection are:

- Animal
- Nuclear technology
- X-Ray
- Ion mobility spectrometry
- Mass spectrometry
- Raman spectroscopy
- Sensors-MEMS
- Terahertz spectroscopy

Some of these techniques are discussed briefly to highlight their advantages and disadvantages compared to terahertz [58].

II.2.1. Animals

The oldest and most used method for explosives detection in public places is animals, especially dogs. They have a high sensitivity in identifying explosives even when are hidden within several types and thickness of objects. However, training dogs needs lots of time, money and trainers. They can respond to the vapor constituent of explosives, such as acetone, toluene and limonene as well as to complex mixture of chemical vapor constituents. However, different dogs may not attend to exactly the same constituent.

II.2.2. Nuclear technologies

Nuclear detection technologies are used in the detection of objects hidden within thick and high density materials. They involve two different aspects:

- Non-neutron-based detection can be based on probing the atom with particles, such as photons and protons, which interact with atoms and gives off a signature according to the properties of the target nuclei.
- Neutron techniques consist of irradiating the target by a neutron flux. The interaction of the neutrons with the target nuclei generates a secondary radiation, which is detected and analyzed. This method is basically used to identify the relative chemical content of specific elements as carbon, oxygen, aluminum, sulfur and many other elements [59]–[61].

The main advantages of using nuclear technologies are they high penetration depth capability, for example into metals, which is one of the reason to be chosen for container screening. It has the specificity to differentiate between organic and inorganic materials. Also, it is easily implemented in working spaces due to the fabricated portable systems. However, the neutron sources produce harmful radiation doses if not shielded properly or at the correct stand-off. Also, the presence of nuclear

material at a site increases the threat from terrorists who may attempt to steal the material or to explosively disperse it [62]–[65].

II.2.3. X-ray

An X-ray beam is a flow of discrete photon particles, each having a specific energy. The attenuation of this photon with matter occurs via four basic modes of interaction: coherent X-ray scatter, incoherent or Compton scatter, photoelectric absorption and pair production.

X-ray scanners are the most used systems in security; they are used for parcel and cargo screening to give detailed images of the contents inside parcels, luggage, etc. They have high resolution and high penetration ability. Although, for better precision, tomographic reconstruction techniques are applied to X-ray data image to provide detailed information about each individual object packed in luggage. These techniques are known by X-ray computer tomography (CT) and they are based on three principles: single-slice CT, multi-slice CT and dual-energy CT. They generate a three-dimensional representation of an object and they measure the X-ray attenuation coefficient μ of every packed object which is proportional to a material's density and the atomic number of the material. Thus, they are able to recognize a wide variety of dangerous and innocuous objects based on tri-color X-ray images assigned code colors as organic, inorganic or metallic, based on material density and effective atomic number Z_{eff}.

Typically, the organic range includes material having $Z_{eff} < 10$, inorganic having $10 \leq Z_{eff} < 18$, and metallic having $Z_{eff} \geq 18$. Metallic threats are well detectable that metallic objects stand out clearly from the background contents, but it is more complex for explosives because, being organic substances, they do not have a distinctive appearance when imaged [66], [67].

An example of X-ray image results is shown in Figure I.6 and Figure I.7. These images were taken especially for the InPoSec project during measurement campaign in La Poste center at Roissy Charles-de-Gaulle airport in Paris.

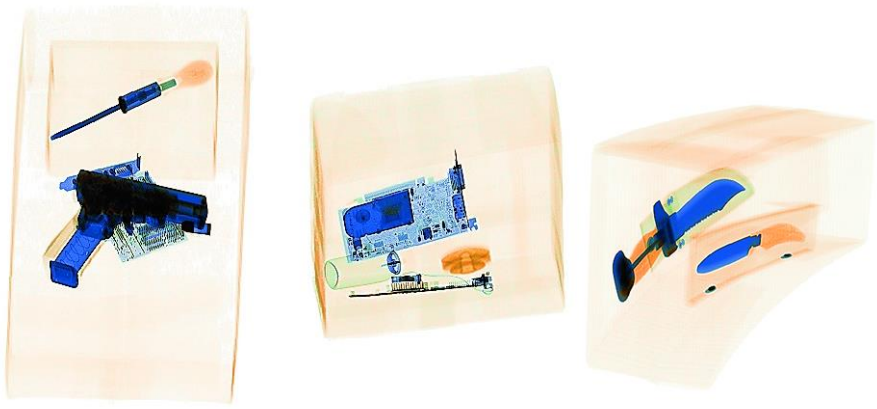

Figure I.6 : X-ray images of three different parcels. The identification of objects is based on the tri-color presentation.

The images in Figure I.6 show clearly the content of the parcels. The different colors in the images indicate the material nature, thus it can be identified as organic inorganic or metallic. As for Figure I.7, the powders are not well identified in the first image and there is no information given on the chemical content of the two bottles.

Even with the high advantage of X-ray scanners over other technologies in security applications, they do not give the complete information needed for explosive recognition. But the notion of dangerous material is quite controversial depending on the different administrative texts.

Figure I.7 : Photo and X-ray images of parcels with organic content: powder and liquid.

II.2.4. Ion mobility spectrometry

Ion mobility spectrometry (IMS) was first developed at the Georgia Institute of Technology in the 1950 to study gas phase ion mobility and reactions. Then it was expanded to airports and used for detection of explosives, drugs and chemical weapons. IMS based explosives detectors can be found in security entrances at airports throughout the world [68]. It was also combined with other techniques as mass spectrometry, gas chromatography and electrospray ionization [69].

IMS technique is based on the measurements of the substance ion mobility differences. The extracted sample of a suspicious object is heated on 200 ºC to generate vapor that is mixed with gas ions, the chemical reaction of the mix generates ions related to the sample. These ions enter a drift tube that contains a weak electric field. As ions move in the tube, they are separated according to their mass, size, shape, and charge. Differential migration time through the tube can be used to identify the components. This technique has a high speed response; a measurement takes tens of milliseconds. However, the analyses are not systematic, it needs the contribution of a human to collect samples and place it in the analyzers [70].

II.2.5. Mass spectrometry

Mass spectrometry (MS) is one of the technologies used for vapor and trace detection of hidden explosives. It identifies the substance by the masses of the atoms and molecules of which materials are composed and depends on the substance mass-to-charge ratio. MS where successively applied to several explosives such as TNT, RDX, HMX, PETN and their mixtures. The systems based on MS can detect in real time small amounts of powders, going to nanograms and even femtograms. The

analysis is made in a few seconds, without any sample preparation, with a high sensitivity and selectivity [71]–[74]. Mass spectrometry offers much better discrimination than IMS but has poor sensitivity relative to IMS.

II.2.6. Raman spectroscopy

Raman spectroscopy is a non-destructive technique widely used for bulk explosives detection. It is a vibrational spectroscopy technique used to collect a unique chemical fingerprint of molecules by illuminating a surface with a laser beam and detect the scattered light corresponding to the phonon generated after the interaction of the laser beam with the matter. The scattered light constitutes the Raman spectrum that is represented as an intensity-versus-wavelength shift. One of the advantages of Raman spectroscopy is the possibility of analysis without any sample preparation and in stand-off configuration [75] [76]. It is able to provide quantitative information of the molecular content of the sample. Several portable Raman systems are already commercialized, and most of them are constitute of diode laser to provide smaller weight and acceptable cost [77]. The response is sensitive to molecular vibrations and the spectrum of Raman scattered light depends on the molecular constituents of the samples.

Moreover, Wentwoth *et al.* demonstrated the possibility to Raman sensor with a hyperspectral imaging design that can provide chemical identification in images. This work was an initiative for combination of Raman spectroscopy and Laser-induced breakdown spectroscopy (LIBS) to provide high sensitivity, low false alarm rate standoff identification for explosives on surfaces [78]. Also Moros *et al.* presented an experimental design that combines both technologies at a stand-off distance of 20 m [79].

II.2.7. Sensors

Sensors are one of the most reliable and sensitive vapor explosives detection methods. They are similar to the dog's keen sense of smell, have a small size and easy to use in any location. Several types of sensors are well developed and used; most of them are based on Microelectromechanical (MEMS) technology. One of the commercial systems is provided by “SpectraFluidics”. It is a microsystem silicon chip based on free-surface microfluidics with surface-enhanced Raman spectroscopy for detection of vapor trace of explosives in the air. Other types of sensors are those based on electrochemical process. The detection concept is based on the chemical interaction of the molecule with the electrode of the sensor that creates an electric current proportional to the gas concentration. The limitation of such a detector is in identification of mixture even binary mixtures [80], [81].

II.2.8. Technology comparison

A comparison of the advantages and disadvantages of each technology discussed earlier is summarized in Table I.2. For parcel inspection, trace detection techniques as MS, IMS are not efficient because most techniques rely on vapor detection. The presence of vapor molecules is extremely small, and when the explosives are concealed in packaging materials, the generation of

vapor is dramatically reduced. As for Raman, the system must be very close to the surface of analysis. So this techniques cannot provide useful information unless, in especial cases, where the parcel can be opened and samples are extracted to be analyzed.

So, bulk detection techniques are the most helpful for forensic security parcel inspection. Among bulk detection techniques, X-ray is the most efficient, with rapid scan, providing detailed 3D images. However, X-ray cannot identify explosive identity.

Thus, THz spectral imaging is very promising for inspection of parcels being able to provide 2D and 3D images of objects through packaging, as well as it is able to identify powders. For these reasons, THz imaging, spectroscopy and spectral imaging was studied in this work, as a complementary technology to the X-rays. Also, chemometric analysis is applied to THz data for extraction of additional information especially for explosive threats. The use of chemometrics is expended to several measuring techniques as Raman and LIBS, and it has a high progress in the last years.

Table I.2 : Basic advantages and disadvantages of several technologies used in explosives detection

Technology	Advantage	Disadvantage
Animal	High degree of sensitivity and selectivity. Easy to use. Portable and mobile. Inexpensive. Gives public reassurance.	Depend on the skills of the dog handler in the interpretation of the dog's response. Cannot identify the identity of the threat: explosive, drug, etc.
Nuclear technologies	High penetration. Elemental identification. Ability to penetrate deep into cargo containers.	Dangerous for health.
X-ray	High resolution. High penetration. Three-Dimensional representation of objects.	No chemical identification of materials. Dangerous on health when people are exposed to X-ray radiations.
Ion mobility spectrometry	Rapid analysis. Developed commercial systems.	Need to collect samples to analyze. Only for trace detection.
Mass spectrometry	High selectivity and sensitivity. Detect small amounts of explosives.	Only for trace detection.
LIBS	Stand-off detection. Qualitative and quantitative identification.	Contact with the sample.
Raman	High sensitivity. Qualitative and quantitative identification.	Contact with the sample.
Sensors	Small, high sensitivity, commercial, easy to use.	Only for vapor detection

III. TERAHERTZ APPLICATIONS TO SECURITY

Development of improved radiation sources and detectors at the end of the twentieth century has enabled considerable progress in the THz systems for threat detection. Being weakly absorbed by most non-conductive materials and providing chemical information, terahertz has a big advantage on other technologies for investigation of parcels. However, it was used in many other security applications for weapon and chemical detection. THz techniques can provide a chemical identification of materials, especially powders at moderate standoff distances.

III.1. TERAHERTZ FOR WEAPONS DETECTION

Detection and identification of objects hidden behind barriers are one of the core requirements for security inspection systems. Two main detection configurations are needed: long and short range detection. Long range systems are dedicated for detection of suicide bombers and weapons hidden under clothes and short range systems are more used for mail inspection as well as for weapons detection. For both configurations, the two technologies can be used: passive and active. As it will be discussed in detail in the next chapters, passive systems are used when the radiation measured is provided by the target itself and with active systems the target is illuminated by a source. Moreover, pulsed or continuous wave systems can be used, but for weapon detection, continuous waves are advantageous due to their higher single frequency dynamic range. Also, they can be chosen in the window of low water vapor absorption, thus is easier to operate at longer standoff distances.

The ability of terahertz waves in clothing penetration, made possible the stand-off detection of concealed weapon, especially those used for terrorist attacks. Thus, one of the main interests of using terahertz in weapons detection is to observe objects underneath people's clothing using passive or active imaging. In this aim, several millimeter-wave systems were developed by many research groups and companies in the past years, which are suitable for stand-off detection of hidden objects in real time. In 1996, TRW space & electronics group demonstrated a sensitive to 0.4 K array for passive imaging using Schottky diodes as detectors [82]. Trex company presented in 2002 the second generation of passive millimeter wave stand-off system operating in real time and having a 2 K temperature sensitivity [83]. In contrast, mechanically scanning passive imager operating at 94 GHz is developed. The optical configuration is designed in a way to reduce the optical aberration. The testing results show a high resolution image with a low noise [84], [85]. Moreover, MC2 technology developed a low cost passive millimeter wave camera based on low noise amplification and detection at 90 GHz [86]. This system is used in this work to demonstrate the potential of this technology in the detection of weapon not only concealed in human body, but also hidden in parcels. Detailed description and analysis are given in the next chapters.

In 2009 the portal scanner based on millimeter waves started to be used in USA airports and in some airports in Europe. In France, these scanners are not frequently used, yet the study on the effect of these scanners did not show any dangerous side effects on human health [87].

The strategy of scanning can be envisaged in two configurations: the first is similar to the scanner in Figure I.8 (a) [88], and the second represents a scanning chamber. Figure I.8 (b) and (c) represents the

scanner made by Millivision [89]. It is self-contained, with imager, power, control and automatic threat recognition. Also, it shows the visualized direct result and the way the software recognizes automatically threat and places markers on the image eliminating any need to view the subject. Another development is presented by the Pacific Northwest National laboratory with an active MMW body scanner known by ProVision (Figure I.8 (d)). It uses coherent millimeter wave radiation emitter and is able to detect amplitude and phase information and provide 2D and 3D images [90] [91].

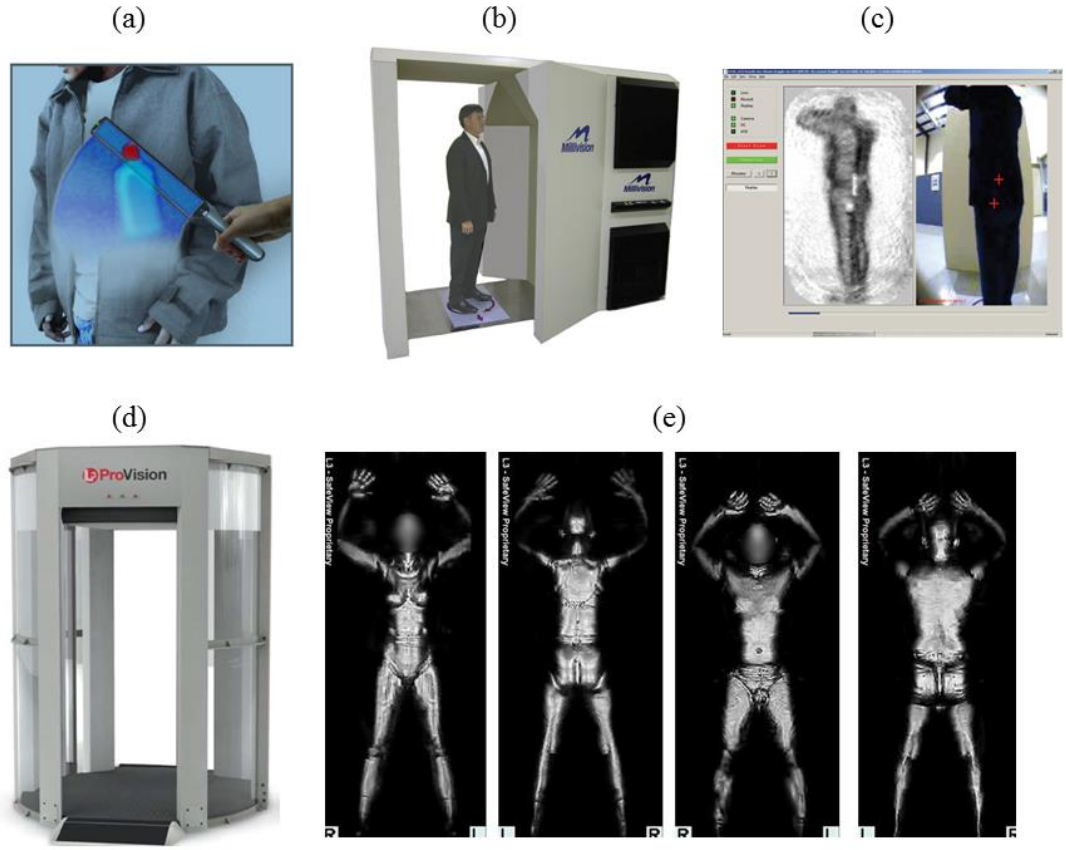

Figure I.8 : (a) Envisaged security screening application developed from electronic beam-forming PMMW imaging technology, (b) A representation of the Millivision Passive Millimeter-Wave whole body, (c) The apparition of the results of hidden object on the image, (d) The ProVision commercial active body scanner, (e) Front and back millimeter-wave whole body imaging results from deploying scanners.

Moreover, the detection of weapons inside parcel was demonstrated at a distance of 2 m using a high speed raster scanning system, based on the principal of radar scanners. The two dimensional scans combined with a high resolution range provides three dimensional images and allows inspection of parcels in depth. One of the technologies in MMW imaging uses a similar concept to the radar imaging and is known by Frequency Modulated Continuous Wave imaging (FMCW). This technology is used in the present work and results of parcel inspection are presented in the next chapters. This technology was used in [92] for luggage screening and the results of gun detection is

shown in Figure I.9 (a). An example obtained using a continuous source of 200 GHz is shown in Figure I.9 (b) [93]. Similar technology is discussed in this work because is one of the main technologies we used to inspect parcels for weapon detection. From another way, technology based on semiconductor such as CMOS provides real time imaging such as INO camera. These technologies are very advantageous for parcel screening and are low cost. An example of concealed blade razor hidden in polyethylene foam imaged at 650 GHz is shown in Figure I.9 (c) [94].

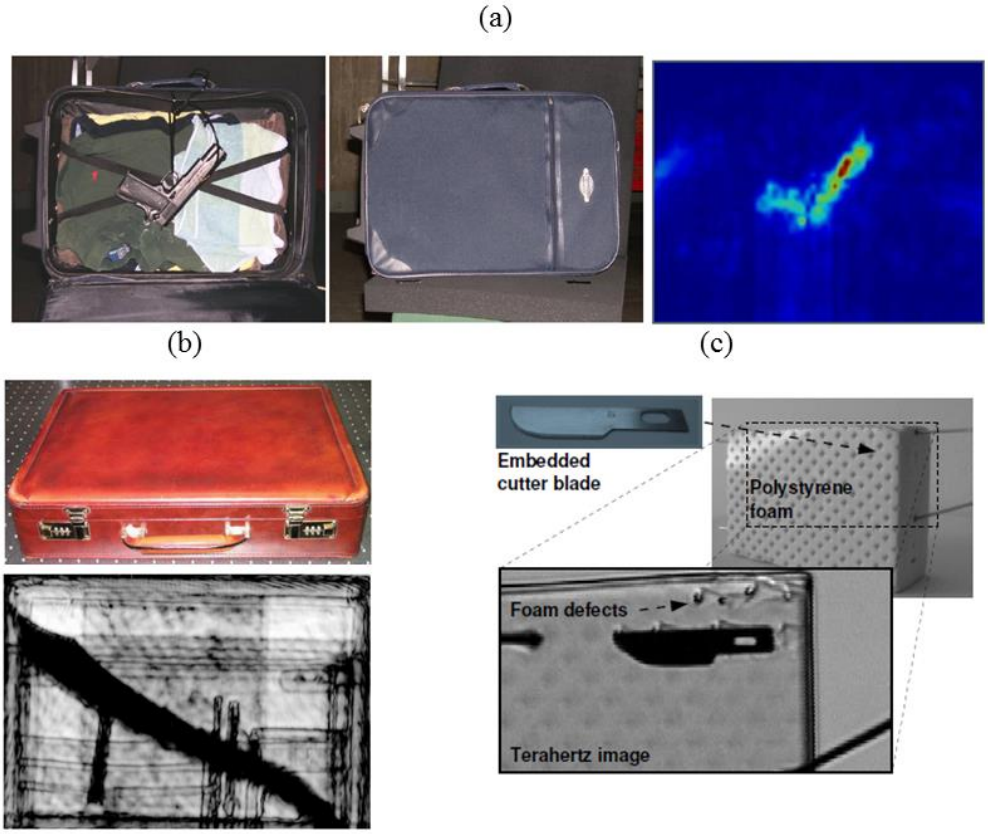

Figure I.9 : (a) Briefcase imaging using radar millimeter wave technology, (b) Optical image and terahertz image at 200 GHz of a leather briefcase containing pens, magazine and a large knife (c) Terahertz image at 0.56 THz of concealed cutter blade in a polystyrene foam using CMOS detectors.

III.2. TERAHERTZ FOR EXPLOSIVES DETECTION

For security mail inspection, in addition to weapons, several threats are searched, those with instantaneous dangerous impact and others that are indirectly dangerous: biological threats as anthrax, chemicals as radioactive materials, explosives and drugs.

Many groups have applied THz spectroscopy with several systems and setup configuration in transmission and reflection configuration for the study of the spectral features of explosives and drugs

[95]–[100]. An example of the spectra of several explosives is shown in Figure I.10 (1). The transmission absorbance spectra between 0 and 4 THz of six common explosives are shown, as well as the attenuation of two luggages and packaging materials: artificial leather and cardboard (Figure I.10 (2)) [101]. Moreover, drugs detection has a high importance in security. Thus, studies for detecting them using terahertz spectroscopy are established. In this aim, cocaine response is measured in transmission through serval type of packaging and the effect of the packages is directly shown on the spectra in Figure I.10 (3). However, for real world scenarios, reflection measurements are preferred since most bulky targets are impossible to measure in a transmission mode, as well as for the stand-off detection of chemicals hidden underneath the clothes transmission through the human body are not possible.

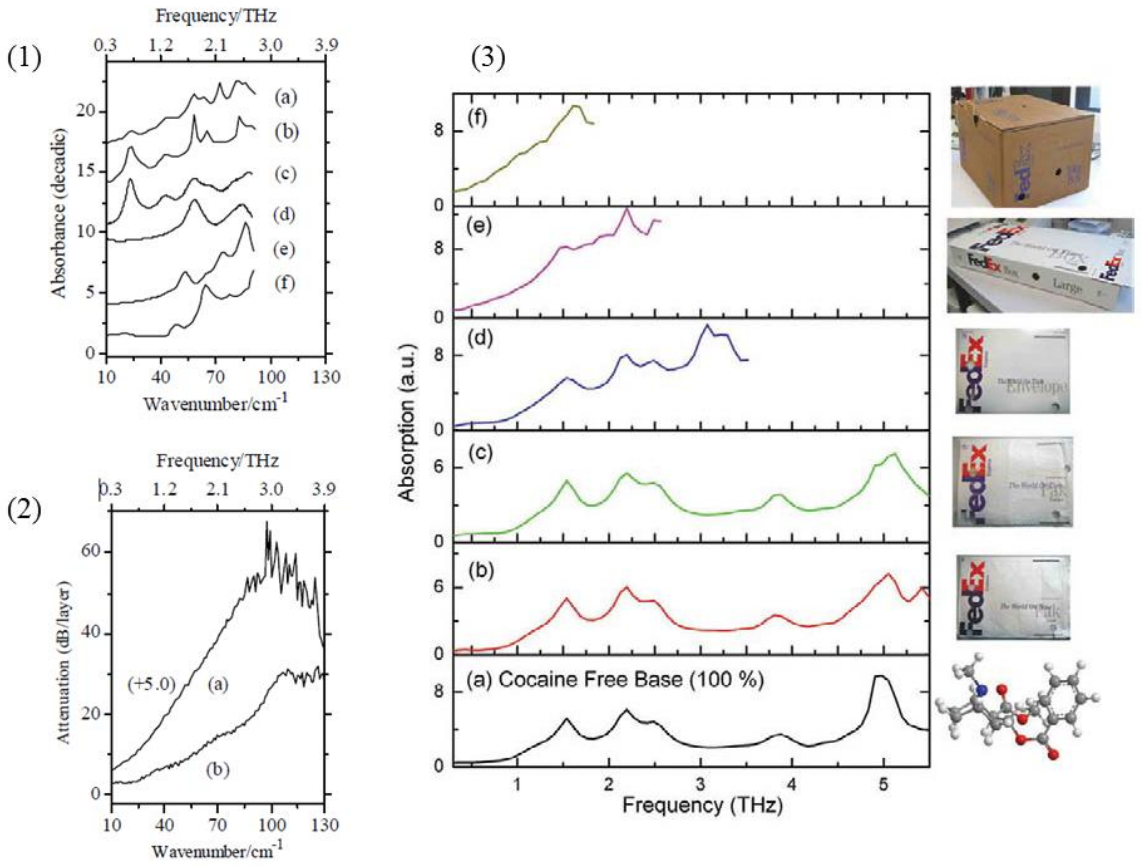

Figure I.10 : (1) Terahertz absorbance spectra of six high explosive materials: (a) Semtex H, (b) PE4, (c) RDX, (d) PETN, (e) HMX, and (f) TNT; (2) Attenuation of luggage and packaging materials: (a) artificial leather from a suitcase and (b) cardboard, (3) THz-TDS spectra of a compressed pellet of pure cocaine free base behind measured in transmission. (a) The spectrum obtained with no covering material, (b), (c), (d), (e) and (f) disc of material cut from a number of different Fed-Ex packages is used as packaging.

In parallel, the combination of THz time-domain spectroscopy system with a diffuse reflectance accessory was capable of detecting and identifying hidden RDX explosives in a diffuse reflection

mode even when covered with paper. The study showed the same spectral feature in reflection as in transmission, as well as the ability of THz diffuse reflection spectroscopy in distinguish the RDX from the polyethylene and flour and identify it even when it is covered [102].

The concept of stand-off detection of chemical concealed in human body that can be possible with reflection setup detection is presented in [103]. However, in such a configuration, terahertz radiations suffer from several problems during its propagation from the source to the detector. The major problem is water vapor absorption lines in several regions in the spectrum. Also, there is the attenuation, reflectivity and scattering caused by the target and the clothes. Some of these problems are reduced for other security application such as letter inspection, where the detection can be made in close environment under dry air at a distance smaller to 1 m of the target.

In addition to solid dangerous powders, inflammable liquid identification in plastic bottle is studied with a TDS in transmission configuration. Usually, inflammable liquid cannot be distinguished from water when they are concealed in plastic bottles. Mid-IR absorption and Raman scattering are possible methods for inspecting inflammable liquids stored in transparent bottles. However, terahertz spectroscopy can distinguish water form inflammable liquid in opaque plastic bottles [104].

Beside simple spectroscopy, chemical mapping had a great interest in THz application. Several demonstrations of the potential of identification of powders by their spectra on images have been carried on using broadband terahertz spectroscopy, in reflection and in transmission. A first study held on terahertz mapping of illegal drugs used in Japan was in 2003, where the spectral fingerprints at seven frequencies was used for discrimination of 20 mg of methamphetamine, MDMA and aspirin concealed in polyethylene bag inside envelopes as shown in Figure I.11 (b). Component spatial pattern analysis was applied to the seven spectral images allowing the extraction of each of the three components separately [105]. Similar study used pulsed THz in reflection mode for identification of powder such as lactose and sucrose in the frequency band [0-2] THz. This study showed the possibility to obtain the spatial distribution of individual chemical components in a mixture [106]. In contrast, another study is held for the discrimination between four chemical compounds in a transmission configuration through 1 cm thick samples (Figure I.10 (a)). The discrimination of the powder was possible with a coefficient proportional to the height of a spectral feature of the absorption spectra [107].

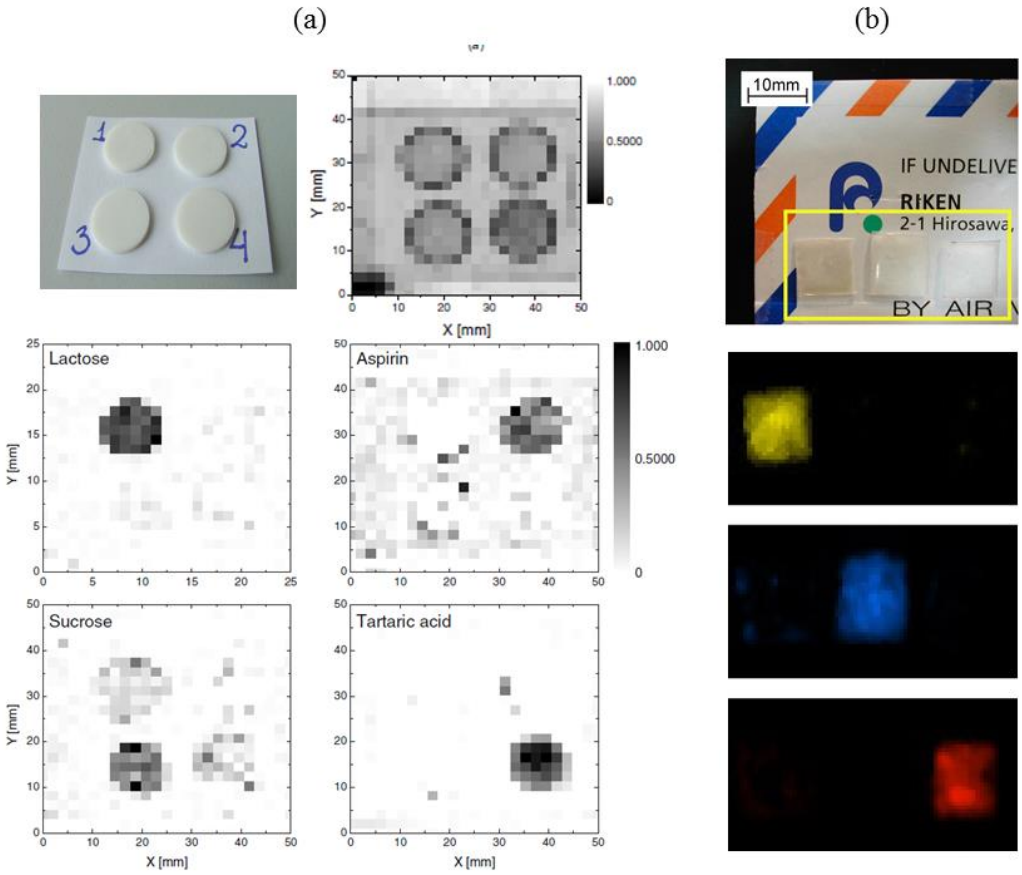

Figure I.11 : (a) Chemical mapping of lactose, aspirin, sucrose and tartaric acid using the higher part of the spectral features of the absorption spectra obtained from a THz-TDS in transmission mode, (b) chemical mapping of MDMA, methamphetamine and aspirin concealed inside envelope using component spatial pattern analysis.

CONCLUSION

Terahertz showed till now a high potential for security application and especially in the postal chain security. In this work, terahertz technology is used specifically for parcel inspection to identify two main threats: weapons and explosives. However, the fact that terahertz waves cannot pass through metals is a limitation when dealing with parcel inspection. For weapon detection, two and three dimension imaging and tomography reconstruction will be studied and tested on several types of parcels. As for explosives identification, terahertz spectroscopy has the main role in spectral recognition of explosive powders. In addition, terahertz spectral imaging also called chemical imaging or hyperspectral imaging is studied to obtain at the same time the identification of the shape, as an image, and the nature, as spectra, of the object under investigation in a parcel. Figure I.12 resumes the use of terahertz technology on each of the threats faced in parcels. In contrast, a high importance was given to the analysis of terahertz data by chemometric tools for two reasons: the complexity of analyzing powder mixtures and the difficulty of analyzing powders through packages. Thus, these

tools were applied to terahertz spectroscopy and chemical imaging to identify qualitatively and quantitatively explosives in pure state and in mixtures.

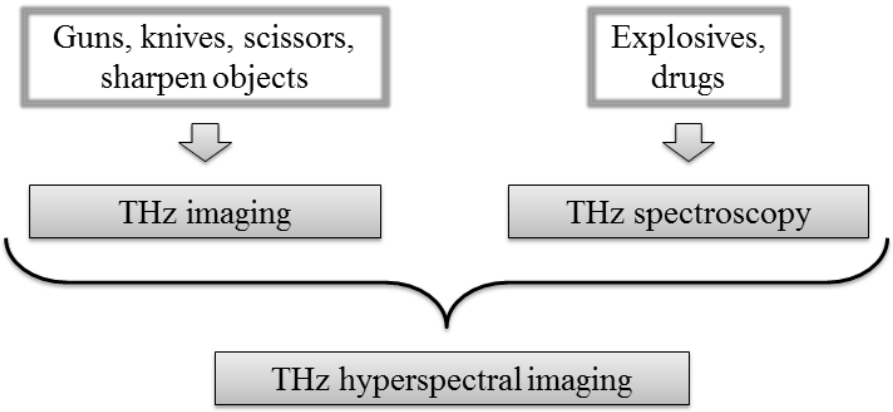

Figure I.12 : Possible threats inspection techniques in terahertz domain: spectroscopy, imaging and spectral imaging.

CHAPTER II

CHEMOMETRICS APPLIED TO TERAHERTZ SPECTROSCOPY AND SPECTRAL IMAGING

In this chapter we give an introduction on THz time-domain spectroscopy (TDS) and describe the experimental setup of TDS that we used to carry out measurements at THz frequencies. We discuss the signal performances and gave suggestions when dealing with various spectroscopic conditions especially with sample made of mixtures of several components. Moreover, the spectroscopy of packaging material is performed and their effect on terahertz spectra and spectral images is shown. Due to complexity of analysis we resort to chemomerics tools to extract significant information of powders mixtures. So first we introduce the concept of chemometrics and explain three techniques of data processing applied to spectroscopic data of explosives. These methods are: principal component analysis (PCA), partial least square (PLS) and partial least square-Discriminant analysis (PLSD-DA) used to visualize, classify and quantify the data, respectively. Furthermore, results on analysis terahertz spectra and spectral imaging with these tools are presented and the application of chemometric tools as image processing tool is discussed.

I. TIME-DOMAIN TERAHERTZ SPECTROSCOPY

I.1. INTRODUCTION TO THZ SPECTROSCOPY

Many materials exhibit characteristic spectral features in the THz frequency range, directly related to their absorption line structures. The spectral features measured in THz spectra are generally attributed to intermolecular vibrations, intramolecular torsions, or even crystal-lattice vibrations. THz radiations probe collective motion of atoms, and by exciting intramolecular and intermolecular vibrations modes, it has the potential to provide both chemical and structural information. Figure II.1 presents molecular motions in the terahertz region [108][109]. Till now, the understanding of the chemical origin of the spectra obtained by terahertz spectroscopy has been difficult. The efforts in molecular spectroscopy have been dedicated to the construction of spectral libraries and models for different product in the THz region to compare and interpret THz spectra. However, for a given product, the reported THz spectra highly differ from author to the other one. On the other hand, several theoretical calculations of solid state products were made such as the solid-state density functional theory (DFT). These calculations were applied to several chemical products, especially explosives like PETN and RDX to understand the molecular motions responsible of specific spectral features obtained after interaction with the terahertz radiation [110][111].

One of the main terahertz coherent spectroscopy methods is the time-domain terahertz spectroscopy (THz-TDS) [112] that we chose to perform THz spectroscopy in the present study. This spectroscopic technique appeared in the mid-1980s in the works of Auston *et al.* [113] and had become an applicable technique for material analysis with the first TDS system designed and reported in 1989 [114]. Recently, time-domain terahertz spectroscopy has found applications in various areas of material science such as gas sensing [115][116], measurement of material properties of solids such as polymers [117], superconductors [118][119] as well as spectroscopy of liquids [104] [120], etc.

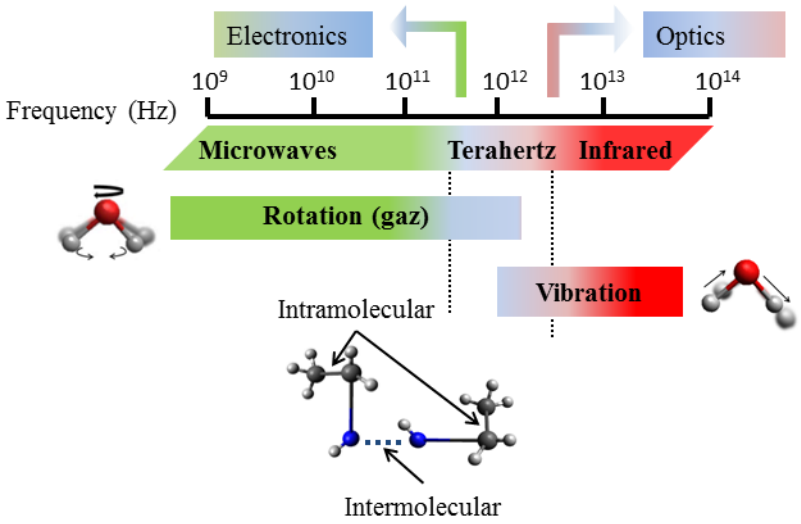

Figure II.1 : Molecular transitions in the terahertz region combining interaction of the optic and electronic domains.

I.2. TRANSMISSION AND REFLECTION SETUPS

Terahertz time-domain spectroscopy (THz-TDS) is a broadband spectroscopic technique based on the use of ultrashort optical pulses to generate and detect a THz coherent pulse. By this method, both amplitude and phase of the THz electric field are measured. This allows direct determination of both the real and imaginary parts of the refractive index without having to resort to Kramers-Kronig-Relations.

In our study, generation and detection of pulsed THz waves were achieved by using a commercial system, the TPS spectra 3000 from TeraView. The same system provides TDS in transmission and reflection modes, as well as spectral imaging also in both modes. The system photograph and the TDS setup in transmission geometry are shown in Figure II.2 (a) and (b), respectively. The setups are constructed with GaAs photoconductive antennas (PC-antennas) as emitter and receiver. A 80-fs Ti:Sa laser operating at 800 nm with a repetition rate of 76 MHz is used as a probe/pump beam. First, the beam is divided into two trajectories by a beam splitter (BS). The pump beam goes into the first PC-antenna to generate the THz pulse. The generated pulse, with duration of several picoseconds, is focused on the sample using parabolic mirrors, and then detected by the second PC-antenna after transmission through the sample. The probe beam passes through a delay line and is injected into the second PC-antenna to trig the detection. Each time the THz beam and the probe beam arrive at the detector at the same moment, a signal is measured. The recorded THz pulse is the resulting of a sampling procedure described in I.5.

This TDS system offers a useful frequency range 0.2 – 3 THz with a maximum dynamic range around 75 dB, a spectral resolution of 0.06 THz and a rapid scan mode at the rate of 30 scans/second. For the transmission setup, the sample is located at the focal point of the THz radiation, midway

between two off-axis parabolic mirrors. A chamber, including the sample as well as the emitter and receiver, is purged with dry air to eliminate water vapor, which induces undesired absorption bands in the spectral window under study. A (X,Y) translating stage positioned in the plane of the sample allows a raster scanning with a maximum area of 16×16 mm^2 and gives access to spectral images in the focal plane (X,Y) after signal conversion from the temporal to the frequency domain. Depending on the scanning parameters, a scan of a 16×16 mm^2 surface can be achieved in a time ranging from 15 min to 3 hours.

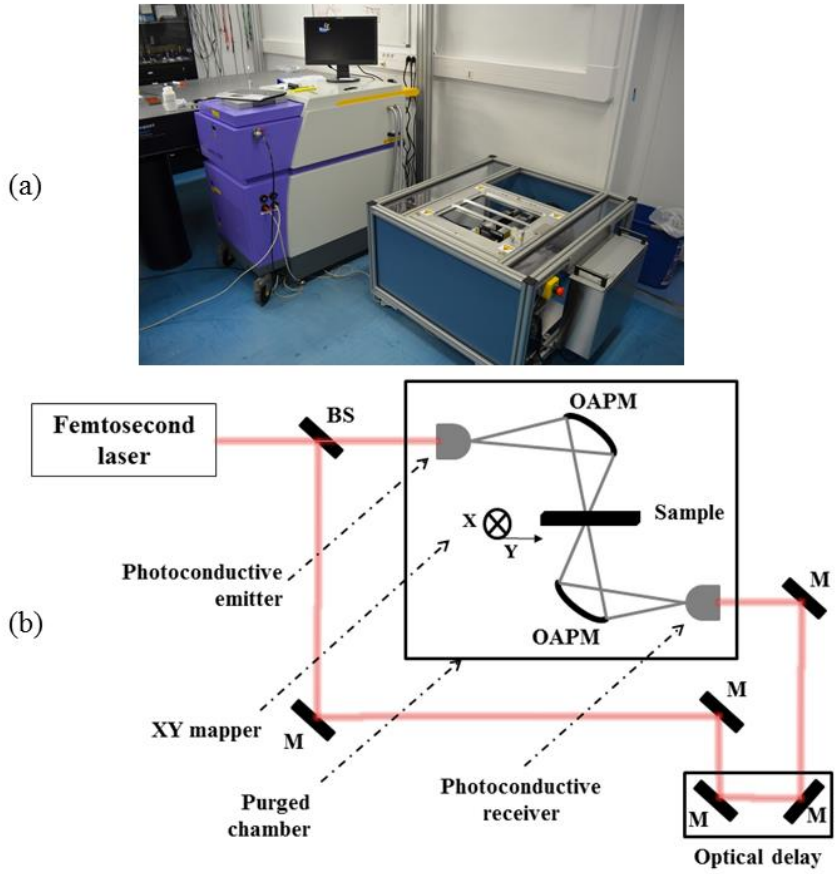

Figure II.2 : (a) Photograph of the THz-TDS spectrometer TPS3000 from Teraview (b) Schematic of the setup in the transmission mode. (OAPM: off axis parabolic mirror, BS: beam splitter, M: mirror).

For the reflection geometry, the same concept is used. Yet, here the laser beams are injected in the PC-antennas using optical fibers. The sample is fixed in this mode and the emitter and receiver are moving along (X,Y) stage with a maximum speed of 50 mm/sec, to scan an image of maximum area of 30×30 cm^2. The THz beam is focused on the sample through a pair of mirrors, and the reflected beam is collected back to a detector as shown in Figure II.3 (a). Two measurements configurations are possible with this part of the setup. The traditional reflection measurements concept, where the first reflected pulse contains the reflection coefficient information, and the second, which is smaller than the first pulse, holds in the material properties. The second way to perform the measurement is a false

transmission configuration, where a metal piece is positioned on the sample (Figure II.3 (b)). This makes the second reflected peak on the sample-metal interface higher than the first one. Reflection configuration is already used in several applications such as cancer diagnosis [121] and explosive detection [122]. However, it is more complex than transmission and high careful should be given to the scattering effects that can occur.

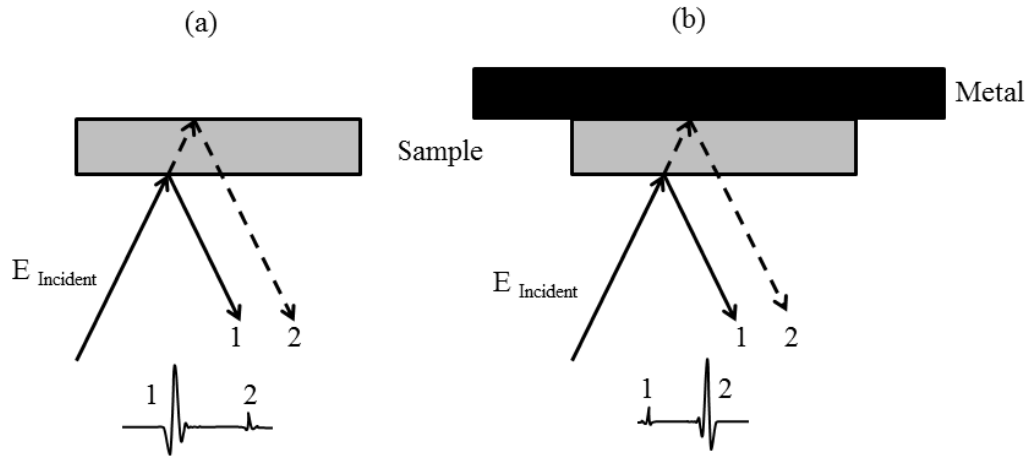

Figure II.3 : Reflection possible configurations: (a) traditional reflection setup, (b) false transmission.

I.3. TERAHERTZ GENERATION AND DETECTION BY PHOTOCONDUCTIVE ANTENNAS

In terahertz domain, photoconductive (PC) antennas are used for both generation and detection of pulsed or continuous waves [123]. The use of PC-antenna allows achieving high signal-to-noise ratio and performing fast scan for imaging and spectroscopy applications. They are constituted by semiconductor substrate and photoconductors, and behave as a Hertzian dipole. The schematic view of the photoconductive device and the emission concept are shown in Figure II.4 in two different views. The most used active layer is LT-GaAs, it has short carrier lifetime, high mobility and high breakdown voltage [124].

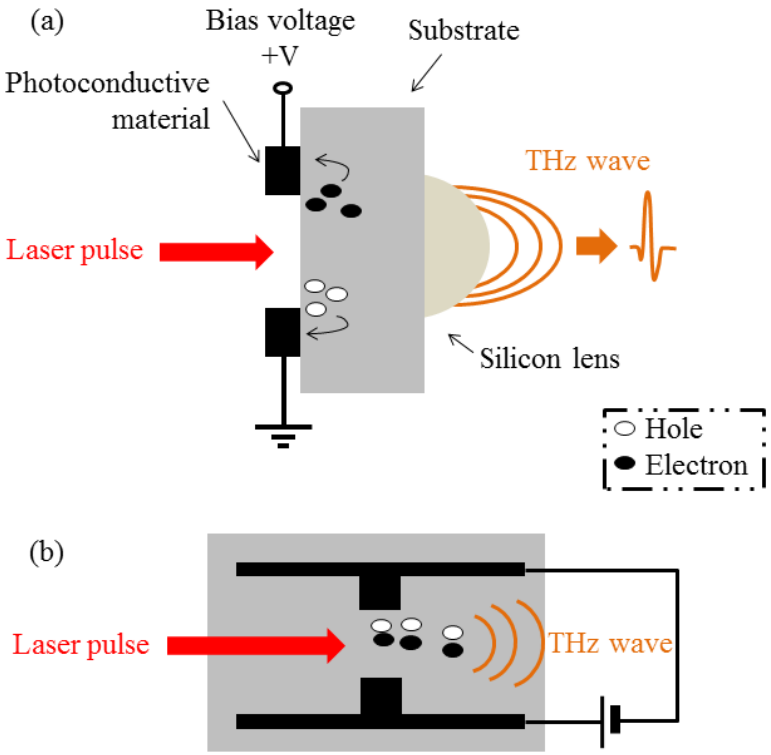

Figure II.4 : (a) Schematic side view and (b) top view of THz emission by photoconductive antenna.

Terahertz wave generation is achieved by pumping the photoconductive gap with femtosecond optical pulses having energy greater than the bandgap of the semiconductor. Thus, pairs of electrons-holes are generated, the electrons will occupy the conduction band, and the holes will be present in the valence band and this will enhance the conductivity of the semiconductor. The charge carriers are then accelerated by the bias voltage and their fast displacement is responsible for the apparition of a brief transient currant *J(t)* which "emits" a sub-picosecond time-domain electromagnetic field representing the THz pulse radiated by the photoconductive device. A PC-antenna has a similar behavior as an elementary Hertzian dipole antenna in free space. In this case, the radiated electric field $E(r, t)$ at a distance r and time t is described as:

$$E(r,t) = \frac{l_e}{4\pi\varepsilon_0 c^2 r} \frac{\partial J(t)}{\partial t} sin\theta \sim \frac{\partial J(t)}{\partial t} \quad (1)$$

where l_e is the effective length of the dipole, ε_0 is the dielectric constant of vacuum, c the velocity of light in vacuum, θ is the angle from the direction of the dipole, and $J(t)$ is the photocurrent in the dipole. $J(t)$ is defined by the convolution product between the optical pulse $I(t)$ and the response of the semiconductor substrate as follows:

$$J(t) = I(t) \otimes [n(t)q\ v(t)] \quad (2)$$

where $n(t)$, q and $v(t)$ represent the density, electric charge and velocity of electrons and holes. After generation, the pulse is emitted and collected by a hemispherical silicon lenses.

In the case of detection by PC-antennas, the dipole detects the photocurrent induced by the incident THz field. Illuminating the PC-antenna by a laser pulse creates charge, in the semiconductor substrate, carriers that have an extremely short lifetime. When the PC-antenna is exposed to an incident THz pulse, the carriers are accelerated and create an electric current in the circuit. This current is proportional to the amplitude of the terahertz field at the moment of illumination. However, the THz electric field is only sampled for an extremely short time interval (fs) of the entire electric field waveform, the temporal position of which can be adjusted via an optical delay line.

I.4. BEAM PROPAGATION PARAMETERS

The silicon lens placed on the back side of the GaAs substrate wafer allows coupling the THz wave into the space without spherical aberration or coma. Without this lens, a large part of the generated THz pulse is reflected from the back of the wafer and stays trapped in the substrate. Silicon is chosen to fabricate these lenses because it has low absorption and a uniform refraction index matching with GaAs (n = 3.42) between 0.2 and 5 THz, so that no chromatic aberration occurs. Moreover, parabolic mirrors are used in the setup, allowing the collection of the maximum of the emitted signal in the forward direction. Thus the amount of lost waves, due to scattering effects, is reduced.

The beam waist measurements of the Teraview transmission geometry are determined experimentally using the knife-edge method. Thus, by scanning a razor blade through the beam and recording the intensity, the values of the full width at half maximum (FWHM) of the signal are calculated at several frequencies. Figure II.5 (a) presents the profile of the THz beam waist at different frequencies: 0.5, 1, 1.5, 2 and 2.5 THz. Figure II.5 (b) shows the calculated values of the horizontal beam waist calculated for frequencies going from 0.2 to 3 THz; using the knife-edge and considering the FWHM. The values of the waist go from 3.1 mm at 0.2 THz to 0.25 mm at 3 THz.

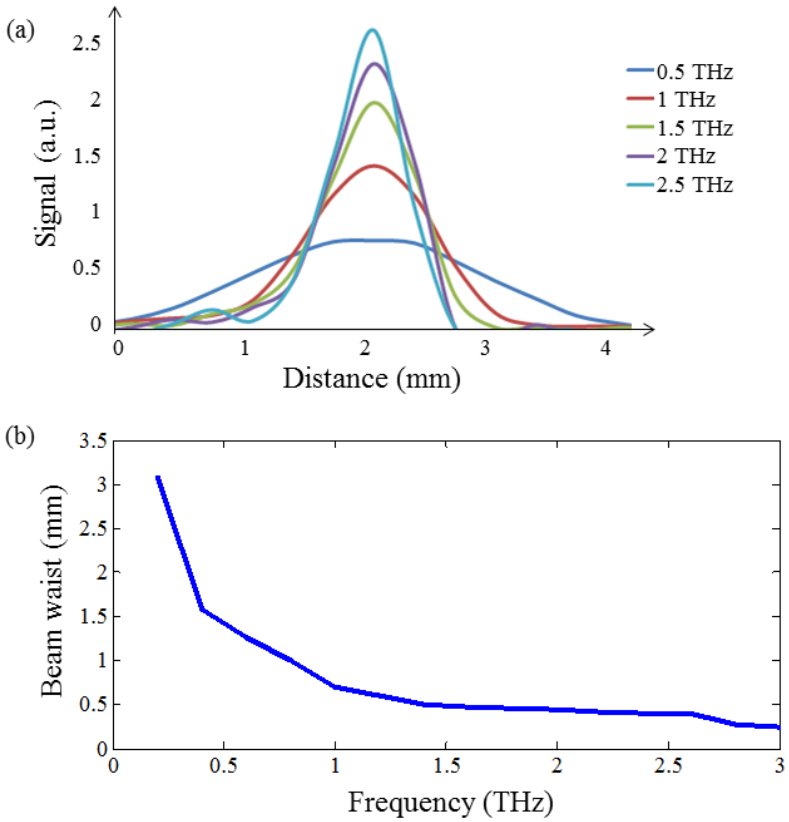

Figure II.5 : (a) Horizontal profile of the THz beam waist for the transmission setup for different frequencies: 0.5, 1, 1.5, 2 and 2.5 THz, (b) Beam waist values for the frequencies between 0.2 and 3 THz calculated by the FWHM with the knife-edge method.

I.5. TIME DOMAIN PRINCIPAL

The time-domain method uses a sampling technique that allows measuring one THz pulse, and is achieved by using an optical delay line. This technique consists in detecting a point from the THz pulse at each temporal position corresponding to the detection of the optical pulse by the PC-antenna. Figure II.6 illustrates the sampling method that allows constructing a THz pulse. For each position of the time delay line, the PC-antenna detects one point from the pulse. By using several measurements along the time delay position, it is possible to reconstruct the final temporal THz pulse as shown in the bottom of Figure II.6.

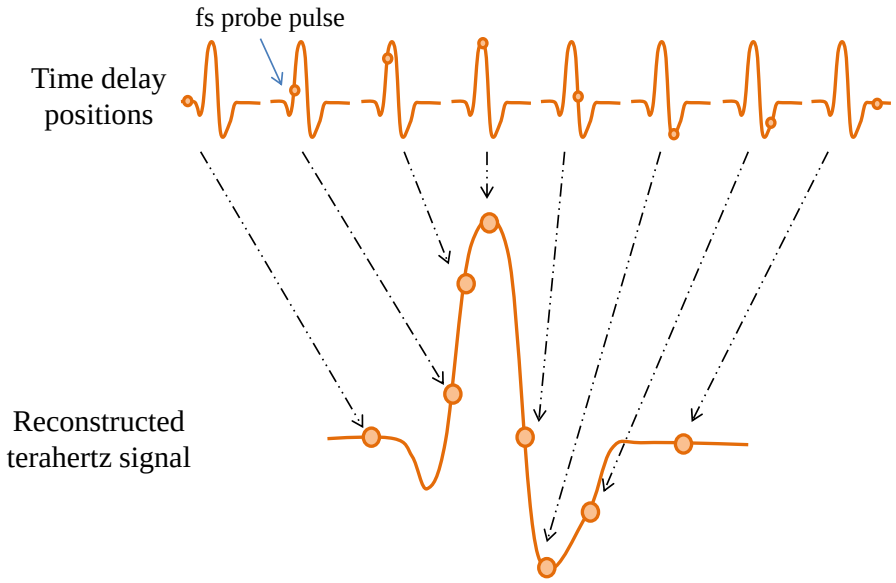

Figure II.6 : Illustration of the sampling concept of reconstruction of the THz temporal pulse detected by a PC-antenna.

The temporal resolution Δt of the reconstructed terahertz signal can be deduced from the spatial increment Δx of the optical delay line as follows:

$$\Delta t = 2\,\Delta x/c \tag{3}$$

where c is the velocity of light in vacuum. The 2 factor in the equation corresponds to the round trip of the delay line. The obtained temporal signal can be used for two main needs:

1- Thickness measurement and depth localization of a sample in a volume.
2- Spectroscopy and optical properties extraction of the material.

Pulsed THz is able to look into sample and reveal structures at different layers. The change of refractive index at interfaces of a sample with layered structures produces multiple reflection peaks in the terahertz waveforms. This allows non-destructive analysis of the coating layer and locating subsurface objects. Figure II.7 (b) shows typical terahertz pulse obtained in transmission mode for a wave propagating in the air (dash line) considered as a reference and a wave transmitted through a sample (plain line). By using the time delay between the sample and reference pulses it is possible to extract depth information about the sample. This procedure is very interesting when doing THz spectral imaging, where the temporal pulse can contribute to do 3D mapping of an object and analyze it in depth [125]. The echoes present in the sample pulse correspond to multiple reflections at the air-sample interfaces. The amplitude of the sample pulse is reduced in comparison to the reference pulse due to the absorption of the wave by the material and the interfaces reflection calculated by the Fresnel coefficients.

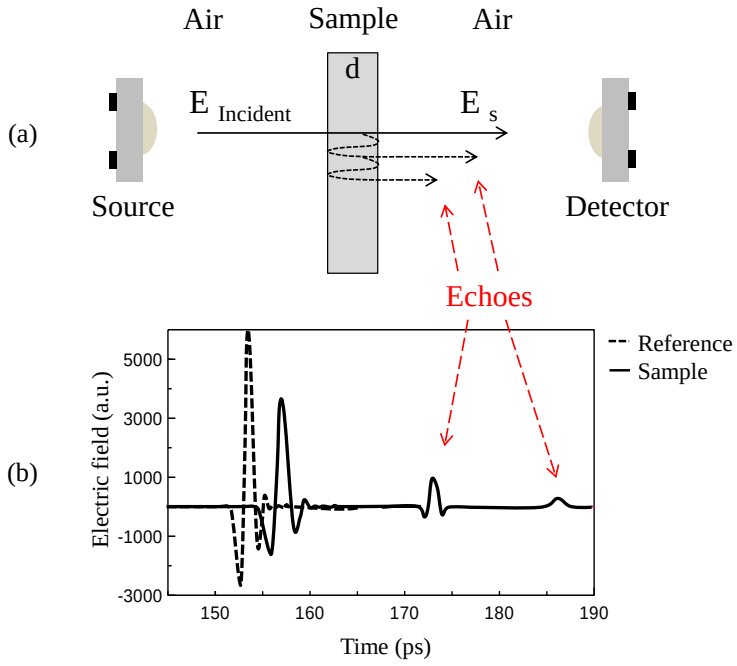

Figure II.7 : (a) Scheme of the time-domain spectroscopy, (b) typical time domain-pulses after propagation in the air (dashed line) and through the sample (plain line).

Application to spectroscopy is possible after applying the fast Fourier transform (FFT) to the temporal pulse. Fourier Transform is used in signal processing to transform temporal representation of a signal to the frequency domain, so it can explain physical concepts in the frequency domain and gives amplitude and phase information of the signal. Moreover, there is a high time-frequency duality; all the information contained in the signal is contained in the spectrum. The conversion of the time-domain signal into frequency domain is made as follows:

$$E(z,w) = \frac{1}{2\pi} \int_{-\infty}^{+\infty} E(z,t) e^{-i\omega t}\ dt \qquad (4)$$

Where *E(z,w)* is the complex electric field spectrum calculated by FFT and *E(z,t)* is the experimentally measured THz pulse electric field in the time domain. Figure II.8 (a) presents the temporal pulse (green) of a 400 mg pellet of 20%-wt lactose and 80%-wt PE. The spectral information is present in the main pulse as well as in the oscillations following the pulse, showed in the zoomed area. The amplitude of the FFT corresponding to the spectra in the frequency band 0-3 THz is represented in Figure II.8 (b) (green). The effective working range shown by the spectrum of the transmitted wave in dry air is between 0.1 and 3 THz. Before 0.1 THz and after 3 THz, the signal is affected by noise. However, sample spectrum can present smaller effective frequency band due to the absorbance of the wave by the sample that causes the reduction of the THz signal. So, the effective working range of the lactose pellet (Figure II.8 (b)) lies between 0.1 and 2.8 THz.

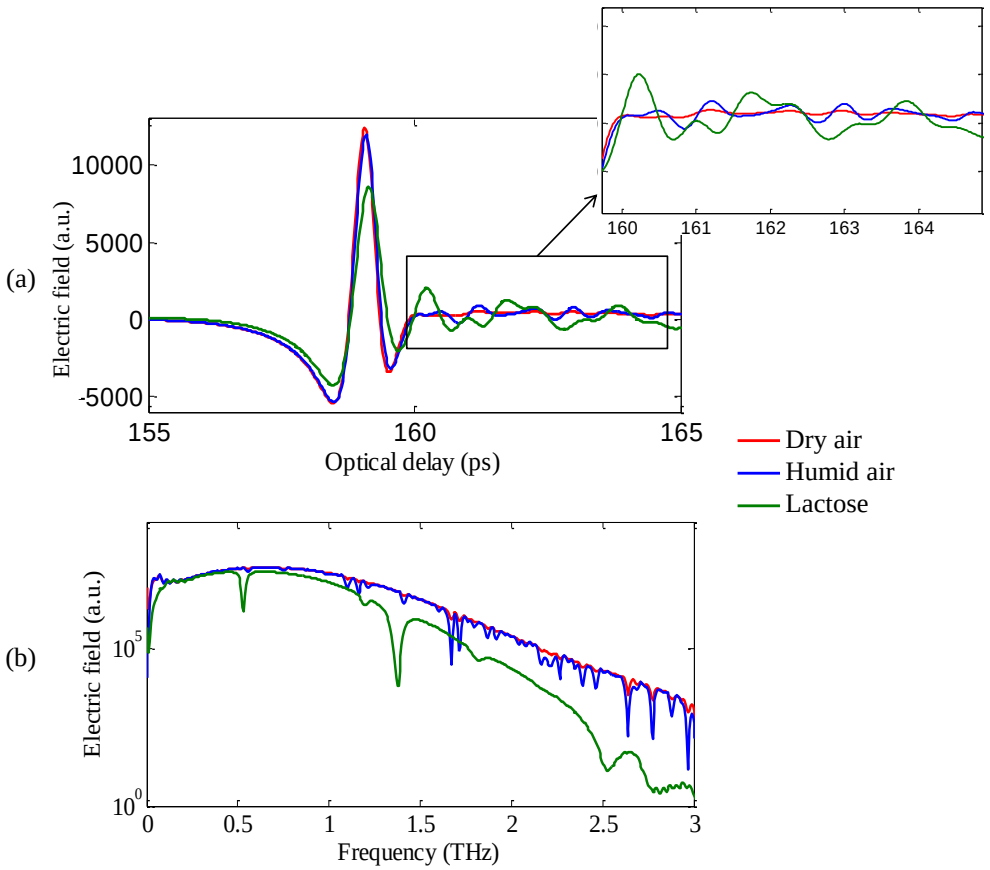

Figure II.8 : (a) Temporal signal and (b) THz electric field in the frequency domain obtained by FFT in three cases: without sample in dry air (red), in humid air (blue) and with a pellet of lactose of 400 mg total weight and 20 wt-% lactose in dry air (green).

The determination of the intrinsic dielectric parameters of a material is performed by analyzing the complex transfer function in the frequency domain, by the intermediation of a reference sample [24] [126]. Let us consider a sample positioned between the source and detector as shown in Figure II.7 (a). The electric fields transmitted through the reference and the sample, $E_r(w)$ and $E_s(w)$ respectively are expressed as follows:

$$E_r(w) = A_r e^{i\varphi_r} \tag{5}$$

and

$$E_s(w) = A_s e^{i\varphi_s} \tag{6}$$

Where A_r, A_s, φ_r, and φ_s are the amplitude and phase of the electric fields of the reference and the sample, respectively. To be able to calculate the complex transfer function of a sample as a function of its refractive index, several approximations should be taken into account. The electromagnetic beam is considered to have a plane wave impinging on the sample at normal incidence. As for the sample, it is considered as:

- Homogeneous, planar with parallel sides;
- Isotropic, without any surface charge;
- Having a linear electromagnetic response.

In this case, the electric field of the sample is expressed in a function of its reflection, transmission and propagation coefficients.

$$E_s(w) = T_{air-s}(w).P_s(w,d_s).T_{s-air}(w).E_{inc}(w).FP(w) \quad (7)$$

Where $T_{air\text{-}s}$ and $T_{s\text{-}air}$ are the transmission coefficients at the interfaces air-sample and sample-air respectively, P_s is the propagation coefficient in the sample, E_{inc} is the incident electric field and *FP* is the Fabry-Perot expression. FP takes into account the multiple reflections at the interfaces sample-air. It is written as follows:

$$FP(w) = \sum_{k=0}^{\infty} \left(R_{air-s}(w).P_s^2(w,d_s).T_{s-air}(w) \right) \quad (8)$$

Where R_{s_air} is the reflection coefficient at the interface air-sample is:

$$R_{s-air}(w) = \frac{\tilde{n}_s - \tilde{n}_{air}}{\tilde{n}_s + \tilde{n}_{air}} \quad (9)$$

The transmission coefficient at the interface air-sample is:

$$T_{s-air}(w) = \frac{2\,\tilde{n}_s}{\tilde{n}_s + \tilde{n}_{air}} \quad (10)$$

The propagation coefficient in the sample is:

$$P_s(w) = \exp\left[-i\,\frac{w\,d_s}{c}\,\tilde{n}_s\right] \quad (11)$$

By using these equations and one experimental value of the transfer function, it is possible to extract the complex refractive index that is expressed as a function of the real refractive index *n* and the extinction coefficient *k* that describes the strength of the relative absorption loss at a particular wavelength, as follow:

$$\tilde{n} = n - ik \quad (12)$$

Thus the absorption coefficient α can be calculated from the extinction coefficient as follow:

$$\alpha = \frac{4\pi w}{c}\,k \quad (13)$$

where c corresponds to the speed of light in vacuum. The complex transfer function corresponds to the ratio of the terahertz electric field in a chosen reference and after being transmitted through the sample, and can be simply expressed as follows:

$$Tr(w) = \frac{E_s}{E_r} = \frac{A_s}{A_r}\, exp[\varphi_s - \varphi_r] \tag{14}$$

where the amplitude and phase take into account the reflection, transmission, propagation coefficients and Fabry-Perot effect. By using the transfer function expression, the absorbance *A(w)* of the sample is calculated:

$$A(w) = -\log(Tr(w)) \tag{15}$$

The absorbance is a positive value without unit used as the spectral feature to identify the product. It is higher when the transmitted signal is lower.

I.6. SIGNAL PROCESSING AND NOISE REDUCTION

A common practice to describe the performance of a particular TDS system is to know its dynamic range (DR) and signal-to-noise ratio (SNR). The DR indicates the minimum detectable signal change and corresponds to the ratio of signal to noise expressed in dB. The SNR reports the extent to which a signal can vary and still be accurately measured; it is the ratio between the largest and smallest measured. For a system like THz-TDS, which measures both the amplitude and the phase, several methods are used to define the SNR and DR. Naftaly *et al.* proposed a procedure to calculate the SNR and DR for the time-domain and the spectra [127]. The main definitions of these two values are:

$$DR = \frac{maximum\ value\ of\ the\ signal}{maximum\ value\ of\ the\ noise} \tag{16}$$

And

$$SNR = \frac{maximum\ value\ of\ the\ signal}{standard\ deviation\ of\ the\ signal} \tag{17}$$

To reduce noise and artifacts on the measured spectra, several actions are made:

1- The measurements are performed in a chamber purged with dry air to eliminate water vapor. Figure II.8 (b) shows the spectra of a measurement made in dry (red), and humid air (blue) by opening the chamber. The blue spectrum represents undesirable absorption bands corresponding to the absorption of the THz waves by water molecules. A hygrometer is added to the setup to control in real-time the relative humidity level, which was kept below 1% by using a flow of dry air.

2- Each spectrum is average over 1000 repetitions to stabilize the signal fluctuations. However, the measurements of repeatability of the system are performed on the same sample several times along a long period of time. Results show a signal variance of less than 1% between one measured signal and the other one from another week. This variance is considered negligible and the signal is considered as repeatable over a long period.

3- An apodization function is applied to the signal to remove some artifacts. Various mathematical apodization functions are available, like Boxcar, triangular, Blackman-Harris

3-term and 4-term. In our study, we chose to apply the Blackman-Harris 3-term provided by the Teraview software to reduce the artifacts in our signal. However, these functions decrease the apparent spectral resolution [128] [129]. Figure II.9 shows the spectrum resulting from a measurement in dry air, where two apodization functions are applied: the Boxcar (red) and the Blackman-Harris 3-term (blue). The Boxcar is already reducing noise from the signal; however Blackman-Harris 3-term can smooth the spectrum and removes every peak with no chemical significance.

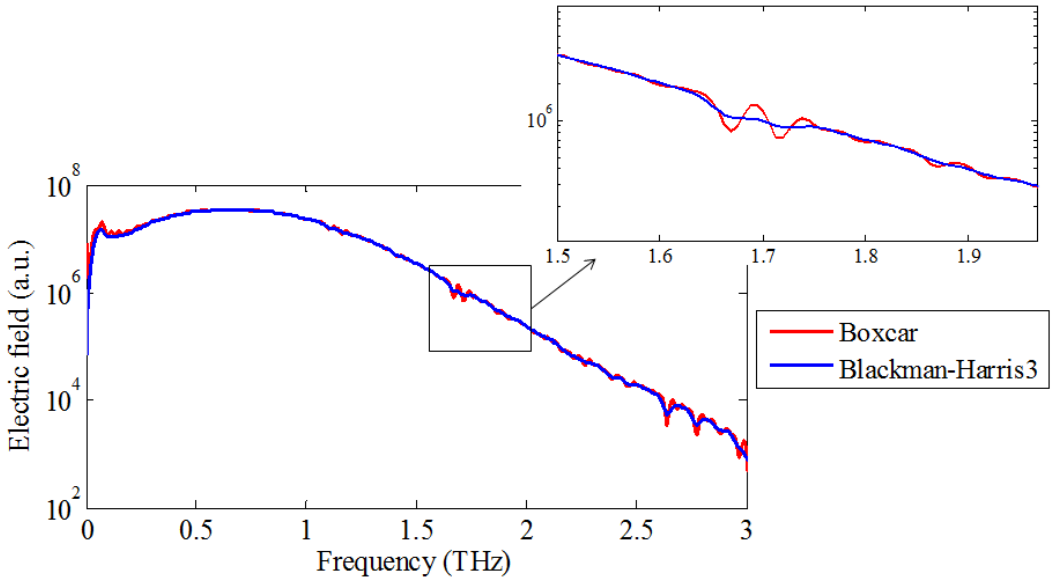

Figure II.9 : Signal measured in dry air conditions with two different apodization functions: boxcar (red) and Blackman-Harris 3-term (blue).

I.7. REFERENCE SELECTION

During the extraction of the absorbance spectrum, a high importance should be given to the selection of the reference, since there is no unique way to determine it. Here we study the effect of selecting different references on the resulting absorbance spectra. Figure II.10 (a) shows the absorbance spectra of a pellet made of 20 wt-% lactose 80 wt-% polyethylene (PE) with a total weight of 400 mg and 3.52 mm thickness. Three different references were used to extract the transfer function:

1- The reference signal is measured when the wave propagates in the air, the resulting absorbance spectrum is shown in pink (air),
2- The reference signal is measured when the wave propagates through a PE pellet of 400 mg and 3.97 mm thickness presented by the green absorbance spectrum (PE400),
3- The reference signal is measured when the wave propagates through a PE pellet of 570 mg and 5. 73 mm thickness, the absorbance spectrum in this case is shown in blue (PE570).

The first two are the most chosen depending on the application. For spectroscopy of chemical products presented as pressed pellets, the chosen reference is a pellet with the same thickness as the sample and constituted of a product transparent in the THz waves and used as the matrix for the pellet fabrication. This material is usually polyethylene. This choice allows reducing the effect of the Fresnel losses. At the opposite, when the sample is totally unknown, it is better to choose the air as a reference to extract the exact dielectric function. Finally, as shown in Figure II.10 (a), the amplitude decreases when increasing the thickness of the reference, and this is in accordance with the absorbance calculation. However, the difference between the spectra does not vary in the same way along the frequency band; it increases with higher frequencies. Table II.1 shows the difference of the absorbance values when selecting air, PE400 and PE570, calculated at the main peaks of the spectra. The variation is greater in the case of air as reference. Moreover, the variation of the baseline is not constant along the frequency band.

Table II.1 : Difference between the absorbance values when changing the reference.

	Peak at 0.533 THz	Peak at 1.192 THz	Peak at 1.374 THz	Peak at 1.814 THz	Peak at 2.529 THz
Air-PE400	0.01	0.16	0.19	0.3	0.56
Air-PE570	0.03	0.25	0.31	0.43	0.82
PE400-PE570	0.01	0.09	0.11	0.12	0.25

These result shows the high sensitivity of the absorbance to the way of selecting the reference signal and comparing the absorbance spectra provided by different laboratories should consequently be done with the greatest attention, especially when a quantitative analysis is conducted where the values of absorbance gives information about the product concentration in the sample. For our study, when dealing with chemical powders the reference chosen to extract the spectral features is a PE pellet with the same thickness as the one of the sample.

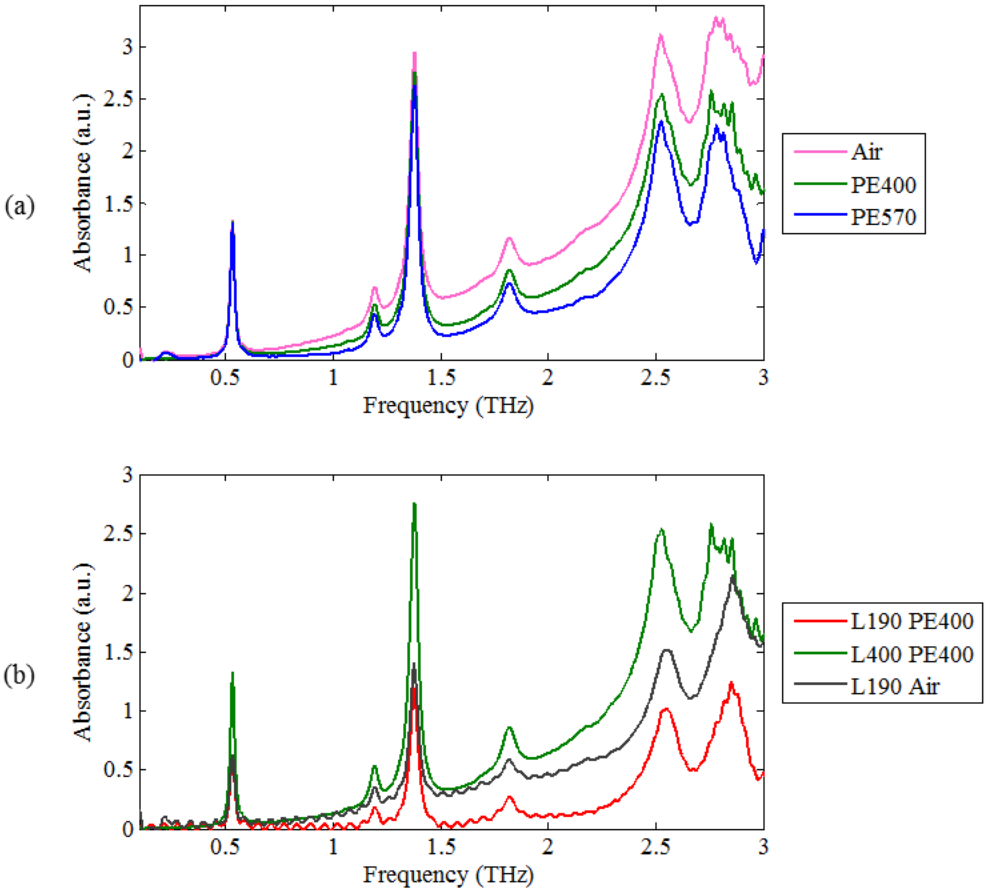

Figure II.10 : (a) Absorbance spectra of a lactose pellet of 400 mg content (20% lactose and 80% PE) and 3.52 mm thickness using three different references: Air (pink), PE pellet of 400 mg and 3.97 mm thickness (green) and PE pellet of 570 mg and 5.73 mm thickness (blue), (b) Absorbance spectrum of the lactose pellet of 190 mg content and 1.64 mm thickness calculated with two references: air (grey) and PE pellet of 400 mg and 3.97 mm thickness (red), also lactose pellet of 400 mg content and 3.52 mm thickness using the 400 mg PE pellet (green).

Another interesting aspect to consider is the size of the pellet itself. Figure II.10 (b) shows the absorbance spectrum of the lactose pellet of 190 mg content (20 wt-% lactose 80 wt-% PE) and 1.64 mm thickness calculated by using two references: air (grey) and PE pellet of 400 mg and 3.97 mm thickness (red). Compared to the ideal measurement where both, sample and reference, are pellets of 400 mg (green), with 20 wt-% lactose 80 wt-% PE and 100 wt-% PE respectively, the 190 mg pellet presents small oscillations in the absorbance spectra. These oscillations are caused by resonance absorption of the sample described by the Fabry-Perot effect. Their presence is due to echoes in the temporal pulse as shown in Figure II.7 (b). So, if Fabry-Perot effects appear in the absorbance spectra, we have to remove the oscillations by numerical filters.

Moreover, the impact of the product measurements in a pure state or in a host matrix is studied. Figure II.11 presents the spectra of three different pellets of citric acid measured with air as reference.

The first one is 100 wt-% citric acid (brown), the second and third ones are made by 20 wt-% citric acid and 80 wt-% PE with 190 mg (green) and 400 mg (orange) total weight respectively. The thickness of the pellet made with pure citric acid is the same as the 190 mg and half of the 400 mg. However, the absorbance is higher due to the high density of citric acid in the pellet. Moreover, the signal after 2 THz is highly absorbed by the pellet and it is not significant. Thus, by dealing with pure samples, the frequency band should be reduced depending on the material absorbance.

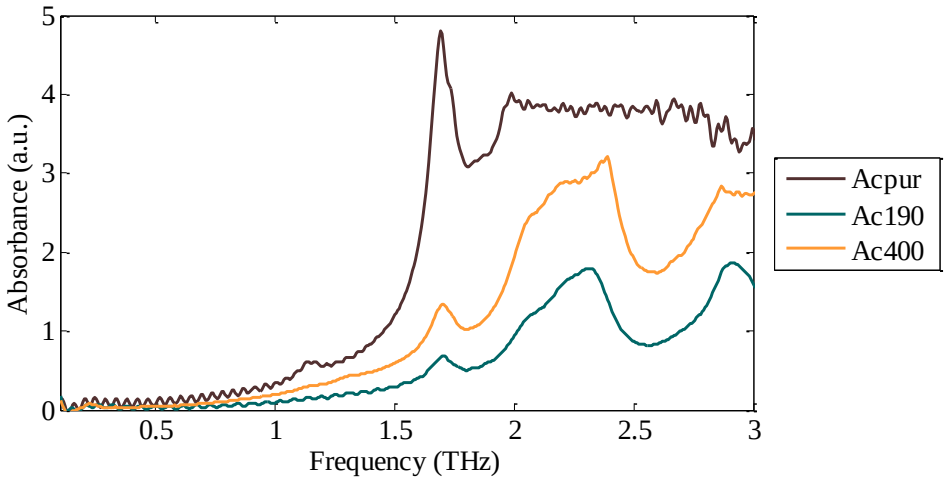

Figure II.11 : Absorbance spectra, using air as reference, for a citric acid pellet in three cases: pellet is made of 100 wt-% citric acid with a 1.85 mm thickness (brown), pellet made with 20 wt-% citric acid and 80 wt-% PE with a total weight and thickness of 190 mg and 1.74 mm (green) and 400 mg and 3.70 mm (orange) respectively.

This shows that the measurements of pure pellets are possible. However, the frequency band is smaller and this can limit the accessible number of fingerprints used to identify the element. Also, some discrepancies could appear, sample to sample, depending on the pellet fabrication.

I.8. MIXTURE SAMPLES ANALYSES

The knowledge of the THz interaction with materials is still very difficult to predict even with crystal materials. When dealing with a mixture, a high importance should be given to understand the difference that the various mixture components could have on the spectrum. With mixing different components, two main quantities are influenced: the thickness of the sample and the definition of its dielectric properties. In pure state different spectral responses are obtained when the same sample is present in various structures. Yet, it is more complicated to extract the effective dielectric response of the sample when it is the result of mixtures of several components. And here, advanced tools are needed for the analysis and the understanding of these mixtures.

The thickness of pellets depends on the weight and physical properties of each individual component. For the same weight two pellets may have different thicknesses if they are composed of different materials. For example, a pellet made of 400 mg PE has a 4.1 mm and a pellet of 400 mg

made with 80 wt-% PE and 20 wt-% lactose have 3.7 mm thickness. Thus, the same weight of components does not mean that the resulting pellet has the same thickness, and this point should be taken into account when measuring the absorbance of a pellet made by mixture.

The variation of the absorbance with the concentration of one of the individual components in a mixture follows the Beer-Lambert law, which is a proportional relationship between the absorbance and concentration of a substance, following:

$$A = \varepsilon\, b\, C \tag{18}$$

Where A is the absorbance, ε is the molar absorptivity of the substance, b is the path length of the propagating wave inside the sample, and C is the concentration. The absorbance of a given mixture is equal to the sum of the absorbance of each individual component. The overall absorbance of the solution can thus be written, at each frequency, as follows:

$$A = \sum_{i=1}^{n} \varepsilon_i\, b\, C_i \tag{19}$$

Where n is the number of components is the mixture. This relation is verified in Figure II.12 (a) that represents the absorbance of three pellets made of 80 wt-% of PE and 20 wt-% of lactose (red), fructose (green) and citric acid (blue). The sum of the absorbance of these three pellets is displayed in purple and compared with three times the absorbance of a pellet made by 6.6 wt-% of each of these three components and 80 wt-% of PE (pink). The multiplication by three is applied to the mixture pellet in order to make both sets of data comparable. However, a small shift appears after 1.4 THz that demonstrates that Beer-Lambert law is not applicable for all frequencies.

On the other hand, a comparison is made between probing pellets of mixed elements of a sequence of pellets made by one single component. Figure II.12 (b) shows two sets of pellets sequence. The first one in blue, represent a sequence of three pellets made by 20 wt-% of the compound and 80 wt-% of PE each, the compounds are: fructose, lactose and citric acid. The other one is a sequence of three identical pellets made by mixture of fructose, lactose and citric acid with 6.6 wt-% of each element and 80 wt-% of PE. The obtained absorbance spectra are identical for both sequences. This shows that the THz beam probes the molecule separately and the presence of one species in a sample does not influence the measurement of another species in the same sample as if the components do not interfere.

Moreover, we studied the effect of permutation of three pellets made of 20 wt-% of citric acid, fructose or lactose and 80 wt-% of PE. By placing fructose/lactose/citric acid or lactose/citric acid/fructose or citric acid/fructose/lactose, the resulting absorbance spectra is the same. So the refraction are kept roughly identical and at negligible level with respect to the transmitted field. Scattering effect is also constant whatever the position of the different pellets.

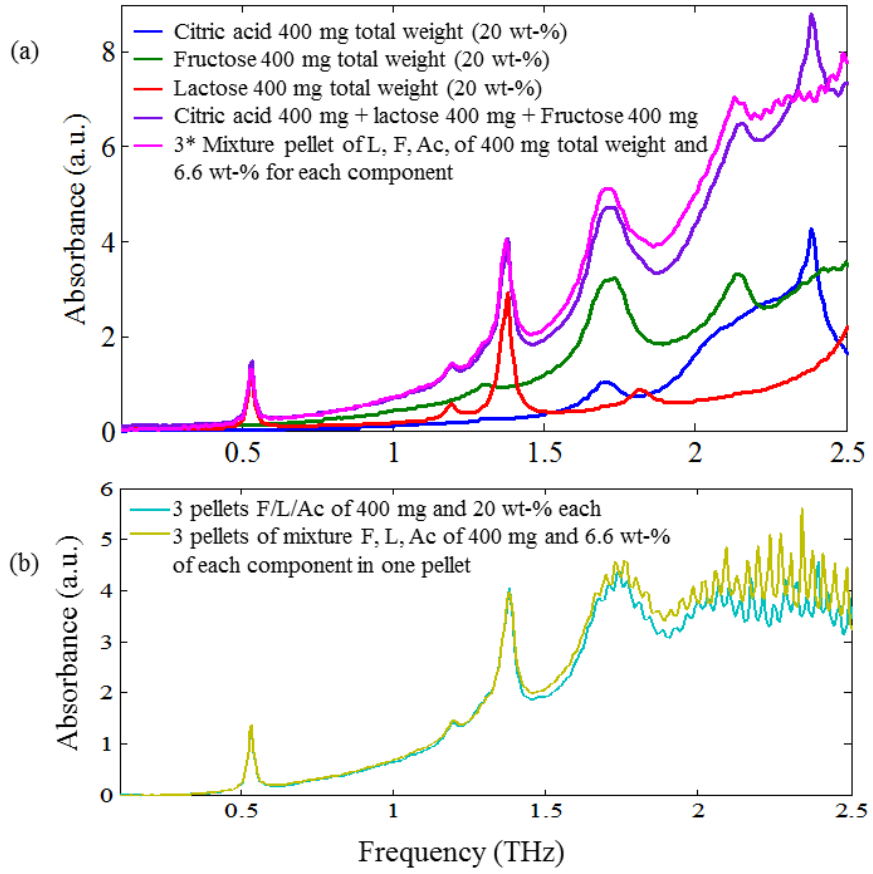

Figure II.12 : (a) Absorbance spectra, using PE as reference, of citric acid (blue), fructose (green) and lactose (red) made of 20 wt-% of each compound and 80 wt-% of PE, sum of the absorbance of the three mentioned pellets (purple), three times the absorbance spectra of a pellet made by mixture of citric acid, fructose and lactose with 6.6 wt-% each and 80 wt-% PE (pink), (b) three pellets placed one after the other of Fructose then lactose then citric acid, each one is constituted by 20 wt-% of compound and 80 wt-% of PE (blue), Absorbance of three pellets of mixture made of 6.6 wt-% of citric acid, fructose and lactose and 80 wt-% PE each (yellow).

I.9. SYNTHESIS

This measurement shows the complexity of extraction of a repeatable response of the material from experimental condition to another. Several elements can be responsible for the variance of a sample spectrum. It can be caused by the scattering effects in the sample, or the measurement of the same product obtained from different providers, as well as the extraction of the spectra at different position on the sample. All this highlights the high level of vigilance that should be taken when proceeding spectroscopy measurements and extracting the dielectric properties of the material. Furthermore, the thickness of the sample under study has an important influence on the response of the material, and with variant thicknesses, of the sample as well as the reference chosen, different reactions can occur. Moreover, these analyses presented the response of mixtures and helped understanding the interaction of the terahertz wave with a medium formed by mixtures of products.

Also, it showed that mixed components do not interfere one to another inside a mixed sample. This agrees with the Beer-Lambert law for some frequencies along the terahertz rang.

II. SPECTROSCOPIC ANALYSIS OF PACKAGING MATERIALS

II.1. SAMPLES USED IN POSTAL CHAIN

Many studies investigated the potential of terahertz spectroscopy to probe through materials and several works focused on the investigation of the spectral response of specific objects like, plastic, cardboard, paper, etc. [130]. The dynamic ranges available with the current sources and detectors allow analyses to a depth of typically several centimeters into common materials. Here, we investigate several types of packaging materials used in postal chain. Figure II.13 (a) show an image of these materials: paper material for letters (S1, S2), paper and bubble wrap (S3), EPP foam (S4), bubble wrap (S5), shipping peanuts (S6, S7, S8).

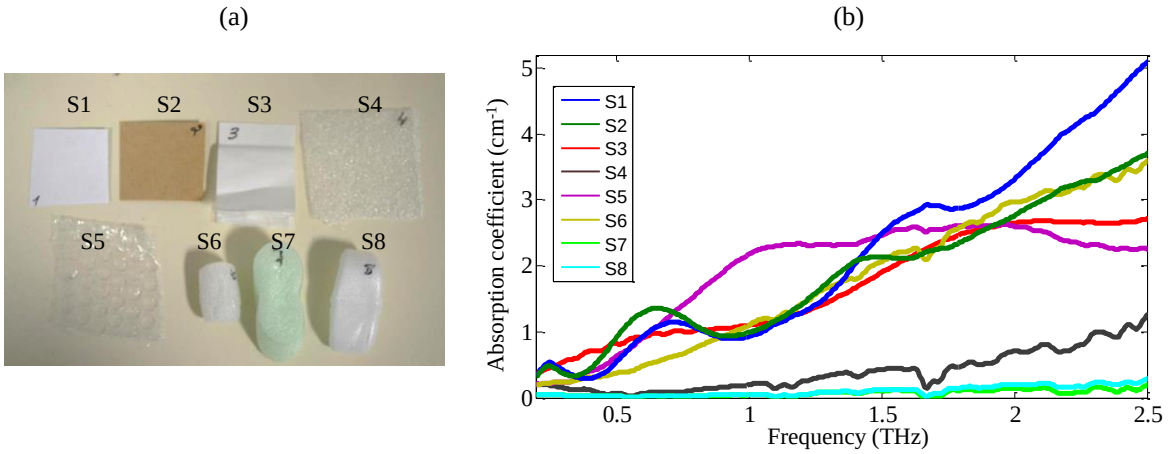

Figure II.13 : (a) Photograph of typical packaging materials samples used in postal chain and their (b) absorption coefficient.

The refractive index of these materials is measured by time-domain spectroscopy in transmission and the values for the frequency range between 0.2 and 2.5 as well as the thickness for each sample are represented in Table II.2. Furthermore, the absorption coefficient was measured for the materials for the frequencies between 0.2 and 2.5 THz (Figure II.13 (b)). This coefficient determines how far into a material a particular wavelength can penetrate before it is absorbed. The relationship between absorption coefficient and frequency makes it so that different frequencies penetrate different distances into a material before most of the light is absorbed. The absorption depth is given by the inverse of the absorption coefficient α^{-1}. It is the most useful parameter which gives the distance into the material at which the light drops to about 36% of its original intensity, or alternately has dropped by a factor of $1/e$. Then, in a material with a low absorption coefficient (typically<5cm^{-1}),

sufficient power can be collected by the detector in transmission mode, which is the case of the eight samples represented here.

For the samples S1, S2, S3, S5 and S6, the absorption coefficient is highly increasing with the frequency remaining lower to 5 cm^{-1}. S1 and S2 present some undulations along the frequency range, due to the measurement made through both interfaces. The materials composing sample S4, S7 and S8 present the lowest absorption coefficient. For S4 this coefficient goes from 0.05 cm^{-1} at 0.5 THz to 1.33 cm^{-1} at 2.5 THz. As for S7 and S8 they have values of the absorption coefficient varying around 0.02 cm^{-1} along the actual frequency band. Consequently, some tradeoff between thickness, resolution and frequency has to be considered according to the sample geometry and the signal to noise ratio of the detection system. Typically, the frequency band between 0.2 and 2.5 THz is a good window to perform in-depth analysis through packaging materials.

Table II.2 : Refractive index of eight packaging materials used in postal chain.

Sample	S1	S2	S3	S4	S5	S6	S7	S8
Thickness (mm)	0.22	0.25	2.5	1.3	1.3	2.88	5.3	6.5
Refractive index	1.42	1.37	1.04	1.01	1.02	1.02	1.006	1.007

II.2. TERAHERTZ SPECTROSCOPY THROUGH PACKAGING

When inspecting parcels, it is important to understand the response of the packaging material. Although low absorbance and the minor presence of significant chemical signature in the packaging materials, it can affect the spectrum of the chemical product when it is analyzed through it. To present this issue, a cardboard sample used for packaging is measured with time-domain THz spectroscopy. Figure II.14 represents the absorbance spectra calculated by taking air as reference, between 0.1 and 3 THz, for four samples: one piece of cardboard (blue), two pieces of cardboards (green), lactose pellet (20 wt-% lactose + 80 wt-% PE) (red) and the same lactose pellet placed between two pieces of cardboard (purple). The spectrum of the cardboard presents no chemical signature; however, it has an effect on the pellet as highlighted in the purple spectra, between 2.3 and 3 THz, where it presents different fingerprints in addition to the ones observed on the single pellet presented by the spectra in red. Moreover, their presence strongly affects the baseline of the absorbance spectra.

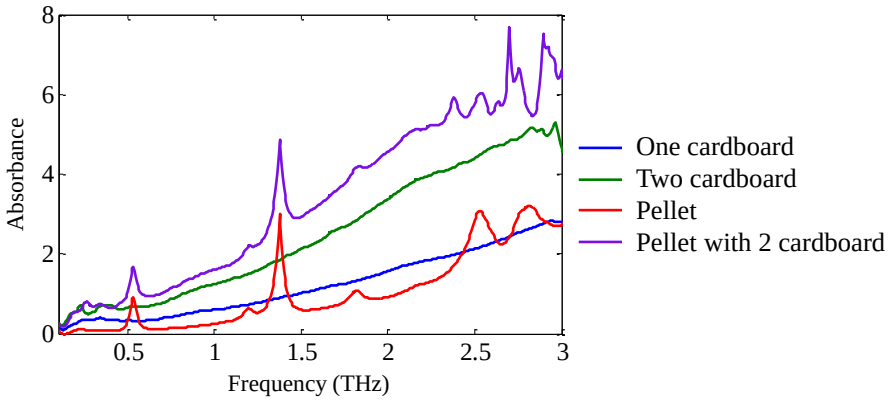

Figure II.14 : Absorbance spectra calculated by taking air as reference, for six samples: one piece of cardboard (blue), two pieces of cardboards (green), lactose pellet (20 wt-% lactose + 80 wt-% PE) (red) and the same lactose pellet placed between two pieces of cardboard (purple).

This analysis illustrates the impact of the packaging materials on the identification of chemical products and underlines the limitation of recognition of the product through packaging. It highlights the importance of using statistical selection methods like chemometric tools used in the present study, in order to extract the signature of the powder and avoids the impact of the packaging materials.

II.3. IMAGING THROUGH PACKAGING

The same configuration of "cardboard1/lactose pellet/cardboard2" measured in spectroscopy is also imaged where the pellet is placed between the two cardboard pieces as shown in Figure II.15 (a). The spectrum, in Figure II.15 (b), is clearly pointing out the fingerprints of the lactose and it is identical at each pixel of the image belonging to the pellets region. However, by analyzing the THz resulting image at different frequencies, 0.21 (d) and 0.52 (e) THz for examples, the image reveals different information. This effect is due to the multilayer structure of the cardboard that presents in depth a various structure affecting the quality of the image. This impact is destructive to the real physical information of the sample and can induce wrong interpretation.

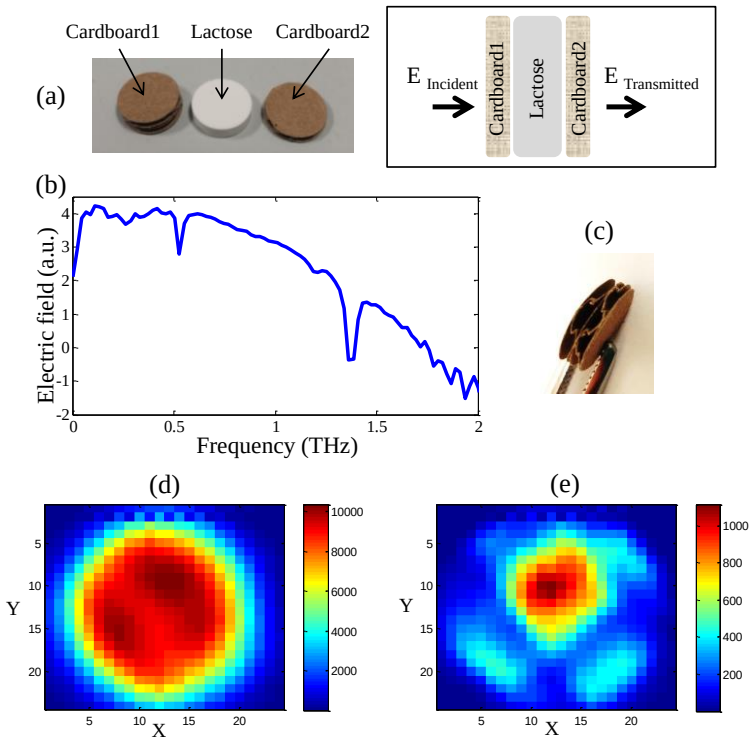

Figure II.15 : (a) Optical image and (b) configuration of lactose pellet (20 wt-% lactose + 80 wt-% PE) between two pieces of cardboard, (b) spectra measured at one pixel through three objects:cardboard1, pellet, cardboard2 , (c) photo of the internal structure of cardboard, THz image extracted at 0.21 THz (d) and 0.52 THz (e).

Reflection spectroscopy could be used for powder analysis through letter. To this aim, lactose in powder state is filled inside a plastic bag and inserted inside a letter as shown in Figure II.16 (a). This measurement is performed using the configuration presented in Figure II.3 (b) where a piece of metal is positioned on the sample. The scanned surface is 17.5×9 cm^2 with an axial resolution of 0.5 mm along *X* and *Y* direction. Figure II.16 (b) represent the terahertz image of the sample at 0.5 THz. In this image, the presence of the lactose powder is revealed even through the letter and the plastic bag. Figure II.17 (c) presents the spectrum of the lactose through the letter and the plastic bag (position (1)) and the spectrum at a position on the letter (position (2)). The reflection measurement was able to extract the lactose signature from the packaging materials. Moreover, THz spectral imaging can separate different object in depth even when they are placed inside letters. This permits thickness measurement of the objects through paper and localize each component without opening the letter. Furthermore, this allows leading qualitative and quantitative chemical analysis through this type of packaging.

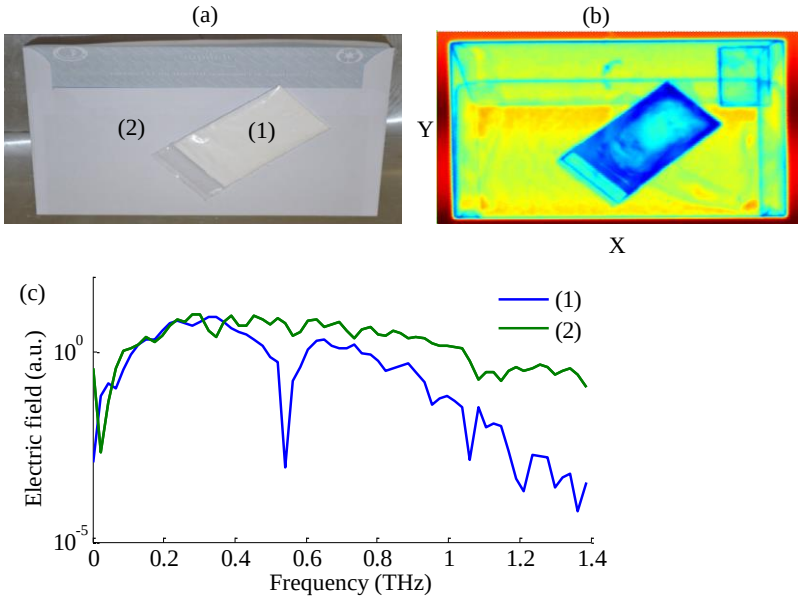

Figure II.16 : (a) Photograph of the lactose powder filled inside a plastic bag and inserted inside a letter, (b) terahertz image at 0.5 THz of the powder imaged through the letter, (c) Terahertz waveform at two positions: (1) at the lactose powder and (2) at the letter.

II.4. SYNTHESIS

These examples illustrate some of the effects caused by the presence of packaging materials, on parcels inspection, when applying terahertz time domain spectroscopy and spectral imaging as investigation techniques.

First, the absorption coefficient measurements of several type of packaging material demonstrated the possibility of measuring through these materials typically between 0.2 and 2.5 THz and even for higher frequencies. Also, the thickness of the package has a high influence on the spectra; by increasing this thickness the transmitted signal is reduced. Yet, terahertz spectroscopy can be established through several centimeters of thickness of these materials.

Despite the neglecting chemical signature, these materials have a high effect on the terahertz spectral measurements. We showed that fluctuation and even additional peaks are affecting the spectra of a single product caused by the presence of the packaging materials, as well as on an entire image scanned through these materials.

These spectra highlight the importance of statistical analysis when dealing with measurements of products through packaging materials. Thus, to be able to extract the chemical signature from the packaging when measuring a powder inside a parcel, chemometric tools, can be efficient because they have the potential of extracting significant information from noise.

III. CHEMOMETRIC TOOLS

Chemometrics is the science of statistical and mathematical methods applied to chemical data to extract the maximum chemical information. The application areas of chemometrics are various going from chemical, physical and biological studies, to food industry [131] and psychology for hedonics analyses [132]. Svante *et al*. discussed in 1998 how successful chemometrics has been used in several applications [133]. Moreover, it has been successfully examined by many spectroscopic methods like Raman and Laser-induce breakdown spectroscopy (LIBS) [134] [135].

One of the basic methods used in chemometrics is the multivariate analysis, which is used to analyze data that arises from more than one variable e.g. frequencies in the THz spectroscopy. One of the powerful advantages of multivariate analysis is the ability to separate out useful information from noise. In this work, we are using three basic multivariate linear techniques: Principal Component Analysis (PCA), Partial Least Square (PLS) and Partial Least Square-Discriminant Analysis (PLS-DA). These techniques are applied to THz spectral data and spectral images, basically on explosives spectra, to extract information about the samples in pure state and in mixtures, such as the material nature, the components concentrations, etc. PCA is used to describe the data and visualize similarities or groupings among the data. PLS-DA is performed in order to classify unknown data into specific classes created by the model. And PLS is used to quantify unknown samples and extract the amount of elements in mixtures. The techniques are computed using commercial software from UMETRICS, the SIMCA-P+12. The detailed mathematical calculations are not developed here, but a brief description of the way that each of these methods work, is presented below [136]. Before discussing each method separately, let us introduce some mathematical parameters that are used in multivariate analysis [137]. In statistical calculations, each group of data has a known type of distribution, where different parameters are important to consider. The most used estimator for the central value is the arithmetic mean $\bar{G}$. For a *G* vector of *n* data G= [G_1, G_2, …, G_n], the mean of the variable is the sum of observed values in a data divided by the number of observations, expressed as follows:

$$\bar{G} = \frac{1}{n}\sum_{i=1}^{n} G_i \tag{20}$$

The classical measure for the variation of the data is the standard deviation *s* that gives an idea about how the data are spread. It is more sensitive to outliers than the mean because it is proportional to the squared deviation. In normal statistical distribution, this measure is widely used. It is calculated as follows:

$$s = \sqrt{\frac{1}{n-1}\sum_{i=1}^{n}(G_i - \bar{G})^2} \tag{21}$$

For multispectral data analysis, the most important calculation is the covariance matrix. It helps understanding the relation between data. Considering *X* matrix with a dimension $n \times m$, *n* is the number of variables corresponding to the number of columns and *m* is the number of rows corresponding to samples.

$$X = \begin{bmatrix} X_{11} & X_{21} & X_{31} & \cdots & \cdots & X_{n1} \\ X_{12} & X_{22} & X_{32} & \cdots & \cdots & X_{n2} \\ \vdots & \vdots & \vdots & \vdots & \vdots & \vdots \\ \vdots & \vdots & \vdots & \vdots & \vdots & \vdots \\ X_{1m} & X_{2m} & X_{3m} & \cdots & \cdots & X_{nm} \end{bmatrix} \quad (22)$$

The covariance matrix of X is a square matrix of $n \times n$ dimension. The diagonal of this covariance matrix corresponds to the variance of each X_i column. The other elements of this covariance matrix correspond to the covariance between two columns of X, because, in opposite to the variance, the covariance is always measured between two dimensions. The covariance value between the first two vectors X_1 and X_2 is written as:

$$cov(X_1, X_2) = \frac{1}{m-1} \sum_{i=1}^{m} (X_{1i} - \overline{X_1})\ (X_{2i} - \overline{X_2}) \quad (23)$$

Where $\overline{X_1}$ and $\overline{X_2}$ are the arithmetic means of the vectors X_1 and X_2, respectively. Knowing that $cov(X_1, X_2) = cov(X_2, X_1)$, and by applying the calculation to the entire columns, the covariance matrix $n \times n$ can be written as:

$$C = \begin{bmatrix} var(X_1) & cov(X_1, X_2) & \cdots & cov(X_1, X_n) \\ cov(X_2, X_1) & var(X_2) & \cdots & cov(X_2, X_n) \\ \vdots & \vdots & \ddots & \vdots \\ cov(X_n, X_1) & cov(X_n, X_2) & \cdots & var(X_n) \end{bmatrix} \quad (24)$$

The sign of the covariance value gives an understanding of the relation between the n vectors. A positive covariance value indicates that both dimensions increase together. A negative value means that when one dimension increases the other decreases. Finally, if the covariance is zero, the two dimensions are independent of each other.

III.1. PRINCIPAL COMPONENT ANALYSIS

Principal component analysis (PCA) is a widely used technique in various domains. It was first invented by Karl Pearson in 1901. Later on, the algorithm was developed for different purposes. Grung *et al.* developed, in 1989, a singular value decomposition (SVD) algorithm to compute missing values when performing principal component analysis on messy data sets and Brown *et al.* evolves a principal component analysis routine that utilizes maximum likelihood theory to compensate for correlated measurement error among the variables in the data matrix [138][139]. Till now, PCA is developed and used in various fields like signal processing and data compression for hyperspectral images analysis [140] [141], in imaging for face recognition [142], in LIBS and Raman spectroscopy for pigments and ink analysis [143], etc.

Principal Component Analysis is a linear transformation method used to reduce the dimensionality of a data set which consists of a large number of variables, while retaining a maximum of the variation present in the data set. The dimensionality reduction is achieved by projecting the data onto a lower-dimensional orthogonal subspace, formed by new components called principal components (PCs) of k dimension ($k<n$). So we are projecting the entire set of data onto a different

subspace and trying to find the axes with maximum variances where the data is most spread [144]–[146]. An example of dimensionality reduction is presented in Figure II.17, where we pass from n=2 dimension space to k=1 vector or PC so that the data are projected differently. This PC is defined in the aim of minimizing the variance which schematically is the distance between the data and the PC vector represented by the red arrows in Figure II.17.

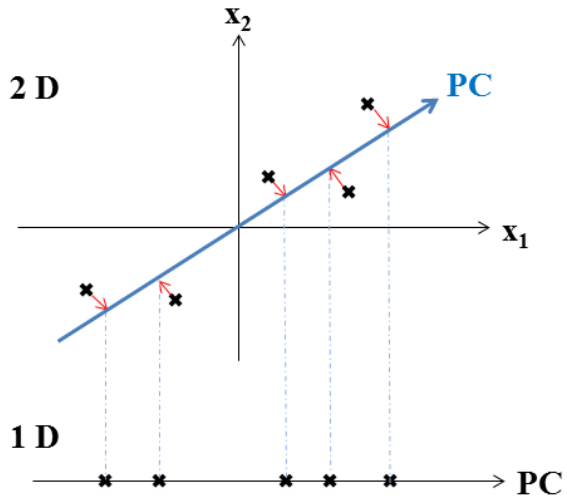

Figure II.17 : Data compression concept: transformation of the data projection space from two dimensions (x_1, x_2) to one dimension vector (PC).

As for the reduction from 2D to 1D, the PCA can reduce *n* dimension vectors onto *k* vectors corresponding to the number of components. The detailed mathematical calculation of PCs is not the aim of this work; just a simple concept is presented.

Before the PCA calculation starts, a scaling of the data is computed to obtain a zero mean matrix. This will be discussed later in detail in III.4 .The next step consists of decomposing the $n \times m$ data matrix into the product of two matrices as follows:

$$X = TP^T + E \tag{25}$$

where E is a residue matrix of the variance, unexplained by TP^T, it represents the deviations between the original values and the projections. T is an $n \times k$ matrix of eigenvalues or scores of the PCs; it describes how the different rows in X (observations) are related to each other. The transpose of P, P^T is a $k \times m$ matrix of the eigenvalues or loadings of the PCs, it represents the weights (influence) of the variables in X on the scores T.

So how the PCs are calculated? There are several PCA algorithms in the literature, namely SVD (singular value decomposition) [147][148], NIPALS (nonlinear iterative partial least squares) [149], and EVD (eigenvalue decomposition) that are used to extract the PCs and calculate the scores and loadings. SVD and EVD extract all the principal components simultaneously, while NIPALS

calculate them sequentially, one PC at a time. It should be mentioned that the eigenvalues and eigenvectors are sorted in order to have a matrix where the first vector corresponds to the eigenvector with the higher eigenvalue. The second column is the eigenvector of the second higher eigenvalue, and so on till arranging all the eigenvectors of the PCs. Basically, the PCs are obtained from the covariance matrix of the measured data. In the iterative method for example, the number of PCs is defined by the estimated error *E* and the iteration stopped when the error reaches a low value. The SVD extract the PC after several matrix calculations starting from the diagonal matrix of the eigenvalues. The last step consists of representing the observations in the new coordinates, the PCs. Thus, the visualization of the data is made by different plots like score and loading plots. Typically, a maximum of seven scores is sufficient to describe more than 95% of the variance.

III.2. PARTIAL LEAST SQUARES

While PCA uses one matrix of data *X*, to explore and visualize the data table, PLS is used when we have two blocks of data *X* and *Y*. It is an iterative algorithm used to correlate the information from one block to the information in the other one and to predict the *Y* value of new samples [150]. Later in this work, for the PLS models, the *X* matrix represents measurements of the absorbance spectra for several samples, and the *Y* matrix contains the concentrations of compounds. PLS is a supervised method and its concept is to create a calibration model from *X* and *Y* and then uses only *X* variables to predict *Y*. So by measuring a new absorbance spectra we can apply the PLS model to predict the components concentrations. To do so, the PLS algorithm develops approximately the same calculation as the PCA, but for the *X* and *Y* matrix. *X* is composed of *n* lines and *m* columns and *Y* is composed of *n* lines and *j* column with $j<<m$. Then, for each matrix we will create a model where a matrix is equal to the product of the scores and loadings plus a residual. Afterwards, the two matrices are optimized numerically in order to maximize the correlation between *X* and *Y*.

$$\begin{aligned} X &= TP' + E \\ Y &= UQ' + F \end{aligned} \tag{26}$$

T and *U* are the scores of the *X* and *Y* matrices respectively, *P'* and *Q'* are the loadings transpose of *X* and *Y* respectively, *E* and *F* are the residues. The scores and loadings are developed in such a way that the i^{th} score in *X* so t_i have the maximum covariance with the i^{th} score in *Y* u_i for i=1,…, k. That means that we can predict the i^{th} score in *Y* from the i^{th} score in *X*. So the score values in *X* allows calculating the score values in *Y*, thus, we can predict *Y* values. The goal of the PLS algorithm is to minimize the residue *F* in *Y* while keeping the correlation between *X* and *Y* by the inner relation U = BT as shown in Figure II.18, where *B* is a regression coefficient relating *X* to *Y* [151] [152].

Two types of PLS exist and are discussed in this work: PLS1 and PLS2. The PLS2 regression is when the *Y* matrix contains two or more variables. Thus PLS1 is when we have only one *Y* variable. The calculations in the both cases are similar [153].

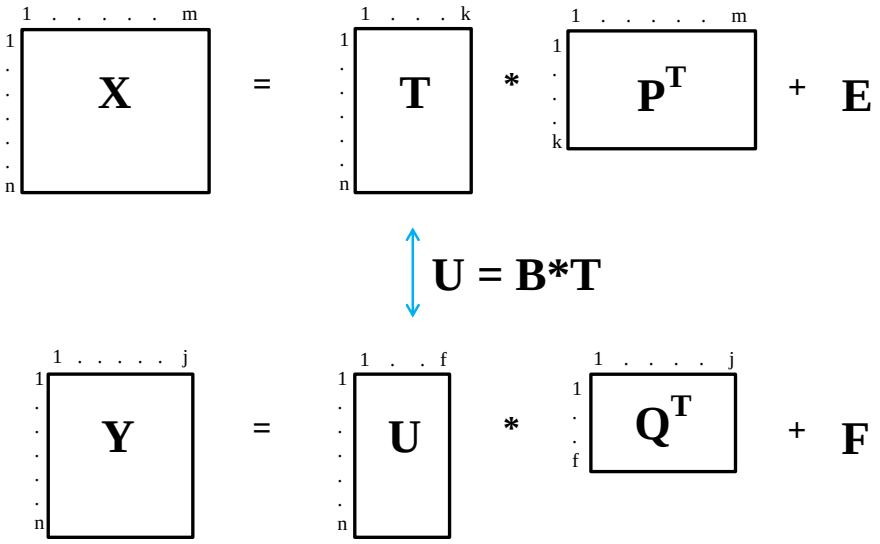

Figure II.18 : PLS concept and matrix decomposition into scores and loadings.

To build a PLS model, the data are divided in two sets. The calibration set used to create the model, and the test set used to predict new samples unknown by the model. The test set shows the prediction potential of a model and its limits in prediction. This is numerically described by special parameter as RMSE and RE discussed later in this chapter.

III.3. PARTIAL LEAST SQUARE-DISCRIMINANT ANALYSIS

PLS Discriminant Analysis is performed in order to sharpen the separation between several groups of observations, by creating PC components to obtain a maximum separation among classes. PLS-DA is a variant of the PLS used when the Y represents a qualitative information expressing the class membership of the statistical units. It is used for several needs in various domains like food analysis with multivariate images [154], in biology [155], oil analysis [156], etc.

PCA can be used for classification purposes by sorting the groups formed by the score plot. However, it is an unsupervised method and gives global visualization of group's repartition. In contrary, PLS-DA is a supervised method, and the classification information is combined with identification of unknown sample by its belonging to a specified class. In this work, PLS-DA is implemented to classify powder samples in classes of pure explosive or mixture, using spectral information, and to group different types of explosives and their mixture in hyperspectral images.

III.4. SCALING

Two types of scaling can be applied to the initial X matrix of the measured data before calculating the principal component: center (ctr) scale and unit variance (UV) scale. This step is

important in order to homogenize the data and remove dispersions. The choice of the scaling depends mainly on the data quality. When the variables have symmetric distribution, then the mean is the proper measure of the center of the data, thus center scale should give a better performance. When the variables have a skewed distribution, the mean can be highly influenced by an observation that falls far from the rest of the data, called an outlier. In this case, a unit variance scale can be more efficient for the data description. Practically, if the variables are all on the same scale such as spectroscopic data then center scale is recommended. If the variables have different scales (i.e. comparing powder with liquid explosives) the unit variance scale is advisable [157].

For the center scale calculation, for i=1,.., n in the original matrix *X*, each value in each of the *n* column is converted as follow:

$$X'_{ij} = X_{ij} - \bar{X}_i \tag{27}$$

where j=1,…, m is the number of rows and $\bar{X}_i$ is the mean of each line of the *X* matrix. For the unit variance scale, an additional step is to divide each value in the column by the standard deviation, so the new value is:

$$X'_{ij} = \frac{X_{ij} - \bar{X}_i}{s_i} \tag{28}$$

where s_i is the standard deviation of the column I in the X matrix.

III.5. NUMBER OF COMPONENTS AND OUTLIERS

The important point when setting up a multivariate model is to make a decision for the optimum number of principal components involved in the model. This can be determined from several rules. Basically, it is done by the “scree” method that is applied by first plotting the eigenvalues as a function of the corresponding principal component. To define the PC number, one should search for the point in the plot called “elbow” which is the point of the graph where the slope goes from “steep” to “flat” and keep only the components which are before the elbow as shown in Figure II.19 (a) [145].

For prediction models (PLS or PLS-DA) the optimum number of components is determined empirically by cross validation [158] using an increasing number of components. Some methods consist of calculating the PRESS (Prediction Residual Sum of Squares) value, corresponding to the sum of squared differences between predicted and observed X-elements. The model with the smallest PRESS value is regarded as the "best" model [159]. It is also possible to obtain this number by calculating the root mean square error of calibration and prediction sets, RMSEC and RMSEP respectively [160]. As shown in Figure II.19 (b), by plotting these two errors as a function of the PC number, the RMSEC will decrease along the chosen PC, and RMSEP will decrease to achieve an elbow point and will start to increase. The corresponding PC number at this point is chosen to create the model. If additional PCs are calculated, the model is considered in an overfitting mode where it describes error instead of real values.

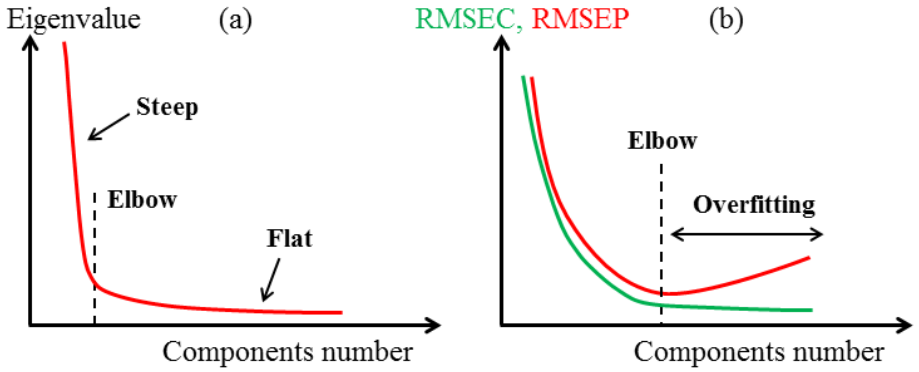

Figure II.19 : The variation of eigenvalue (a), RMSEC and RMEP (b) as a function of the number of the principal components. This evolution allows defining the ideal number of PCs for the model.

As for outliers, they are observations that are not conforming to the general distribution of the data due to a shift in the experimental measurements, or that the observation derives from a different type of products. In this case, the decision of leaving or extracting outliers goes to the analyst and his understanding to the dataset. Recognition of outliers is defined by a confidence level that is usually represented by an ellipse where all the observations outside this ellipse are considered as outliers.

III.6. DATA SCATTER PLOT

The scatter plots are used to displays the observations and the variables in the new space obtained from the principal components. Three basic plots are important for data understanding: the score scatter plot t_1/t_2, the loadings scatter plot p_1/p_2, the loadings scatter plot p_1/variables or p_2/variables. Here, t_1 and t_2, p_1 and p_2 are the scores and loadings of the two first PC respectively. Basically, the first and second components are sufficient to give a global understanding, but in some cases, additional components plots can reveal interesting information.

The score scatter plot gives a global visualization of how the observations are distributed one to the other. The loading plot p_1/p_2 shows the correlations between a component and a variable to estimate the information they share. It indicates which variables give similar information, which ones are negatively or positively correlated or not even correlated. Also it shows the variables that are not explained by the model (the one with value close to zero). The loading plots p/variables indicates which variables are responsible for the patterns found in the scores, and which one have the highest weight that provides the biggest variance in the model. Comparing the loadings plot to the scores plot enables to understand how the variables are related to the observations [161].

III.7. VALIDATION PARAMETERS

As mentioned before, PCA is an unsupervised model. The results obtained are used for the visualization. Hence, no validation parameter is needed. However, a great careful should be given to the choice on PC number when creating the model.

As for the multispectral prediction model, to judge a quantification model results (PLS), several parameters can be used. The correlation coefficient *r* measures the strength of the linear relation between the *X* and *Y* variables and it is used to estimate the degree of interdependence between the variables, free from the effects of measurement units.

$$r = \frac{\sum_{i=1}^{n}(x_i - \bar{x})\,(y_i - \bar{y})}{\sqrt{\sum_{i=1}^{n}(x_i - \bar{x})^2}\,\sqrt{\sum_{i=1}^{n}(y_i - \bar{y})^2}} \tag{29}$$

Where $\bar{x}$ and $\bar{y}$ are the mean values of *x* and *y* respectively, and *n* is the number of lines in each matrix. The values of *r* range from -1 to +1. A correlation coefficient close to +1 means that variables are highly positively interdependent, whereas a correlation coefficient close to -1 shows that the variables are negatively interdependent, the value of one variable decreases as the other increases. A correlation coefficient close to zero indicates that the variables are linearly independent.

Another important coefficient is the Root Mean Square Error (RMSE) defined as:

$$RMSE = \sqrt{\frac{1}{N}\sum_{\mathrm{i=1}}^{\mathrm{N}}(\mathrm{y_{ipred}} - \mathrm{y_i})^2} \tag{30}$$

Where y_i corresponds to the actual value of concentration of the sample *i*, y_{ipred} is the predicted value by the model and *N* is the number of the samples in the dataset. This error can be calculated for a training set (RMSEC) as well as for the test set (RMSEP). RMSEC and RMSEP values close to zero indicate a better prediction ability of the model. RMSE being a mean value it is important to estimate the error in prediction for every set of similar concentrations. This is achieved by calculating the relative error (RE) for different sets of samples.

$$RE = \frac{1}{N_n}\sum_{\mathrm{i=1}}^{\mathrm{N}}\frac{|\mathrm{y_{ipred}} - \mathrm{y_i}|}{\mathrm{y_i}} \times 100 \tag{31}$$

Where y_i defines the actual concentration value of a sample, y_{ipred} is the corresponding predicted value by the model and N_n is the number of samples in each set of concentration [157].

As for a classification model where, the *Y* matrix corresponds to values related to classes, the evaluation of the model can be performed by using, in addition to the RMSE, a confusion matrix or a table where each column of the matrix represents the number of observations in a predicted class while each row represents this number in an actual class [162] [163].

III.8. SYNTHESIS

Finally, to perform a chemometric analysis, several steps should be considered. First, the aim of the analysis should be defined. When dealing with an unknown set of data and the purpose is visualization of the samples distribution and understanding the relation between the elements, PCA model should be used. To begin, the scaling of the model should be fixed depending on the nature of the data under study. Hereafter, the importance is in the choice of the number of PCs when building the model. Then, the score and lodging plots lead to the understanding of the unknown samples and reveal groups or similarities among them. If the goal is to predict unknown samples, first, the type of prediction should be fixed. If it consists of quantitative prediction such as concentration estimation, PLS algorithm is applied. If a qualitative prediction such as class number is needed, then PLS-DA model should be performed. Hereafter, the same proceeding as in the case of PCA is established, by specifying the scale and the PCs number. Then, a calibration model should be created and used to predict the unknown samples. To validate the performance of prediction of a PLS model, *r*, RMSE and RE metrics are calculated and the judgment of the results depends on the application and the rate of precision needed. As for a PLS-DA model, a confusion matrix permits the attribution of the data inside or outside each of the created classes and defines the correct rate of prediction of elements in the right class.

IV. CHEMOMETRICS APPLIED TO TERAHERTZ SPECTROSCOPY FOR EXPLOSIVE DETECTION

The most interesting advantage of the THz pulsed spectroscopy is the capability for the spectroscopic recognition of materials by analyzing their spectra. This is possible when dealing with a sample made of pure elements. However, with mixtures of complex powders, advanced techniques like chemometrics are needed to extract the interesting spectral information about the sample. Many technology tools already exist for explosive identification. Most of them rely on multivariate and statistical analysis after physical measurements of the sample. Recently, several chemometric techniques were applied to the terahertz domain and demonstrated their efficiency for qualitative and quantitative analysis of terahertz data [164] [165]. These analytical methods were applied to terahertz spectroscopy measurements for analyzing pesticides [166], chemical mixtures [167] and identification of isomers [168]. In particular, partial least squares regression models were successfully applied to terahertz spectra for quantitative analysis [169] in several applications like estimating the degree of crystallinity in sucrose [170] and differentiating between different historically black inks [171]. In this section, we applied chemometric analysis to terahertz spectra, measured in transmission configuration, to investigate explosive materials made of pure elements or mixtures.

IV.1. SAMPLE PREPARATION PROTOCOL

In this study, we were interested in two specific explosives, namely cyclotrimethylene-trinitramine and pentaerythritoltetranitrate, hereafter called RDX and PETN, respectively. The mixture of these two creates another type of explosives, the Semtex, a very popular plastic explosive

within terrorist organizations because it was, until recently, extremely difficult to detect. The absorption peaks of these two explosives in PE matrix are "0.80, 1.45, 1.50, 1.98, 2.20, 2.95" for RDX and "1.82, 2.63, 4.12, 5.20, 5.52" for PETN [110] [111]. It should be mentioned that the peak position can varies by varying the matrix nature.

The analysis is conducted on different samples composed of either one single explosive or a mixture of both of them with varying weight-percent (wt-%). The polyethylene (PE) is used as a binder for all samples. Thirty six samples were carefully prepared from powders of pure explosives mixed with PE as a binder. We used the same explosive provider for all samples to avoid any fluctuations in the absorption level above 1.5 THz, due to different material crystallization quality [172]. Moreover, the grain size has a strong influence on the porosity of the PE-based samples and consequently on the scattering effect [173]. Therefore, the explosive powders were first ground using a mortar and pestle to reduce their particle sizes and avoid scattering losses. Next, powders of both explosives and high grade PE with particle sizes below 80 µm were mixed together and pressed using a manual hydraulic press (7 tons/cm^2 during 2 minutes). Finally, we prepared 36 pellets with a 400 mg total weight and a 13 mm diameter. Two replicates of each of the 36 samples were prepared for reproducibility assessment, and thus 72 pellets were analyzed. It should be mentioned that the quality of the samples was assessed from the THz-TDS spectra with the goal of reducing the scattering effects.

In the ternary diagram shown in Figure II.20, the squares represent the concentrations of the manufactured samples. Three poles labeled as PE, PETN and RDX represent the following concentrations: 400 mg (or 100 wt-%) PE (left), 100 mg PETN/300 mg PE (top) (or 25 wt-% PETN), and 100 mg RDX/300 mg PE (bottom) (or 25 wt-% RDX), respectively. Samples representing binary mixtures of PE and PETN (or RDX) are marked on the axis PETN (or RDX), respectively. Squares inside the diagram show the rest of the samples containing PE, PETN and RDX.

As an example, let us provide the characteristics of the sample encircled in Figure II.20. The blue arrows indicate the projections of the sample onto the three axes, which give the weights (in mg) of the three individual products. One can conclude that this sample contains 20 mg RDX, 20 mg PETN and 360 mg PE. Additionally, a 400 mg pellet of pure polyethylene was prepared as the reference for all spectroscopic measurements. The distribution of the samples between training and test set is made for the chemometric analysis applied further in this section.

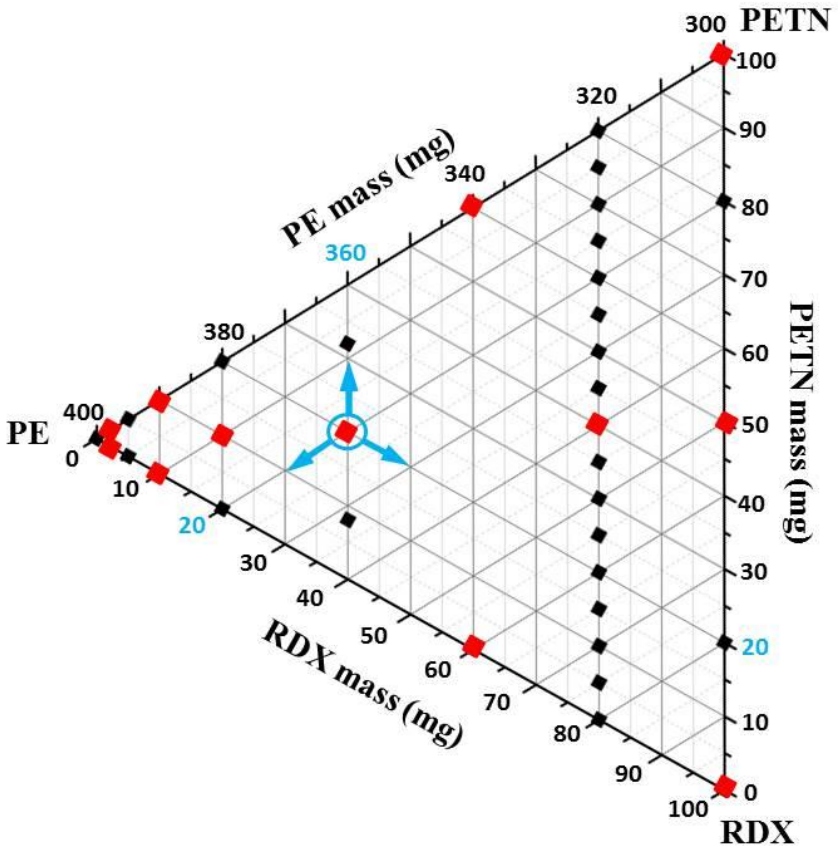

Figure II.20 : Ternary diagram displaying the compositions of the manufactured samples and the datasets selected for data processing: the training set (red) and the test set (black), blue arrows indicate the direction of projection on each axis.

IV.2. ABSORBANCE SPECTRA OF RDX AND PETN EXPLOSIVES

RDX and PETN absorbance spectra have been previously investigated between 0.5 and 6 THz [174], and the results revealed an important spectral overlap that concealed the PETN spectral signature in presence of RDX. In the present study, we focused our attention on the spectral window ranging between 0.2 and 3 THz, limited by our experimental setup. In this case, a dramatic spectral overlap can be observed in the 1.8-3 THz range. Consequently, it offers a unique opportunity to demonstrate the ability of chemometrics to predict the concentration values of each single product even from highly interfering spectra. Figure II.21 displays spectra of 400 mg pellets containing different amounts of RDX (a) or PETN (b), ranging from 10 to 100 mg and completed to 400 mg with PE. It also indicates that we cannot only select one absorption peak for detection purposes.

From the spectra displayed in Figure II.21 (a) and (b) one can easily verify that common univariate analysis could be efficiently applied to predict the weights of either RDX or PETN since they are not mixed together. Actually, the RDX amounts could be retrieved from univariate analysis

around 0.8 THz, while the PETN weights could be deduced from univariate analysis around 2 THz. In both cases, the linear regression describing the predicted weights as a function of the actual values is characterized by the coefficient of determination R^2 = 0.99. On the other hand, in the case of RDX/PETN mixtures, RDX concentrations could also be predicted from the univariate regression around 0.8 THz, however predicting the PETN concentrations appears to be impossible based on a univariate approach due to the dramatic overlap between the RDX and PETN spectra. The red arrows displayed in Figure II.21 highlight this spectral overlap around 2 THz. To discuss this point in more detail, Figure II.21 (c) shows three absorbance spectra corresponding to samples containing 100 mg RDX/300 mg PE (blue), 100 mg PETN/300 mg PE (red) and 50 mg RDX/50 mg PETN/300 mg PE (green). One can notice that, around 2 THz, the spectrum of the mixture (green) cannot be easily distinguished from the spectrum of the sample characterized by 100 mg PETN/300 mg PE (red). More precisely, in the case of a univariate model applied at 2 THz in order to predict the concentrations of PETN, the value of R^2 was too low to consider this approach as acceptable. To tackle this analytical problem, multivariate quantitative analysis has been achieved, based on partial least squares (PLS) regression.

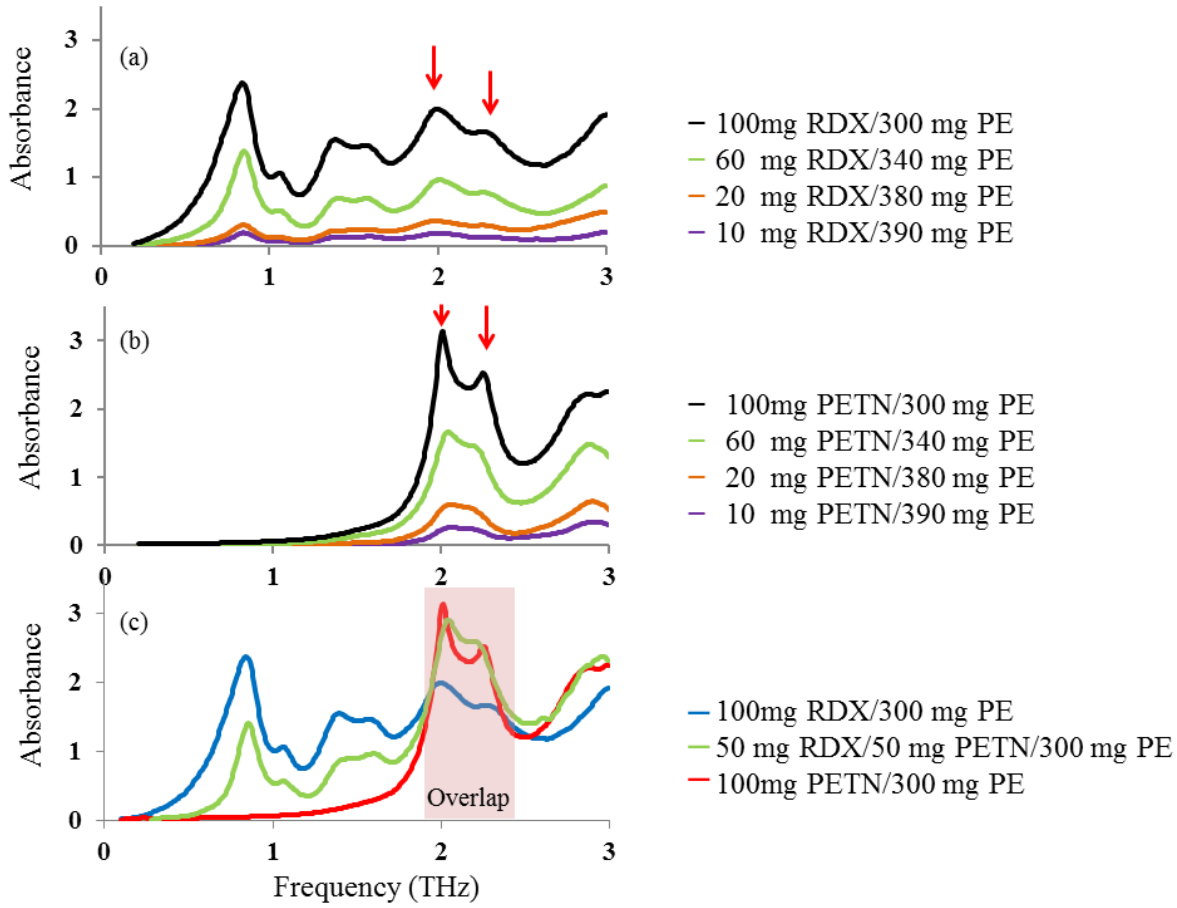

Figure II.21 : THz absorbance spectra of pure RDX (a) and pure PETN (b) inside 400 mg pellets containing different amounts of RDX, PETN and PE. The red arrows highlight the risk of interference between the spectra, (c) Absorbance spectra of 400 mg pellets containing 300 mg of PE and 100 mg of RDX (blue), 300 mg of PE and 100 mg of PETN (red, and 300 mg of PE, 50 mg of RDX and 50mg of PETN (green).

IV.3. PARTIAL LEAST SQUARE ANALYSIS FOR QUANTIFICATION OF EXPLOSIVES

PLS1 and PLS2 were performed on a series of terahertz absorbance spectra. PLS1 was built to retrieve the weights (in mg) of PETN in mixture samples while PLS2 was built to simultaneously predict the weights (in mg) of RDX and PETN. We decided to focus our attention on the analysis of PETN, because predicting the concentration values of RDX was not challenging, due to clearly isolate spectral features easily treated by univariate approach.

To generate the PLS models, the experimental data were split into two independent subsets: the training set containing data used to calibrate the model and the test set containing data, totally independent from the previous ones and used to test the prediction ability of the model. All the spectral data were centered as preprocessing of the PLS models and the analysis is applied to raw

data, no transformation as 1st or 2sd derivative was used, since, for the present set of data, the raw data gave sufficient performance in chemometric analysis.

In Figure II.20, the 12 samples belonging to the training set are displayed in the ternary diagram as red squares. Briefly, the training dataset was made of 4 samples containing RDX, but no PETN, another 4 samples containing PETN but no RDX and finally 4 last samples containing both RDX and PETN in equal mass proportion. The other 24 samples represented in black belong to the test set: 3 samples contained RDX but no PETN, the 3 other ones contained PETN but no RDX, 14 samples contained mixtures of RDX and PETN with the same amount of PE (320 mg) as a binder, and finally, two other samples contained mixtures of RDX and PETN completed with 360 mg of PE, and two last samples contained mixtures of RDX and PETN completed with 300 mg of PE.

The PLS1 algorithm was built to retrieve the concentrations of PETN. After a training step, the concentrations of the test set samples are predicted from this model. Figure II.22 displays the predicted scores in the plane of the two first principal components (PC1 and PC2), i.e. the two most descriptive latent variables. In this score-plot, the samples are displayed inside a kind of triangular area limited by two segments: one (top-black line) related to PETN samples (without RDX) and another (bottom- red line) related to RDX samples (without PETN). All the samples displayed between these two lines are the result of mixtures of RDX and PETN. While one can observe the small dispersion of each group of points, the plane defined by the first two components of the PLS1 model in Figure II.22 allowed retrieving quite well the ternary diagram given in Figure II.20. More precisely, the three poles of the triangle in Figure II.22 correspond to the three products composing the samples, namely RDX, PETN and PE. The samples related to binary mixtures were correctly displayed on the two lines limiting the triangle displayed in Figure II.22. As a first conclusion, one can state that this PLS1 model is quite efficient in analyzing the THz absorbance spectra data. Actually, the ternary diagram was correctly retrieved and the relative positions between the samples were in good agreement with the ones given in Figure II.20. This demonstrates that the THz absorbance spectra contain very informative features to describe the samples, mixtures of three products. In addition, for this PLS1 model, the first component (PC1-horizontal axis) allowed explaining more than 80% of the variance. Thus, the most concentrated samples (in either RDX or PETN) were displayed on the right part of the graph in Figure II.22 while the samples containing mainly the PE (the binder) were displayed on the left part of the graph. Moreover, the second principal component (PC2-vertical axis) allowed separating the samples containing either RDX or PETN. In this case, positive values of the PC2 scores were related to samples rich in the PETN while negative values corresponded to samples rich in RDX. This result was confirmed by the loadings plots displayed in Figure II.23 (a) and (c).

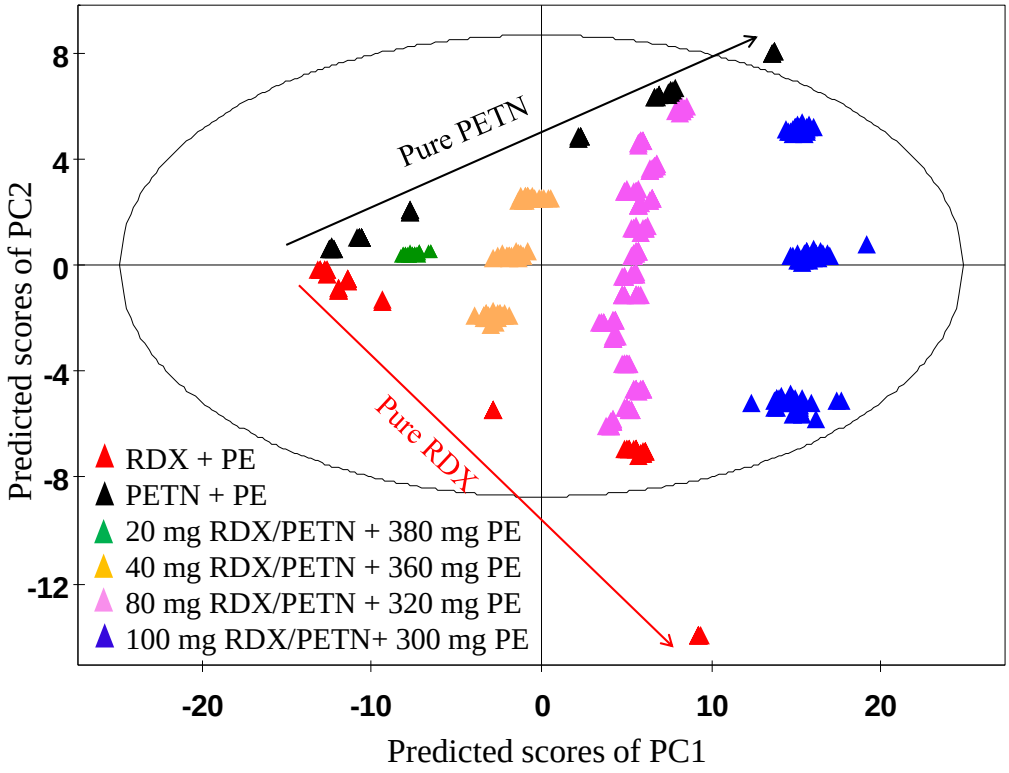

Figure II.22 : Predicted scores of the two first principal components PC1 and PC2 of the PLS model based on PLS1 algorithm dedicated to the prediction of PETN concentrations.

Actually, the loading plot illustrates the influence of each variable in the correlation between the X matrix (input) and the Y vector (output). Figure II.23 (a) and (c) shows the loadings of the first two principal components of the PLS1 model related to the analysis of PETN and linked to the scores presented in Figure II.22.

Figure II.23 (a) shows that all the samples under study, i.e. containing either RDX or PETN, share the same absorption band in the 1.8-3 THz range, at the origin of the main part of the variance of the dataset. In addition, Figure II.23 (c) illustrates the fact that the spectral features at 0.8 and 2 THz vary in opposite directions and explains why the samples rich in RDX are displayed in the lower part of Figure II.22 (negative values) and the samples rich in PETN are displayed in the upper part of Figure II.22 (positive values). This result was not surprising since, in this study, the total weight of pellets being constant and equal to 400 mg, higher concentration of RDX corresponds to lower concentration of PETN and vice versa.

Subsequently, a PLS2 algorithm allowing simultaneous prediction of the concentrations of RDX and PETN was applied to the same calibration set as the one described earlier in this paper, and the loadings of the two first components are displayed in Figure II.23 (b) and (d). It is interesting to note the difference between (a), (c) and (b), (d), highlighting the fact that the principal components are significantly different between the two models, i.e. PLS1 and PLS2. Figure II.23 (b) reveals that the loadings-plot of the first component is very similar to the absorbance spectrum of the mixture

RDX/PETN shown in Figure II.21 (c) (green curve). This indicates that for the PLS2 model, both the spectral features related to RDX (around 0.8 THz) and PETN (around 2 THz) contribute to the separation of samples (score-plot not shown here) since the PLS2 model was built to simultaneously predict RDX and PETN. Moreover, Figure II.23 (d), which is quite similar to (c), shows the two frequencies responsible for RDX and PETN separation over the PC2 axis of the PLS2 scores plot (not shown here because it is quite similar to the score plot of PLS1 shown in Figure II.22). Also, the reverse amplitude of the loadings around 0.8 THz (negative value) and 2 THz (positive value) explains the variation of RDX and PETN in opposite directions on the PC2 axis of this scores plot.

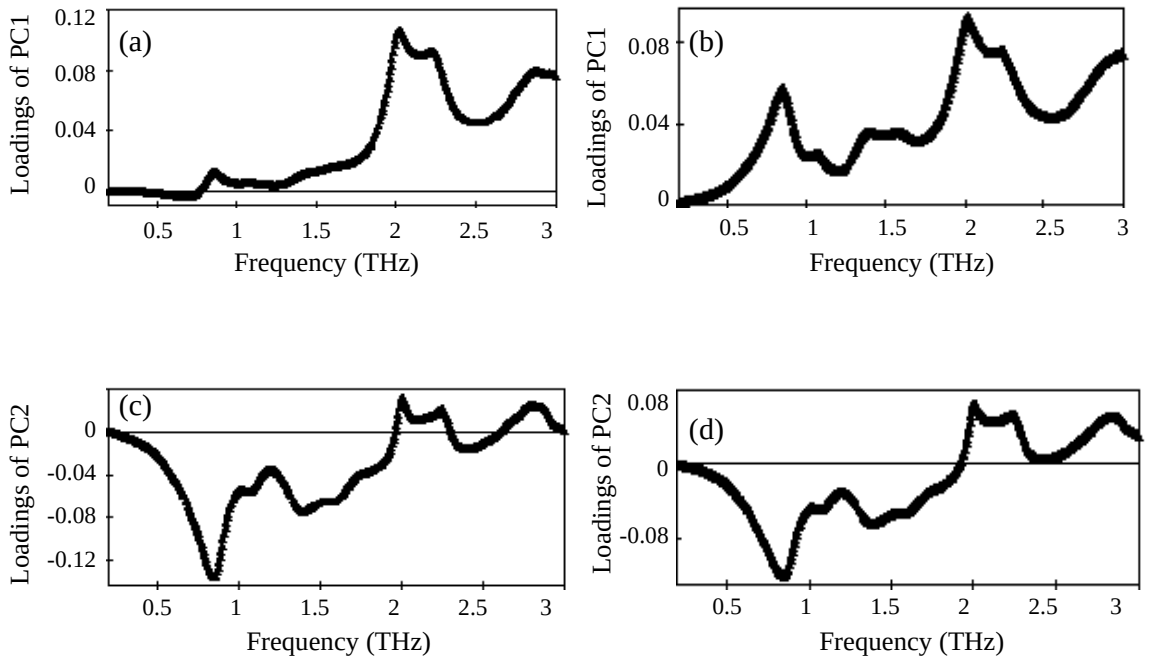

Figure II.23 : Loadings of (a) PC1 and (c) PC2 for the PLS-1 model optimized to predict the concentrations of PETN, loadings of (b) PC1 and (d) PC2 for the PLS2 model optimized to simultaneously predict the concentrations of PETN and RDX.

The RMSEP values of PLS1 and PLS2 are respectively 4.4 and 3.4 mg, indicating better performance of the PLS2 model. These values should be compared to the total weight of the pellets, which is 400 mg, and also to the amount of explosive inside the pellets.

However, RMSE is a mean value calculated for all samples with different amounts of RDX and PETN, varying from 2 mg to 100 mg in the entire pellet weight (400 mg), it is important to highlight the error in the prediction for the low and high concentrations. For that, the relative error RE was calculated for different sets of samples. Based on the PLS2 model described above, the percentage error of the concentration value of PETN varies from 2% for the samples containing the highest concentrations of explosives (i.e. 100 mg of explosive and 300 mg of PE) to 38% for the samples

containing the lowest concentrations of explosives (i.e. 2 mg of explosives and more than 398 mg of PE). So clearly, a higher prediction error is committed for low concentrations.

From the other hand, the spectral overlap between the RDX and PETN spectra mainly exists in the spectral window ranging between 1.8 and 3 THz, we decided to study the predictive ability of a new PLS model from this reduced spectral band. Our objective was to investigate the influence of the input variables onto the models and more precisely to assess how selecting a reduced spectral window presenting dramatic overlap between the absorbance spectra could affect the predictive ability of the model. Thus, a new PLS2 model was built from input data limited to the spectral window 1.8-3 THz and the X matrix of input data was made of 622 spectra and 192 variables. The same training and test sets as described earlier were considered. The prediction result gives a RMSEP of 4.8 mg. By comparing this result to the PLS2 model using the entire spectral band, one can conclude that reducing the spectral window increased the RMSE values, which was not surprising, since the absorption band of RDX at 0.8 THz has been removed from the input data. However, it is interesting to notice that the prediction ability was quite similar in both cases with only a slight enhancement of the RMSE values when reducing the spectral bandwidth. This result clearly emphasizes the very good predictive ability of the PLS models even when the input data correspond to highly interfered spectral features, as demonstrated here in the case of mixtures of RDX and PETN analyzed on a reduced spectral window.

Finally, these results published in 2015 [175], indicated that for samples made of binary mixtures, PLS2 gave better performance for quantification of individual element. However, this result may not be the same when dealing with ternary mixtures. In this study, we limit the analysis on binary mixtures, but it will be important to investigate the performance of the PLS model with more complex mixtures. In the other hand, we demonstrate that a PLS analysis can be performed on a restricted frequency band and is still able to retrieve the amounts of elements in mixtures. This shows that when using this analysis technique, it is not necessary to extend the frequency band of measurements.

V. CHEMOMETRICS APPLIED TO TERAHERTZ SPECTRAL-IMAGING

Recently, terahertz imaging of chemical products has been taking a lot of interest and several methods was investigated in order to identify the chemical content of an image [107]. Watanabe *et al.* used principal component analysis to do chemical mapping of the spatial distribution of different products on an image. The analytical calculation was performed on terahertz reflection measurements of aspirin, palatinose and riboflavin samples [176]. Moreover, Zhang *et al.* present a method based on component analysis to quantify benzoic acid and its monomethyl-substituted derivatives measured with a TDS system in transmission configuration [177]. Newly, another analytical model, known as k-means clustering, is used for terahertz image segmentation and tested on powders to retrieve the features that are responsible of their discrimination [178].

V.1. PRE-PROCESSING

Images of explosives samples are recorded in transmission configuration with the TPS3000 imager. A scan step of 0.5 mm is set for the XY translation stage. Each pixel is a resulting of the

transmitted THz signal at a specific point on the image and the resulting data is a (X,Y,t) 3D matrix. Then, the same signal processing used on individual transmitted THz pulse discussed before, is applied to each pixel of the image. So first a FFT is performed on all the pixels given (X,Y,f) 3D matrix with a frequency ranging between 0.1 and 3 THz and spectral resolution of 6 GHz, thus 469 frequency values are obtained. Then the absorbance is calculated for every pixel in the image and the resulting matrix is (X,Y,A) formed by the (X,Y) image and the value of the absorbance at each pixel for the frequencies between 0.1 and 3 THz as shown in Figure II.24 (a) and (b).

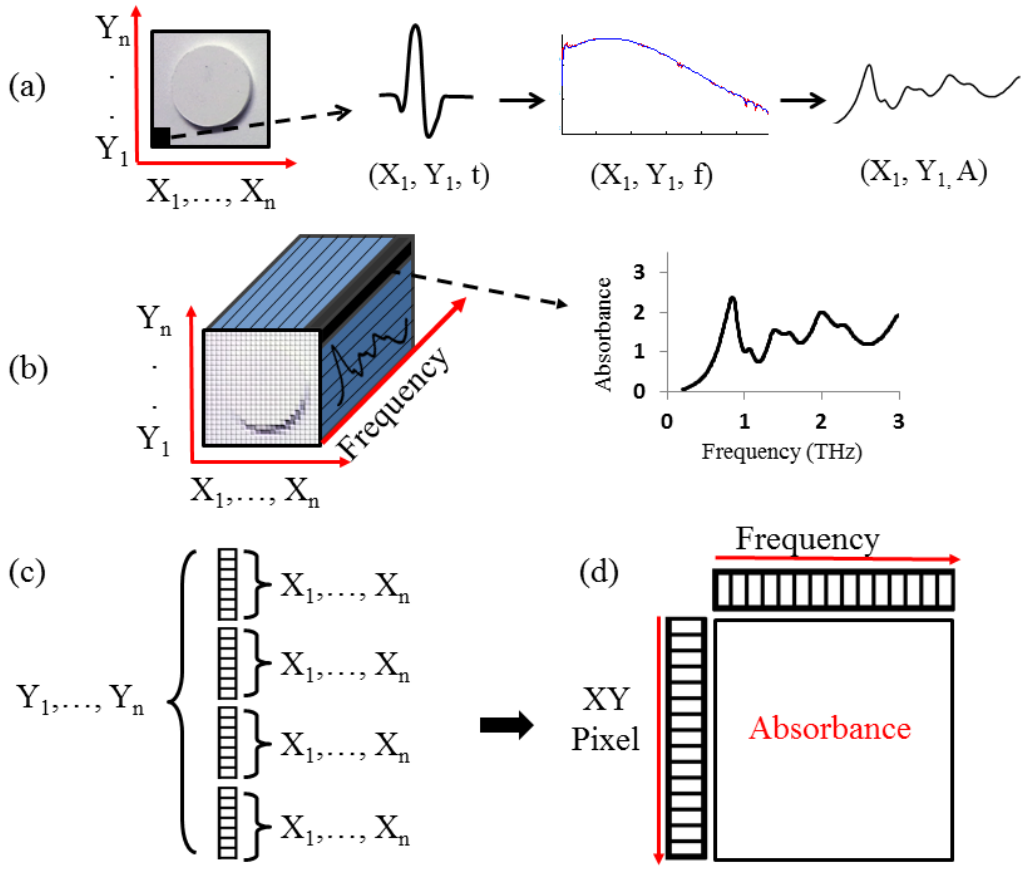

Figure II.24 : (a) Transformation diagram of temporal pulse to absorbance for one pixel, (b) 3D resulting image of the TDS spectral imaging where each pixel corresponds to an absorbance spectra, (c) unwrapping process transforming 2D matrix to 1D table, (d) resulting 2D matrix after unwrapping.

The measurement area in the imaging setup is limited to 16×16 mm^2, which can fits for imaging only one pellet. Hence, the final image should contain several samples to compare them. For this aim, a single resulting image was built from the juxtaposition of several images related to the (X,Y) measurement of one sample. This resulting image is a 3D matrix that should be unwrapped into a 2D matrix in order to apply multivariate analysis on it. The transforming process shown in Figure II.24 (c) and (d) consists of extracting the (X,Y) image at one frequency and unfolded into one vector.

The resulting 2D matrix is formed by X×Y line and *F* column, where each column is an entire (X,Y) image at one frequency.

This matrix is used to perform the chemomteric models. Then, the score values of the PCs resulting from the model, that are vector of X×Y length, are refolded and rearranged in a 2D matrix of *X* line and *Y* column, corresponding to the image resulting from the multivariate analysis.

V.2. IMAGE DESCRIPTORS

In the image processing domain, applying any processing to an image may cause loss of information or quality, so a variety of ways is used to describe the image. Image quality evaluation methods can be subjective, based on a human judgment or objective, where numerical criteria are calculated. Common criteria are used to evaluate information about the image, like color, texture, shape, etc. In our work, retrieving meaningful information while keeping good image quality is the main interest. For that, several descriptors are used to compare the resulting images from a multivariate analysis.

One of the parameters is the contrast of the image. Various measurements of the contrast have been employed like simple contrast, Weber contrast, Michelson contrast, and root-mean-squared contrast (RMS contrast) [179]. The latest is able to predict the thresholds of the human contrast detection quite well and better than other common measurements of contrast [180].

Considering an image of *M* lines and *N* columns, where each pixel has intensity *I*, the root mean squared contrast is defined by:

$$RMS = \sqrt{\frac{1}{MN}\sum_{i=0}^{N-1}\sum_{j=0}^{M-1}\left(I_{ij} - \bar{I}\right)^2} \tag{32}$$

where $\bar{I}$ is the mean value of all the intensity values in the image.

Another interesting descriptor is the equivalent (or effective) number of looks (ENL), which is a parameter used for multi-look radar images to describe the degree of averaging applied to the synthetic aperture radar (SAR) measurements during data formation and post-processing [181]. ENL has influence on the accuracy of the information extracted by methods based upon statistical modelling of multi-look SAR data. It is defined as:

$$ENL = \frac{\bar{I}^2}{variance} \tag{33}$$

In the present study, ENL is used to compare the score images obtained from different PCs to the images obtained directly from the terahertz measurements.

V.3. CHEMOMETRIC ANALYSIS APPLIED TO TERAHERTZ IMAGES

V.3.1. Principal component applied to pellet of compact powder

To test the potential of the chemometric tools in the analysis of terahertz spectral image, harmless powder as lactose and fructose are used in a compact configuration. Thus, a white pellet of 13 mm diameter is formed by two parts with different components in each. The measurements are performed for an image size of 16×16 mm^2 and a resolution of 0.2 mm. The first part is made of 40 wt-% lactose and 60 wt-% of PE, the second part is formed by 40 wt-% of fructose and 60 wt-% of PE. The spectra of lactose and fructose present characteristic peaks at specific frequencies: 0.53, 1.37 and 1.81 THz for the lactose and 1.3, 1.71 and 2.13 THz for the fructose. By selecting a specific position in the temporal pulse or by selecting the peaks of each of the products, it is possible to reveal in the image the presence of two different products in the pellet. However, to eliminate this complexity and the errors that can be committed when pursuing these specific positions, a multivariate analysis of the data is applied. Thus, a PCA model is performed for this sample using the amplitude of the FFT, so no need to have a reference. The model is carried out using a matrix of 6240 lines and 272 columns. The lines in this matrix correspond to the number of observations which is the number of pixels X×Y=78×80 in the image, where *X* is the number of column and *Y* is the number of lines. The columns of the PCA matrix represent the frequencies going from 0.2 to 2.9 THz. The model is created with 6 PCs where the first two PCs explain more than 87% of the variance.

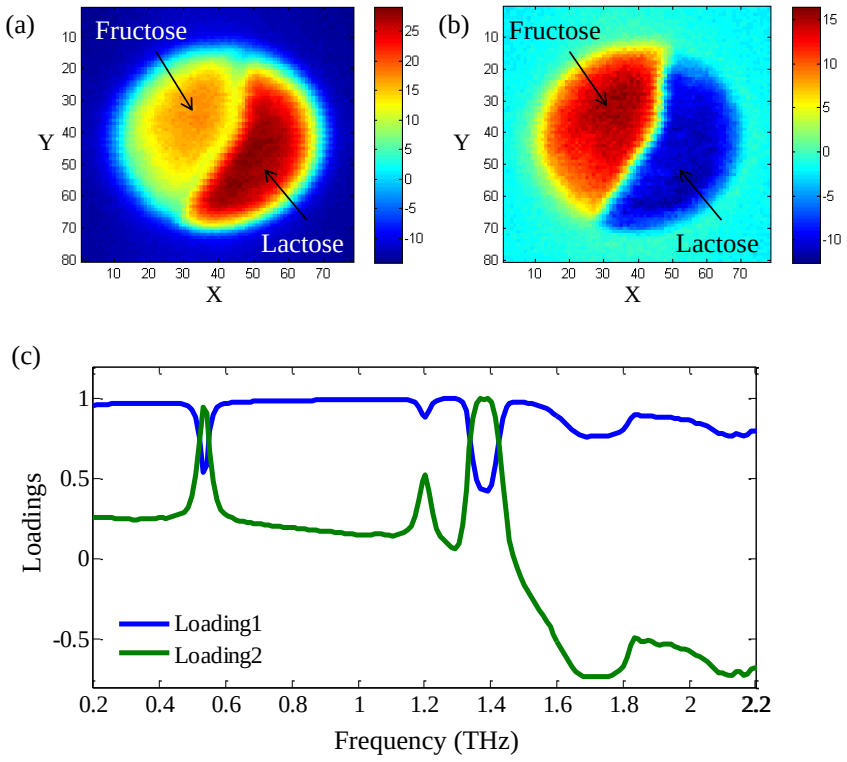

Figure II.25 : Score image of the (a) PC1 and (b) PC2 of a pellet made from two parts constituted of fructose and lactose each with 40 wt-% of element and 60 wt-% of PE, (c) loading plots of the first two PCs of the PCA model: loading PC1 (blue) and loading PC2 (green).

In this model, the scores of the first two PCs are chosen to create the PCA score images shown in Figure II.25 (a) and (b). The score images reveal automatically the presence of both products, but without recognition of the material. The score of PC1, Figure II.25 (a), highlights the presence of the lactose, thus the intensity of the lactose is higher in the image. As for the PC2 score image in Figure II.25 (b), it reveals more the presence of fructose in the image. This is also explained by the loading of PC1 and PC2 shown in blue and green respectively in Figure II.25 (c). The loading of PC1 presents the spectral features of the lactose and the loadings of PC2 shows the contribution of the fructose with a small effect from the lactose.

The score images are compared to the THz electric field images by using the RMS contrast and ENL as metrics. The results presented in Table II.3, are calculated for the PC1 and PC2 scores and for some raw images at the characteristic frequencies of lactose and fructose: 0.52, 1.37, 1.71 and 1.81 THz. These calculations are applied to normalized images in such a way to be able to compare them.

Table II.3: RMS contrast calculation of the scores of PC1 and PC2 images, and for the images at specific frequencies: 0.52, 1.37, 1.71 and 1.81 THz representing the characteristic frequencies of the lactose and fructose.

	Score PC1	Score PC2	0.52 THz	1.37 THz	1.71 THz	1.81 THz
RMS	0.003	0.0006	0.0018	0.0015	0.0014	0.0017
ENL	0.335	0.815	0.079	0.06	0.054	0.074

The PC1 score image has the highest RMS and ENL values, indicating that this image gives a better contrast than the raw image selected at the product fingerprints. As for the PC2 score image, the calculated values of both metrics are lower than those of the PC1. This was expected since the PCA model is calculated in a way that the highest variance of the data is expressed by the first score, thus the resultant image of PC1 score shows a higher contrast between the elements of the image.

This comparison of RMS and ENL highlights the advantage of the score image, especially the first PC that contains most of the model variance, in revealing contrast between the elements of the image. Thus, the PC1 score image gives an automatic discrimination and a good image quality compared to the THz raw images.

V.3.2. Principal component applied to non-compact powder in transmission

In real cases, harmful powders are not transported in pellets, then, it is important to study the substances in a powder state. Usually, powders are very absorbent for terahertz waves, and with a high material density, the transmitted signal is dramatically reduced and reflection configuration may be more efficient in analysis these powders. To test the feasibility of powders detection in images, a sample is made using harmless chemicals, namely lactose, fructose and citric acid in a powder state. The sample consists of a cube of polyethylene where three holes of 1 mm diameter are filled with the three powders. Figure II.26 presents the sample configuration (a), an image of the terahertz signal extracted at 0.8 THz (b), and the waveform of the electric field for a specific point on the image where the lactose powder is present (c). To find the resulting image presented in (b), first, all the pixels must be swept to find the one presenting a chemical features and revealing some difference in the constituent of the image. Then, by sweeping all the frequencies in the chosen spectra, the image that reveals the highest contrast between the products can be extracted. However, this procedure is long and depends highly on the human eye capacity in finding specific features and retrieving the right information. To remove this complexity, chemometric tools are the ideal solution. An important point to mention for this sample is that there is a difficulty in detecting the fructose and citric acid due to the nature of the grains that are very diffracting, thus most of the signal is lost.

Having no information about the sample, an unsupervised model should be applied to visualize the data. So a PCA model is carried out using a matrix of 3400 lines and 676 columns. The lines in this matrix correspond to the number of observations which is the number of pixels X×Y=68×50 in the image, where *X* is the number of column and *Y* is the number of lines. The columns of the PCA matrix represent the frequencies going from 0.3 to 1.6 THz. The model is created with 6 PCs where the PC1 explains more than 89% of the model variance. Figure II.26 (d) and (e) present the image extracted from the values of PC1 scores and the loading of PC1 respectively. This result is achieved in

an automatic, unsupervised way without looking for specific positions or chemical features. It reveals, in the image, the same discrimination obtained from the best image of the THz raw images. Considering the loading, it reveals the fingerprint at 0.8 THz, which is the frequency that gives the differentiation between the products. In addition, the loading shows another feature at 0.4 THz that is not present in the spectra in Figure II.26 (c). The raw image at 0.4 THz (not shown here) presents discrimination between the powders. This indicates the capacity of the loadings in extracting additional frequencies where the products are discriminated.

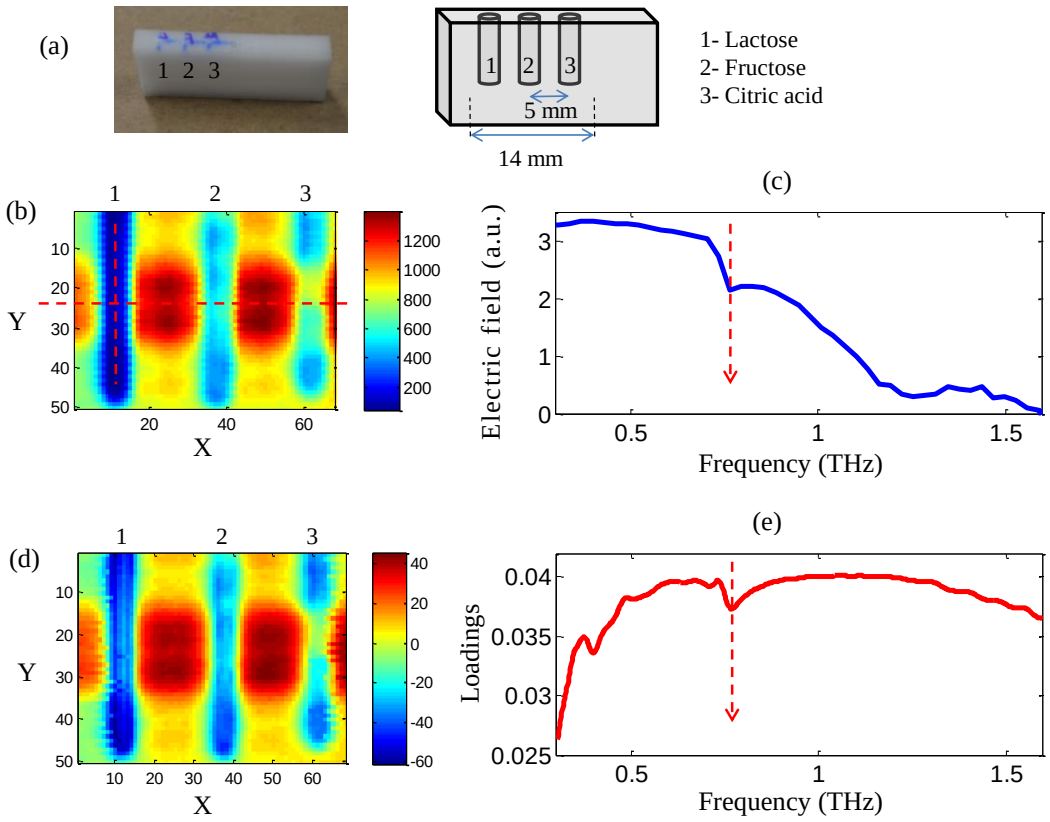

Figure II.26 : (a) Photo and representation of the sample made by a piece of polyethylene with three holes of 1mm diameter containing three powders: lactose, fructose, citric acid, (b) image obtained at the frequency 0.8 THz, (c) waveform of the THz electric field at a specific position highlighted by dashed lines in image (b), (d) image of the PC1 score of the PCA model, (d) loadings of PC1.

From the other hand, to compare the image at 0.8 THz and the PC1 score image, their RMS contrast and ENL are calculated and the results are listed in Table II.4. Both images are normalized so that it is possible to compare them. The values of RMS and ENL are higher for the PC1 image, showing that the latest has a higher contrast than the image at the frequency 0.8 THz. These results demonstrate the potential of PCA in providing automatic discrimination of product in a powder state in image with a better contrast.

Table II.4: RMS contrast calculation in the case of the sample made of pure powder, for the image extracted at 0.8 THz from the terahertz signal, and the score image of PC1 and PC2 for normalized data.

	Score PC1	Frequency 0.8 THz
RMS	0.0014	0.0012
ENL	1.429	1.262

V.3.3. Principal component applied to non-compact powder in reflection

Another test on powders in a non-compact state is made in reflection mode. The analysis of the signal in reflection is more complex, but this configuration is more suitable for real-life situations such as postal chain inspection. Figure II.27 (a) represents the sample made of five powders inside a plastic box. The studied powders are formed by three elements in pure sate namely lactose (1), fructose (2), citric acid (3) and two mixtures of lactose with fructose (4) and lactose with citric acid (5). The spectra of the pure samples shown in Figure II.27 (b), obtained from measurements in reflection, present no significant fingerprints that can be recognized by the eye. In order to test the performance of chemometric tools in differentiating the powders even when their spectra presents no significant peaks, a PCA model is build using the reflection spectra of 45 observations corresponding to the number of pixels in the center of each one of the five components of the image, between 0.1 and 2.7 THz. The first two principal components explain more than 78 % of the variance in the model. Thus, the score plot of these two PCs, presented in Figure II.27 (c), reveals the highest variance among the data. Despite the impossibility to recognize the powders from their spectra presented in Figure II.27 (b), the score plot was able to qualitatively separate them in groups. Along the PC1 score, the data are divided into two groups: with and without lactose. Those with lactose, pure or mixture, presented in red, orange and grey, are localized in the left side of the PC1 score axis. As for the powder without lactose, they present anti-correlation with the first set, and are projected on the right side of the PC1 score axis, presented in blue and green.

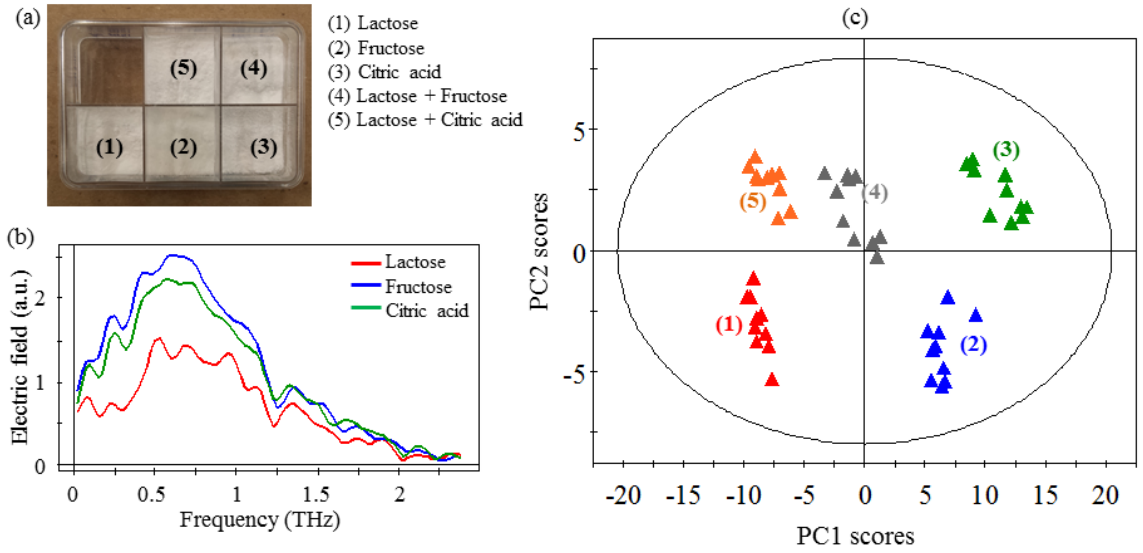

Figure II.27 : (a) Photograph of the sample composed of a plastic box filled with five powders: three pure namely lactose (1), fructose (2), citric acid (3) and two mixtures of lactose with fructose (4) and lactose with citric acid (5), (b) spectra of lactose (red), fructose (blue) and citric acid (green) extracted from reflection measurements, (c) the PC1 and PC2 scores plot of the powders from the PCA model.

This analysis demonstrates that PCA model is capable to retrieve qualitative discriminating information about the data, even when the spectra of the powders present no significant discriminating fingerprints.

V.4. CHEMOMETRICS APPLIED TO TERAHERTZ EXPLOSIVE IMAGES

All the essays presented before, are made using harmless white powder such as fructose, lactose and citric acid, due to the difficulty of the access and the manipulation of real explosive. Hence, the collaboration with the Institute of Optoelectronics in the Military University of Technology in Warsaw, allowed us to obtain real explosives data. Having the same TDS imaging system and working in similar experimental conditions, made possible the analyzing of the data.

Three samples-pellets are made and imaged:

1. Pellet of pure RDX constituted of 20 wt-% RDX and 80 wt-% PE,
2. Pellet of pure PETN constituted of 20 wt-% PETN and 80 wt-% PE,
3. Pellet of the mixture of RDX and PETN constituted of 10 wt-% RDX, 10 wt-% PETN and 80 wt-% PE.

They have a total weight of 400 mg, a 13 mm diameter, with a thickness varying between 3.6 and 3.7 mm from a sample to another. In addition, a pellet with the same dimension made by 100 wt-% PE is imaged and used as a reference to calculate the absorbance.

Terahertz time-domain spectral-imaging measurements were realized in transmission mode via the THz-TDS spectral-imager with a step of 0.5 mm on the XY translation stage. Being limited in the scanning area, each pellet of 22*22 pixels is imaged separately. A single synthetized image was built from the juxtaposition of the three images related to the three samples. This final image is composed of 22*66 pixels. The recorded data corresponds to the temporal pulse at each pixel on the image. Then an FFT is applied to the signal to calculate the transfer function, using the FFT of the PE pellet. This allows calculating the absorbance values of the components of the final image between 0 and 3 THz with a frequency resolution of 6 GHz.

This acquisition produces a 3D matrix of (X,Y) pixels and one absorbance information at each pixel. It is unwrapped as shown in Figure II.24 to obtain a 2D matrix of 1452 lines corresponding to each X×Y pixel and *F* column representing the 486 frequency values. This matrix is used to perform the chemometric models.

V.4.1. Description by principal component analysis

First, a PCA model is performed to visualize our data. This step is necessary when facing an unknown object. It enables the recognition of the sample, and can highlight similarities between the constituents of the image. The PCA model is created with 1452 observations (the pixels) and 469 variables (the frequencies), where the frequencies between 0 and 0.1 THz are retrieved from the raw matrix because they add only noise. Two scales are tested on the samples: the center scale and unit variance (UV) scale. The PC1 and PC2 in the UV model explain respectively more than 43% and 18% of the variance in the model. As for the center scaled model, the PC1 and PC2 variances are more than 49% and 24% respectively. For each case, the score plot in the plane of the first two components is displayed in Figure II.28 (a) and (b) for the UV and center scale respectively. In this plot, the observations, corresponding to the pixels in the image, are organized into three main groups of points corresponding to the three types of explosives, namely RDX (red), PETN (blue) and mixture of both (green). Moreover, the points displayed in black correspond to the background values and this is why they are widely spread on this plot. The background values are related to pixels of the image located outside the pellets, which consequently don't bring significant spectral information. Both plots show the same accuracy and are able to reveal the presence of three different groups of substances. However, to correctly understand the model, the loadings of the first two PCs are plotted for both scales, for the frequency band [0.1-3] THz. Figure II.28 (c) and (d) display the loadings of the PC1 (black) and PC2 (red) of the UV and the center scale models respectively. The loadings of the centered model have more similarities with the absorbance spectra of the samples presented in Figure II.21. Loading 1 shows that the fingerprints of RDX and PETN around 0.8 and 2 THz respectively, are anti-correlated. This is well explained in Figure II.28 (b) where the PETN scores have negative values and RDX have positive ones. As for the loading 2 in the centered model, it reveals more the presence of RDX. By comparing the two scales, the centered model describes our data. It should be noted that the absorbance spectra obtained by imaging present more noise than the spectra obtained in Figure II.21 and it affects the loading results of the PCA that present noise after 1.5 THz. This is due to the fact that the apodization function was not applied to the images and the averaging was reduced to over 500 repetitions per spectra to minimize the measurement time.

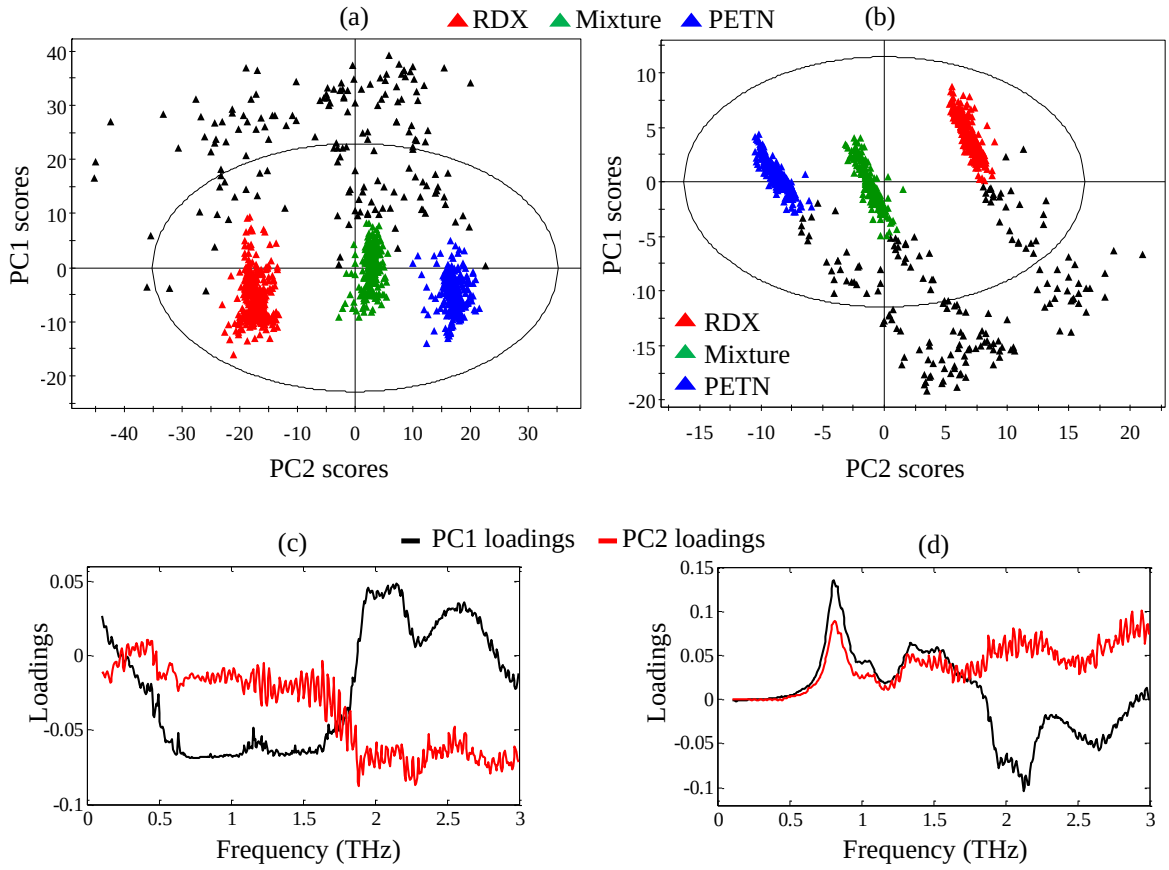

Figure II.28 : (a) Score plot of the PCA model in the plane of the two first components for a data set of 1452 spectra containing 469 variables each with a unit variance (a) and center (b) scales. The plot represents three classes: RDX (red), mixture (green) and PETN (blue), loadings of PC1 (black) and PC2 (red) for the PCA model for the unit variance (c) and center (d) scales.

The pertinence of the centered model is noticed with the absorbance score images of the PC1 and PC2 of both scales. Figure II.29 displays the PC1 score images for the UV (b) and centered (c) models as well as the PC2 score images for the UV (d) and centered (e) models.

The loadings of the UV model presented in Figure II.28 (c) show that the frequency bands [0.1-1.8] and [1.8-3] THz vary in opposite directions; however, it does not explain the characteristic peaks of the components. For the centered scale, the PCs loadings explain the discrimination of the three products in the image. As mentioned before, PC1 loading shows an anti-correlation between the fingerprints of RDX and PETN thus the presence of the three products is clearly revealed. As for the PC2 loading, it has a small shift of the RDX fingerprints compared to the others, this is why it is more revealed in Figure II.29 (e).

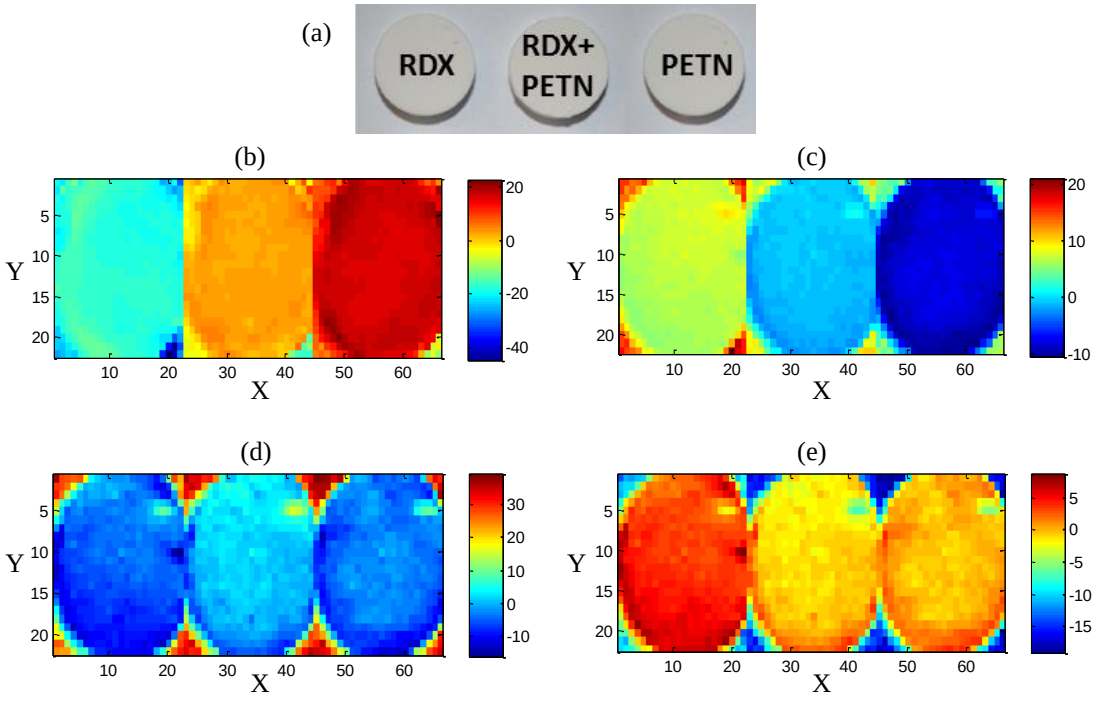

Figure II.29 : (a) Optical image of the sample consisting of three different pellets: RDX (20% wt-%), PETN (20% wt-%) mixture (10% wt-% RDX and 10% wt-% PETN) ; PC1 score images for the UV (b) and centered (c) models, PC2 score images for the UV (d) and centered (e) models.

PCA is unsupervised, it is not possible to perform a blind prediction and attribute the pixel to a specific explosive without additional learning step. It can be considered as a preliminary step to recognize the content of our sample and define the similarities or the differences that will determine specific regions of interest (ROI). In the case of the sample presented in Figure II.29, three ROI can be delimited consisting of the central parts of each of the three pellets.

V.4.2. Classification by partial least square-discriminant analysis

Six different PLS-DA models are created to compare their performance in classification. Three parameters are varying between these models: (i) the number of classes chosen to calibrate the model, (ii) the number of elements (observations) in each calibration class and (ii) the scale used: UV or centered. The model details are presented in Table II.5 where 469 variables (frequencies), in the frequency band [0.1-2.9] THz, are used. It should be noted that M1, M2, M3 have the same (i) and (ii) parameters as M5, M6, M7 respectively. The difference is that, for the first set of the models, the scale is UV and for the second set, it's a centered scale.

Table II.5: PLS-DA model parameters.

Model	Observation	C1 (RDX)	C2 (Mixture)	C3 (PETN)	Scale
M1	270	90	90	90	UV
M2	90	30	30	30	UV
M3	60	30	-	30	UV
M4	270	90	90	90	Centered
M5	90	30	30	30	Centered
M6	60	30	-	30	Centered

The classes are designed as follows:

- Class1 (C1) corresponds to the pixels of RDX image,
- Class2 (C2) corresponds to the pixels of the mixture image,
- And class3 (C3) corresponds to the pixels of PETN image.

Four models consist of three classes where the mixture contributes to the calibration. While M3 and M6 are formed by two classes, no information is given to the model about the mixture. The effect of the number of elements in the classes can be investigated by analyzing the performance of M1 and M2 or M4 and M5, where the number is reduced and passes from 90 to 30 observations per class. Finally, the impact of choosing two classes instead of three is studied with the models M3 and M6.

These model are used to predict the entire 1452 pixels of the image, which englobe the pixels used in the calibration and the other pixels of the image unknown to the model (number of unknown pixels = 1452 – pixels chosen for calibration). The prediction error RMSEC of the calibration set and RMSEP of the prediction set are listed in Table II.6.

Table II.6: RMSEC and RMSEP values obtained for the different PLS-DA models built with

Model	RMSEC	RMSEP	Model	RMSEC	RMSEP
M1	0.052	0.623	M4	0.030	0.430
M2	0.049	1.001	M5	0.029	0.497
M3	0.036	0.420	M6	0.009	0.283

The values of RMEC and RMSEP for each two similar models M1and M4 or M2 and M5 or M3 and M6 are smaller when the model is centered scale. This demonstrates that the performance of the centered scale is better for the samples and it confirms the results obtained by PCA model, where the centered scale gave a better description.

For that, the three centered scale models are compared with each other. The results of classification of the pixels are shown in Table II.7 for M4, in Table II.8 for M5 and in Table II.9 for M6.

Table II.7: Confusion matrix related to the classification of the observations in C1, C2 and C3 for the model M4.

		Predicted class				
		C1	C2	C3	Members	Correct
Actual class	C1	444	40	0	484	91.7%
	C2	0	444	40	484	91.7%
	C3	0	51	433	484	89.4%
	Total	444	535	473	1452	90.9%

Table II.8: Confusion matrix related to the classification of the observations in C1, C2 and C3 for the model M5.

		Predicted class				
		C1	C2	C3	Members	Correct
Actual class	C1	442	42	0	484	91.3%
	C2	0	415	69	484	85.7%
	C3	0	49	435	484	89.8%
	Total	442	506	504	1452	88.9%

Table II.9: Confusion matrix related to the classification of the observations in C1 and C3 for the model M6.

		Predicted class			
		C1	C3	Members	Correct
Actual class	C1	484	0	484	100%
	C3	43	441	484	91.1%
	No class	13	471	484	-
	Total	540	912	1452	95.5%

The calculation of the correct estimation in one class, and the correct rate of prediction for the entire model, can be calculated as follows:

$$Correct(class) = \frac{number\ of\ correct\ predictions\ in\ the\ class}{total\ number\ of\ members\ in\ the\ class} \times 100$$

$$Correct\ (model) = \frac{\sum correct(class)}{number\ of\ classes} \quad (34)$$

Note that the members in each class englobe the pellet and the background. After Table II.6, the values of RMEC and RMSEP are lower for M6. Also, the classification results present a higher correct rate in the case of M6 with 95.5% of correct classification of pixel in the right class. This demonstrates that the best accuracy is produced with the model M6 where two classes are created for calibration.

To better understand and visualize the reparation of the pixels in the classes, the predicted values are created in an image. Each class gives a repartition for the entire sample. The predicted values vary between 0 and 1. Four prediction ranges are present:

- If the predicted value is equal to 1: the pixel belongs to the class;
- If the predicted value equal to zero: the pixel does not belong to the class;
- If the predicted value is smaller to zero or higher to 1: the prediction cannot be trusted and the pixel is not correctly classified;
- If the value varies between 0 and 1, it explains the probability of being in the class, as an example a value of 0.5 means that the pixel is 50% belonging to the class.

Figure II.30 display the images of the predicted values for the two classes of M6, where Figure II.30 (a) and (b) correspond respectively to the prediction of the class 1 and the class 2.

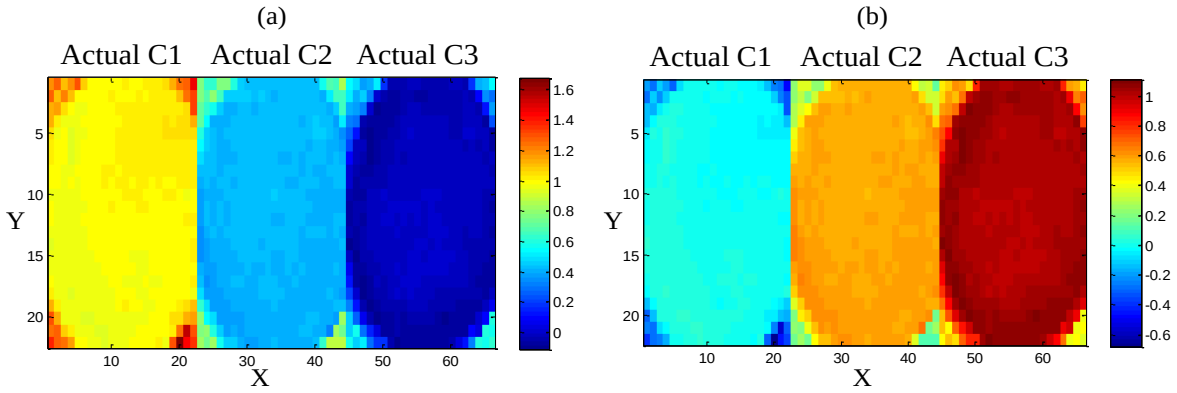

Figure II.30 : PLS-DA prediction of model M6 for the class 1 (a) and class 3 (b).

For the estimation of class 1 presented in Figure II.30 (a), the pellet of RDX (actual C1) presented in yellow, has a predicted value of 1 indicating that all the pixel of this pellet belong to C1. As for PETN pellet (actual C3), the predicted values of zero indicate that the pixel of this pellet do not belong to C1. For the mixture pellet (actual C2), the predicted pixels have a value of 0.5 indicating that this sample can 50% be a C1. Similarly, Figure II.30 (b) represents the prediction of each pixel in the class 3. The results show that the entire pixels that actually belong to C3 are correctly predicted. Finally, the image shows that the background of the pellet has values smaller than zero or greater than 1, which means that the model was not able to correctly classify them.

V.4.2.1. Central zone of the pellets

The background of the pellet cannot be properly predicted. For that, a study is performed on pixels from only the pellets. Three different ROI are chosen from the three pellets based on the PCA score image obtained in an unsupervised way. Then, the classification of the three ROI is performed by a PLS-DA to allocate to the sample one of the three classes: C1 (RDX), C2 (mixture) or C3 (PETN). For this aim, 360 pixels from the PC1 score image were selected from the central parts of the

three pellets. Among them, 30 are used for calibrating the model where each 10 pixels are assigned to one of the three classes.

After the learning step, the PLS-DA model is built with 2 PCs, based on an RMSEC of 0.09 and RMSEP of 0.1. This model is applied to the remaining 330 selected data points for sorting the pixels and the results are given through confusion matrix presented in Table II.10.

Table II.10: Confusion matrix related to the classification into three classes C1, C2, C3 after PLS-DA model of the central parts of the explosive pellets.

		Predicted class				
		C1	C2	C3	Members	Correct
Actual class	C1	110	0	0	110	100%
	C2	0	110	0	110	100%
	C3	0	0	110	110	100%
	Total	110	110	110	330	100%

The prediction results show a 100% of the correct perdition assignment of each pixel in the right class. This demonstrates the high potential of the PLS-DA in classifying the three explosives and highlights on the possibility of a wrong classification when facing non-physical data of the measured pixels.

V.4.2.2. Restricted frequency band [1.5-3] THz

As mentioned before, no procedure is applied to remove the noise from the image spectra, and this noise is dramatically affecting the spectra between 1.5 and 2.9 THz, as shown in Figure II.31. In addition, this frequency band represents an overlapping region highlighted before in this study.

Thus, a PLS-DA model is applied to this restricted frequency band, to study the performance of the model when is facing limiting noisy spectra. The model created is the same as the model with the best accuracy obtained before, the M6. It is centered scale with 60 pixels used for calibration: 30 pixels in class1 and 30 pixels in class2. The classification results for the 1452 pixels of the image are presented in a confusion matrix in Table II.11.

Table II.11: Confusion matrix related to the classification of the observations of C1 and C3 for the model M6.

		Predicted class			
		C1	C3	Members	Correct
Actual class	C1	484	0	484	100%
	C3	364	120	484	24.7%
	No class	46	438	484	-
	Total	894	558	1452	62.3%

The correct classification percentage decreases from 95.5% in the case of M6 for the entire frequency band to 62.3% in the case of restricted band. This decreasing value is related to the wrong prediction of PETN pixels due to the noisy spectra in the range of PETN fingerprints. Table II.11 shows that all RDX pixels are correctly classified, yet only 24.7% of PETN pixels are predicted in the right class.

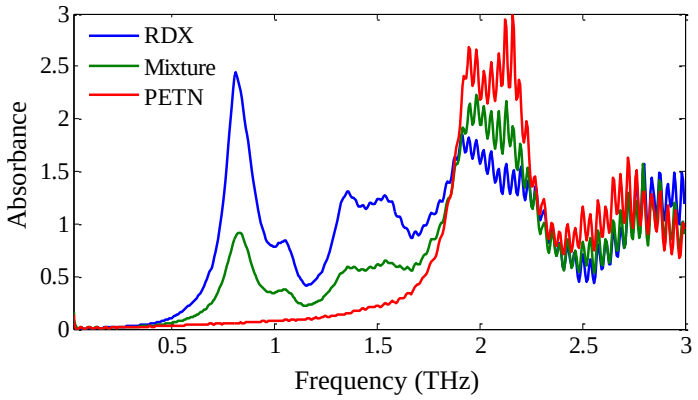

Figure II.31 : Absorbance spectra of 400 mg pellets constituted of 20 wt-% RDX and 80 wt-% PE (blue), 10 wt-% RDX + 10 wt-% PETN+ 80 wt-% PE (green), 20 wt-%PETN and 80 wt-% PE (red).

V.4.3. Merging PLS spectral and spectral-imaging models

To test the capacity to predict sample on images using spectroscopy calibration models, the same PLS model used for quantification in section IV is performed to predict and quantify pixels from the image. Six pixels are chosen from the central part of each of the three pellets. Figure II.32 shows the prediction score in the plane of the first two principal components, of the samples measured by spectroscopy represented before in the ternary diagram, as well as the predicted scores of some of pixels chosen from the central part of the explosives image. The pixels are correctly projected in the diagram, in the line corresponding to the binary mixture of explosives in 80 wt-% of PE. The mixture pixels are projected in the exact position of 50 RDX/50 PETN. As for RDX and PETN, a small shift is occurring from the exact position. This is normal due to the RMSEP value equal to 5.63 mg, corresponding to the prediction error of these pixels by the model.

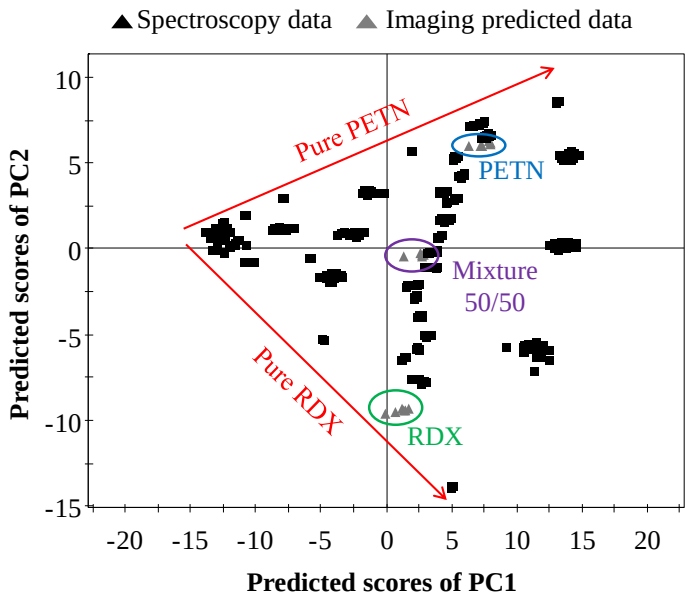

Figure II.32 : PC1 and PC2 predicted score of a PLS model.

This result shows the possibility to use a PLS model created from spectroscopy measurements, to quantify elements on the image by using their absorbance spectra extracted from one pixel with terahertz spectral-imaging technique.

CONCLUSION

This chapter studied THz spectroscopy and spectral imaging, and applied chemometric tools to investigate explosives in pure state and in mixture.

First, we highlight on the importance of the reference chosen to extract the absorbance spectra and the effect that can induce this choice on the absorbance values, and we brought out the impact of the pellet size on the spectra. We compared, in transmission configuration, the absorbance spectra of a powder when it is mixed with the PE matrix and when it is made of pellet without any binder. The results show that some of the fingerprints are lost with powder without the binder, due to the reduction of the frequency band caused by the higher absorbance of the pure product. When performing reflection measurements, this problem can be reduced, however, the extraction of the signal is more complicated. Moreover, we discussed different configuration of pure elements or mixtures propped by the Beer-Lambert law.

From the other side, terahertz spectroscopy is performed on several types of packaging materials to show their effects on terahertz spectra and spectral images when samples are measured through these materials. Although the minor effect of some of these materials on the spectra, they can have a destructive impact on the spectral images and lead to a wrong interpretation of the content of

the image. Generally, careful attention must be paid for multilayered spectroscopy analysis without precise information of the different layers.

Moreover, we demonstrate the potential of chemometrics applied to THz spectra in describing and quantifying data of pure and mixed explosive, by using partial least square analysis. By performing a quantitative PLS2 model, we were able to predict the concentration of pure explosives and mixtures, with an impressive RMSEP value of 3.4 mg. We demonstrated that a PLS2 model applied to these data has better performance than PLS1. Also, we showed that even by reducing the frequency band of analyses to a region, where an overlap between the different spectra is present, we are able to predict the concentration with an acceptable RMSEP of 4.8 mg.

For the imaging application, we demonstrated by using two metrics, RMS contrast and ENL, that the quality of the images resulting from a PCA model is better than the raw images chosen near the fingerprint frequency of the products. This demonstration is performed for two different samples: compact and non-compact powders.

As for explosive samples, and based on the successful results of chemometrics applied to spectra, we applied the same methods on THz spectral images. First, the PCA model is performed on unknown data, to understand, compress the data and visualize the image. It was able to reveal three different products in the image, and allows choosing three regions of interest to carry out, supervised analysis, in order to define the nature and the concentration of the three components in the image. Then, the results of different PLS-DA models showed that an optimum model of classification is created with two classes where 30 pixels, from each of RDX and PETN pellets, are used to calibrate the model. The prediction applied to all the 1452 pixels of the image gives a 95.5% correct classification. However, by reducing the prediction pixels to few points belonging to the central part of each of the three pellets, an impressive classification of 100% is achieved. Finally, the possibility of quantifying the spectral-imaging data from the spectral is considered by using the PLS2 model performed on the spectral data before. This model was able to predict 18 pixel concentrations from the central zones of the image and project them in the correct position in the ternary diagram, with an RMSE of 5.63 mg.

These results on chemometic analysis applied on terahertz spectroscopy are at the state of art and have the route for the industrial transfer of this recent and complementary technique.

CHAPTER III

TWO AND THREE DIMENSION MILLIMETER WAVE IMAGING FOR PACKAGES INSPECTION

INTRODUCTION

Several imaging devices including THz technologies are used for security applications. In this chapter, three different imaging techniques are discussed and results on scanning postal packages are shown. Since each system uses different emission and detection techniques, three experimental setups are presented. The first one is a passive camera, i.e. without an excitation source, and the two others are based on active imaging involving continuous waves (CW) and frequency modulated continuous waves (FMCW). These setups can provide either the amplitude or both the amplitude and the phase of the detected signal. The advantages of each of the three techniques in the frame of postal control and safety are discussed in this chapter. Moreover, the importance of visualizing in 3D the objects contained inside parcels lead us to apply tomographic reconstruction, which is discussed in the last section of this chapter.

I. PASSIVE MILLIMETER WAVE IMAGING

Among millimeter imagers, one commonly distinguishes between passive systems, that record the contrast in radiometric temperature within a scene, and active systems that are sensitive to the contrast in the scattered radiance within a scene when it is illuminated with excitation sources [182]. A comparison between active and passive imaging have been already published [183], but in the present work, we describe each of these techniques to present their potentials in the frame of parcels inspection. One of the main interests of the millimeter waves in imaging is its ability of producing images even in difficult scenes and atmospheric conditions such as low-light or fog as well as its ability to pass through different types of materials like walls, clothes, plastic, paper, etc. Finally, the low energies of the photons related to the millimeter waves make them safe to human health [184]. However, human body has a special feature in the millimeter domain; it can be considered as a millimeter source. This is explained by the radiance of the body determined by Planck law.

I.1. PLANCK'S LAW AND BODY EMISSION

According to the Planck's law, any object at a temperature above absolute zero emits electromagnetic waves covering the entire frequency range of the electromagnetic spectrum. The Planck's law provides the spectral energy distribution of the radiation emitted by a "blackbody", called radiance *B(f,T)*, calculated for different temperatures *T* as a function of frequency as follows:

$$B(f,T) = \frac{2hf^3}{c^2} \frac{1}{\exp\left(\frac{hf}{K_B T}\right) - 1} \tag{35}$$

In the international system of unities, *B(f,T)* is given in $W.m^{-2}.sr^{-1}.Hz^{-1}$, *h* is the Planck's constant equal to 6.625×10^{-34} J.s, *c* is the speed of light in the vacuum equal to 3×10^{8} $m.s^{-1}$, K_B is the Boltzmann's constant equal to 1.38066×10^{-23} J/K and *T* is the temperature of the body in K.

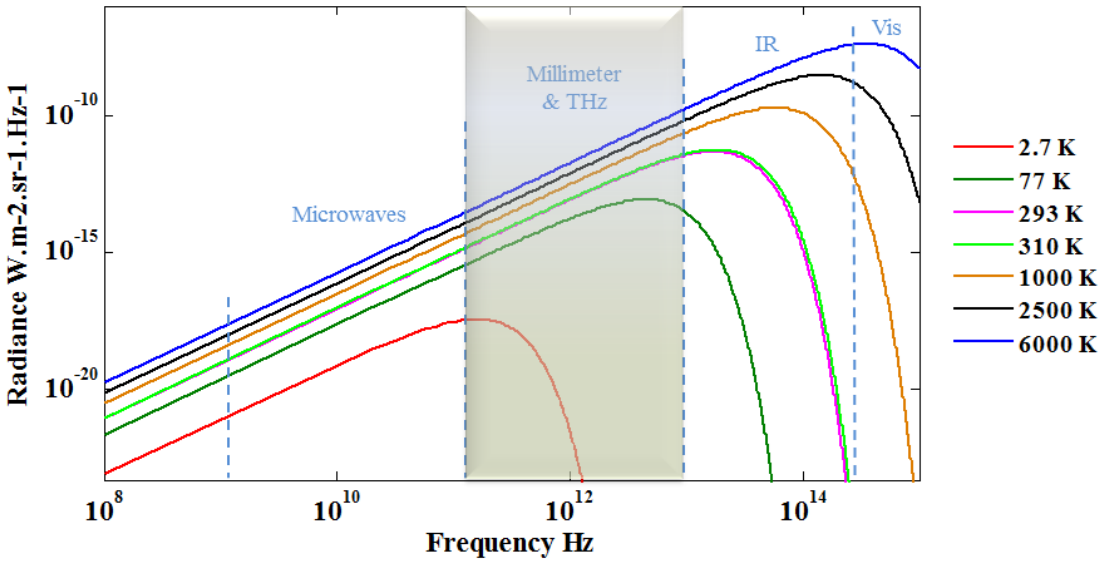

Figure III.1 : The radiance as a function of frequency, as defined in Planck's Law, calculated for seven different frequencies: Cosmic background radiations (2.7 K), liquid nitrogen (77 K), room temperature (293 K), human body (310 K), incandescent lamp (2500 K), and sun surface temperature (6000 K).

Figure III.1 presents the radiance as a function of frequencies for different source temperatures. The graph at 310 K, which is the temperature of a human body, shows a significant radiance in the THz domain. As a consequence, imaging human beings in this frequency range with passive techniques is possible. For higher temperatures, the maximum of radiance is in the infrared and then in the visible domain. In addition, millimeter-wave radiations are far less attenuated when they propagate in air than visible or infrared radiations. This is precisely the key-advantage of passive millimeter-wave (PMMW) imaging. Moreover, PMMW imaging is almost unaffected by sun or artificial lights. Therefore, it can operate with equivalent performance in clear or low-visibility conditions, namely by day or the night. More precisely, four spectral windows at 35, 94, 140, and 220 GHz are characterized by very low attenuation in clear air as well as in the presence of fog, and this is one of the reasons why PMMW is intendent to stand-off detection[185].

In the case of grey body and for low frequencies, the Rayleigh-Jeans law provides the radiance as follow:

$$B(f,T) = \frac{2K_B T f^2}{c^2} \tag{36}$$

where T is the physical thermodynamic temperature of an object. With this approximation, the radiance of a grey body is only a portion of the blackbody radiance and it is determined by its emissivity $\varepsilon = T_b / T$, where T_B is the object's surface brightness (or radiometric) temperature. The emissivity describes the efficiency with which a material radiates. It is a function of its dielectric properties, the roughness of its surface, and the observation angle. A blackbody has an emissivity of 1

and no other material can radiate more thermal energy at a given temperature. An object with an emissivity of 0 emits no energy and is considered as a perfect reflector with a reflectivity ρ=1 since the reflectivity and the emissivity are complementary[186] [187].

Table III.1 : Radiatives properties of different materials at 100 and 500 GHz: emissitivity and reflectivity.

	Emissivity (ε)		Reflectivity (ρ)	
	100 GHz	500 GHz	100 GHz	500 GHz
Metal	0	0	1	1
Skin	0.65	0.91	0.35	0.09
Explosive	0.76	0.95	0.24	0.05
Denim	0.09	0.49	0.01	0.01
Tee-shirt	0.04	0.2	0	0

The variation in emissivity and temperature of common materials in a scene is an important factor for the contrast of images. As it is shown in Table III.1 [188], human skin has a typical value of emissivity of 0.65 at 100 GHz increasing to about 0.91 at 500 GHz, while the emissivity of metal is equal to zero for these two frequencies. This significant difference induces a very good contrast between skin and metals in passive imaging. In addition, the emissivity of explosives is very high compared to the plastic, paper and ceramics, and they are consequently expected to be well contrasted in PMMW images.

I.2. PASSIVE IMAGING CONCEPT

Passive millimeter wave imaging is similar to common imaging, except that the examined object is the source itself, being considered as an emitter like a blackbody. Passive imaging is based on the detection of the radiations emitted by the different part of the scene. In addition, millimeter waves can propagate through clothes and parcels. Knowing that the human body emits in the millimeter region, a hidden item underneath clothing with different emissivity creates a contrast which is used to reveal the item. This technique has been intensively used in security applications in airports for detection of hidden objects under clothes [189]–[192]

I.3. PASSIVE MILLIMETER WAVE SETUP

I.3.1. PMM-Imager90

One of the main uses of the millimeter-wave passive imaging is the detection of concealed weapons hidden under clothing. The PMM-Imager90, known as Millicam, is a millimeter-wave

radiometric imaging system fabricated by the company MC2 technologies. It is a real-time mechanically scanned imaging system. It is based on ultra-sensitive receivers in the millimeter-wave range capable to detect minute amounts of power emitted by human beings. The camera operates in the 75-110 GHz range (wavelength around 3 mm). It produces one image in about 3 to 10 seconds with a working range distance between 1 to 10 m and a resolution of 2.5 cm at 2.5 m.

The receiver array is formed by 8 pixels: antennas and Schottky diode detectors. The antennas receive the thermal emission from the target. The reception of waves is followed by low noise amplification. To generate the radiometric image, a mechanical scanning is used with a vibrating mirror [193]. Single movement of the mirror deflects radiations to the antennas, and forms 8 vertical lines for the image. Thus, all the collected beams, from all the mirror positions, create an entire image of 82×200 pixels. Two polyethylene lenses are used to image the sample target with an area of 2x1 m² at 2.5 m distance. The first one, with 100 cm diameter, is fixed on the first external side of the Millicam, the other one, lens 2 in Figure III.2, moves vertically to change the focalization distance. Verity *et al.* developed a similar passive imager that also goes to 10 m in the detection of weapon hidden under clothing; in addition, it can be used to visualize remote targets at a distance of 170 m. The frequency of this camera is around 90 GHz, with a gain between 40 and 52 dB [194].

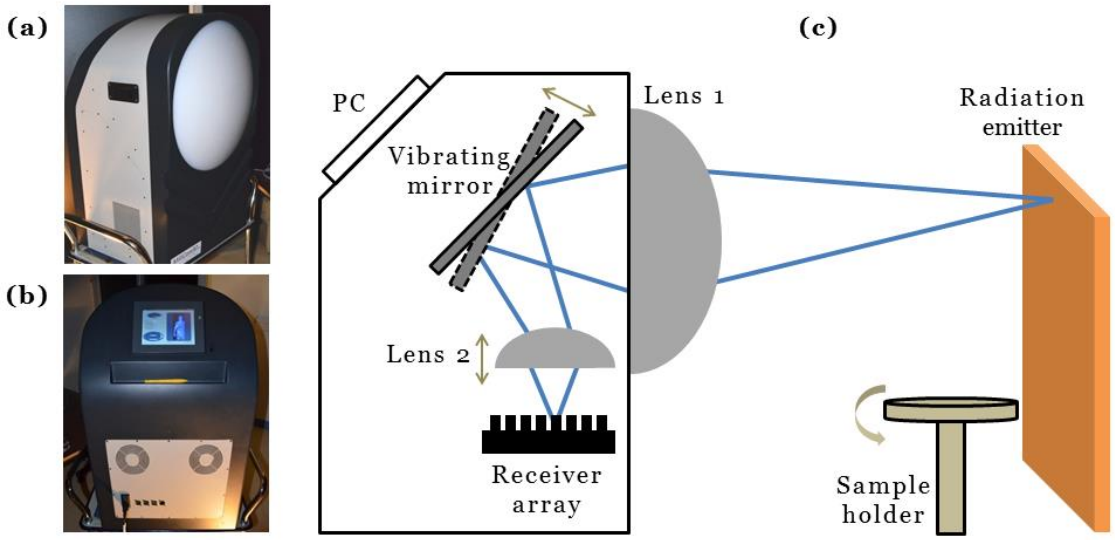

Figure III.2: (a), (b) Photograph and (c) setup of the Millicam90 system from MC2 company.

For human screening, the sensors detect radiation emitted from the body with a temperature of 310 K. When facing an object, these waves are attenuated or blocked. For a weapon for example, the ideal metal surface completely blocks the emitted waves, and thus the system will detect the shape of the weapon by showing the contrast between the transmitted radiation through the object and the blocked radiation by the metal. Figure III.3 shows the results given by the system for the detection of two metallic guns hidden under clothes at a distance of 1 m. No processing is carried out on the

displayed image, however, it is always possible to apply a special algorithm to improve the quality of the image as it was done by Kowalski *et al.* in 2012, to enhance the low image quality obtained from commercial THz cameras [195].

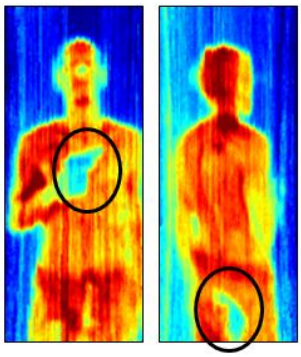

Figure III.3 : Passive millimeter-wave images of two hidden guns underneath clothes made with the Millicam90 system.

However, in the present work, we focused on the detection of dangerous objects inside parcels. We characterized several cardboard materials that are intensively used in the postal chain, and they have low absorption at 90 GHz. For that, we used the Millicam90 and we optimized the system to image parcels without opening them. First, we placed a radiative source as shown in Figure III.2, emitting at 343 K. At this temperature, and for the frequency range of the camera, the radiance calculated by the Planck's law (Figure III.1) becomes near to the maximum peak, which is sufficient to be detected by the sensitive sensors. To form an image, a parcel is placed between the source and the camera; it either blocks, or totally or partially transmits the emitted radiation, depending on the parcel and its content. This configuration is similar to imaging in the transmission mode, where the object transmits partially or blocks the waves emitted from the source and thus creates a contrast on the image.

In every image obtained by the Millicam90, a calibration procedure is applied to enhance the quality of the image by reducing the environmental noise. A calibration of the signal detected by each pixel is possible referencing it to the top lines of each 8 arrays. When these pixels are drowned in a high noise, it affects the quality of the entire image. The noise was lowered by using absorber material, placed in the upper part of the imaged area, to prevent the radiation received from the region outside the emitter. This raise up the contrast and minimize the noise effect. Figure III.4 shows the intensity distribution at two different positions in the image, at the background defined by position 1, and at the emitter presented by position 2. As Figure III.4 (c) shows, the intensity in the background could vary in an arbitrary way. By adding the absorber, this intensity is almost stable compared to the other position. From the other side, Figure III.4 (d) presents the intensity values at a position of the thermal source, with no sample, in the two cases, with and without the absorber. First, the intensity with the absorber is more constant and a gain of more than 4.7% is achieved. Thus, the use of the absorber was efficient to enhance the image quality by improving the signal captured by the camera.

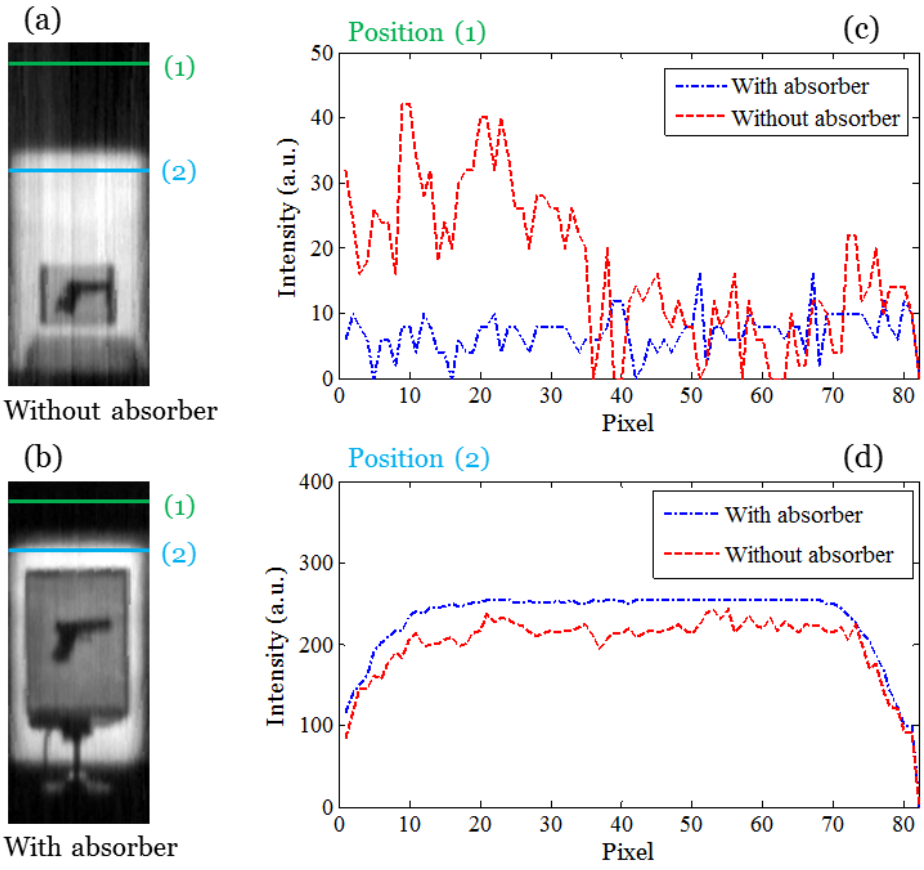

Figure III.4 : Passive images produced by the Millicam90 in two cases (a) without absorber and (b) with absorber. Intensity distribution at two positions for each image: (c) position 1 outside the radiation emitter and (d) position 2 at the upper part from the radiation emitter.

I.3.2. Passive Millimeter waves imaging results

The potential of the setup in detecting various objects hidden in different types and sizes of parcels was studied by imaging several parcels, with 12 sec scanning time for each image. Figure III.5 (a) and (b) shows the PMMW images of metallic weapons, guns, bullets and knife, hidden in a parcel of 33×21×9 cm^3. In each of the images, the shape of the guns and knives can be identified. However, the bullets cannot be clearly recognized due to their small sizes. In Figure III.5 (c) and (d) two parcels of 33×21×9 cm^3 and 45×31×16 cm^3, containing a disassembled metallic gun and a concealed metallic gun and tools are analyzed with the PMMW system. Despite the low resolution and limited noise equivalent power (NEP), the images reveal a good ability for the recognition of the shape of the objects, even when the gun was disassembled or partially concealed by another object. Moreover, applying shape recognition algorithm on images allowed for the automatic recognition of the threats hidden inside the parcels.

Although shape recognition was thus evidenced at 100 GHz (Table III.1), no chemical identification could be achieved by this technique since we measured only one transmission frequency. Actually, Figure III.5 (e) displays a Millicam image of one plastic bottle of water and one glass bottle of wine, but neither the amounts of liquids neither their chemical nature could be determined. Additionally, Figure III.5 (f) displays a Millicam image of a series of various materials such as medicine, soap, powder, correction fluid, placed inside a bubble wrap. The image resolution limited to 1 cm was poor, and neither relevant information about the shapes, nor chemical distinction was accessible.

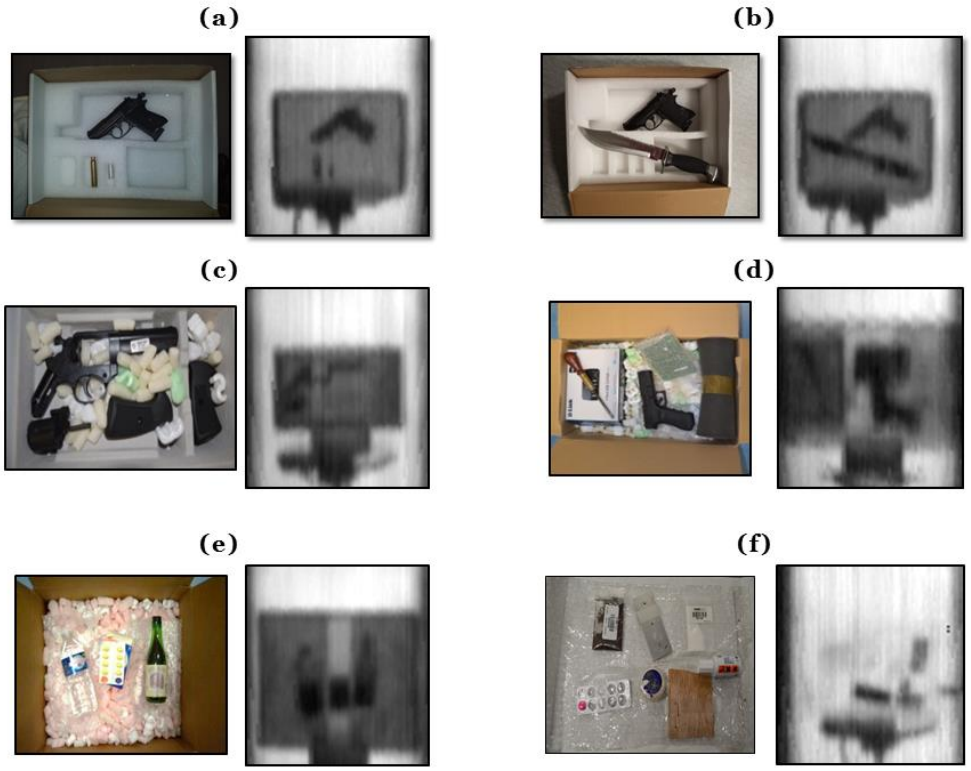

Figure III.5 : Optical images and PMMW images of five different parcels and threats: (a) gun and bullet, (b) gun and knife, (c) disassembled metallic gun, (d) metallic gun and tools concealed by paper, box and foam, (e) two different liquids in a plastic and glass bottles, (f) different object such as medicine, soap, powder, correction fluid, etc.

Despite of its general limited ability to achieved high contrast imaging, the Millicam setup allowed in a few cases to image the internal content of parcels in few seconds with acceptable contrast and resolution. But getting the image for only one single plane of the parcel could not be enough. The object position at this specific plane could be masked and prevents a reliable judgment on the object shape. For this reason, we adapted the PPMW setup with a rotational stage, described below, that provides a series of images of the sample at different angles of view.

Finally, more complex objects placed inside different types and shapes of cardboard boxes and letters were thus tested to simulate the real life conditions that might be observed in the postal chain, including various types of holders and packaging materials like foams, plastic film, etc.

Table III.2: Capabilities and limitation of Millicam system in packaging investigation.

Positive	Limitations
Identification of metallic weapons through all types of parcels and letters. Recognition of objects shape inside parcels and letters. Visualization of the content of plastic and glass bottles.	Maximum length and width at 1 m: 120×49cm^2. Maximum thickness: >25cm. One frequency at a time. Identification of the objects is not possible when wrapped in dense boxes. No chemical recognition. No identification when the object is overlapped by another.

I.3.3. Rotational stage

For parcel inspection, 2D imaging is not sufficient in most of the cases for instance, when an object is facing the detector and is concealed by another object. Consequently, 3D imaging of parcels has become mandatory and this is the reason why we developed a homemade tomographic reconstruction algorithm that will be presented later in this chapter. To provide data for tomographic reconstruction, we optimized the experimental setup by placing the sample holder onto a rotation stage and we recorded a series of images per sample, one image at each angle of the rotation stage. Angular steps of 10º represented the optimized conditions to manage both the acquisition time and resolution. The automation of the image acquisition was performed through a homemade LabVIEW program, allowing the acquisition of 36 images corresponding to 36 projections in approximately 9 minutes. In order to demonstrate for the first time the feasibility of tomographic reconstruction applied to PMMW images, a parcel of 55×36 cm^2 containing a metallic gun and a metallic knife covered by foam was selected. By applying special tomographic reconstructions, it was possible to reconstruct and visualize in 3D the content of the parcel (Figure III.26). This result represents a significant progress in terahertz 3D imaging since it is the first time that tomographic reconstruction was achieved from a series of images obtained from a PMMW imaging system.

I.4. SYNTHESIS

Finally, the results of passive imaging setup show a high potential in the use of this technology for parcels inspection. However, the resolution in our setup was not sufficient for identification of small objects. This problem can be easily resolved because recently, new passive imaging systems exist with higher frequencies (200 GHz) occurring better resolution. Moreover, it is possible to

perform measurements in real time with a good signal-to-noise ratio. Finally, this technique is very efficient for human screening being able to detect hidden object through clothes without causing dangerous effects on human health. In contrast, we showed that PMMW imaging can be well performed on parcel inspection, and by using images at different angle and applying special tomographic reconstruction algorithm, it is possible to retrieve the shape of the object in volume, inside parcels.

II. ACTIVE CONTINUOUS WAVE IMAGING

Active imaging differs from passive imaging by the need of a radiative source. In this chapter, two types of coherent, active imaging systems are discussed. The choice of the sources and detectors varies depending on the application. The choice of the emission frequency is linked to the available power, which is a technological limitation. For the postal chain security, high-speed imaging is mandatory, and thus the higher the THz radiation power, the best will be the images, allowing to overcome the absorption of the THz waves by the different materials. Based on this, two imaging active techniques were chosen. The first one based on continuous wave (CW) imaging only gives access to the amplitude of the wave. The second one, known as frequency modulated continuous wave (FMCW) technique gives access to both the amplitude and the phase of the wave. The details of these two techniques, as well as the results obtained in the frame of parcels inspection are presented hereafter.

II.1. SOURCE

For the CW imaging, Gunn diodes are used to generate the millimeter waves. A Gunn diode consists of only N-doped semiconductor materials, and involves the negative resistance effect. This effect allows generating oscillations determined by the semiconductor properties. To produce higher frequency, the size of the semiconductor should be reduced and thus the power is lower. Once generated in a cavity, lumped elements improve impedance matching and optimize power generation. Finally, the wave is emitted by a specially designed horn antenna coupled to the Gunn-diode. To have access to other frequencies and to increase the output frequency of the emitter, frequency multiplier chain can be used but obviously leading to a decrease in the output power.

The sources we have been using to generate the continuous waves in the present work were two Gunn diodes characterized as follows. The first one is a diode coupled to a frequency tripler, the WAX3 from “Wasa MilliMeter Wave” [196]. It has an output frequency range of 261-315 GHz and delivers a maximum output power of 14 mW at 287 GHz. The second one is the GDM-10 Gunn diode from “millitech” [197]. It emit in the 75-90 GHz frequency range delivering a maximum output power of 51 mW at 84 GHz. Each diode is coupled to output horn antenna. The advantage of the WAX3 is essentially the better spatial resolution owing to the shorter wavelength, whereas the GDM-10 has a much larger output power.

II.2. DETECTOR

The detection is performed by two zero-bias Schottky diodes from "Virginia Diodes" combined with lock-in amplifier and involving the use of mechanical choppers to modulate the incoming wave intensities. The Schottky diodes implemented in the present work are the WR10 operating in the frequency range of 75-110 GHz and the WR3.4 operating in the frequency range of 220-330 GHz, with a noise equivalent power (NEP) of 13.2 pW/√Hz and 17.6 pW/√Hz respectively. The WR10 guide is equipped with a 17-mm diameter cylindrical horn antenna and the WR3.4 are coupled to a pyramidal horn antenna of 9 mm. The typical responsivity of the WR10 and WR3.4 diodes along their frequency range is 2000 V/W and 1500 V/W respectively.

The experimental environment emits terahertz radiation that can generate noise. The lock-in amplifier is able to extract a very small signal even when it seems to be concealed by noise by modulating the incident radiation in this case at low frequency. In our experimental setup, we use two mechanical choppers with two different modulation frequencies of typically hundreds of hertz. The parameters of the lock-in amplifier were set in accordance with the modulation reference frequency, namely the time constant that should be at least three times higher than the period of modulation, to make sure that more than one full period of the modulated signal is detected. In addition, the response time of the Schottky diodes should be ten times smaller than the reference period. For those used in our setup, the response time is several ns, which is comfortable to achieve the mentioned requirement. Another important parameter of the lock-in amplifier is the sensitivity. Changing the sensitivity may change the dynamic reserve, and highlights different details in the sample to image. A low sensitivity may lead to a saturation effect of the resulting image if the objet to image presents different materials with variant absorbance.

II.3. CONTINUOUS WAVE SETUP

The system is based on raster scan single-pixel in transmission geometry, where the incident beam is focused onto the sample with a pair of 50 mm diameter high-density polyethylene (PEHD) lenses. Depending on the size of the object to be imaged, the focal length can be set to 50 mm or 100 mm. The detection is made point-by-point by moving the sample thanks to a 2-axis translation stage by step of 0.5 mm in both directions, and simultaneously producing two images at 84 GHz and 287 GHz, representing the amplitude of the THz wave at each pixel. Here the translation stages velocity and the response time of the detectors limit the imaging speed. Considering the speed 40 pixels/sec for the translation stages, a 100×100 pixels image can be made in about 28 minutes. An alternative configuration consists in continuously moving the sample along the X-axis thus decreasing the acquisition time to 8 minutes but also reducing the image quality. Considering the time necessary to reconstruct an image, the present system is far from allowing real-time imaging. Finally, the sample is rotated from 0 to 180°, by steps of 5° or 10°, thus providing 18 or 36 projections. Figure III.6 shows the basic optical and electrical setups for single-pixel scanned-imaging in transmission-mode.

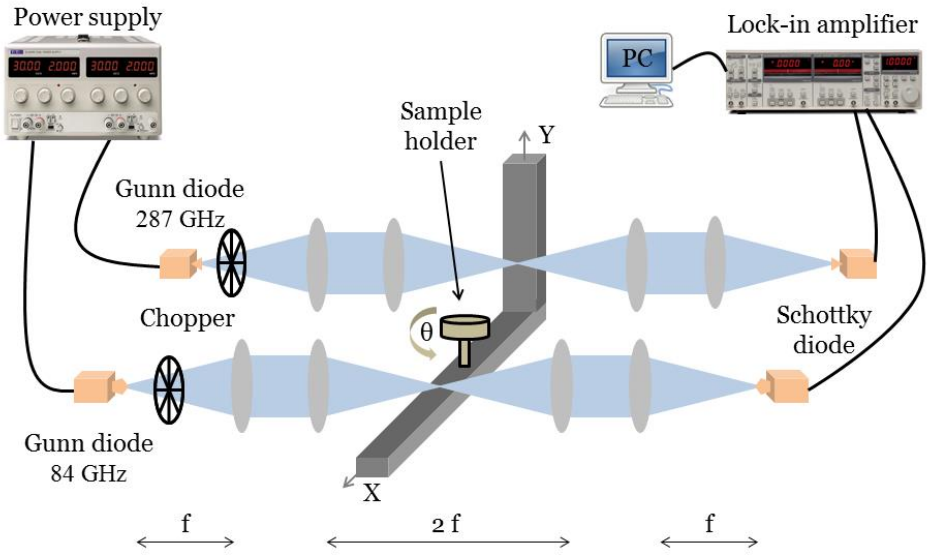

Figure III.6 : Optical and electrical configuration of the raster scanning continuous wave setup.

II.4. BEAM PROPAGATION PARAMETERS AND RESOLUTION CRITERIA

THz beam can be approximated by a Gaussian beam with an intensity profile corresponding to the theoretical TEM_{00} mode. The knowledge of the special characteristics of the propagation of the beams through optical systems and the definition of their characteristic parameters has an important impact on the awareness of the dimensions of the sample that can be imaged. The amplitude of the electric field in the transversal direction x and along the axial direction z corresponding to the propagation, can be written:

$$E(x,z) = E_0 \sqrt{\frac{2}{\pi}} \frac{\omega_0}{\omega(z)} \exp\left(-\frac{x^2}{\omega^2(z)}\right) exp\left(-i\left(\frac{kx^2}{2R(z)} - [\phi_0 - \phi(z)]\right)\right) \quad (37)$$

Where:

$E_0 = E(0,0)$ is the amplitude and phase of the electric field at the origin at time zero;

ω_0 is the beam waist;

$\omega(z)$ is the radius of the beam along z;

$k = 2\pi/\lambda$ is the wave number for the wavelength λ;

$R(z)$ is the radius of curvature of the wave front of the Gaussian beam;

$\Phi(z)$ is the Gouy phase shift;

$$\begin{aligned} \omega(z) &= \omega_0 \sqrt{1 + \left(\frac{z}{z_R}\right)^2} \; ; \\ R(z) &= z \left[1 + \left(\frac{\pi \omega_0^2}{z \lambda}\right)^2\right] \; ; \\ \phi(z) &= arctan\left(\frac{Z}{Z_R}\right) \end{aligned} \tag{38}$$

Where z_R is the Rayleigh range. The imaginary part of *E(x,z)* is related to the phase of the beam, and the real part is connected to the transversal distribution of irradiance *I(x)* of the beam

$$I(x) = I_0 \exp(-2x^2/\omega^2(z)) \tag{39}$$

The first parameter to be considered in the Gaussian beam propagation is the beam waist ω_0. It depends on the optical configuration and choice of the lens and it corresponds to the smallest waist for a Gaussian beam at the focal point. It is determined by using the beam spreading angle θ shown in Figure III.7 (a) and calculated using the relation:

$$tan\theta \approx \theta = \frac{\lambda}{n \pi \omega_0} \tag{40}$$

Where *n* is the refractive index of the medium. The angle θ is calculated using the lens diameter D and the focal distance f. The other important parameter is the Rayleigh length z_R, which is the distance along *z* where the beam radius is $\sqrt{2}$ times larger than it is at the focal point. Z_R defines the depth of focus where the Gaussian beam is considered as collimated with plane wave [198] [199].

$$z_R = \frac{\pi n \omega_0^2}{\lambda} \tag{41}$$

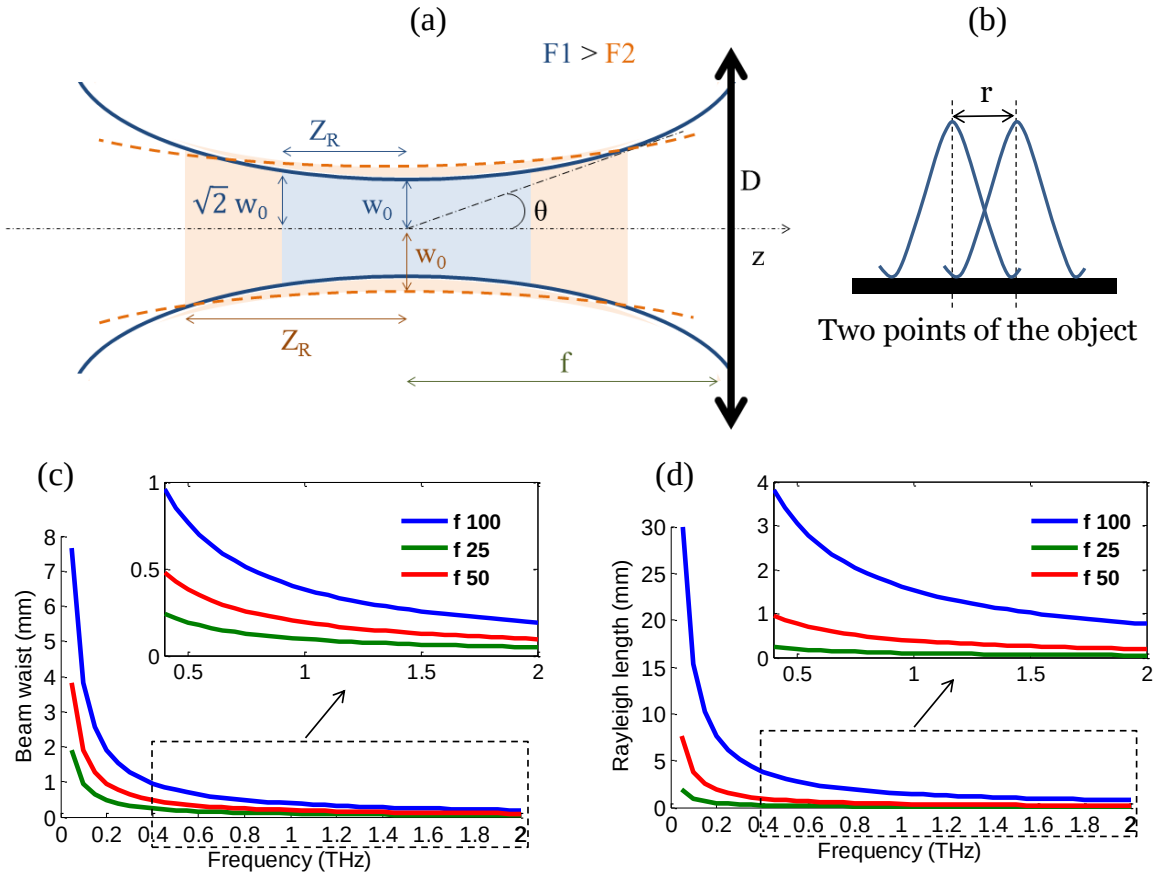

Figure III.7 : (a) Gaussian distribution of a terahertz beam in a focalized configuration for two different frequencies. The higher the frequency, the smaller the waist and the shorter the Rayleigh range; (b) theoretical calculation of the beam waist and (c) Rayleigh length for a Gaussian beam for frequencies between 0.1 and 2 THz.

A theoretical calculation of the waist value and Rayleigh length is necessary for the choice of the configuration in function of the object. This calculation is made using a lens of 50 mm diameter and a focal length of 100, 50 and 25 mm and are presented in Figure III.7 (c) and (d). The beam waist ω_0 values obtained by theoretical calculation using a 100 mm focal length are 1.27 mm at 287 GHz and 3.82 mm at 84 GHz. Experimental evaluation of the beam waist was made by using the knife-edge technique and calculating the diameter of the beam at $1/e^2$ from the maximum intensity. The calculated value of ω_0 using a 100 mm focal length is 1.5 mm at 287 GHz.

When dealing with imaging, an important feature should be considered: the resolution. This term has several definitions depending on the domain of study and several methods are used to calculate it. Every image has several resolution parameters that should be taken into consideration depending on the way this image is obtained. There is the resolution depending on the measuring system as sensors, detectors, lens, etc., and on the measurement acquisition parameters. So by talking about resolution, we should differentiate the spatial resolution of an optical system (laterally and in depth), the spatial resolution of an image, and finally the spectral resolution.

Resolution is the capability of the sensor to observe or measure the smallest object clearly with distinct boundaries and the ability of a lens to produce sharp images of two closely spaced point objects. It is defined as the minimum distance between two objects that can be distinguished in the image as illustrated in Figure III.7 (b). The smaller the distance by which two objects can be separated and still be seen as distinct, the greater the resolution. According to the Rayleigh criterion, and for the small angle approximation, lateral resolution is defined as the distance between two points that can be resolved and is determined as follows:

$$r = \frac{1.22\ \lambda\ f}{D} \tag{42}$$

Where:

- r is the minimum distance between resolvable points, measured in a unit of distance such as mm;
- λ is the wavelength of light;
- D is the diameter of the aperture of the lens;
- f is the focal distance of the lens.

Higher value of r indicates a better distinguish between two points, thus better spatial resolution. The spatial resolution can be limited by diffraction, as well as by aberrations, imperfect focus, and atmospheric distortion. Also, the lenses display and alignment has a high effect on the variation of the resolving power of an imaging setup. So a great carful should be considered when building the setup.

The values ω_0 contribute to the maximum resolution that can be achieved. As shown in the plot of the beam waist, decreasing the focal length at a given frequency reduces the value of the waist, which is proportional to the resolution, and thus a smaller resolution value with the 25 mm focal indicates a better resolution. However, the need of space for imaging large objects (more than 10cm) leads to the use of the 100 mm focal length. However, for higher focal length, the distance between the source and the detector will be larger and with the available power, the signal will be attenuated by the long propagation distance. Also, the decreasing of the beam waist with the frequency indicated that better resolution is obtained with higher frequencies. As for Rayleigh length, it contributes to the depth of focus where the beam is considered collimated and it helps defining the thickness of the object that we can image. For lower frequencies, the Rayleigh zone is larger, and is recommended for large object.

However, when dealing with imaging, acquisition parameters contributes in the resolution determination. The pixel size chosen, defined by the translation step size, contribute to the resolution determination too. It is assumed that the pixel size is chosen to be equal to the full width at half maximum (FWHM) spot size. More pixels can be fit into the same display area by choosing the pixel size smaller than the FWHM spot size. To take this into consideration, another way can be used to evaluate the limit of resolution in an imaging setup, which consists of using the USAF target shown in Figure III.8 (a), and identifies the element corresponding to the first resolved lines. The USAF target is a resolution test target widely used to test the resolution of optical imaging systems such as

microscope and cameras. As shown in Figure III.8 (b) and (c), the MMW image at 287 shows a limit of distance where the two lines can be differentiated. This limit is considered as the resolution and can be calculated as follows:

$$Resolution = 2^{\left(group+\left(\frac{element-1}{6}\right)\right)} \text{ (lp/mm)} \quad (43)$$

The lp corresponds to one black and one white lines. For our setup, at 287 GHz the bars that cannot be distinguished correspond to the element 6 from the group -3. Yet, the minimum discernable elements in this group are elements 5, indicating a resolution of 2.5 mm. Resolution evaluation is important for the knowledge of the limitation of the size of objects that can be imaged.

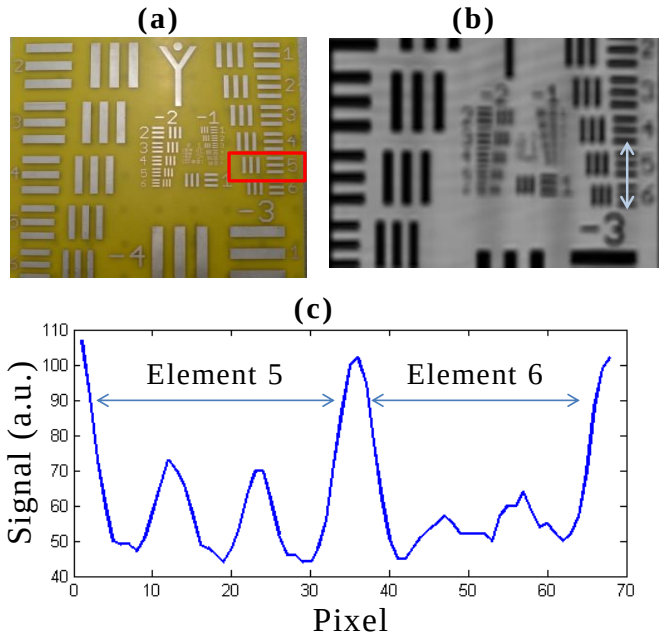

Figure III.8 : (a) Photograph and (b) image at 287 GHz of the USAF test target with 100 mm focal length, (c) variation of the transmitted signal through the elements 3 and 4 showing the limit of resolution.

Finally, the spectral resolution represents the spectral bandwidth and the sensitiveness of a detector, and describes its ability to distinguish between wavelength intervals in the electromagnetic spectrum. The finer the spectral resolution, the narrower the wavelength ranges for a particular band.

II.5. IMAGING RESULTS

Here we present some of the imaging results that have been performed with this setup. The sample shown in Figure III.9 (a) is a plastic gun made from polymer using a 3D printer. With the development of 3D printers, this type of gun becomes more accessible in the market. It has a high

danger and is not easily recognized by X-ray scanners especially when it is disassembled. Millimeter and terahertz waves have the potential in analyzing such materials. Figure III.9 (c) represents some of the optical properties of the material constituting the gun. The absorption coefficient and the refractive index between 0.1 and 1.9 THz are obtained by terahertz time-domain spectroscopy. These results showed a constant refractive index all over the frequency band from 100 GHz to 1.9 THz, and the absorption coefficient indicates a low absorption between 100 and 300 GHz. The MMW image at 84 GHz represented in Figure III.9 (b) allows seeing the external shape of the gun as well as details from its internal structure, like holes and cavities due to the transmission of the waves through the polymer material. These imaging information's, external and internal, are complementary and important when it comes to object recognition.

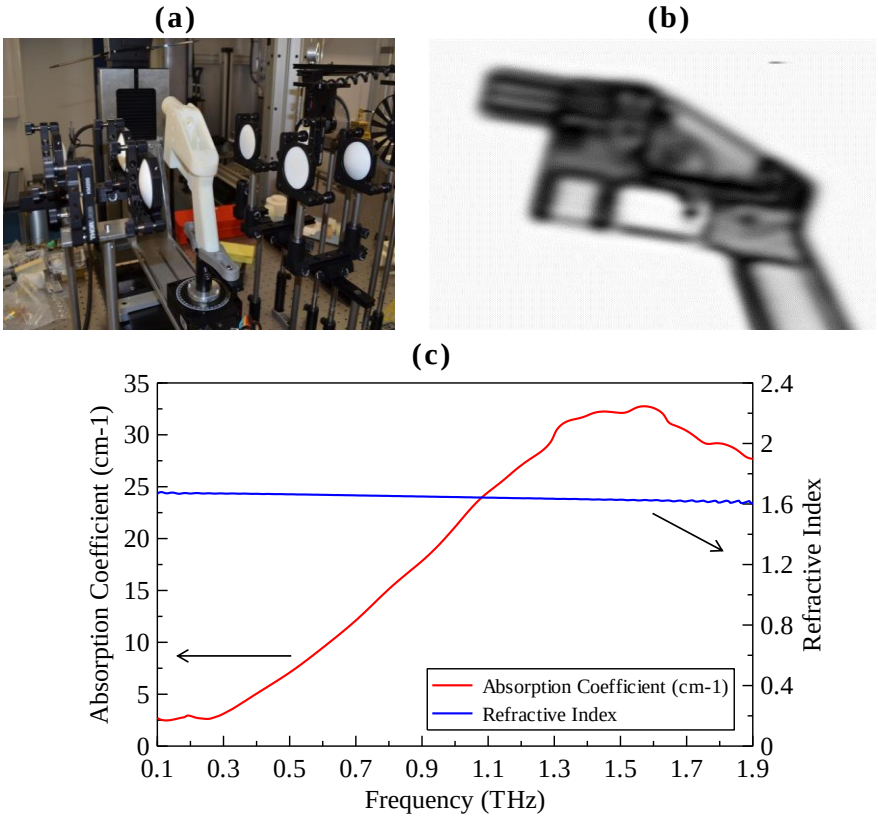

Figure III.9 : The liberator gun (a) photograph and (b) mm image at 84 GHz, (c) refractive index and absorption coefficient of the polymer material constituent of the gun obtained by terahertz time-domain spectroscopy.

Another example of a ceramic knife, imaged at 287 GHz, is presented in Figure III.10. The interesting part in such a sample is the difference in the surface treatment applied to the blade. The surface 1 of the cutting part of the knife with 1.8 mm thickness has a refractive index of 1.48 between 0.1 and 1.6 THz, measured by terahertz time-domain spectroscopy and is partially transparent to THz

waves. However, the treatment applied to the material, leading to surface 2, makes the surface more reflective and diffractive which can be a limitation in the interpretation of the object.

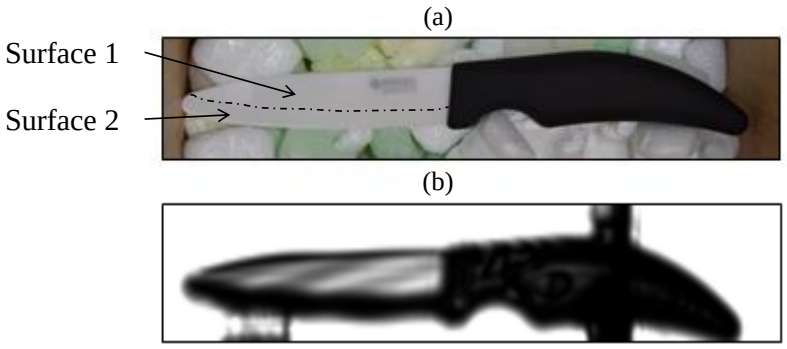

Figure III.10 : (a) Photograph and (b) image at 287 GHz of a ceramic knife. The same ceramic material with two different treatments reveals two different results on the image.

II.6. ARTIFACTS

Before investigating objects in parcels, it should be noticed that several limitations and artifacts can be present while imaging. Some of these problems came from the setup itself that causes sometimes confusion between the real physical state of the objects and the obtained image. Thus, the image can present unphysical information and this affects the interpretation of the result as well as the tomographic reconstruction. Different reasons cause this effect:

- Misalignment and defocusing of the source, detector and lenses. This can lead to the loss of a portion of the beam either on the lenses when the beam divergence is larger than the lens diameter or on the detector surface when the focalization point is shifted and reduce the detection to just a portion of the beam. Also, the spherical surface of the lenses can produce different types of aberrations such as spherical aberrations. In fact, the incident rays which are parallel to the optic axis and positioned at different distances from the optic axis, fail to converge to the same point. This is detected by measuring the beam waist at different position around the focusing spot, and if the smaller waist does not correspond to the focal point, the lenses should be realigned. For multiple lenses, spherical aberrations can be canceled by overcorrecting some elements.
- The dimension, shape and nature of the object to image. When it presents parts with a dimension smaller than the beam waist, these parts won't be accessible for imaging. This problem is related to the resolution. Moreover, if the object presents cylindrical of spherical surfaces this can creates aberration due to refraction effect, or sometimes it can be helpful and correct the misalignment of the setup if it exists. Also, if the surface of the sample is highly reflective, or the medium is very refractive, this can lead to the loss of the entire beam. In addition, diffraction and interference phenomena can be significant especially when the object contains small parts compared to the wavelength.

An example of the resolution limitation is observed in Figure III.11, where one of the scissor edges is partly invisible. As shown the images, this problem is less damaging with the 287 GHz wave where the resolution is better than the 84 GHz. It is also related to the loss of the signal by reflection and diffraction of the wave on the circular part of the scissor. These limitations prevent the clear observation of several specific shapes, especially those having a reflecting surface or cylindrical forms and the problem is worth when the object is placed inside a box as in Figure III.11 (c).

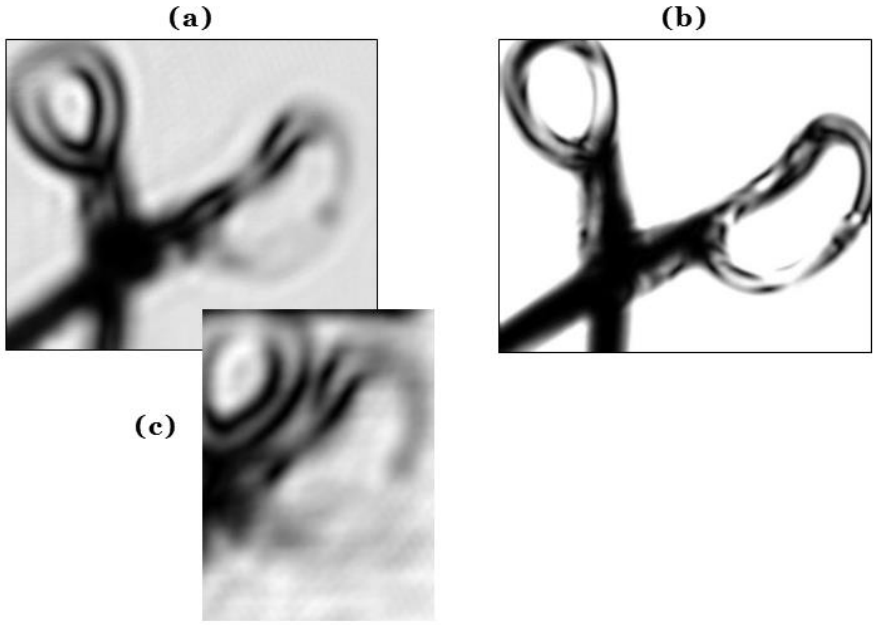

Figure III.11 : Scissor image at (a) 84 GHz, (b) 287 GHz, (c) 84 GHz inside a box.

To clarify several problems and point out on the misunderstanding interpretation and the aberration that can be present, some calculations are made to embrace the wave propagation after interaction with an object.

First, part of the problem is represented by a ray tracing of the wave propagation into a sphere of 50 mm using Optgeo software. Figure III.12 shows respectively the propagation of the beam without the object, when the center of the sphere is placed on the focal point, then by moving the sphere up perpendicularly to the optical axis. This shows that a small deviation of the object's center from the focal point will induce a high deviation of the beam. To illustrate the artefact effects, a cylindrical object is chosen and several configurations are tested.

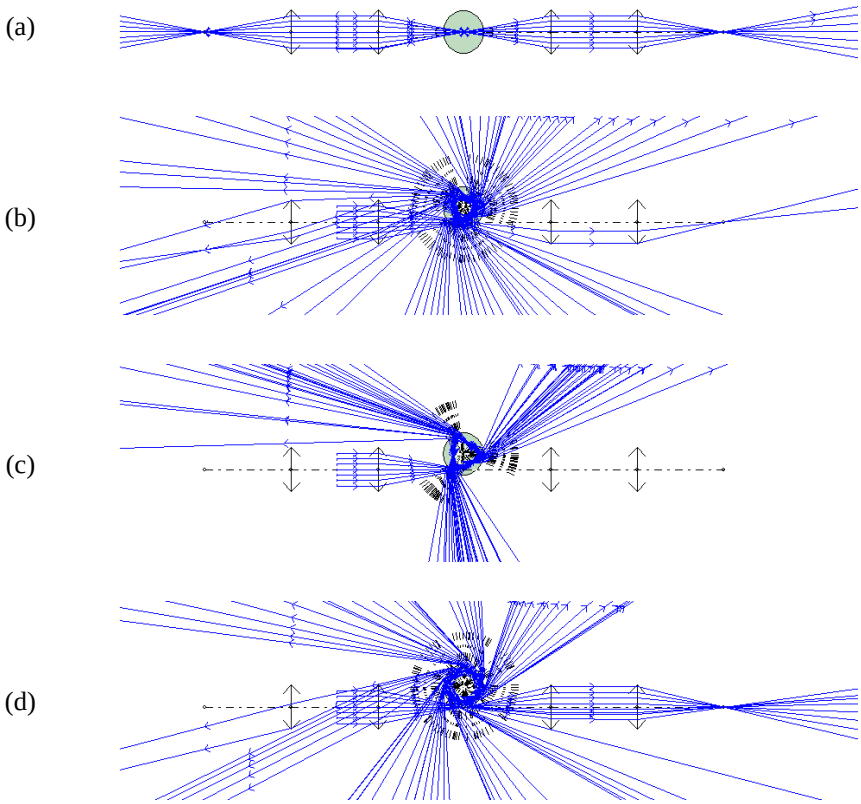

Figure III.12 : Simulation of the diffraction effect of a sphere placed at different position along the perpendicular to the optical axes. (a) The center of the sphere is on the optical axis for Y=375, moving the sphere up (b) Y= 391, (c) Y=393, (d) Y=399.

When imaging a cylinder, the refraction effects are as complex as the case of a sphere presented in the simulation. Figure III.13 shows the millimeter image at 287 GHz of a full cylinder made by polyethylene (PE) with a 50 mm diameter. The resulting images indicate the presence of a high intensity "hole" inside the cylinder, which is not physically present. Also, the intensity of the wave at the middle of the cylinder is slightly higher than the wave intensity passing in the air, indicating that the presence of the cylinder changed the focalization point and improves the signals collection. The same effect is observed for different diameters of PE as well as for other materials like Topaz. Actually, this is problematic when performing tomographic reconstruction on the images, especially for inspection of hidden objects. Having an unknown internal structure, the tomographic reconstruction can predict the presence of holes and cavities. To attenuate this problem, we proposed an index matching configuration by introducing the object inside liquid paraffin [200].

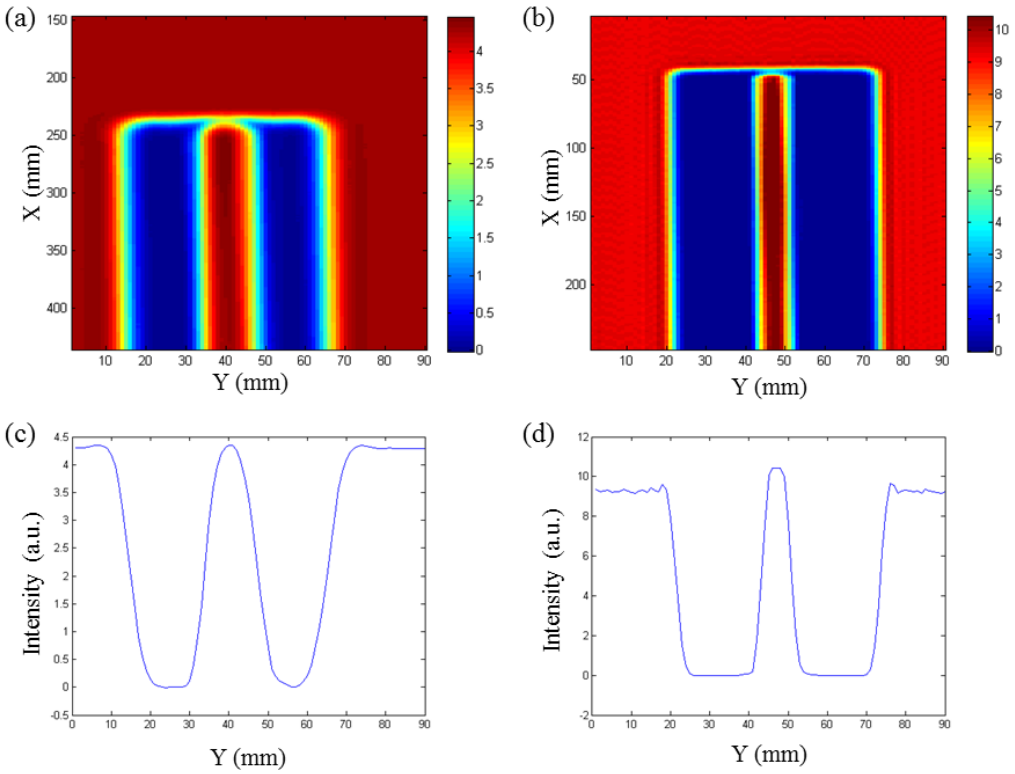

Figure III.13 : MMW images of a polyethylene cylinder of 50 mm diameter, without holes, positioned horizontally, at (a) 84 GHz and (b) 287 GHz; Intensity distribution along Y axes for (c) the 84 GHz image at X= 360 mm and (d) the 287 GHz image at X= 150 mm.

To go further in the inspection of the problem, PE cylinders are imaged using the terahertz time domain setup in transmission, in order to check if the effect varies with higher frequencies. The cylinder tested here has a diameter of 6 mm, smaller than the cylinders tested before due to the XY surface scanning limitations in the TDS system. The cylinder contains no holes.

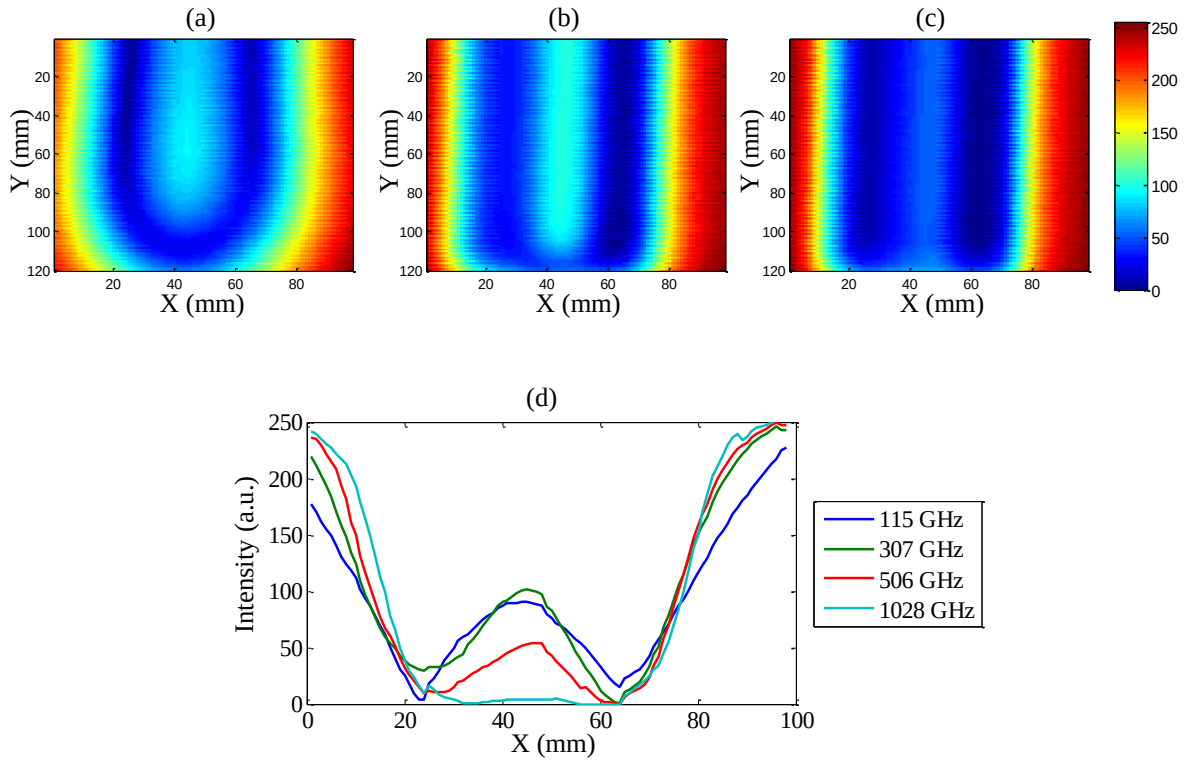

Figure III.14 : Terahertz image obtained from the TDS system in transmission, for a PTFE cylinder of 6 mm diameter, at: 115 GHz (a), 307 GHz (b) and 506 GHz (c), (d) the terahertz signal distribution for four specific frequencies along the band [0.1-3] THz for the position Y=40.

The images are acquired with a step size of 0.5 mm along X and Y axis and the result for four specific frequencies 115 GHz, 307 GHz and 506 GHz are represented in Figure III.14 (a), (b) and (c) respectively. The presence of an intensity variation is identified for the frequencies 115 and 307 GHz. The signal distribution at Y=40 is shown in Figure III.14 (d) for the three mentioned frequencies as well as for 1028 GHz. This plot shows the variation of the holes dimension, it is decreasing when increasing the frequency and disappears after 1028 GHz. This indicates that this effect is not constant for all the frequencies and the size of the area is reduced when the frequency increases. However, the noisy signal between 0 and 200 GHz made confusing the signal intensity distribution between 115 and 307 GHz visualized in Figure III.14 (d).

To quantify the presence of this higher intensity in the center of the cylinder, we developed a goniometer setup where we can quantify the refraction effect and the key role played by the collected lens leading the beam, to the detector. In this setup, the source used is the ‘millitech’ Gunn diode and the detector is the Schottky diodes. The detector is placed on a home-made goniometer and rotated between 180 ° and -180°, leading to the measurement of the intensity value at each angular position around the source. As for the optical configuration, we use four PTFE lenses of 50 mm focal length and the setup performing in transmission is shown in Figure III.15 (a). We chose to characterize

different polymer cylinders varying in diameter and in material such as PE, PTFE and foam. However, the result shown here corresponds to a PE cylinder of 25 mm diameter. Yet, the analysis performed on the other cylinders, gave similar results.

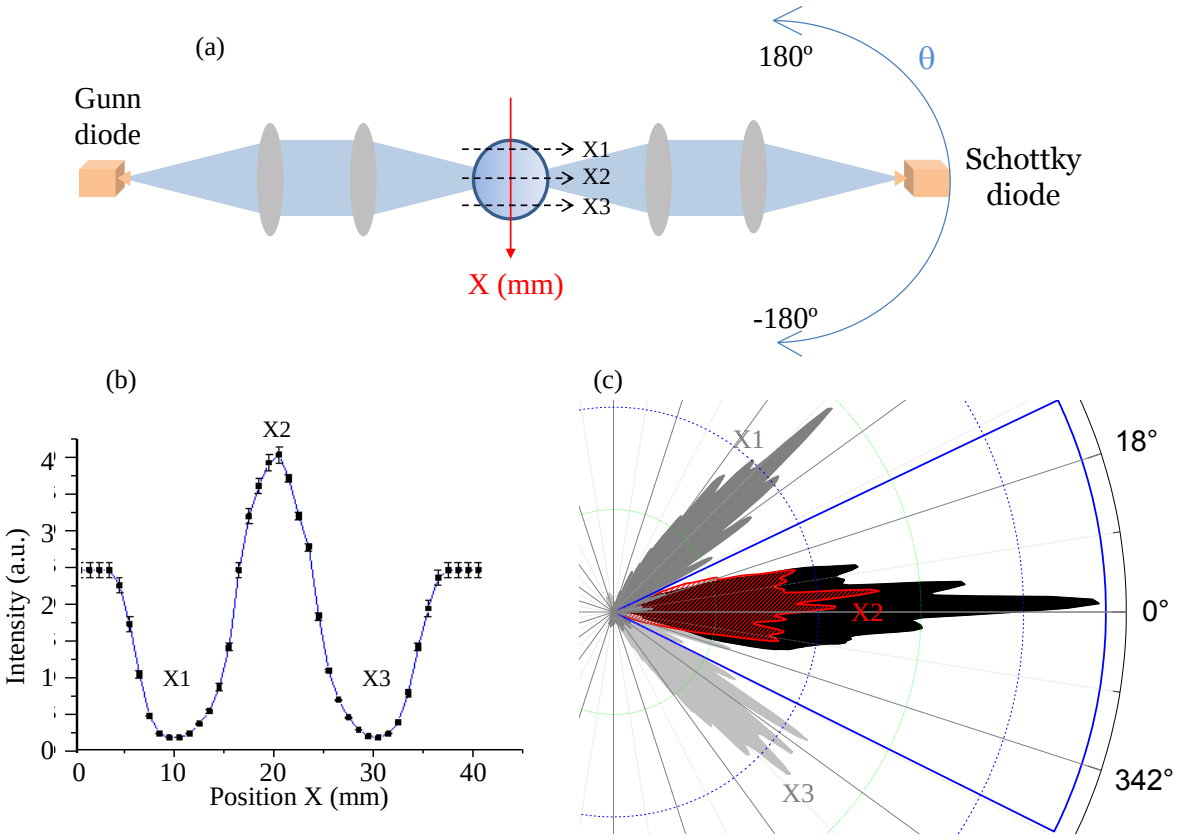

Figure III.15 : (a) Optical configuration of the continuous wave combined to a goniometer, (b) intensity distribution, using the four lenses configuration, when the detector is fixed and the PE cylinder of 25 mm diameter is moving along X axes, (d) intensity angular distribution by removing lenses between the focalization point and the detector, for four cases: without any object (black), center of the cylinder in positioned in the focal point (X2 in red), the focalization is positioned between the center of the cylinder and its border (X1 and X3 in grey) .

First, the intensity propagation of the beam emitted from the source is measured by using the four lenses configuration, keeping the detector fixed and moving the cylinder along X axes. The intensity plot in Figure III.15 (b) represents the intensity values when moving the cylinder from X= 0 mm where it is totally outside the beam, to 10 mm (X1) where the beam crosses a point of the cylinder between the center and the border, to 20 mm (X2) where the beam passes in the center of the cylinder, then to X = 30 mm (X3) where once again the beam passes at a point of the cylinder between the center and the border and finally to X=40 mm where the cylinder is once again outside the beam. The result shows that the intensity value is higher when the beam passes in the center of the cylinder compared to the case where no object is blocking the beam propagation. This highlights the

idea that the transmittance is higher in the cylinder than in the air. Physically, this is not possible. To understand the reason of that, the two lenses between the focal point and the detector, are removed, and the angular intensity distribution is calculated by moving the detector from -180° to 180°. The measurement is performed in three cases: without any object, when the beam passes in the center of the cylinder (X2), and when the beam is in a point between the cylinder center and the edge (X1 and X3). The result presented in Figure III.15 (c) first shows that in X1 and X3 position, the beam is totally deviated from the lenses aperture and thus no beam is detected when the lenses are placed. This is similar to the simulation in Figure III.12 (c) where the entire beam is lost by refraction effect. Another interesting point is that without the lenses, the intensity in the air is higher from the case where the beam passes in cylinder center. This results show that the higher intensity obtained in X2 position in Figure III.15 (b) came from beam steering effect with respect to the detector. In fact, the cylinder is a cylindrical lens; it focuses more the beam and modifies his propagation. So if a misalignment occurs, the presence of the cylinder can correct this issue and leads to obtain higher intensity then in the air. These results demonstrate how the setup misalignment and defocusing can affect the images.

Another artifact revealed in polymer cylinders, it is the interference of the diffracted beams. Diffraction fringes result from the interference of the external edge or near the hole's edge inside the material, it appears only where these two beams overlap. This also leads to a wrong understanding of the image, where the interference points appear as holes. Figure III.16 (a) shows a cylinder with 25.7 mm diameter containing two holes of 10 and 4.4 mm, imaged at 287 GHz. The resulting image presents interference fringes around the real holes. Figure III.16 (b), (c) and (d) represents the intensity distribution along Y axes at X= 76 mm, X= 100 mm and X= 140 mm respectively.

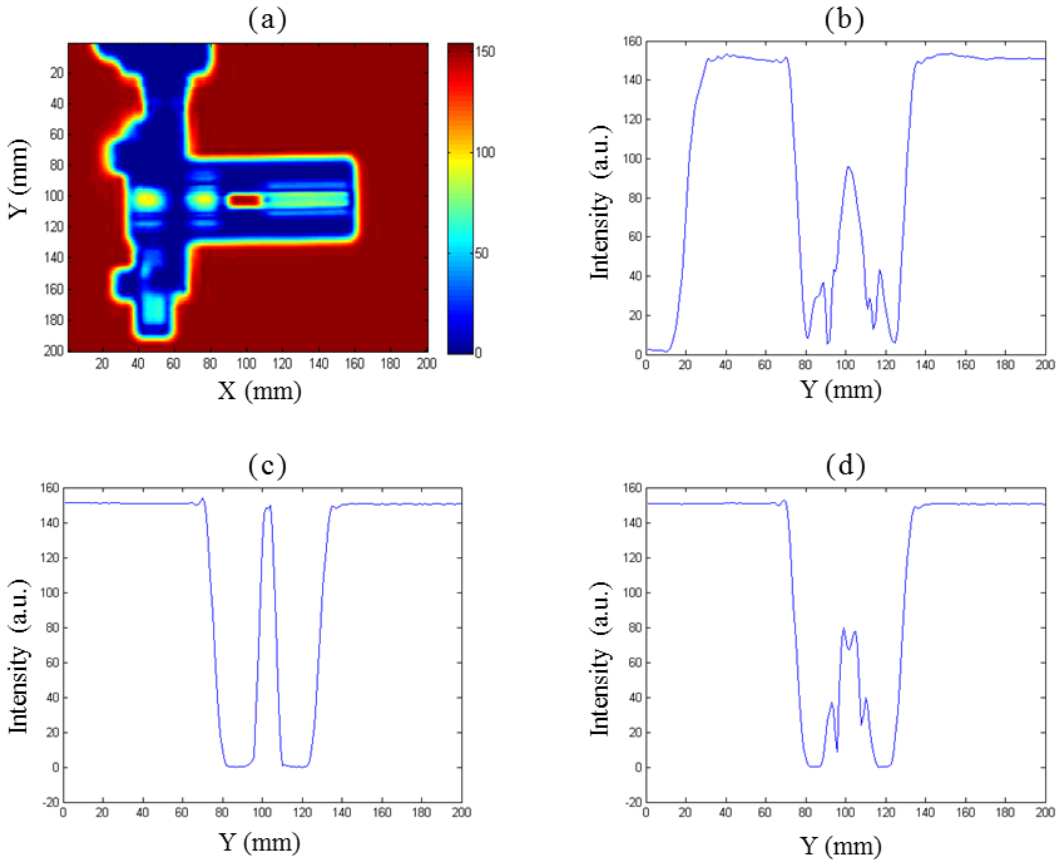

Figure III.16 : (a) MMW images at 287 GHz of a polyethylene cylinder of 25.7 mm diameter, positioned horizontally, representing to hole with different diameters; Intensity distribution along Y axes at (b) X= 76 mm, (c) X= 100 mm and (d) X= 140 mm.

II.7. SYNTHESIS

Finally, we presented a continuous wave imaging setup, able to raster scan samples at two frequencies in transmission and providing intensity measurements at each pixel. With this setup, we described the different artifacts that can occur when dealing with terahertz imaging, especially for specific objects such as cylinders. We demonstrated the problematic of misunderstanding the real structure of an object due to artifacts occurred from the measurements. Moreover, we highlighted the importance of taking this phenomenon into consideration when dealing with tomography reconstruction. Further work will be dedicated to integrate this problem when applying tomographic algorithms.

III. FREQUENCY MODULATED CONTINUOUS WAVE IMAGING

III.1. CONCEPT DESCRIPTION

Frequency-modulated continuous-wave (FMCW) technique was originally investigated in radar science for locating a distant object by means of a reflected radio wave [201] [202]. Contrarily to the continuous wave systems, FMCW has the possibility to provide information on the time delay. By modulating the frequency, the concept of the technique is equivalent to putting a unique "time stamp" on the emitted wave at every instant. First, the frequency is modulated with a triangle waveform by using a voltage-controlled oscillator (VCO), which varies the frequency between a maximum and a minimum value while changing the voltage. Then, the emitted signal is frequency-multiplied and amplified to reach the working frequency. This signal is considered as a reference signal and is emitted by a horn antenna. After being transmitted or reflected by the sample, the signal is detected and mixed with the reference signal using a multiplexer [203]. The mixing produces a beat signal at a frequency f_b, which is directly proportional to the time delay τ, as shown in Figure III.17. This signal contains amplitude and phase information.

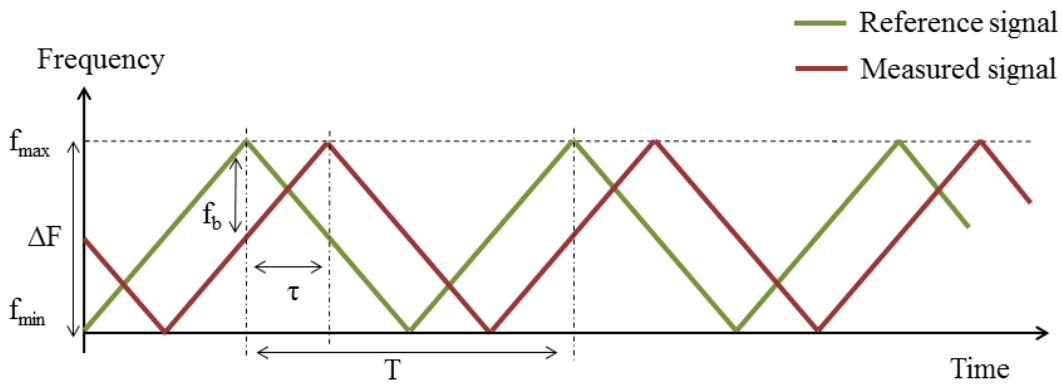

Figure III.17 : Frequency modulation continuous wave concept

The beat frequency f_b depends on the rate of change of frequency (chirp slope). It is constant and equal to the total frequency excursion Δf ($f_{max} - f_{min}$) divided by the period T [204], and given by

$$f_b = \frac{\Delta f}{T}\tau \qquad (44)$$

The second active imaging system used in this study is based on the FMCW technology.

III.2. FMCW SETUP

The FMCW system, provided by SynView technology, combines a XY scanning stage with a frequency modulation technique to acquire 3D millimeter wave data. It uses electronic emitters at the

frequency range 60-110 GHz (SynViewScan 100) and/or 230-320 GHz (SynViewScan 300) with a dynamic signal range of 50 dB. It consists of four heads and motion controller piloting three axes.

The measurements at 100 and 300 GHz are accessible in transmission and reflection mode at the same time. From one side, two heads containing the source and the reflection detectors. From the other side two heads are used for the transmitted wave detection after passing through the object. Photographs of the system, the scheme of the optical configuration as well as photos of the emission and detection heads are presented in Figure III.18.

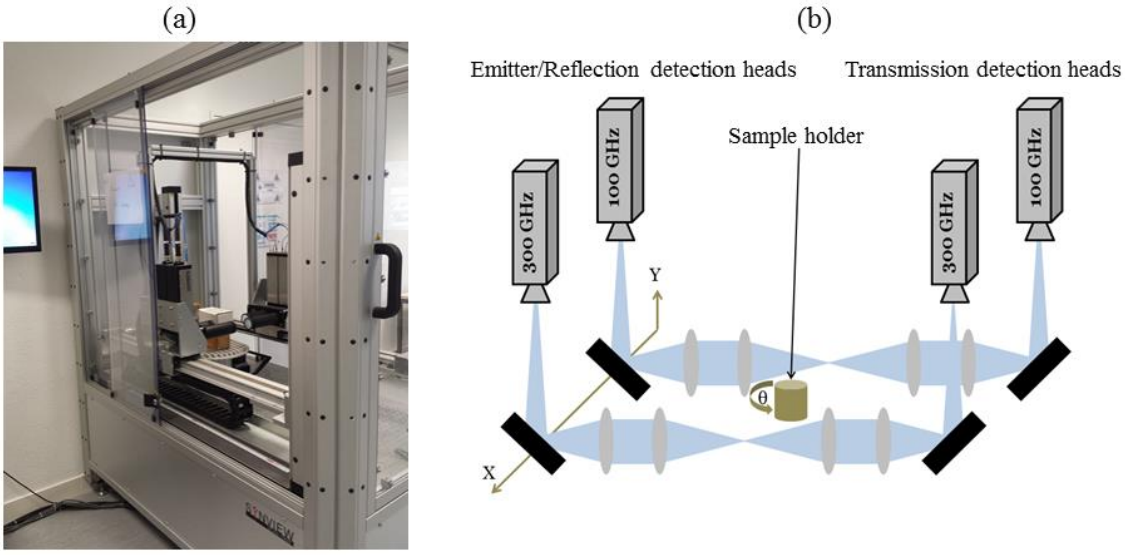

Figure III.18 : (a) SynView entire system photograph, (b) scheme of the setup.

In the actual configuration, the heads are moving along two axes to form a measurement area (X,Y). The sample is fixed on a rotating stage θ that is used to provide projections at different angles for the tomographic reconstruction. The movement at the X stage is continuous, and at the Y stage the step size can be varied from 1 mm to several mm. Before each X line measurement, a calibration process can be made by taking in consideration four particular positions on metallic object: one for zero reflection, and three others for 100 reflections one shifted from the other at z 0 mm, -3 mm and –10 mm (z-direction being the direction parallel to the wave propagation and through it is obtained the depth information). The optics used in the system are Teflon lenses with 50, 100 or 200 mm focal length. The theoretical beam waist calculations made for a focal length of 50 mm, presented in Figure III.7, are 1.9 mm at 100 GHz and 0.7 mm at 300 GHz. The experimental resolution of the Synview system is operated with the same way as the CW setup, using the USAF target. The resolution in this configuration is similar to the CW setup with a value of 2.5 mm.

The measured information on the images, obtained by the system, represents the intensity *I* at each pixel, which is proportional to the product of the electric field with his complex composition.

Being frequency modulated, the SynView system has a big advantage in our study. It has the possibility to access the amplitude and the phase of the reflected and transmitted wave, and allows obtaining the information in depth about the object by measuring the time-of-flight. By propagating in depth, going from outside to inside the parcel along the beam direction (z-direction), it is possible to get 2D projections for every slice. The obtained images represent the value of the electric field intensity transmitted or reflected by the sample. Moreover, this technique allows fast scanning, so a surface of 10×10 cm^2 is imaged in approximately two minutes. It can be considered as close to real time measurement as Fabien Frederich *et al.* presented in [205]. By using several transmitters and receivers, they were able to measure a 7.5×7.5 cm object in 200 ms.

Figure III.19 explains visually the potential of the FMCW technique in parcel inspection. It allows obtaining in real time an image at different (X,Y) plane along z axis. In Figure III.19, a parcel containing the ceramic gun made by 3D printer and a ceramic knife are imaged. Six (X,Y) projections are shown; they allow inspection of the parcel at different depth position. The highest dynamic range is obtained in the fourth image, at the central position of the parcel and the two objects. This is also a way to obtain an approximate idea about the dimension of each object inside the parcel. By extracting one cross section, projection at (X,Z) plane, it is possible to estimate the dimension of the object along the X axis. However, for precise measurements, the tomography algorithm developed by our group, is able to quantify the distances and gives the thickness of the samples.

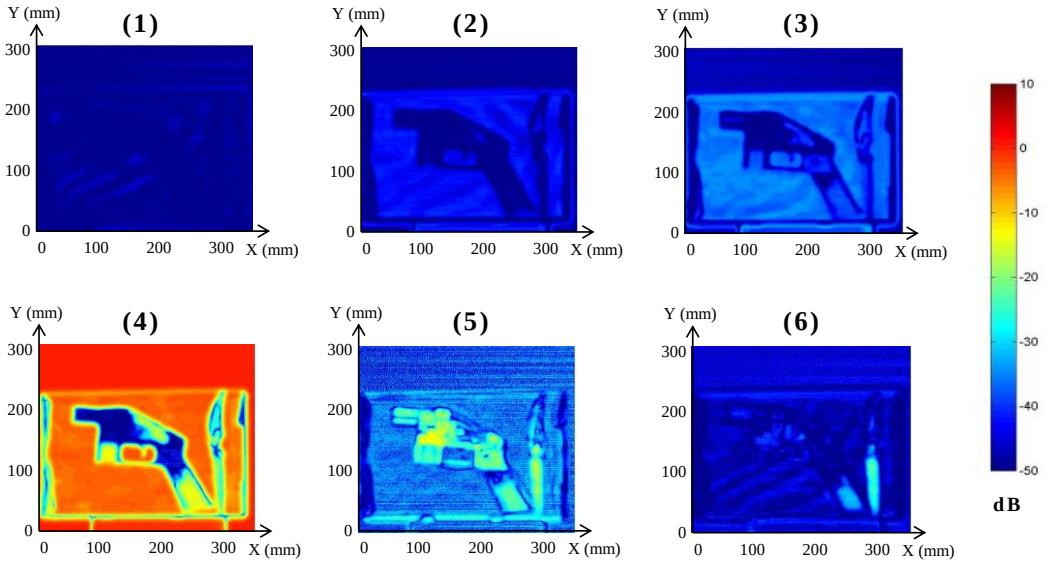

Figure III.19 : Images obtained at 100 GHz at different time of flight (1) z=-117 mm, (2) z=-104 mm, (3) z=-78 mm, (4) z=0 mm, (5) z=26 mm, (6) z= 52 mm.

III.3. IMAGING RESULTS

The main advantage of the SynView system is the real time imaging due to one acquisition speed; the scan is faster compared to the CW setup, which reduces the measurement time and provide

scans of larger parcels. Figure III.20 presents four different parcels with different content imaged at both frequencies in transmission mode. Two different metallic guns are imaged, in Figure III.20 (a) the gun and the bullets are identified, however, the positioning of object near to the edge creates confusions, in Figure III.20 (b) even when disassembled, the gun is recognized and each part of it, even the plastic is discerned. In Figure III.20 (d), the gun is concealed with other metallic object and the metallic tool is hidden in two packages. This wasn't a limitation to identify the shape of the objects even through four layers of parcels. An example of the imaging results with the head 100 is presented in Figure III.20 (c). Even with a lower resolution compared to the frequency of the head 300, this frequency is able to give pertinent results in parcels investigation. The MMW is able to recognize the content of the parcel containing two ceramic and metallic knifes, wrapped and placed in their packaging.

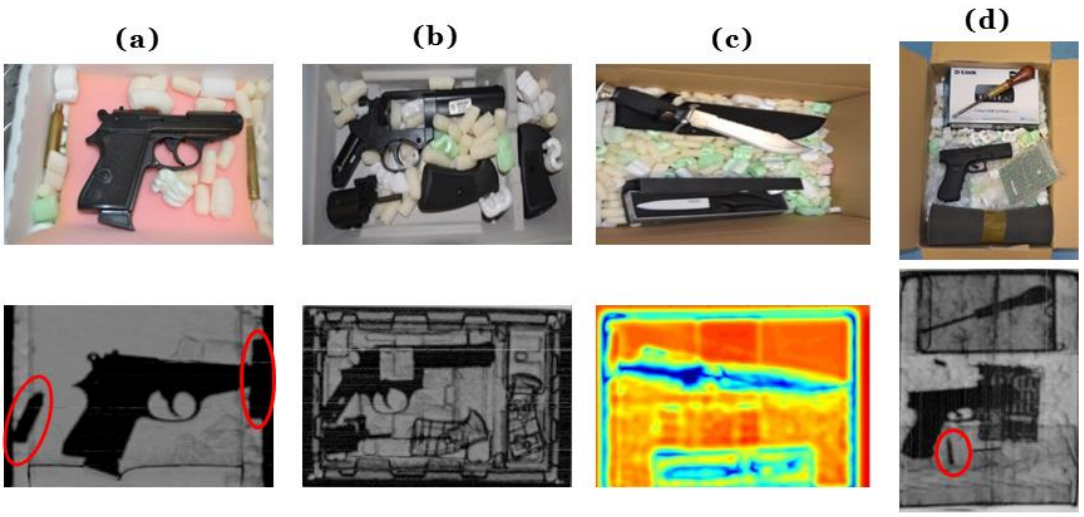

Figure III.20 : Transmission image of (a) metallic gun and bullets at 300 GHz, (b) disassembled gun at 300 GHz, (c) metallic gun and knife, hidden in different types and size of parcels, at 100 GHz, (d) metallic gun concealed by tools at 300 GHz.

A second series of examples is shown in Figure III.21. These objects were scanned with the passive system and the results did not provide recognition of the objects inside the parcel. In Figure III.21 (a), six different powders are imaged through a 15 cm large parcel. Though the chemical constitution is not determined at this narrowed frequency bandwidth, it is possible to identify the presence of the six powders even with this small quantity (few mg). Figure III.21 (b) present a plastic bottle of water, a glass bottle of wine and some medicine. Also here, no chemical identification of the content is possible. However, the liquid content is differentiable from the other part of the bottle in the case of plastic. In the case of glass bottle, the material is very absorbent which makes it appears similar to its liquid content. For the measurements made with the 300 THz, a comparison between reflection and transmission images is presented in Figure III.21 (c) and (d). An envelope containing several objects such as medicine, powder, soap, correction fluid, a piece of wood and a piece of metal

are imaged. Transmission mode gives better accuracy in objects recognition, especially for powders placed in a plastic bag as well as in reflection mode, the reflected signal can be lost by the diffraction on the objects surface.

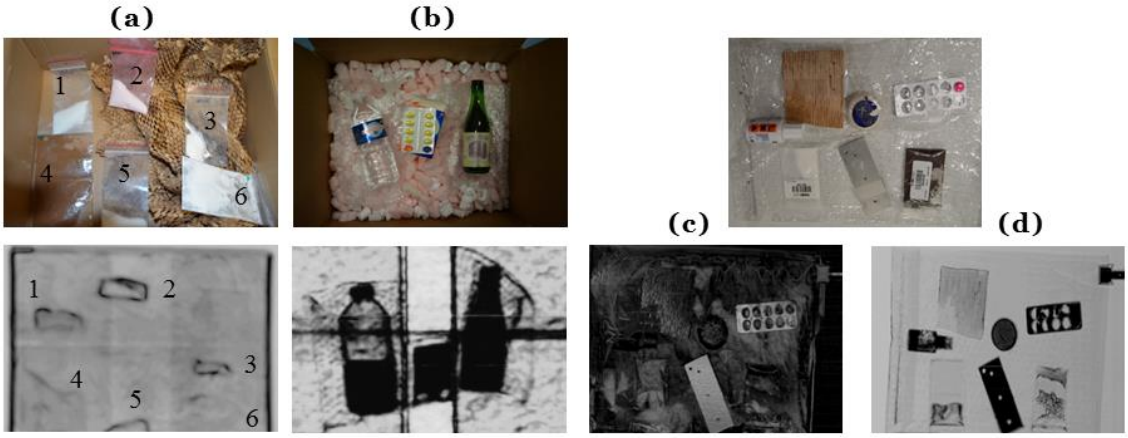

Figure III.21 : Photographs and millimeter images at 300 GHz in transmission mode of packaging containing (a) different type of powders, (b) plastic and glass bottles filled with different type of liquids. Photograph and MMW images of an envelope containing several object such medicines, powders, soap, etc., at 300 GHz in (c) reflection and (d) transmission mode.

In order to obtain additional information on the imaged sample at the same time, we applied image fusion algorithm on images at both frequencies in reflection and transmission modes. Figure III.22 (a), (b) and (c) presents a comparison between the results obtained at 100 GHz in transmission mode and 300 GHz in transmission and reflection modes respectively, for the same object, the ceramic gun. By looking to the image separately, the information about the object is not complete. The image at 100 GHz (Figure III.22 (a)) presents a blurring effect that prevents recognition of the precise external shape. The 300 GHz image (Figure III.22 (b)) in transmission allows a representation of the exact shape of the object with good resolution; however, the transmission information through the object is not understood. As for the 300 GHz image in reflection mode (Figure III.22 (c)), part of the object is missing in the image due to the beam reflection on the cylindrical objects that prevents the detection of the signal. By combining each two images, we are able to reveal additional complete information in one image. Figure III.22 (d) is the fusion of (a) with (b), Figure III.22 (e) is the fusion of (a) with (c) and Figure III.22 (f) is the combination of (b) with (c). The combination in Figure III.22 (d) is conserved the exact extremal shape of the object but could not extract the correct transmission information. The fusion in Figure III.22 (f) was able to correct the missing part of the object. However, the most successful combination is obtained in Figure III.22 (e) where the external correct shape is conserved, the transmission information is correct and the cavities are revealed. This analysis is just a simple demonstration of the importance of image fusion. And in our case, the accuracy of combining the 100 GHz transmission image with the 300 GHz reflection is the best for identification of the ceramic gun.

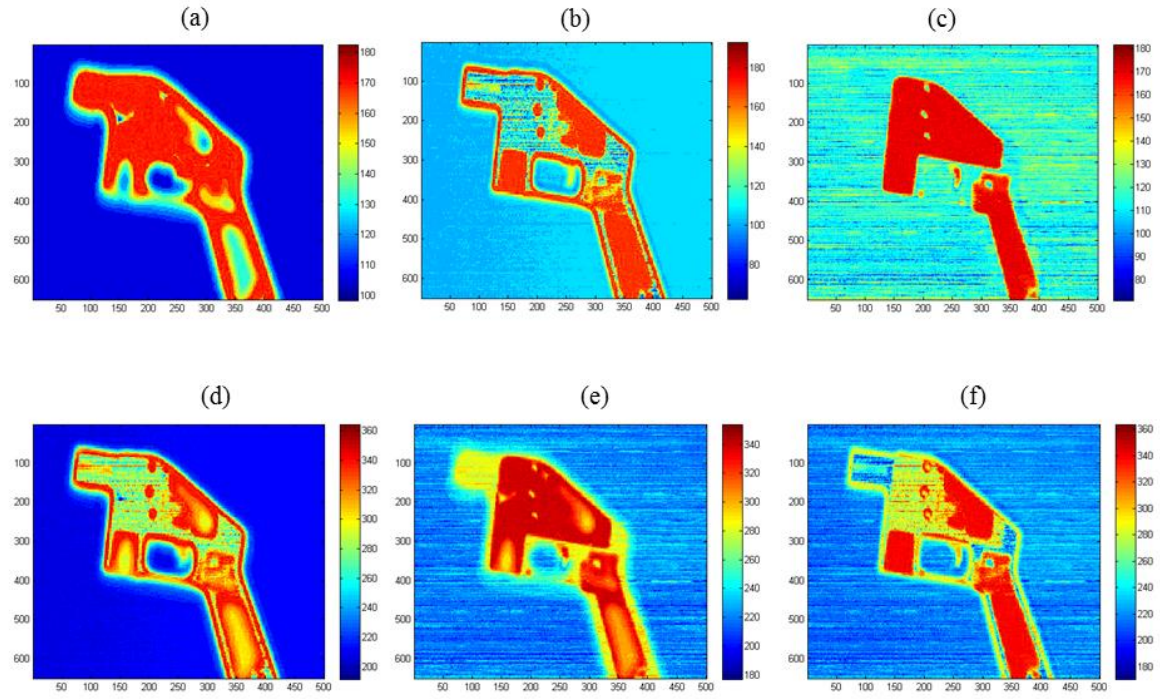

Figure III.22 : MMW images obtained by the SynView system in transmission mode at (a) 100 GHz and (b) 300 GHz, and (c) in reflection mode at 300 GHz, the combined image of (d) the 100 GHz with the 300 GHz in transmission, (e) the 100 GHz with the 300 in reflection, (d) the 300 in transmission with the 300 in reflection.

III.4. SYNTHESIS

Finally, we presented the FMCW concept and his advantages in performing fast raster scanning. The used system provides intensity images at two frequencies in reflection and transmission modes. This setup presents the best accuracy for parcel inspection among the three techniques introduced in this chapter. It provides fast scanning with good resolution able to identify object through parcels of tens of centimeters thickness. Image fusion method showed the possibility of using such a system to generate various images at different frequencies in several configurations, and combines it to reveal in one image various information about the inspected sample. Yet, no chemical signature can be obtained.

IV. TERAHERTZ COMPUTED TOMOGRAPHY

IV.1. INTRODUCTION TO COMPUTED TOMOGRAPHY

Electromagnetic waves such as X-ray and terahertz are able to pass through several types of materials. While traversing the object, the wave is attenuated proportional to the material properties. Computed tomography (CT) is an imaging technique that consists of reconstructing the volume of an object using a series of measurements performed from the outside of the object, by taking into account

the superposition of the wave when traversing all the materials to form the resulting image. Each voxel of the volume is given a number that is proportional to the attenuation of the X-ray waves by the object, depending on the material properties. The transmitted beam at each angle corresponds to the sum of the attenuation values of all materials traversed by the collimated beam. For X-ray CT, several configurations are possible, where the source and detectors are moving around the sample, or where the sample is rotated between the emitter and the receiver. In an X-ray scanner, a 2D section of the object is acquired by measuring the attenuated rays at different angles as shown in Figure III.23 (a). For each angle, this attenuation represents a projection of the object, that is to say a 1D radiograph of the traversed material. One method of retro-projection consists of combining the set of the entire X-rays, which allows the reconstruction of the 2D section of the object. Then the final 3D image is obtained by stacking together all the cross-sectional images. The most widely used algorithm to reconstruct these measured data is based on the inverse Radon transform, usually applied with special filters in the frequency range for image enhancement [206]. This stabilized transform is called BFP, which is invented by Bracewell and Riddle in 1967 [207]. The BFP algorithm uses Fourier theory to arrive at a closed form solution to the problem of finding the linear attenuation coefficient at various points in the cross section of an object. The fundamental result linking Fourier transforms to cross-sectional images of an object is the Fourier slice theorem [208]. The radon transform a 2D function *f(x,y)* into 1D projection along an angle θ as follow:

$$P_\theta(t) = \int\int f(x,y)[\,\delta\,(xcos\theta + ysin\theta - t)]\;dx\,dy \tag{45}$$

where θ and t are the angular and radial coordinates of the projection line (θ,t) and δ is the Dirac impulse. The function $P_\theta(t)$, which is the Radon transform of the 2D object, represents the attenuated sum of all points traversed by the line and corresponds to the theoretical attenuation of the radiation into the matter along this line. As the parameters t and θ vary, the function $P_\theta(t)$ provides a 2D image referred as the "Sinogram" of the corresponding cross section of the sample.

Initially, tomography started to be developed and used for X-ray medical scanners and recently, it is spread and is used in other domains like terahertz. X-ray CT is less efficient for materials with low absorption of X-ray frequencies such as polymers, plastic, papers. However, THz waves have the potential in analyzing such materials. Thus, to go further in THz imaging, and obtain volume inspection of the sample instead of 2D images, the same concept of X-ray CT is applied to the terahertz waves. Yet, for THz wave, the beam is not collimated. As shows Figure III.23 (b), the propagation of a terahertz waves is considered as Gaussian beam propagation, and the beam is collimated only in the Rayleigh zone. Thus, depending on the setup optical configuration and parameters, the limitation of the thickness of the object to be imaged is defined.

The most used THz tomography setups have their source and detector fixed and the sample is rotated. The acquisition gives access to 2D projections with (X,Y,θ) data. By applying CT, the data will be expressed by (X,Y,Z) information, which corresponds to the volume of the object. To perform tomography, the sample is first raster scanned along the *x* and *y* directions with a step size of 0.5 mm, to form a 2D image. Then, the sample is rotated using the rotational stage and an (X,Y) raster scan is performed to finally obtain a 2D image at each angle position, from 0 to 180°. This provides a

sinogram that represents a section in depth for the entire angles, at each Y position as shown in Figure III.23 (c). The acquisition time depends upon the sample dimensions, the step size and the number of points taken in the temporal domain. Approximatively, 10 to 15 min are needed for one 2D projection, thus the acquisition time will be equal to the time of one 2D image acquisition, multiplied by the number of angles. The complete 3D object structure is reconstructed by stacking all the sinograms at all the Y positons.

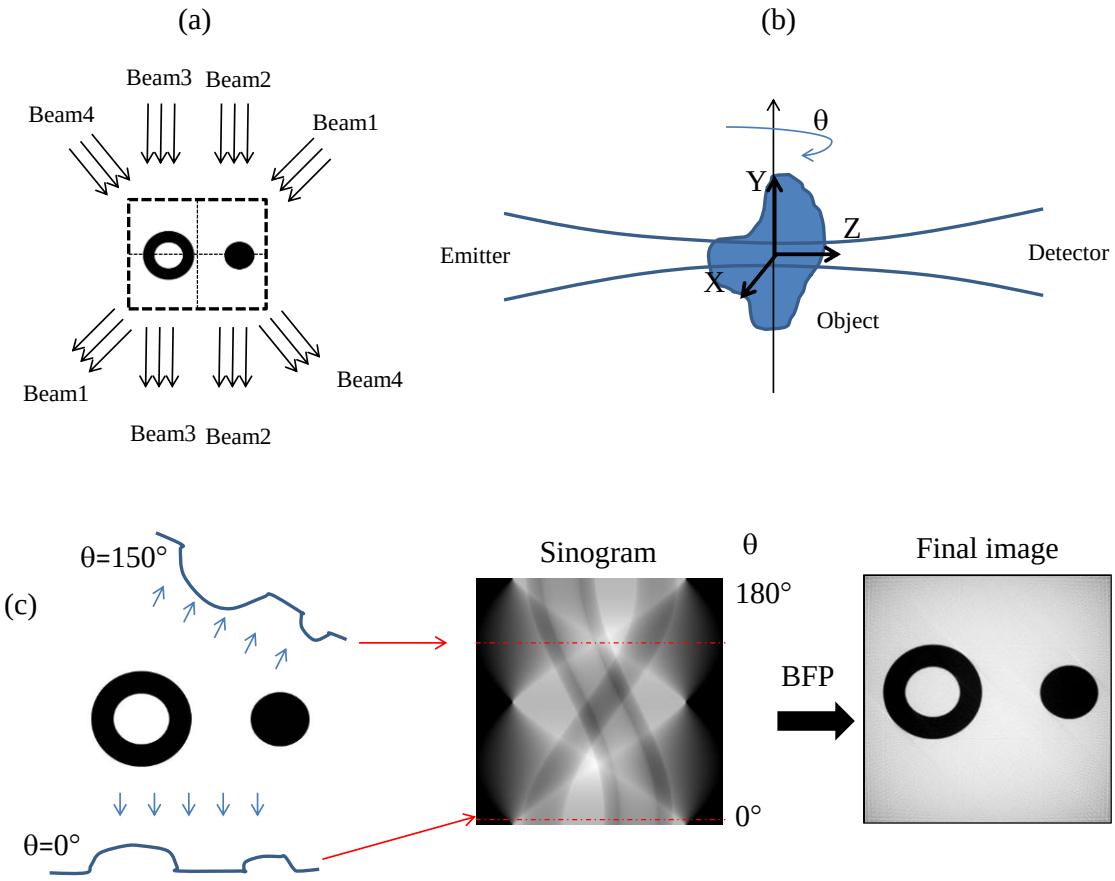

Figure III.23: Schematic representation of the CT concept in X-ray (a) and terahertz (b) domains. Horizontal slice, sinogram, and the final reconstructed cross-sectional image by BFP algorithm, at one Y position of the (X,Y) image, for a sample consisted of two cylindrical bars.

IV.2. ITERATIVE ALGORITHMS FOR CW TERAHERTZ TOMOGRAPHY

Whatever is the used imaging modality and the mathematical algorithm used for reconstruction, a tomography process is decomposed into three different phases. The first one describes the model acquisition parameters obtained from the physical series of measurements. The second phase shows the way of reconstructing the volume of the acquired data. The third part consists of an image processing process for 3D volume visualization such as rendering. The schematic representation of the entire process is shown in Figure III.24 (a).

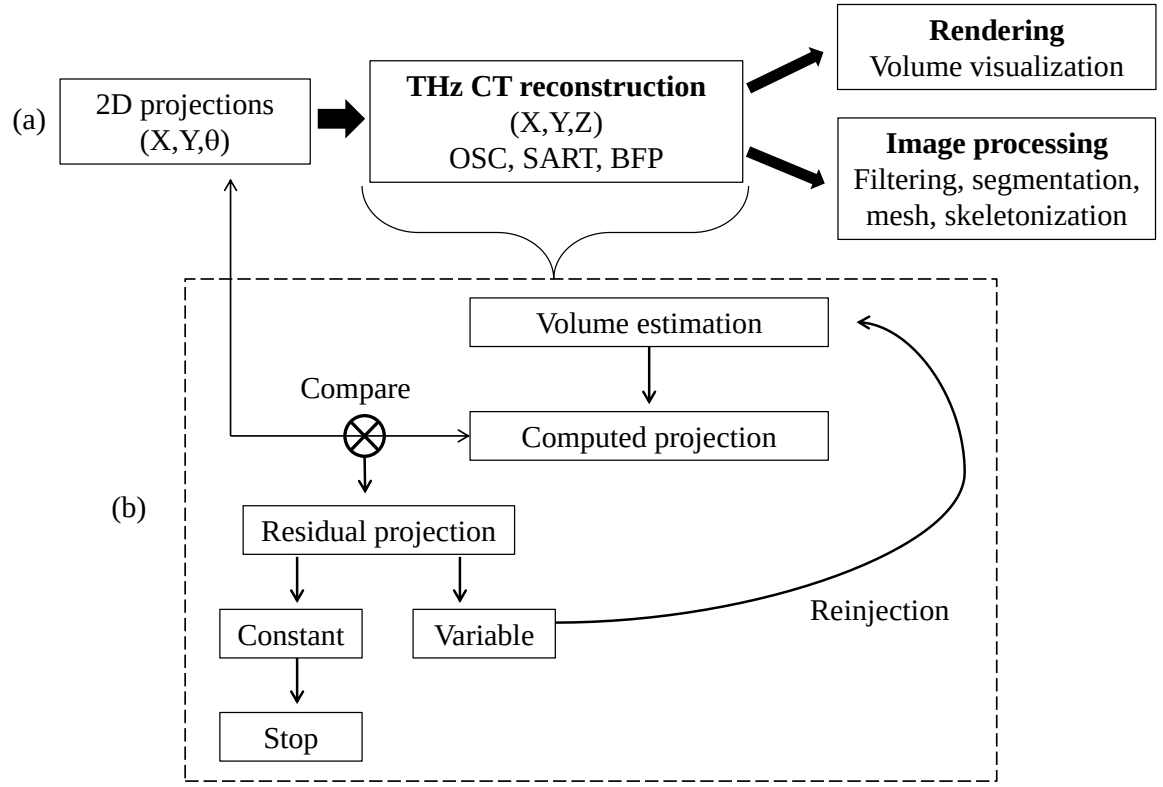

Figure III.24 : (a) Procedure of information extraction by CT in terahertz, (b) organigram of the iterative CT concept.

Several THz CT techniques have been developed based on different mathematical calculations in order to exploit the high transparency of non-polar, non-metallic materials in the THz range [209] [210]. Each of the techniques needs special algorithm of reconstruction, and some are able to maintain the spectroscopic information about the sample [211]. B. Recur *et al.* discussed the potential of three different reconstruction methods, used initially for X-Ray CT, in the reconstruction of large size 3D objects imaged with THz continuous wave system [212]. These methods are: back-projection of the filtered projections (BFP), Simultaneous Algebraic Reconstruction Technique (SART) and Ordered Subsets Expectation Maximization (OSEM). SART and OSEM are two iterative methods where the Gaussian approximation of the beam can be considered. They take into consideration the absorption information and allow reducing the acquisition time by reducing the projection number, without noticeable quality and accuracy losses. In 2012, Recur *et al.* compared the efficiency of the three methods: THz-SART, BFP and Maximum Likelihood for TRansmission tomography (ML-TR) also named Ordered Subsets Convex (OSC) [213].

The computing organigram of an iterative process is shown in Figure III.24 (b). The principal of this process consists of iterating in order to update each voxel of the volume until convergence of the solution and the pixel correction is done according to the error measured between an initial

sinogram and the one recomputed from the image for the previous iteration. So first the volume is estimated, and then a simulation of a real acquisition is made by taking into consideration the Gaussian beam propagation. This is compared to a projection obtain from the acquisition and the residual error is calculated and injected in the estimated volume. The process continues until getting a stable residual error. The advantages of having an iterative process are:

1- These processes are less sensitive to noise, which induce noise reduction in the reconstructed volume,
2- They are more efficient when dealing with less projection used for reconstruction,
3- They allow simulating more realistic acquisition, where the Gaussian beam propagation is taken into consideration.

The comparison results between BFP, SART and ML-TR are shown in Figure III.25 using a head-spray sample made with plastic. The acquisition is made with the CW setup at 287 GHz, with a step size of 1 mm, using 36 projections and the cross-sections are represented for different y positions along the image, corresponding to y=15, 30, 45, 60, 75 and 90 when going from left to right in Figure III.25. The BFP algorithm does not provide real and right information about the outer shape of the object. Though, the SART method is less dramatic and reveals partial information about the external form of the sample, while the ML-TR method allows 3D visualization without noise or artifacts. However, the ML-TR result in (d) present holes in the sample. These holes are not physically real and represent artifacts caused by the imaging setup, which induces limitations on the reconstruction algorithm. This experimental issue is due to the low absorption of these regions that makes their intensity mingled with the region of the maximum transmitted signal. The rendering shows better efficiency with the ML-TR algorithm obtained without any preprocessing applied to remove artifacts [214].

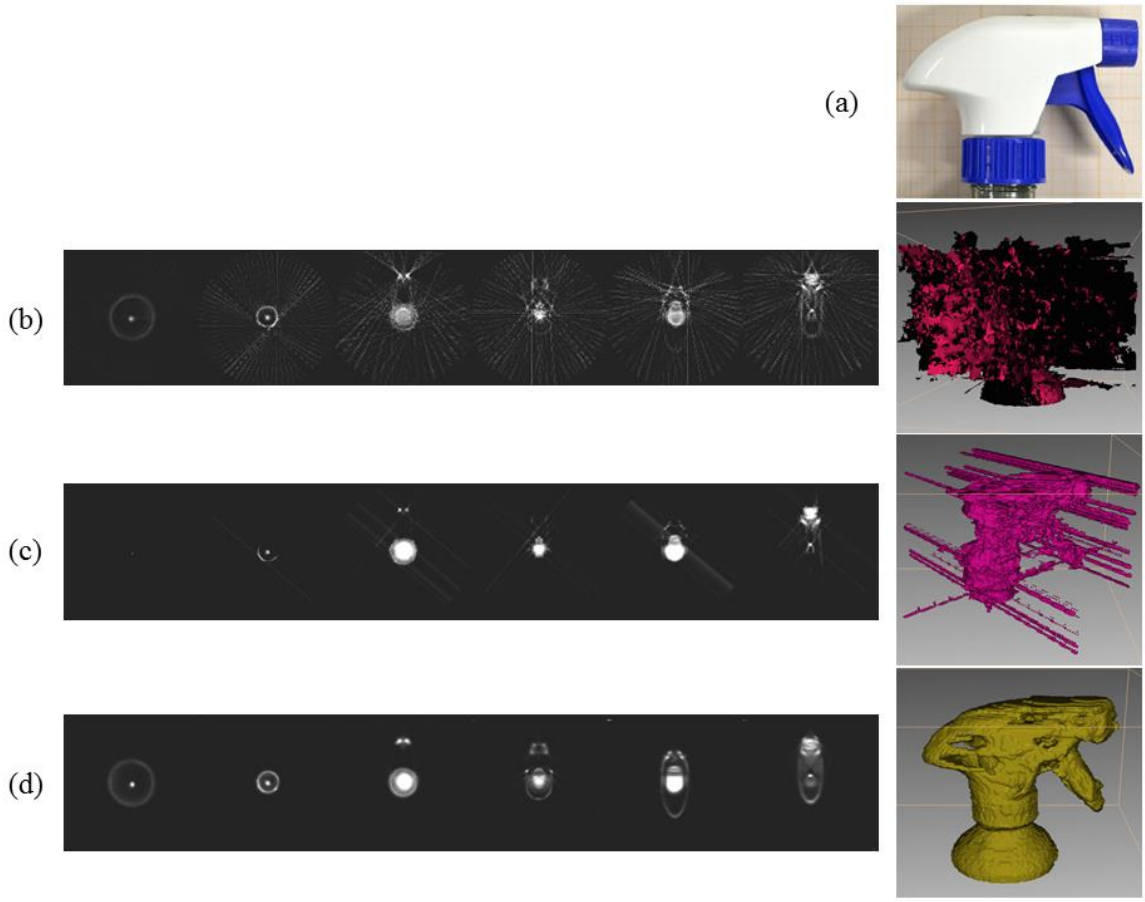

Figure III.25 : (a) Photograph of the sample, cross section along Y direction and 3D visualization using (b) BFP (c) SART (d) THz ML-TR without Gaussian beam approximation. The cross-sections corresponds, from left to right to y=15, 30, 45, 60, 75 and 90.

IV.3. OSC RECONSTRUCTION APPLIED FOR PARCELS INSPECTION

The Ordered Subsets Convex reconstruction is applied on each of the three imaging setups used in this study. The first setup is the passive millimeter wave system presented in section I of this chapter. Here, a parcel containing a metallic gun and metallic knife covered by foam was selected. Figure III.26 (a) shows the most interesting 2D projections obtained during the acquisition while the sample was rotated. When the object was facing the camera (0°), we obtained a global identification of the content of the parcel. At the opposite, from 60° to 120° it was really hard to recognize the hidden items, and especially at 90° where all the items were visualized as rectangular shapes. Applying the tomographic reconstruction made possible the 3D visualization of the items without need to select any projection. Figure III.26 (b) shows a reconstructed volume based on the OSC algorithm, and displayed in false color. Three objects were revealed in this image: a gun, a knife and a metallic part of a holder. However, for some object like the knife in this case, we observed that the external dimensions measured on the reconstructed 3D volumes were not identical to the actual ones. This problem was due to a small shift of the reference in the 2D images recorded at each angle, caused by the vibration of the mirror of the system. The reconstructed image presented here is given

by a series of unprocessed 2D projections, but further works will be based on processing the series of 2D images prior to the 3D reconstruction in order to improve the image quality.

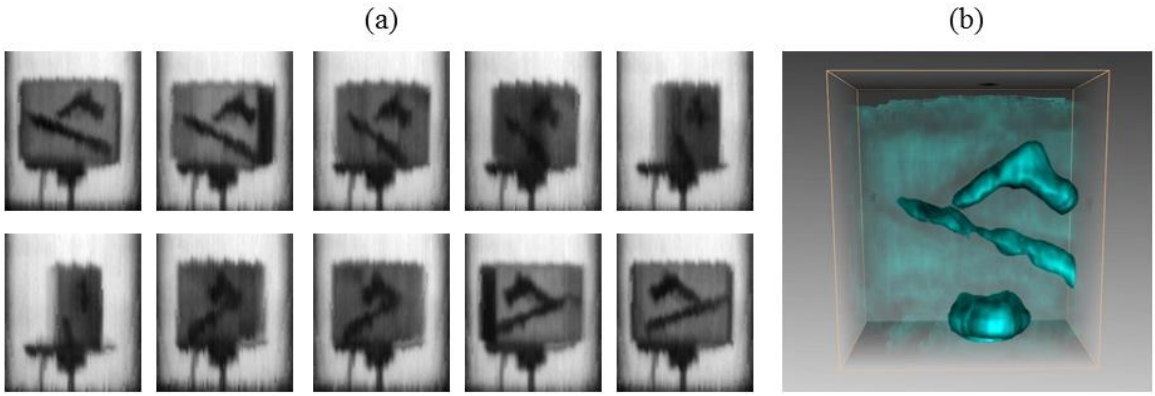

Figure III.26: (a) PMMW images of metallic gun and knife inside parcel at different projection angles, (b) tomographic reconstruction using OSC algorithm.

The second setup is the CW used to image the plastic gun without a parcel. In fact, the CW setup configuration limits the size of the scanned object to a maximum of 20 cm. This prevents the possibility of imaging the plastic gun when it is inside a package. Figure III.27 (a) and (b) present one 2D projection of the gun at 0° for the frequencies 84 and 287 GHz, respectively. Figure III.27 (c) and (d) shows the OSC reconstruction of the liberator gun at 84 GHz and 287 GHz, respectively. Here, the reconstructions are performed using 36 projections from the CW system at both frequencies. Also, Figure III.27 (e) and (f) present a section of both reconstructed volumes, at 84 and 287 GHz, respectively. Each of these two frequencies brings different information. The reconstruction at 84 GHz does not adduce the complete external shape of the gun. This problem is related to the resolution limitation in the setup, also to the diffraction and scattering limitations. As for the reconstruction at 287 GHz, the external shape is correctly extracted, yet the cavities are less well represented compared to the reconstructed volume at 84 GHz.

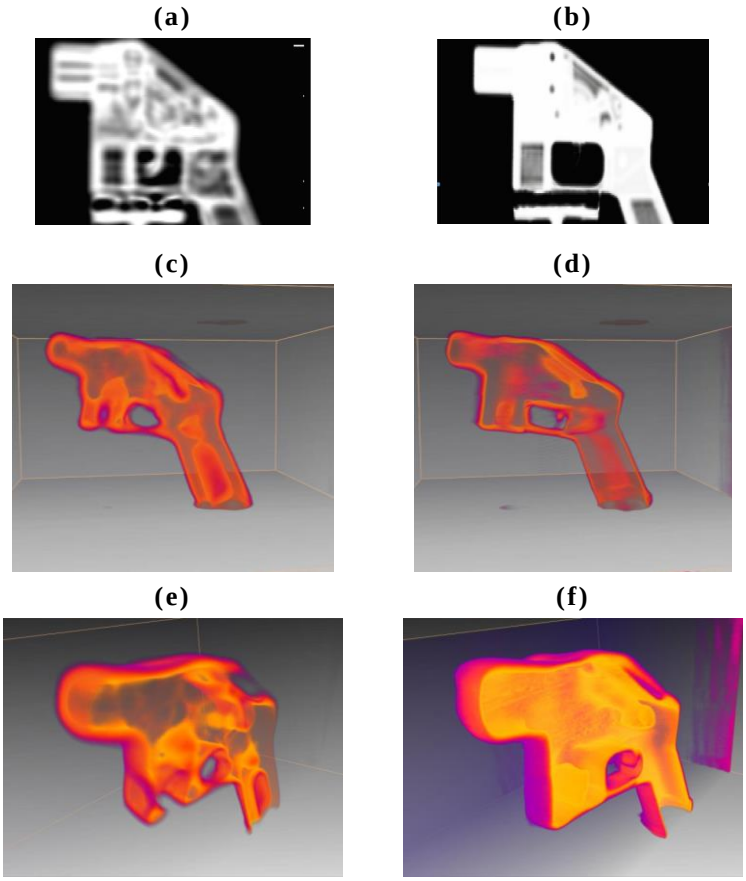

Figure III.27 : Projection of the liberator gun at 0° at (a) 84 GHz and (b) 287 GHz, OSC reconstruction of the liberator gun at (c) 84 GHz and (d) 287 GHz, transverse section of the OSC reconstruction of the gun at (e) 84 GHz and (f) 287 GHz.

The third system, the FMCW, is used to image the plastic gun when placed inside a parcel and covered by foam. The acquisition is made in the transmission configuration of the head T300, with a step size of 1 mm. Four projections are represented in Figure III.28 (a), (b), (c) and (d), corresponding to the angle 0°, 70°, 85° and 130°, respectively. The OSC tomographic reconstruction is applied to the parcel and its content, using 36 projections and the result is presented in Figure III.28 (e).

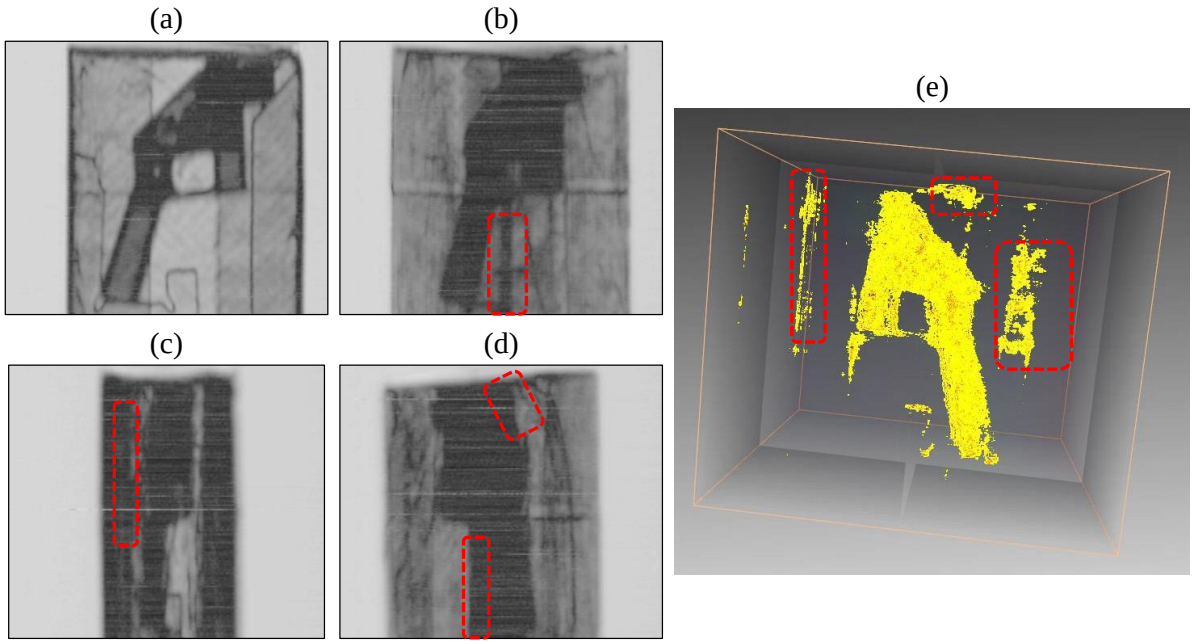

Figure III.28 : 2D projections of the plastic gun inside a parcel, scanned with the head T300 of the Synview system at (a) 0°, (b) 70°, (c) 85° and (d) 130°, (e) OSC reconstruction of the plastic gun inside a parcel using 36 projections.

In this reconstruction, some parts of the object are lost. In fact, the parcel edges highlighted in red in Figure III.28 (b), (c) and (d), imply a damaging effect on the reconstruction. This is visualized on the reconstructed volume shown in Figure III.28, where the zones highlighted in red result from the presence of intensity values of the edges in the 2D images. Also, some parts of the gun are smashed because of these edges that are obscuring some information related to the sample. In addition, the barrel piece is totally missed due to the artifacts of cylindrical objects.

IV.4. SEGMENTATION OF THE RECONSTRUCTED VOLUME

For additional dimension measurements, segmentation methods are applied to the OSC reconstruction. This segmentation is realized using new codes developed in our group which performs processing sequences to analyze 3D THz images [215]. The main interest in applying segmentation is to extract different VOIs from the reconstructed volume that reveal several materials in the sample. Also, it is used to measure the volume or surface characteristics of each VOI which can help to determine in precision the nature of the object under investigation. Segmentation is performed directly from the reconstructed images, without any preprocessing or pre-filtering because, even if they give better 3D visualization, they can reduce or erase important data. An example of the segmentation and rendering results for a mango fruit is shown in Figure III.29, where the different VOI regions are presented in different colors. This figure also shows the picture of the object, the 36 projections used for the OSC reconstruction. The acquisition is made with the CW setup at 287 GHz, with a step size of 0.5 mm using 36 projections.

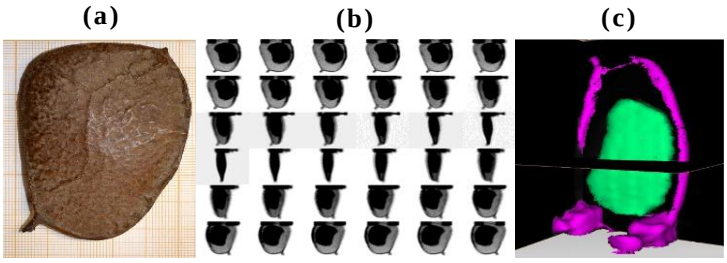

Figure III.29 : (a) Photograph, (b) radiographs and (c) 3D visualization after rendering and segmentation applied to OSC reconstruction of a mango fruit.

The result shows two components for the mango; there is the outer part and the inner seed in purple and green respectively. In addition, the processing used, provides quantitative information about the samples, like the surface and volume of each VOI. The quantification results for these two samples are presented in Table III.3.

Table III.3 : Quantitative characteristics of the plastic mango after segmentation and rendering processing.

Sample	Area (cm^2)	Volume (cm^3)
Mango outer part	23.67	1.83
Mango inner part	32.80	2.35

This segmentation procedure can be very helpful when inspecting parcels. It can reveal the various content of the package as different VOI and give the exact dimension of each region. This can help to define the rate of risk of a dangerous object in a parcel by knowing their dimensions.

IV.5. SYNTHESIS

The potential of the tomographic reconstruction in the THz security applications is in the recognition of the internal content of parcels. As for the X-ray reconstructions, T-Rays showed successful ability in tomographic reconstruction of several object and it is very essential in the case when the simple projections are not able to recognize the object. For parcels inspection, the comparison of the three setups demonstrates the potential of terahertz waves in performing 3D visualization of the internal content of the parcel. Moreover, after applying the OSC reconstruction, the rendering and the segmentation, a separation of the VOI leads to the recognition of several objects placed inside the parcels as well as their dimension.

CONCLUSION

In this chapter we presented three different imaging techniques and the tomography reconstruction possible in this domain. The results are shown for parcels inspection application. Yet, the choice of the technology and the frequency depends on the need: acquisition time, resolution, power, penetration, etc.

The accuracy of the passive imaging is not the best between the three systems, and cannot be trusted for complex parcels. However, it is fast and easy to establish in public places. It is more adequate for body screening than for parcels inspection.

As for the active imaging, both show good accuracy and robust results in parcel inspection. The CW setup is presented for two different frequencies in transmission mode. The 84 GHz have a higher power and can penetrate thicker parcels compared to the 287 GHz. Also it has a larger Rayleigh zone that allows imaging into a larger thickness. However, the resolution is better for the 287 GHz and is more compatible with small parcels containing tiny details that should be recognized.

On the other hand, the resolution of the SynView setup is better than the CW, and has additional advantages. By using the FMCW technique, it is possible to access time-of-flight and phase information thus the ability to image in real time different depth positions inside the parcel. For this setup, the T300 head in transmission mode showed the best accuracy for parcels screening. Moreover, we showed that the combination of frequencies and modes is the ideal way for visualization various type of information in the same image.

Nevertheless, these three technologies cannot be used in security applications only by using 2D projections. As demonstrated, one projection isn't sufficient for identification of all threats. Also, the interpretation of several 2D projections is difficult to be made by human. Thus, the need of applying tomographic reconstruction on these technologies to provide 3D visualization and inspection of objects such parcels and their contents. Also, without tomography, a simple 2D image does not give the positioning of the objects in the volume and the understanding of the object in question is not totally possible. For these reasons, a special tomographic algorithm, OSC, is developed for terahertz Gaussian beam propagation and the results showed a successful 3D reconstruction in passive and active imaging. However, some limitations prevent obtaining similar performance as in X-ray tomography. First, the 2D projections suffer from various artifacts that can yield to wrong understanding of the physical state of an object. Also, the technology limitations in terahertz domain especially the low penetration power demean the signal after traversing thick objects and that influences the tomographic reconstruction.

GENERAL CONCLUSION AND PERSPECTIVES

The objective of the present study was to investigate the potential of terahertz in being a complimentary solution for inspection of specific packages from the postal chain, after being scanned by X-ray and still suspicious. Two types of threats are seeking: weapons and explosives and three investigation methods are performed: terahertz spectroscopy, imaging and spectral imaging.

The state of art presented for the different techniques used for threat detection, showed the need of terahertz technology for non-contact, non-ionizing inspection of parcels, to provide imaging and spectral information especially for powder samples. In fact, the high potential of THz radiation compared to the used technologies in the postal chain, such as X-ray, is the possibility of the chemical identification of powder.

For that, we studied the performances of terahertz technology for explosives detection in parcels. This was achieved by performing terahertz spectroscopy and spectral imaging measurements using time-domain technology. This advanced technology presents a high signal to noise ratio and an acceptable effective frequency band, [0-4] THz, which made her an efficient reliable instrument. With this system, one spectrum needs several tens of ms to be measured. As for spectral imaging, one image acquisition takes longer time due to the need of a raster-scan, which for the postal chain, can be sometimes considered as long scanning time.

For postal needs, we performed spectroscopic analysis on several packaging materials. The results show the possibility of measuring through these materials for a frequency up to 3 THz. However, the influence of these materials on the obtained spectra is not neglected, and high carful should be considered when passing through multi-layered package. Moreover, the spectral analysis was performed in laboratory conditions, with high careful, in order to extract low noise, repeatable signal. Yet, the measurements are very sensitive, and a variation in the product signature is occurred by:

- Changing the measurement position on a pellet, the signal can varies from point to point on the same side or from side to another,
- Measuring the same sample obtained from two providers, that can gave variant spectra,
- The method of the signal extraction, and the reference chosen to do so,
- Dealing with different sample configuration: the product is in powder state, or it is made into pellet, with or without binder,
- Dealing with pure elements or mixture of products,
- Having overlap between the spectra, which make impossible to identify each element when they are in mixture.

All these reasons make complicated the transfer of the technology to the industrial world especially when we need to detect mixtures of components. However, by using statistical methods to analyze the response of the material, such as chemometric tools, it is possible to extract significant information about the data. In our study we applied three of these tools on terahertz spectra and spectral images. PCA was performed to visualize and understand unknown set off data, PLS was used to create a model able to quantify unknown sample and PLS-DA was established to create a model able to classify unknown explosives.

The quantitative analysis was performed on terahertz spectra by PLS model, on two explosives: RDX and PETN explosives as well as their mixture, with variant concentrations. The PLS2 model showed better performances than the PLS1, with a prediction error of less than 3.5 mg in a mass of 400 mg. This result is considered very acceptable, yet, the prediction performances are better to be fixed by the user. Moreover, The PLS2 model was able to quantify explosives sample in restricted region even when it presents an overlap. This shows that it is not necessarily to have access to broadband frequency to be able to quantify explosives.

To overtake the limitation of analysis on only spectral measurements, and to be able to analyze sample directly from an image, chemometric tools was applied on terahertz spectral images. PCA analysis showed a capability in providing automatically a good contrasted image of an unknown set of data, where it is possible to identify similarity and groups, and understand the variety of elements on the image. Then, region of interest can be extracted to apply a classification model and identify each component. To do so, the PLS-DA algorithm was performed and the optimum calibration model that can be created to classify unknown data was demonstrated. This model was able to achieve a successful prediction with 100% of correct classification. Moreover, we demonstrated that a model created by data of spectroscopic measurements is able to quantify, with an error less than 6 mg inside a 400 mg pellet, explosives spectra carried out using spectral-imaging measurements.

These models are the first demonstration of the algorithm that can be incorporated into industrial systems and use terahertz technology to automatically analyze spectral information, even on images, to identify, discriminate and quantify explosives and explosive mixtures. However, in this study, we were limited by the variety of samples, due to the difficulty to access such products, and only binary mixtures are analyzed, yet it is recommended to test the performances of the presented models, when dealing with ternary mixtures and a larger number of samples.

To go further in terahertz spectroscopy for parcels inspection, the response of explosives in powders should be analyzed by chemometric tools, because pellets are not the real life state of explosives. In contrast, this cannot be achieved by transmission configuration due to the high absorbance of the powder. Thus, reflection geometry should be performed on explosive. Furthermore, the performances of the models should be tested using spectra of powders measured though packaging.

As for imaging, we compared the potential of three different millimeter wave imaging techniques in parcel inspection. The first one is a passive system that is able to image large parcels in few seconds, yet, the resolution and the signal-to-noise ratio are not efficient for parcels. However, higher frequencies should be considered.

Active imaging was also tested using two different technologies, CW and FMCW, in transmission and reflection configuration at two frequencies. The power emitted by the sources of these two setups was capable to traverse parcels of tens of centimeter thick with good resolution and low noise. The reflection configuration presents several limitations that cause the loss of information on the image due to the loss of the signal by artifacts. As for transmission configuration, although the good performances that it showed, when the content of the parcel presents several juxtaposed objects, the identification of each of them is difficult. In this case, a tomographic reconstruction can be the

solution. For that, we developed the OSC algorithm that is compatible with tomographic reconstruction when dealing with a Gaussian propagation like in the case of the THz waves. In comparison to the existent tomographic algorithm, the OSC showed fewer artifacts obtained from the reconstruction. However, it cannot remove the physical artifacts caused by the measurement. Using this algorithm, we performed for the first time, a tomographic reconstruction from data obtained from a passive system; also we showed the capacity in reconstructing an object inside a parcel. However, the low penetration power limits the reconstruction performances.

This study successfully demonstrates the potential of 2D and 3D millimeter wave imaging in detecting threats through packaging; however, terahertz technology cannot perform with the same efficiency as X-ray systems, which are the main technology used in postal sorting centers. It suffers from several limitations like the impossibility of measuring through metal.

Finally, terahertz technology showed good and promising performances in parcel inspection for explosives and weapons detection. Yet, a lot of technological developments are needed in order to incorporate terahertz technology in industry.

BIBLIOGRAPHY

[1] A. J. Kerecman, "Real Time Millimeter Wave Imaging," in *DEvelopments in Electronic Imaging Techniques. International Society for Optics and Photonics*, 1973, pp. 69–76.

[2] D. J. Paul, "The progress towards terahertz quantum cascade lasers on silicon substrates," *Laser Photon. Rev.*, vol. 4, no. 5, pp. 610–632, 2010.

[3] B. Gutschwager, C. Monte, H. Delsim-Hashemi, O. Grimm, and J. Hollandt, "Calculable blackbody radiation as a source for the determination of the spectral responsivity of THz detectors," *Metrologia*, vol. 46, no. 4, p. S165, 2009.

[4] A. Svetlitza, M. Slavenko, T. Blank, I. Brouk, S. Stolyarova, and Y. Nemirovsky, "THz measurements and calibration based on a blackbody source," *Terahertz Sci. Technol. IEEE Trans.*, vol. 4, no. 3, pp. 347–359, 2014.

[5] J.-S. Rieh, D. Yoon, and J. Yun, "An overview of solid-state electronic sources and detectors for Terahertz imaging," in *Solid-State and Integrated Circuit Technology (ICSICT), 2014 12th IEEE International Conference on*, 2014, pp. 1–4.

[6] J. H. Booske, R. J. Dobbs, C. D. Joye, C. L. Kory, G. R. Neil, G.-S. Park, J. Park, and R. J. Temkin, "Vacuum electronic high power terahertz sources," *Terahertz Sci. Technol. IEEE Trans.*, vol. 1, no. 1, pp. 54–75, 2011.

[7] P. Tan, J. Huang, K. Liu, Y. Xiong, and M. Fan, "Terahertz radiation sources based on free electron lasers and their applications," *Sci. China Inf. Sci.*, vol. 55, no. 1, pp. 1–15, 2012.

[8] V. S. Cherkassky, B. A. Knyazev, V. V Kubarev, G. N. Kulipanov, G. L. Kuryshev, A. N. Matveenko, A. K. Petrov, V. M. Popik, M. A. Scheglov, and O. A. Shevchenko, "Imaging techniques for a high-power THz free electron laser," *Nucl. Instruments Methods Phys. Res. Sect. A Accel. Spectrometers, Detect. Assoc. Equip.*, vol. 543, no. 1, pp. 102–109, 2005.

[9] Y. U. Jeong, G. M. Kazakevitch, H. J. Cha, S. H. Park, and B. C. Lee, "Application of a wide-band compact FEL on THz imaging," *Nucl. Instruments Methods Phys. Res. Sect. A Accel. Spectrometers, Detect. Assoc. Equip.*, vol. 543, no. 1, pp. 90–95, 2005.

[10] C. Sung, S. Y. Tochitsky, J. E. Ralph, S. Reiche, J. B. Rosenzweig, C. Pellegrini, and C. Joshi, "High-gain seeded FEL amplifier tunable in the terahertz range," in *Proceedings of the 27th International Free Electron Laser Conference, California*, 2005, vol. 87, p. 90.

[11] B. A. Knyazev, G. N. Kulipanov, and N. A. Vinokurov, "Novosibirsk terahertz free electron laser: instrumentation development and experimental achievements," *Meas. Sci. Technol.*, vol. 21, no. 5, p. 54017, 2010.

[12] T. Idehara, T. Saito, H. Mori, H. Tsuchiya, L. Agusu, and S. Mitsudo, "The first experiment of a THz gyrotron with a pulse magnet," *Int. J. Infrared Millimeter Waves*, vol. 27, no. 3, pp.

319–331, 2006.

[13] G. Dammertz, S. Alberti, A. Arnold, E. Borie, V. Erckmann, G. Gantenbein, E. Giguet, R. Heidinger, J. P. Hogge, S. Illy, W. Kasparek, K. Koppenburg, M. Kuntze, H. P. Laqua, G. LeCloarec, Y. LeGoff, W. Leonhardt, C. Lievin, R. Magne, G. Michel, G. Müller, G. Neffe, B. Piosczyk, M. Schmid, K. Schwörer, M. K. Thumm, and M. Q. Tran, "Development of a 140-GHz 1-MW continuous wave gyrotron for the W7-X stellarator," *IEEE Trans. Plasma Sci.*, vol. 30, no. 3 I, pp. 808–818, 2002.

[14] M. Y. Glyavin, N. S. Ginzburg, A. L. Goldenberg, G. G. Denisov, and A. G. Luchinin, "THz Gyrotrons : Status and Possible Optimizations," vol. 5, no. 2, pp. 67–77, 2012.

[15] B. Gompf, M. Gerull, T. Müller, and M. Dressel, "THz-micro-spectroscopy with backward-wave oscillators," *Infrared Phys. Technol.*, vol. 49, no. 1, pp. 128–132, 2006.

[16] B. Gorshunov, A. Volkov, I. Spektor, A. Prokhorov, A. Mukhin, M. Dressel, S. Uchida, and A. Loidl, "Terahertz BWO-spectrosopy," *Int. J. Infrared Millimeter Waves*, vol. 26, no. 9, pp. 1217–1240, 2005.

[17] A. Dobroiu, M. Yamashita, Y. N. Ohshima, Y. Morita, C. Otani, and K. Kawase, "Terahertz imaging system based on a backward-wave oscillator," *Appl. Opt.*, vol. 43, no. 30, pp. 5637–5646, 2004.

[18] P. Dean, A. Valavanis, J. Keeley, K. Bertling, Y. L. Lim, R. Alhathlool, A. D. Burnett, L. H. Li, S. P. Khanna, and D. Indjin, "Terahertz imaging using quantum cascade lasers—a review of systems and applications," *J. Phys. D. Appl. Phys.*, vol. 47, no. 37, p. 374008, 2014.

[19] B. S. Williams, H. Callebaut, S. Kumar, Q. Hu, and J. L. Reno, "3.4-THz quantum cascade laser based on longitudinal-optical-phonon scattering for depopulation," *Appl. Phys. Lett.*, vol. 82, no. 7, pp. 1015–1017, 2003.

[20] C. Worrall, J. Alton, M. Houghton, S. Barbieri, H. E. Beere, D. Ritchie, and C. Sirtori, "Continuous wave operation of a superlattice quantum cascade laser emitting at 2 THz," *Opt. Express*, vol. 14, no. 1, pp. 171–181, 2006.

[21] A. W. M. Lee, B. S. Williams, S. Kumar, Q. Hu, and J. L. Reno, "Real-time imaging using a 4.3-THz quantum cascade laser and a 320/spl times/240 microbolometer focal-plane array," *Photonics Technol. Lett. IEEE*, vol. 18, no. 13, pp. 1415–1417, 2006.

[22] D. Turčinková, G. Scalari, F. Castellano, M. I. Amanti, M. Beck, and J. Faist, "Ultra-broadband heterogeneous quantum cascade laser emitting from 2.2 to 3.2 THz," *Appl. Phys. Lett.*, vol. 99, no. 19, p. 191104, 2011.

[23] Y. C. Shen, P. C. Upadhya, H. E. Beere, E. H. Linfield, A. G. Davies, I. S. Gregory, C. Baker, W. R. Tribe, and M. J. Evans, "Generation and detection of ultrabroadband terahertz radiation using photoconductive emitters and receivers," *Appl. Phys. Lett.*, vol. 85, no. 2, pp. 164–166, 2004.

[24] J.-L. Coutaz, *Optoélectronique térahertz*. 2008.

[25] A. Rice, Y. Jin, X. F. Ma, X. Zhang, D. Bliss, J. Larkin, and M. Alexander, "Terahertz optical rectification from< 110> zinc-blende crystals," *Appl. Phys. Lett.*, vol. 64, no. 11, pp. 1324–1326, 1994.

[26] D. J. Cook and R. M. Hochstrasser, "Intense terahertz pulses by four-wave rectification in air," *Opt. Lett.*, vol. 25, no. 16, pp. 1210–1212, 2000.

[27] K. L. Yeh, M. C. Hoffmann, J. Hebling, and K. A. Nelson, "Generation of 10 J ultrashort terahertz pulses by optical rectification," *Appl. Phys. Lett*, vol. 90, no. 17, p. 171121, 2007.

[28] F. Simoens, "THz Bolometer Detectors," in *Physics and Applications of Terahertz Radiation*, Springer, 2014, pp. 35–75.

[29] W. Knap, M. Dyakonov, D. Coquillat, F. Teppe, N. Dyakonova, J. Łusakowski, K. Karpierz, M. Sakowicz, G. Valusis, and D. Seliuta, "Field effect transistors for terahertz detection: physics and first imaging applications," *J. Infrared, Millimeter, Terahertz Waves*, vol. 30, no. 12, pp. 1319–1337, 2009.

[30] N. Karpowicz, H. Zhong, J. Xu, K.-I. Lin, J.-S. Hwang, and X.-C. Zhang, "Non-destructive sub-THz CW imaging," in *Integrated Optoelectronic Devices 2005*, 2005, pp. 132–142.

[31] M. Tani, M. Herrmann, and K. Sakai, "Generation and detection of terahertz pulsed radiation with photoconductive antennas and its application to imaging," *Meas. Sci. Technol.*, vol. 13, no. 11, p. 1739, 2002.

[32] D. Saeedkia, "Terahertz photoconductive antennas: Principles and applications," in *Proceedings of the 5th European Conference on Antennas and Propagation (EUCAP)*, 2011.

[33] Q. Wu and X.-C. Zhang, "7 terahertz broadband GaP electro-optic sensor," *Appl. Phys. Lett.*, vol. 70, no. 14, pp. 1784–1786, 1997.

[34] Q. Wu and X.-C. Zhang, "Design and characterization of traveling-wave electrooptic terahertz sensors," *Sel. Top. Quantum Electron. IEEE J.*, vol. 2, no. 3, pp. 693–700, 1996.

[35] M. R. Scarfi, M. Romano, R. Di Pietro, O. Zeni, A. Doria, G. P. Gallerano, E. Giovenale, G. Messina, A. Lai, and G. Campurra, "THz exposure of whole blood for the study of biological effects on human lymphocytes," *J. Biol. Phys.*, vol. 29, no. 2–3, pp. 171–176, 2003.

[36] A. Markelz, S. Whitmire, J. Hillebrecht, and R. Birge, "THz time domain spectroscopy of biomolecular conformational modes," *Phys. Med. Biol.*, vol. 47, no. 21, p. 3797, 2002.

[37] B. M. Fischer, M. Walther, and P. U. Jepsen, "Far-infrared vibrational modes of DNA components studied by terahertz time-domain spectroscopy," *Phys. Med. Biol.*, vol. 47, no. 21, p. 3807, 2002.

[38] P. H. Bolivar, M. Brucherseifer, M. Nagel, H. Kurz, and A. Bosserhoff, "Label-free probing of genes by time-domain terahertz sensing," *Phys. Med. Biol.*, vol. 47, no. 21, p. 3815, 2002.

[39] V. P. Wallace, A. J. Fitzgerald, S. Shankar, N. Flanagan, R. Pye, J. Cluff, and D. D. Arnone, "Terahertz pulsed imaging of basal cell carcinoma ex vivo and in vivo," *Br. J. Dermatol.*, vol. 151, no. 2, pp. 424–432, 2004.

[40] R. M. Woodward, V. P. Wallace, R. J. Pye, B. E. Cole, D. D. Arnone, E. H. Linfield, and M. Pepper, "Terahertz pulse imaging of ex vivo basal cell carcinoma," *J. Invest. Dermatol.*, vol. 120, no. 1, pp. 72–78, 2003.

[41] K. J. Siebert, T. Löffler, H. Quast, M. Thomson, T. Bauer, R. Leonhardt, S. Czasch, and H. G. Roskos, "All-optoelectronic continuous wave THz imaging for biomedical applications," *Phys. Med. Biol.*, vol. 47, no. 21, p. 3743, 2002.

[42] L. Ho, R. Müller, M. Römer, K. C. Gordon, J. Heinämäki, P. Kleinebudde, M. Pepper, T. Rades, Y. C. Shen, and C. J. Strachan, "Analysis of sustained-release tablet film coats using terahertz pulsed imaging," *J. Control. release*, vol. 119, no. 3, pp. 253–261, 2007.

[43] P. F. Taday, I. V Bradley, D. D. Arnone, and M. Pepper, "Using terahertz pulse spectroscopy to study the crystalline structure of a drug: a case study of the polymorphs of ranitidine hydrochloride," *J. Pharm. Sci.*, vol. 92, no. 4, pp. 831–838, 2003.

[44] J. A. Zeitler, D. A. Newnham, P. F. Taday, T. L. Threlfall, R. W. Lancaster, R. W. Berg, C. J. Strachan, M. Pepper, K. C. Gordon, and T. Rades, "Characterization of temperature-induced phase transitions in five polymorphic forms of sulfathiazole by terahertz pulsed spectroscopy and differential scanning calorimetry," *J. Pharm. Sci.*, vol. 95, no. 11, pp. 2486–2498, 2006.

[45] J. B. Jackson, J. Bowen, G. Walker, J. Labaune, G. Mourou, M. Menu, and K. Fukunaga, "A survey of terahertz applications in cultural heritage conservation science," *IEEE Trans.*

Terahertz Sci. Technol, vol. 1, no. 1, pp. 220–231, 2011.

[46] K. Fukunaga and I. Hosako, "Innovative non-invasive analysis techniques for cultural heritage using terahertz technology," *Comptes Rendus Phys.*, vol. 11, no. 7, pp. 519–526, 2010.

[47] E. Abraham, A. Younus, J.-C. Delagnes, and P. Mounaix, "Non-invasive investigation of art paintings by terahertz imaging," *Appl. Phys. A*, vol. 100, no. 3, pp. 585–590, 2010.

[48] L. Bassel, J. B. Perraut, J. BouSleiman, B. Bousquet, H. Ballacey, B. Recur, H. Coqueugniot, N. Del, P. Solar, and R. Chapoulie, "3D terahertz versus X-ray imaging for Mochica ceramic investigation," *sub. IRMMW-THz*, 2014.

[49] G. Ducournau, P. Szriftgiser, A. Beck, D. Bacquet, F. Pavanello, E. Peytavit, M. Zaknoune, T. Akalin, and J.-F. Lampin, "Ultrawide-bandwidth single-channel 0.4-THz wireless link combining broadband quasi-optic photomixer and coherent detection," *Terahertz Sci. Technol. IEEE Trans.*, vol. 4, no. 3, pp. 328–337, 2014.

[50] T. Kleine-Ostmann and T. Nagatsuma, "A review on terahertz communications research," *J. Infrared, Millimeter, Terahertz Waves*, vol. 32, no. 2, pp. 143–171, 2011.

[51] J. Federici and L. Moeller, "Review of terahertz and subterahertz wireless communications," *J. Appl. Phys.*, vol. 107, no. 11, p. 111101, 2010.

[52] Y. Guan, M. Yamamoto, T. Kitazawa, S. R. Tripathi, K. Takeya, and K. Kawase, "A Concealed Barcode Identification System Using Terahertz Time-domain Spectroscopy," *J. Infrared, Millimeter, Terahertz Waves*, vol. 36, no. 3, pp. 298–311, 2015.

[53] C. O. Marshall, Maurice; Jimmie, *Aspects of explosives detection. Elsevier*. 2011.

[54] U. S. D. of State, "Overseas bomb threat awareness," 2001.

[55] K. Podoliak, "The Evolution of the Detonator," in *New Leaders' Conference*, 2004.

[56] Tenney L. Davis and T. L. Davis, *The Chemistry of Powder and Explosives*. John Wiley, 1943.

[57] D. Cranney and W. Sudweeks, "Chemical explosives," in *Handbook of Industrial Chemistry and Biotechnology*, 2012, pp. 1473–1495.

[58] H. Schubert and K. Andrey, *Detection of liquid explosives and flammable agents in connection with terrorism*, no. 1. Springer Science & Business Media, 2008.

[59] T. J. Shaw, D. Brown, J. D'Arcy, F. Liu, P. Shea, M. Sivakumar, and T. Gozani, "Small threat and contraband detection with TNA-based systems," *Appl. Radiat. Isot.*, vol. 63, no. 5, pp. 779–782, 2005.

[60] D. Strellis and T. Gozani, "Classifying threats with a 14-MeV neutron interrogation system," *Appl. Radiat. Isot.*, vol. 63, no. 5, pp. 799–803, 2005.

[61] D. Sudac, S. Blagus, and V. Valkovic, "Chemical composition identification using fast neutrons," *Appl. Radiat. Isot.*, vol. 61, no. 1, pp. 73–79, 2004.

[62] R. Osman, Ahmad; Abd-elrhman, Ashraf; Bashter, ll; Megahid, "Detection and Identification of Contraband in Air Cargo Containers Using Neutron Based Techniques," *J. Nucl. Energy Sci. Power Gener. Technol.*, vol. 2, no. 3, pp. 2–6, 2013.

[63] W. A. Megahid, R.M., Osman, A.M., Kansouhfg, "Neutron Based Techniques for the Detection of Illicit Materials and Explosives," 2009.

[64] T. Gozani, "The role of neutron based inspection techniques in the post 9/11/01 era," *Nucl. Instruments Methods Phys. Res. Sect. B Beam Interact. with Mater. Atoms*, vol. 213, pp. 460–463, 2004.

[65] D. Sudac, S. Blagus, and V. Valkovic, "Inspections for contraband in a shipping container using fast neutrons and the associated alpha particle technique: Proof of principle," *Nucl.*

Instruments Methods Phys. Res. Sect. B Beam Interact. with Mater. Atoms, vol. 241, no. 1, pp. 798–803, 2005.

[66] G. Harding, "X-ray scatter tomography for explosives detection," *Radiat. Phys. Chem.*, vol. 71, pp. 869–881, 2004.

[67] K. Wells and D. A. Bradley, "A review of X-ray explosives detection techniques for checked baggage," *Appl. Radiat. Isot.*, vol. 70, no. 8, pp. 1729–1746, 2012.

[68] R. Ewing, "A critical review of ion mobility spectrometry for the detection of explosives and explosive related compounds," *Talanta*, vol. 54, pp. 515–529, 2001.

[69] G. Reid Asbury, J. Klasmeier, and H. H. Hill, "Analysis of explosives using electrospray ionization/ion mobility spectrometry (ESI/IMS)," *Talanta*, vol. 50, no. 6, pp. 1291–1298, 2000.

[70] A. B. Kanu and H. H. Hill, "Ion mobility spectrometry: recent developments and novel applications," *LabPlus Int. April.*, no. May, pp. 20–26, 2004.

[71] Z. Takáts, I. Cotte-Rodriguez, N. Talaty, H. Chen, and R. G. Cooks, "Direct, trace level detection of explosives on ambient surfaces by desorption electrospray ionization mass spectrometry.," *Chem. Commun. (Camb).*, no. 15, pp. 1950–1952, 2005.

[72] J. M. Nilles, T. R. Connell, S. T. Stokes, and H. Dupont Durst, "Explosives detection using direct analysis in real time (DART) mass spectrometry," *Propellants, Explos. Pyrotech.*, vol. 35, no. 5, pp. 446–451, 2010.

[73] Y. Zhang, X. Ma, S. Zhang, C. Yang, Z. Ouyang, and X. Zhang, "Direct detection of explosives on solid surfaces by low temperature plasma desorption mass spectrometry.," *Analyst*, vol. 134, no. 1, pp. 176–181, 2009.

[74] D. R. Justes, N. Talaty, I. Cotte-Rodriguez, and R. G. Cooks, "Detection of explosives on skin using ambient ionization mass spectrometry.," *Chem. Commun. (Camb).*, no. 21, pp. 2142–2144, 2007.

[75] N. Gupta and R. Dahmani, "AOTF Raman spectrometer for remote detection of explosives," *Spectrochim. Acta Part A Mol. Biomol. Spectrosc.*, vol. 56, no. 8, pp. 1453–1456, 2000.

[76] J. C. Carter, S. M. Angel, M. Lawrence-Snyder, J. Scaffidi, R. E. Whipple, and J. G. Reynolds, "Standoff detection of high explosive materials at 50 meters in ambient light conditions using a small Raman instrument," *Appl. Spectrosc.*, vol. 59, no. 6, pp. 769–775, 2005.

[77] D. S. Moore and R. J. Scharff, "Portable Raman explosives detection," *Anal. Bioanal. Chem.*, vol. 393, no. 6–7, pp. 1571–1578, 2009.

[78] R. M. Wentworth, J. Neiss, M. P. Nelson, and P. J. Treado, "Standoff Raman hyperspectral imaging detection of explosives," in *Antennas and Propagation Society International Symposium, 2007 IEEE*, 2007, pp. 4925–4928.

[79] J. Moros, J. A. Lorenzo, P. Lucena, L. Miguel Tobaria, and J. J. Laserna, "Simultaneous Raman Spectroscopy− Laser-Induced Breakdown Spectroscopy for instant standoff analysis of explosives using a mobile integrated sensor platform," *Anal. Chem.*, vol. 82, no. 4, pp. 1389–1400, 2010.

[80] S. Singh, "Sensors—an effective approach for the detection of explosives," *J. Hazard. Mater.*, vol. 144, no. 1, pp. 15–28, 2007.

[81] L. Senesac and T. G. Thundat, "Nanosensors for trace explosive detection," *Mater. Today*, vol. 11, no. 3, pp. 28–36, 2008.

[82] G. S. Dow, D. C. W. Lo, Y. Guo, E. W. Lin, T. T. Chung, M. D. Biedenbender, O. Miromontes, A. Marashi, L. Yujiri, and P. S. C. Lee, "Large scale W-band focal plane array

for passive radiometric imaging," in *Microwave Symposium Digest, 1996., IEEE MTT-S International*, 1996, vol. 1, pp. 369–372.

[83] C. Martin, S. Clark, J. Galliano, and J. Lovberg, "Advances in millimeter-wave imaging technology for enhanced vision systems," in *Digital Avionics Systems Conference, 2002. Proceedings. The 21st*, 2002, vol. 2, pp. 11D4–1.

[84] R. Appleby, R. N. Anderton, S. Price, N. A. Salmon, G. N. Sinclair, P. R. Coward, A. R. Barnes, P. D. Munday, M. Moore, and A. H. Lettington, "Mechanically scanned real-time passive millimeter-wave imaging at 94 GHz," in *AeroSense 2003*, 2003, pp. 1–6.

[85] R. N. Anderton, R. Appleby, J. E. Beale, P. R. Coward, and S. Price, "Security scanning at 94GHz," in *Defense and Security Symposium*, 2006, p. 62110C–62110C.

[86] J. Lampin, M. Zaknoune, X. Wallart, L. Desplanque, E. Peytavit, and G. Ducournau, "Millimeter wave passive radiometric imaging system," 2012.

[87] B. Rajaonah, J.-B. Ravenel, J. C. Castelli, A. Osmont, P. Cabrol, and G. Le Fur, "Acceptabilité des scanners de sûreté dans les aéroports français," in *Workshop Interdisciplinaire sur la Sécurité Globale-WISG2013*, 2013.

[88] N. A. Salmon, J. Beale, S. Hayward, P. Hall, R. Macpherson, R. Metcalfe, and A. Harvey, "Compact and light-weight digital beam-forming passive millimetre-wave imagers," in *SPIE Europe Security and Defence*, 2008, p. 711709.

[89] A. Luukanen, R. Appleby, M. Kemp, and N. Salmon, "Millimeter-wave and terahertz imaging in security applications," in *Terahertz Spectroscopy and Imaging*, Springer, 2012, pp. 491–520.

[90] D. L. McMakin, P. E. Keller, D. M. Sheen, and T. E. Hall, "Dual-surface dielectric depth detector for holographic millimeter-wave security scanners," in *SPIE Defense, Security, and Sensing*, 2009, p. 73090G–73090G.

[91] D. M. Sheen, D. L. McMakin, and T. E. Hall, "Three-dimensional millimeter-wave imaging for concealed weapon detection," *Microw. Theory Tech. IEEE Trans.*, vol. 49, no. 9, pp. 1581–1592, 2001.

[92] H. Essen, R. Zimmermann, S. Hantscher, and N. Pohl, "3D millimetre-wave scanner for luggage and parcels," in *SPIE Security+ Defence*, 2012, p. 854406.

[93] H.-B. Liu, H. Zhong, N. Karpowicz, Y. Chen, and X.-C. Zhang, "Terahertz Spectroscopy and Imaging for Defense and Security Applications," *Proc. IEEE IEEE*, vol. 95, no. 8, pp. 1514–1527, 2007.

[94] E. Öjefors, N. Baktash, Y. Zhao, R. Al Hadi, H. Sherry, and U. R. Pfeiffer, "Terahertz imaging detectors in a 65-nm CMOS SOI technology," in *ESSCIRC, 2010 Proceedings of the*, 2010, pp. 486–489.

[95] D. G. Allis, D. A. Prokhorova, A. M. Fedor, and T. M. Korter, "First principles analysis of the terahertz spectrum of PETN," in *Defense and Security Symposium*, 2006, p. 62120F–62120F.

[96] R. Beigang, S. G. Biedron, S. Dyjak, F. Ellrich, M. W. Haakestad, D. Hübsch, T. Kartaloglu, E. Ozbay, F. Ospald, and N. Palka, "Comparison of terahertz technologies for detection and identification of explosives," in *SPIE Sensing Technology+ Applications*, 2014, p. 91020C–91020C.

[97] A. G. Davies, A. D. Burnett, W. Fan, E. H. Linfield, and J. E. Cunningham, "Terahertz spectroscopy of explosives and drugs," *Mater. today*, vol. 11, no. 3, pp. 18–26, 2008.

[98] Y. Hu, P. Huang, L. Guo, X. Wang, and C. Zhang, "Terahertz spectroscopic investigations of explosives," *Phys. Lett. A*, vol. 359, no. 6, pp. 728–732, 2006.

[99] M. R. Leahy-Hoppa, M. J. Fitch, and R. Osiander, “Terahertz spectroscopy techniques for explosives detection,” *Anal. Bioanal. Chem.*, vol. 395, no. 2, pp. 247–257, 2009.

[100] N. Palka, “Identification of concealed materials, including explosives, by terahertz reflection spectroscopy,” *Opt. Eng.*, vol. 53, no. 3, p. 31202, 2014.

[101] W. R. Tribe, D. A. Newnham, P. F. Taday, and M. C. Kemp, “Hidden object detection: security applications of terahertz technology,” in *Integrated Optoelectronic Devices 2004*, 2004, pp. 168–176.

[102] H.-B. Liu, Y. Chen, G. J. Bastiaans, and X.-C. Zhang, “Detection and identification of explosive RDX by THz diffuse reflection spectroscopy,” *Opt. Express*, vol. 14, no. 1, pp. 415–423, 2006.

[103] M. C. Kemp, “Explosives detection by terahertz spectroscopy—a bridge too far?,” *Terahertz Sci. Technol. IEEE Trans.*, vol. 1, no. 1, pp. 282–292, 2011.

[104] T. Ikeda, A. Matsushita, M. Tatsuno, Y. Minami, M. Yamaguchi, K. Yamamoto, M. Tani, and M. Hangyo, “Investigation of inflammable liquids by terahertz spectroscopy,” *Appl. Phys. Lett.*, vol. 87, no. 3, p. 34105, 2005.

[105] K. Kawase, Y. Ogawa, Y. Watanabe, and H. Inoue, “Non-destructive terahertz imaging of illicit drugs using spectral fingerprints,” *Opt. Express*, vol. 11, no. 20, pp. 2549–2554, 2003.

[106] Y. C. Shen, P. F. Taday, D. A. Newnham, and M. Pepper, “Chemical mapping using reflection terahertz pulsed imaging,” *Semicond. Sci. Technol.*, vol. 20, no. 7, p. S254, 2005.

[107] B. Fischer, M. Hoffmann, H. Helm, G. Modjesch, and P. U. Jepsen, “Chemical recognition in terahertz time-domain spectroscopy and imaging,” *Semicond. Sci. Technol.*, vol. 20, no. 7, p. S246, 2005.

[108] Y. Ueno and K. Ajito, “Analytical terahertz spectroscopy,” *Anal. Sci.*, vol. 24, no. 2, pp. 185–192, 2008.

[109] M. Hangyo, M. Tani, and T. Nagashima, “Terahertz time-domain spectroscopy of solids: a review,” *Int. J. Infrared Millimeter Waves*, vol. 26, no. 12, pp. 1661–1690, 2005.

[110] D. G. Allis and T. M. Korter, “Theoretical analysis of the terahertz spectrum of the high explosive PETN,” *ChemPhysChem*, vol. 7, no. 11, pp. 2398–2408, 2006.

[111] D. G. Allis, J. A. Zeitler, P. F. Taday, and T. M. Korter, “Theoretical analysis of the solid-state terahertz spectrum of the high explosive RDX,” *Chem. Phys. Lett.*, vol. 463, no. 1, pp. 84–89, 2008.

[112] G. Kozlov and A. Volkov, “Coherent source submillimeter wave spectroscopy,” in *Millimeter and submillimeter wave spectroscopy of solids*, Springer, 1998, pp. 51–109.

[113] D. H. Auston, K. P. Cheung, and P. R. Smith, “Picosecond photoconducting Hertzian dipoles,” *Appl. Phys. Lett.*, vol. 45, no. 3, pp. 284–286, 1984.

[114] M. Van Exter, C. Fattinger, and D. Grischkowsky, “Terahertz time-domain spectroscopy of water vapor,” *Opt. Lett.*, vol. 14, no. 20, pp. 1128–1130, 1989.

[115] D. M. Mittleman, R. H. Jacobsen, R. Neelamani, R. G. Baraniuk, and M. C. Nuss, “Gas sensing using terahertz time-domain spectroscopy,” *Appl. Phys. B Lasers Opt.*, vol. 67, no. 3, pp. 379–390, 1998.

[116] R. A. Cheville and D. Grischkowsky, “Far-infrared foreign and self-broadened rotational linewidths of high-temperature water vapor,” *JOSA B*, vol. 16, no. 2, pp. 317–322, 1999.

[117] T.-I. Jeon, D. Grischkowsky, A. K. Mukherjee, and R. Menon, “Electrical characterization of conducting polypyrrole by THz time-domain spectroscopy,” *Appl. Phys. Lett.*, vol. 77, no. 16, pp. 2452–2454, 2000.

[118] S. D. Brorson, R. Buhleier, I. E. Trofimov, J. O. White, C. Ludwig, F. F. Balakirev, H.-U. Habermeier, and J. Kuhl, "Electrodynamics of high-temperature superconductors investigated with coherent terahertz pulse spectroscopy," *JOSA B*, vol. 13, no. 9, pp. 1979–1993, 1996.

[119] I. Wilke, M. Khazan, C. T. Rieck, P. Kuzel, C. Jaekel, and H. Kurz, "Time-domain Terahertz spectroscopy as a diagnostic tool for the electrodynamic properties of high temperature superconductors," *Phys. C Supercond.*, vol. 341, pp. 2271–2272, 2000.

[120] N. Vieweg, B. M. Fischer, M. Reuter, P. Kula, R. Dabrowski, M. A. Celik, G. Frenking, M. Koch, and P. U. Jepsen, "Ultrabroadband terahertz spectroscopy of a liquid crystal," *Opt. Express*, vol. 20, no. 27, pp. 28249–28256, 2012.

[121] M.-A. Brun, F. Formanek, A. Yasuda, M. Sekine, N. Ando, and Y. Eishii, "Terahertz imaging applied to cancer diagnosis," *Phys. Med. Biol.*, vol. 55, no. 16, p. 4615, 2010.

[122] C. Baker, W. R. Tribe, T. Lo, B. E. Cole, S. Chandler, and M. C. Kemp, "People screening using terahertz technology (Invited Paper)," 2005, vol. 5790, pp. 1–10.

[123] Y. Huang, N. Khiabani, Y. Shen, and D. Li, "Terahertz photoconductive antenna efficiency," in *Antenna Technology (iWAT), 2011 International Workshop on*, 2011, pp. 152–156.

[124] K. Sakai and M. Tani, "Introduction to terahertz pulses," in *Terahertz optoelectronics*, Springer, 2005, pp. 1–30.

[125] Y.-C. Shen, P. F. Taday, D. A. Newnham, M. C. Kemp, and M. Pepper, "3D chemical mapping using terahertz pulsed imaging," in *Integrated Optoelectronic Devices 2005*, 2005, pp. 24–31.

[126] Dexheimer Suzan, Ed., *Terahertz spectroscopy principales and applications*. 2007.

[127] M. Naftaly and R. Dudley, "Methodologies for determining the dynamic ranges and signal-to-noise ratios of terahertz time-domain spectrometers," *Opt. Lett.*, vol. 34, no. 8, pp. 1213–1215, 2009.

[128] M. Aarstol and M. B. Comisarow, "Apodization of FT-ICR spectra," *Int. J. Mass Spectrom. Ion Process.*, vol. 76, no. 3, pp. 287–297, 1987.

[129] O. M. Solomon Jr, "The use of DFT windows in signal-to-noise ratio and harmonic distortion computations," *Instrum. Meas. IEEE Trans.*, vol. 43, no. 2, pp. 194–199, 1994.

[130] M. Naftaly, J. F. Molloy, G. V Lanskii, K. a Kokh, and Y. M. Andreev, "Terahertz time-domain spectroscopy for textile identification.," *Appl. Opt.*, vol. 52, no. 19, pp. 4433–7, 2013.

[131] L. Munck, L. Nørgaard, S. B. Engelsen, R. Bro, and C. a. Andersson, "Chemometrics in food science - A demonstration of the feasibility of a highly exploratory, inductive evaluation strategy of fundamental scientific significance," *Chemom. Intell. Lab. Syst.*, vol. 44, no. 1–2, pp. 31–60, 1998.

[132] D. MacKay, "Chemometrics, econometrics, psychometrics-How best to handle hedonics?," *Food Qual. Prefer.*, vol. 17, pp. 529–535, 2006.

[133] S. Wold and M. Sjöström, "Chemometrics, present and future success," *Chemom. Intell. Lab. Syst.*, vol. 44, no. 1–2, pp. 3–14, 1998.

[134] J. El Haddad, L. Canioni, and B. Bousquet, "Good practices in LIBS analysis: Review and advices," *Spectrochim. Acta Part B At. Spectrosc.*, vol. 101, pp. 171–182, 2014.

[135] R. B. Shah, M. A. Tawakkul, and M. A. Khan, "Process analytical technology: Chemometric analysis of Raman and near infra-red spectroscopic data for predicting physical properties of extended release matrix tablets," *J. Pharm. Sci.*, vol. 96, no. 5, pp. 1356–1365, 2007.

[136] M. J. Adams, *Chemometrics in analytical spectroscopy*. Royal Society of Chemistry, 2004.

[137] J. Isotalo, "Basics of Statistics," *University of Tampere*. pp. 0–82, 2001.

[138] B. Grung and R. Manne, “Missing values in principal component analysis,” *Chemom. Intell. Lab. Syst.*, vol. 42, no. 1–2, pp. 125–139, 1998.

[139] C. D. Brown and P. D. Wentzell, “Hazards of digital smoothing filters as a preprocessing tool in multivariate calibration,” *J. Chemom.*, vol. 13, no. 2, pp. 133–152, 1999.

[140] G. Shaw and D. Manolakis, “Signal processing for hyperspectral image exploitation,” *IEEE Signal Process. Mag.*, vol. 19, no. January, pp. 12–16, 2002.

[141] Q. Du and J. E. Fowler, “Hyperspectral image compression using JPEG2000 and principal component analysis,” *Geosci. Remote Sens. Lett. IEEE*, vol. 4, no. 2, pp. 201–205, 2007.

[142] M. A. O. Vasilescu and D. Terzopoulos, “Multilinear Image Analysis for Facial Recognition,” in *International Conference on Pattern Recognition*, 2002, pp. 1–4.

[143] M. Hoehse, A. Paul, I. Gornushkin, and U. Panne, “Multivariate classification of pigments and inks using combined Raman spectroscopy and LIBS,” *Anal. Bioanal. Chem.*, vol. 402, no. 4, pp. 1443–1450, 2012.

[144] G. Julnes, *Handbook of Research Methods in Public Administration edited by*. 1999.

[145] H. Abdi and L. J. Williams, “Principal Component Analysis,” *Wiley Interdiscip. Rev. Comput. Stat.*, vol. 2, no. 4, pp. 433–459, 2010.

[146] W. Elmi Rayaleh, “Extraction des connaissances en imagerie microspectrométrique par analyse chimiométrique. Application à la caractérisation des constituants d’un calcul urinaire.,” 2006.

[147] J. J. Gerbrands, “On the relationships between SVD, KLT and PCA,” *Pattern Recognit.*, vol. 14, no. 1, pp. 375–381, 1981.

[148] N. Halko, P.-G. Martinsson, Y. Shkolnisky, and M. Tygert, “An algorithm for the principal component analysis of large data sets,” *SIAM J. Sci. Comput.*, vol. 33, no. 5, pp. 2580–2594, 2011.

[149] P. R. C. Nelson, P. a. Taylor, and J. F. MacGregor, “Missing data methods in PCA and PLS: Score calculations with incomplete observations,” *Chemom. Intell. Lab. Syst.*, vol. 35, no. 1, pp. 45–65, 1996.

[150] B.-H. Mevik and R. Wehrens, “The pls package: principal component and partial least squares regression in R,” *J. Stat. Softw.*, vol. 18, no. 2, pp. 1–24, 2007.

[151] S. Wold, M. Sjöström, and L. Eriksson, “PLS-regression: a basic tool of chemometrics,” *Chemom. Intell. Lab. Syst.*, vol. 58, no. 2, pp. 109–130, 2001.

[152] S. Joe Qin, “Recursive PLS algorithms for adaptive data modeling,” *Comput. Chem. Eng.*, vol. 22, no. 4, pp. 503–514, 1998.

[153] R. Rosipal, N. Kr, and N. Krämer, “Overview and recent advances in partial least squares,” in *Subspace, Latent Structure and Feature Selection*, 2006, pp. 34–51.

[154] S. Chevallier, D. Bertrand, A. Kohler, and P. Courcoux, “Application of PLS-DA in multivariate image analysis,” *J. Chemom.*, vol. 20, no. MAY, pp. 221–229, 2006.

[155] M. Pérez-Enciso and M. Tenenhaus, “Prediction of clinical outcome with microarray data: a partial least squares discriminant analysis (PLS-DA) approach.,” *Hum. Genet.*, vol. 112, no. 5–6, pp. 581–592, 2003.

[156] O. Galtier, O. Abbas, Y. Le Dréau, C. Rebufa, J. Kister, J. Artaud, and N. Dupuy, “Comparison of PLS1-DA, PLS2-DA and SIMCA for classification by origin of crude petroleum oils by MIR and virgin olive oils by NIR for different spectral regions,” *Vib. Spectrosc.*, vol. 55, no. 1, pp. 132–140, 2011.

[157] H. Martens and N. Tormod, *Multivariate calibration*. John Wiley & Sons, 1992.

[158] L. Stahle, “Partial least squares analysis with cross-validation for the two-class problem : a Monte Carlo study,” *J. Chemom.*, vol. 1, no. February, pp. 185–196, 1987.

[159] P. Geladi and B. R. Kowalski, “Partial Least-Squares Regression: A tutorial,” *Anal. Chim. Acta*, vol. 185, pp. 1–17, 1986.

[160] J. El Haddad, “Chimiométrie appliquée à la spectroscopie de plasma induit par laser (LIBS) et à la spectroscopie terahertz.” Université Sciences et Technologies-Bordeaux I, 2013.

[161] Umetrics, “User guide to SIMCA-P+ 12,” 2008.

[162] D. Ballabio and V. Consonni, “Classification tools in chemistry. Part 1: linear models. PLS-DA,” *Anal. Methods*, vol. 5, no. 16, pp. 3790–3798, 2013.

[163] A. C. Silva, L. F. B. L. Pontes, M. F. Pimentel, and M. J. C. Pontes, “Detection of adulteration in hydrated ethyl alcohol fuel using infrared spectroscopy and supervised pattern recognition methods,” *Talanta*, vol. 93, pp. 129–134, 2012.

[164] J. El Haddad, B. Bousquet, L. Canioni, and P. Mounaix, “Review in terahertz spectral analysis,” *TrAC Trends Anal. Chem.*, vol. 44, pp. 98–105, 2013.

[165] Q. Wang and Y. Ma, “Qualitative and quantitative identification of nitrofen in terahertz region,” *Chemom. Intell. Lab. Syst.*, vol. 127, pp. 43–48, 2013.

[166] Y. Hua and H. Zhang, “Qualitative and quantitative detection of pesticides with terahertz time-domain spectroscopy,” *Microw. Theory Tech. IEEE Trans.*, vol. 58, no. 7, pp. 2064–2070, 2010.

[167] J. El Haddad, F. De Miollis, J. Bou Sleiman, L. Canioni, P. Mounaix, and B. Bousquet, “Chemometrics applied to quantitative analysis of ternary mixtures by terahertz spectroscopy,” *Anal. Chem.*, vol. 86, no. 10, pp. 4927–4933, 2014.

[168] Z. Zhang, X. Yu, H. Zhao, T. Xiao, Z. Xi, and H. Xu, “Component analysis to isomer mixture with THz-TDS,” *Opt. Commun.*, vol. 277, pp. 273–276, 2007.

[169] R. Nishikiori, M. Yamaguchi, K. Takano, T. Enatsu, M. Tani, U. C. de Silva, N. Kawashita, T. Takagi, S. Morimoto, and M. Hangyo, “Application of partial least square on quantitative analysis of L-, D-, and DL-tartaric acid by terahertz absorption spectra,” *Chem. Pharm. Bull.*, vol. 56, no. 3, pp. 305–307, 2008.

[170] I. Ermolina, J. Darkwah, and G. Smith, “Characterisation of crystalline-amorphous blends of sucrose with terahertz-pulsed spectroscopy: the development of a prediction technique for estimating the degree of crystallinity with partial least squares regression,” *AAPS PharmSciTech*, vol. 15, no. 2, pp. 253–260, 2014.

[171] T. Bardon, R. K. May, P. F. Taday, and M. Strlič, “Systematic study of terahertz time-domain spectra of historically informed black inks,” *Analyst*, vol. 138, no. 17, pp. 4859–4869, 2013.

[172] M. Franz, B. M. Fischer, and M. Walther, “The Christiansen effect in terahertz time-domain spectra of coarse-grained powders,” *Appl. Phys. Lett.*, vol. 92, pp. 10–13, 2008.

[173] A. Bandyopadhyay, A. Sengupta, R. B. Barat, D. E. Gary, J. F. Federici, M. Chen, and D. B. Tanner, “Effects of scattering on THz spectra of granular solids,” *Int. J. Infrared Millimeter Waves*, vol. 28, pp. 969–978, 2007.

[174] M. R. Leahy-Hoppa, M. J. Fitch, X. Zheng, L. M. Hayden, and R. Osiander, “Wideband terahertz spectroscopy of explosives,” *Chem. Phys. Lett.*, vol. 434, pp. 227–230, 2007.

[175] J. Bou Sleiman, B. Bousquet, N. Palka, and P. Mounaix, “Quantitative Analysis of Hexahydro-1, 3, 5-trinitro-1, 3, 5, Triazine/Pentaerythritol Tetranitrate (RDX–PETN) Mixtures by Terahertz Time Domain Spectroscopy,” *Appl. Spectrosc.*, vol. 69, no. 12, pp. 1464–1471, 2015.

[176] Y. Watanabe, K. Kawase, T. Ikari, H. Ito, Y. Ishikawa, and H. Minamide, "Component analysis of chemical mixtures using terahertz spectroscopic imaging," *Opt. Commun.*, vol. 234, no. 1, pp. 125–129, 2004.

[177] Z. Zhang, X. Yu, H. Zhao, T. Xiao, Z. Xi, and H. Xu, "Component analysis to isomer mixture with THz-TDS," *Opt. Commun.*, vol. 277, no. 2, pp. 273–276, 2007.

[178] M. W. Ayech and D. Ziou, "Terahertz image segmentation using k-means clustering based on weighted feature learning and random pixel sampling," *Neurocomputing*, vol. 175, pp. 243–264, 2016.

[179] E. Peli, "Contrast in complex images," *JOSA A*, vol. 7, no. 10, pp. 2032–2040, 1990.

[180] P. J. Bex and W. Makous, "Spatial frequency, phase, and the contrast of natural images," *JOSA A*, vol. 19, no. 6, pp. 1096–1106, 2002.

[181] S. N. Anfinsen, A. P. Doulgeris, and T. Eltoft, "Estimation of the equivalent number of looks in polarimetric synthetic aperture radar imagery," *Geosci. Remote Sensing, IEEE Trans.*, vol. 47, no. 11, pp. 3795–3809, 2009.

[182] M. Moreno-Moreno, J. Fierrez, and J. Ortega-Garcia, "Millimeter- and Submillimeter-Wave Imaging Technologies for Biometric Purposes," in *Proceedings of XXIV Simposium Nacional de la Union Cientifica Internacional de Radio*, 2009, p. 244.

[183] D. T. Petkie, C. Casto, F. C. De Lucia, S. R. Murrill, B. Redman, R. L. Espinola, C. C. Franck, E. L. Jacobs, S. T. Griffin, C. E. Halford, J. Reynolds, S. O'Brien, and D. Tofsted, "Active and passive imaging in the THz spectral region: phenomenology, dynamic range, modes, and illumination," *J. Opt. Soc. Am. B*, vol. 25, no. 9, pp. 1523–1531, 2008.

[184] B. R. Appleby and R. N. Anderton, "Millimeter-Wave and Submillimeter-Wave Imaging for Security and Surveillance," *Proc. IEEE IEEE*, vol. 95, no. 8, pp. 1683–1690, 2007.

[185] L. Yujiri, M. Shoucri, and P. Moffa, "Passive millimeter-wave imaging," *IEEE microwave magazine*, vol. 1, no. September, pp. 39–50, 2003.

[186] R. A. Lewis, *Terahertz Physics*. Cambridge University Press, 2013.

[187] C. Johnson, "Mathematical Physics of BlackBody Radiation," *Icarus iDucation. Sk. för datavetenskap och Kommun. K. Tek. Högskolan, Stock.*, 2012.

[188] R. Appleby and H. B. Wallace, "Standoff detection of weapons and contraband in the 100 GHz to 1 THz region," *IEEE Trans. Antennas Propag.*, vol. 55, no. 11 I, pp. 2944–2956, 2007.

[189] H. Sato, K. Sawaya, K. Mizuno, J. Uemura, and M. Takeda, "Passive millimeter-wave imaging for security and safety applications," in *Terahertz Physics, Devices, and Systems IV: Advanced Applications in Industry and Defense*, 2010, vol. 7671, pp. 1–11.

[190] L. Yujiri, "Passive Millimeter wave imaging," in *Microwave Symposium Digest*, 2006, no. 3, pp. 98–101.

[191] Y. A. Pirogov, "Passive millimeter-wave imaging," *Radiophys. Quantum Electron.*, vol. 46, pp. 660–670, 2003.

[192] E. Grossman, C. Dietlein, J. Ala-laurinaho, M. Leivo, L. Gronberg, M. Gronholm, P. Lappalainen, A. Rautiainen, A. Tamminen, and A. Luukanen, "Passive terahertz camera for standoff security screening," *Appl. Opt.*, vol. 49, no. 19, pp. 106–120, 2010.

[193] R. Appleby, R. N. Anderton, S. Price, N. A. Salmon, G. N. Sinclair, P. R. Coward, A. R. Barnes, D. Munday, M. Moore, A. H. Lettington, S. A. Rd, and G. Malvern, "Mechanically scanned real time passive millimetre wave imaging at 94GHz," in *Passive Millimeter-Wave Imaging Technology VI and Radar Sensor Technology VII*, 2003, vol. 5077, pp. 1–6.

[194] A. Vertiy, S. Ozbek, A. Pavlyuchenko, M. Tekbas, A. Kizilhan, H. Cetinkaya, A. Unal, and S.

B. Panin, “Short-and long-range passive imaging in millimeter-wave-band,” in *General Assembly and Scientific Symposiumm IEEE*, 2011, pp. 1–4.

[195] M. Kowalski, N. Palka, M. Piszczek, and M. Szustakowski, “Processing of THz images acquired by passive camera,” *Photonics Lett. Pol.*, vol. 4, no. 3, pp. 97–99, 2012.

[196] “Wasa Millimeter Wave , Wax3-864,” Sweden, 2014.

[197] Millitech, “Mechanically-Tuned Gunn Oscillators,” 2004. .

[198] J. Alda, “Laser and Gaussian Beam Propagation and Transformation,” *Opt. Eng.*, vol. 110, pp. 999–1013, 2003.

[199] G. Gbur and E. Wolf, “The Rayleigh range of Gaussian Schell-model beams,” *J. Mod. Opt.*, vol. 48, no. 11, pp. 1735–1741, 2001.

[200] J. B. Perraud, J. Bou Sleiman, F. Simoens, and P. Mounaix, “Refractive index matching for 2D and 3D terahertz imaging improvement,” in *40th International Conference on Infrared, Millimeter, and Terahertz waves*, 2015, p. 1.

[201] H. P. Marshall and G. Koh, “FMCW radars for snow research,” *Cold Reg. Sci. Technol.*, vol. 52, no. 2, pp. 118–131, 2008.

[202] O. Postolache, R. N. Madeira, P. S. Girão, and G. Postolache, “Microwave FMCW Doppler radar implementation for in-house pervasive health care system,” *Med. Meas. Appl. Proc.*, pp. 47–52, 2010.

[203] C. Am Weg, W. Von Spiegel, R. Henneberger, R. Zimmermann, T. Loeffler, and H. G. Roskos, “Fast active THz cameras with ranging capabilities,” *J. Infrared, Millimeter, Terahertz Waves*, vol. 30, no. 12, pp. 1281–1296, 2009.

[204] G. M. Brooker, “Understanding Millimetre Wave FMCW Radars,” no. 2, pp. 152–157, 2005.

[205] F. Friederich, W. Von Spiegel, M. Bauer, F. Meng, M. D. Thomson, S. Boppel, A. Lisauskas, B. Hils, V. Krozer, S. Member, A. Keil, T. Löf, R. Henneberger, A. K. Huhn, G. Spickermann, P. H. Bolívar, and H. G. Roskos, “THz Active Imaging Systems With Real-Time Capabilities,” *IEEE Trans. TERAHERTZ Sci. Technol.*, vol. 1, no. 1, pp. 183–200, 2011.

[206] G. N. Ramachandran and A. V Lakshminarayanan, “Three-dimensional reconstruction from radiographs and electron micrographs: application of convolutions instead of Fourier transforms,” *Proc. Natl. Acad. Sci.*, vol. 68, no. 9, pp. 2236–2240, 1971.

[207] R. N. Bracewell and Ac. Riddle, “Inversion of fan-beam scans in radio astronomy,” *Astrophys. J.*, vol. 150, p. 427, 1967.

[208] L. A. Shepp and B. F. Logan, “The Fourier reconstruction of a head section,” *Nucl. Sci. IEEE Trans.*, vol. 21, no. 3, pp. 21–43, 1974.

[209] J. P. Guillet, B. Recur, L. Frederique, B. Bousquet, L. Canioni, I. Manek-Hönninger, P. Desbarats, and P. Mounaix, “Review of terahertz tomography techniques,” *J. Infrared, Millimeter, Terahertz Waves*, vol. 35, pp. 382–411, 2014.

[210] B. Ferguson, S. Wang, D. Gray, and D. Abbott, “Towards functional 3D T-ray imaging,” *Phys. Med. Biol.*, vol. 47, p. 3735, 2002.

[211] H. Jiang, *Computed tomography principales, design, artifacts, and recent advances*, no. 2. SPIE, 2009.

[212] B. Recur, a Younus, S. Salort, P. Mounaix, B. Chassagne, P. Desbarats, J.-P. Caumes, and E. Abraham, “Investigation on reconstruction methods applied to 3D terahertz computed tomography.,” *Opt. Express*, vol. 19, no. 6, pp. 5105–5117, 2011.

[213] B. Recur, H. Balacey, J. Bou Sleiman, J. B. Perraud, J.-P. Guillet, a. Kingston, and P. Mounaix, “Ordered subsets convex algorithm for 3D terahertz transmission tomography,” *Opt.*

Express, vol. 22, no. 19, p. 23299, 2014.

[214] B. Recur, J. P. Guillet, I. Manek-Hönninger, J. C. Delagnes, W. Benharbone, P. Desbarats, J. P. Domenger, L. Canioni, and P. Mounaix, "Propagation beam consideration for 3D THz computed tomography," *Opt. Express*, vol. 20, no. 6, p. 5817, 2012.

[215] H. Balacey, J.-B. Perraud, J. Bou Sleiman, J.-P. Guillet, B. Recur, and P. Mounaix, "Processing sequence for non-destructive inspection based on 3D terahertz images," *Proc. SPIE*, vol. 9275, p. 92750J, 2014.

AUTHOR CONTRIBUTION

Journal papers

Year 2016

- **Advanced processing sequence for 3D THz imaging**

Hugo Balacey, Benoit Recur, Jean-Baptiste Perraud, Joyce Bou Sleiman, Jean-Paul Guillet, and Patrick Mounaix , IEEE transactions on terahertz science and technology, vol. 6, no. 2, march 2016.

Year 2015

- **Quantitative Analysis of Hexahydro-1,3,5-trinitro-1,3,5, Triazine/Pentaerythritol Tetranitrate (RDX–PETN) Mixtures by Terahertz Time Domain Spectroscopy**

Bou Sleiman, J., Bousquet, B., Palka, N., & Mounaix, P. (2015). Quantitative Analysis of Hexahydro-1, 3, 5-trinitro-1, 3, 5, Triazine/Pentaerythritol Tetranitrate (RDX–PETN) Mixtures by Terahertz Time Domain Spectroscopy. *Applied spectroscopy*, *69*(12), 1464-1471.

- **Low-frequency noise effect on terahertz tomography using thermal detectors**

Guillet, J. P., Recur, B., Balacey, H., Sleiman, J. B., Darracq, F., Lewis, D., & Mounaix, P. (2015). Low-frequency noise effect on terahertz tomography using thermal detectors. *Applied optics*, *54*(22), 6758-6762.

Year 2014

- **Processing sequence for non-destructive inspection based on 3D terahertz images**

Balacey, H., Perraud, J. B., Sleiman, J. B., Guillet, J. P., Recur, B., & Mounaix, P. (2014, November). Processing sequence for non-destructive inspection based on 3D terahertz images. In *SPIE/COS Photonics Asia* (pp. 92750J-92750J). International Society for Optics and Photonics.

- **Ordered subsets convex algorithm for 3D terahertz transmission tomography**

Recur, B., Balacey, H., Bou Sleiman, J., Perraud, J. B., Guillet, J. P., Kingston, A., & Mounaix, P. (2014). Ordered subsets convex algorithm for 3D terahertz transmission tomography. *Optics express*, *22*(19), 23299-23309.

- **Chemometrics Applied to Quantitative Analysis of Ternary Mixtures by Terahertz Spectroscopy**

El Haddad, J., de Miollis, F., Bou Sleiman, J., Canioni, L., Mounaix, P., & Bousquet, B. (2014). Chemometrics applied to quantitative analysis of ternary mixtures by Terahertz spectroscopy. *Analytical chemistry*, *86*(10), 4927-4933.

****

Conference proceedings

Year 2015

- **Discrimination and identification of RDX/PETN explosives by chemometrics applied to terahertz time-domain spectral imaging (invited oral)**

Bou-Sleiman, J., Perraud, J. B., Bousquet, B., Guillet, J. P., Palka, N., & Mounaix, P. (2015, October). Discrimination and identification of RDX/PETN explosives by chemometrics applied to terahertz time-domain spectral imaging. In *SPIE Security+ Defence* (pp. 965109-965109). International Society for Optics and Photonics.

- **Chemical imaging and quantification of RDX/PETN mixtures by PLS applied on terahertz time-domain spectroscopy (Poster)**

Sleiman, J. B., Perraud, J. B., Bousquet, B., Palka, N., Guillet, J. P., & Mounaix, P. (2015, August). Chemical imaging and quantification of RDX/PETN mixtures by PLS applied on terahertz time-domain spectroscopy. In *Infrared, Millimeter, and Terahertz waves (IRMMW-THz), 2015 40th International Conference on* (pp. 1-1). IEEE.

- **Immersion in refractive index matching liquid for 2D and 3D terahertz imaging (oral)**

Perraud, J. B., Sleiman, J. B., Simoens, F., & Mounaix, P. (2015, August). Immersion in refractive index matching liquid for 2D and 3D terahertz imaging. In *Infrared, Millimeter, and Terahertz waves (IRMMW-THz), 2015 40th International Conference on* (pp. 1-1). IEEE.

Year 2014

- **Ordered subsets convex algorithm and automatic image processing sequences: the solid bases for 3D THz inspection (poster)**

Balacey, H., Perraud, J. B., Bou Sleiman, J., Recur, B., Mounaix, P., Duka, M. V., ... & Sulatsky, M. I. (2014, October). Ordered subsets convex algorithm and automatic image processing sequences: the solid bases for 3D THz inspection. In *International Symposium on Ultrafast Phenomena and Terahertz Waves* (p. MS3_2). Optical Society of America.

- **Qualitative and quantitative analysis of explosives by terahertz time-domain spectroscopy: application to imaging (poster)**

Sleiman, J. B., El Haddad, J., Perraud, J. B., Bassel, L., Bousquet, B., Palka, N., & Mounaix, P. (2014, September). Qualitative and quantitative analysis of explosives by terahertz time-domain

spectroscopy: application to imaging. In *IRMMW-THz 2014 39th International Conference on IEEE* (pp. 1-2).

- **3D terahertz versus X-ray imaging for Mochica ceramic investigation (oral)**

Bassel, L., Perraut, J. B., BouSleiman, J., Bousquet, B., Ballacey, H., Recur, B., ... & Mounaix, P. (2014). 3D terahertz versus X-ray imaging for Mochica ceramic investigation. *sub. IRMMW-THz*.

****

Conference and communication without proceedings

Year 2015

- **Identifying explosives by chemometrics with terahertz spectral imaging**

Joyce Bou Sleiman, Jean-Baptiste Perraud, Bruno Bousquet, Jean-Paul Guillet, Norbert Palka and Patrick Mounaix, SPIE newsroom/Defense and security, 03 November 2015

- **THz detection and identification of dangerous objects and substances (invited oral)**

NATO ARW on THz Diagnostics of CBRN effects and Detection of Explosives & CBRN

3-6 November 2015, Izmir, Turkey

Collaboration with:

Military University of Technology, Warsaw, Poland

Fraunhofer Institute for Physical Measurement Techniques IPM, Kaiserslautern, Germany

- **3D-THz imaging vs X-Ray tomography: Applications to material inspection (oral)**

2nd International Conference on Tomography and Materials and Structures (ICTMS)

29 June - 3 July 2015, Quebec, Canada

- **Terahertz Imaging and Spectroscopy: Applications To Defense And Security (Poster)**

3th Laphia International Symoisium, 2-3 July 2015, Bordeaux, France

- **Chemical imaging of RDX PETN explosives by chemometrics applied on terahertz time-domain spectroscopy (oral)**

8Th Terahertz Days Conference, 31March- 2 April 2015, Arêches-Beaufort, France

- **Multivariate analysis of terahertz absorbance spectra: classification and quantitation of explosives mixtures of RDX and PETN (poster)**

8Th Terahertz Days Conference, 31March- 2 April 2015, Arêches-Beaufort, France

- **Ordered subsets convex algorithm and automatic image processing sequences: the solid bases for 3D THz inspection (oral)**

H. Balacey[a,b], J.-B. Perraud[a], J. Bou Sleiman[a], B. Recur[c] and P. Mounaix[a], 8Th Terahertz Days Conference, 31March- 2 April 2015, Arêches-Beaufort, France

- **Qualitative And Quantitative Analysis of Explosives by Terahertz Time domain Spectroscopy: Application to Imaging (poster)**

Congrès annuel de Chimiometrie XVI, 20-21 January 2015, Genève, Suisse

Year 2014

- **Spectroscopy and terahertz imaging for Anthropology science (oral)**

3rd International congress Biomedical Sciences and Methods in Archaeology, 6-9 November 2014, Bordeaux, France

- **Detection of Nonmetallic Guns by Millimeter and submillimeter imaging (poster)**

6th International Workshop on Terahertz Technology and Applications, 11-12 March 2014, Kaiserslautern, Germany

- **Imagerie et spectroscopie Terahertz: applications aux problématiques de défense et de sécurité**

ED SPI day, 6 March 2014

****

Conferences participation

Year 2015

- SPIE Security+ Defence

21-24 September 2015, Toulouse, France, Invited oral

- 2nd International Conference on Tomography and Materials and Structures (ICTMS)

29 June - 3 July 2015, Quebec, Canada, Oral

- 8Th Terahertz Days Conference

31March- 2 April 2015, Arêches-Beaufort, France, Oral and Poster

- Congrès annuel de Chimiometrie XVI

20-21 January 2015, Genève, Suisse, Poster

Year 2014

- 39th International Conference on Infrared, Millimeter, and Terahertz Waves (IRMMW-THz)

14-19 September 2014, University of Arizona,Tucson, USA, Oral and Poster

- 6th International Workshop on Terahertz Technology and Applications

11-12 March 2014, Kaiserslautern, Germany, Poster

Year 2013

- 38th International Conference on Infrared, Millimeter, and Terahertz Waves (IRMMW-THz)

1-6 September 2013, Mainz, Germany, Presentation of 4 poster of the group

****

Activities and distinctions

Teaching at university of Bordeaux (2014-2015).

Science diffusion in high schools (2013-2014).

Vice-president of the 'SPIE Student Chapter Bordeaux', (since March 2015).

Vice-president of the PhD student association SPIDoc, (since July 2014)

PhD student representative in the doctoral school SPI, (March 2014 till February 2015).

****

Distinctions

Best student paper presentation

« SPIE defense and security » conference, Toulouse, 2015

Audience Awards

FameLab competition, France national final, cite des Sciences, Paris.

****